The Dissertation Committee for Ankit Agrawal Certifies that this is the approved version of the following dissertation:

TUNABLE MULTISCALE INFRARED PLASMONICS WITH METAL OXIDE NANOCRYSTALS

Committee:

Delia Milliron, Supervisor

John B. Goodenough

Carlton Grant Willson

Brian A. Korgel

Thomas M. Truskett

TUNABLE MULTISCALE INFRARED PLASMONICS WITH METAL OXIDE NANOCRYSTALS

by

Ankit Agrawal

Dissertation

Presented to the Faculty of the Graduate School of

The University of Texas at Austin

in Partial Fulfillment

of the Requirements

for the Degree of

Doctor of Philosophy

The University of Texas at Austin

December 2017

Acknowledgements

Austin has been wonderful and kind to me from the very moment I set foot in an unknown country, thousands of kilometer away from my family, friends and known territory. Over the past four years, I have made friends both at work and outside who are part of my family now. They not only thought me how to ask right scientific questions but also all the personal experience I had and its impact on my life cannot be expressed in word or quantified in chapters of this dissertation.

First, I would like to thank my advisor Dr. Delia Milliron for always encouraging curiosity and enabling us to explore both definitive and non-definitive ideas. She was always there to teach us the knows and learn along with us the unknowns. I have always been amazed seeing her enthusiasm and energy she puts into getting work done to perfection. Nothing I achieved academically would be possible without your guidance and support.

Each one of my projects is the result of collaboration and hours of discussions with some of the incredible scientists, ever-curious undergraduates, and friends. Evan and Ilka, both of you were great mentors. Jongwook, Ajay, Yang, and Omid(all Drs. aka PostDocs)- it was a pleasure working with you all, without you guys none of my projects would have been possible (literally not possible). It was always so easy to work with each one of you, your experience helped drive the projects, guided my simulations, and come up with innovative but simple solutions to complex problems. Amita, Gabriel, Anthony, and ByungHyo (also Drs aka PostDocs)- we did not work on any project directly, but the countless science discussion we had during the group meeting and in the lab was always constructive. Rob, you made my life difficult by asking all the tough questions all the

time, but I am glad you did that. Clay, you are an awesome happy person, it was always fun discussing plasmon with you. Corey, Camila, Sungyeon, ShinHum, Lauren, Stephen, and Manny – almost every day for past four years I have learned something new from you all. Specially Camila, without you, the lab would have been a mess all the time. Sincere thanks for taking care of us and preventing a bunch of toddlers from accidentally getting hurt. Now, Gary Ong, co-worker and friend, if I need to pick one person as my ideal science buddy, with whom I would like to do and think science with, it will always be you. Your never ending quest for making thing perfect and getting perfect results was little irritating some time but was commendable and motivating. Gary and Dainah, Y'all are more than a co-worker, I can say that no friend has ever had this big impact on my personal evolution as much as you two had in last six month. Dainah, Alex and Danny (undergrads)- it was a pleasure working with you guys and thanks for always being around to make the thing work. I would also like to thank Dr. Edison and Delia for giving me the opportunity to be the teaching assistant in their class. All the collaborators at Rice University and Lawrence Berkeley National Lab, I had a great time working with you all.

Finally, I would thank my family and friends for their support. None of what I am today would have been possible without the support and struggle of my parents. I cannot thank them enough for all they endured in making sure I receive the best education possible.

Abstract

Tunable multiscale infrared plasmonics with metal oxide nanocrystals

Ankit Agrawal, Ph.D.

The University of Texas at Austin, 2017

Supervisor: Delia Milliron

Degenerately doped semiconductor nanocrystals (NC) exhibit a localized surface plasmon resonance (LSPR) that falls in the near- to mid-IR range of the electromagnetic spectrum. Unlike metal, the metal oxide LSPR characteristics can be further tuned by doping, and structural control, or by in situ electrochemical or photochemical charging. Here, we illustrate how intrinsic NC attributes like its crystal structure, shape and size, along with band structure and surface properties affects the LSPR properties and its possible applications. First, the interplay of NC shape and the intrinsic crystal structure on the LSPR was studied using model systems of In:CdO and Cs:WO_3, the latter of which has an intrinsic anisotropic crystal structure. For both systems, a change of shape from spherical to faceted NCs led to as anticipated higher near field enhancements around the particle. However, with Cs:WO_3, presence of an anisotropic hexagonal crystal structure, leads to additional strong LSPR band-splitting into two distinct peaks with comparable intensities. Second, plasmon-molecular vibration coupling, as a proof of concept for sensing applications, was shown using newly developed F and Sn codoped In_2O_3 NCs to couple to the C-H vibration of surface-bound oleate ligands. A combined theoretical and experimental approach was employed to describe the observed plasmon-plasmon coupling, the influence of coupling strength and relative detuning between the

molecular vibration and LSPR on the enhancement factor, and the observed Fano lineshape by deconvoluting the combined response of the LSPR and molecular vibration in transmission, absorption, and reflection. Third, plasmon modulation through dynamic carrier density tuning was investigated using thin films of monodisperse ITO NCs with various doping level and sizes along with an in situ electrochemical setup. From the combination of the in-situ spectroelectrochemical analysis and optical modeling, it was found that often-neglected semiconductor properties, such as band structure modification upon doping and surface chemistry, strongly affect the LSPR modulation behavior. The influence of band structure and effects like Fermi level pinning by surface defect states were shown to cause a surface depletion layer that alters the LSPR properties, namely the extent of LSPR modulation, near field enhancement, and sensitivity of the LSPR to the surrounding.

Table of Contents

List of Tables

List of Figures

Chapter 1

Control of Localized Surface Plasmon Resonances in Metal Oxide Nanocrystals

This chapter is adapted from the work "Ankit Agrawal, Robert W. Johns, Delia J. Milliron. Control of Localized Surface Plasmon Resonances in Metal Oxide Nanocrystals. *Annu. Rev. Mater. Res.*, **2017**, 47:1-31.". My contribution to this work included the discussions on physics of metal oxide LSPR and its application for both dynamic and static application.

1.1 Introduction

A plasmonic response occurs when electromagnetic radiation induces delocalized charge carriers to collectively resonate within a material [1]. In bulk metals, surface plasmon resonances (SPR) propagate along a metal-dielecitric interface carrying energy *via* displacement of charge carriers in the metal. Upon nano-structuring, this resonance is confined to sub-wavelength dimensions, resulting in a non-propagating plasmonic resonance within the volume of the nano-object. These localized surface plasmon resonances (LSPR) amplify the electromagnetic field both within the structure and around it in the form of a strong near field created by the polarization of charge carriers. These resonances have a large extinction cross-section and can be used to concentrate electric fields to nanoscopic length scales well below the diffraction limit. This concentration of light can direct its energy into heat [2–4], electronic state transitions [5,6], and molecular vibrations [7,8]. Energy transfer is enabled by a resonant interaction between the acceptor and the LSPR. The features of a LSPR depend upon the dispersive property of the material, and its interaction with the surroundings. Dispersion of a material is a

frequency dependent property, and for a free electron gas this is expressed using the Drude-Lorentz model (Equation 1.1).

$$\epsilon_p = \epsilon_\infty - \frac{\omega_p^2}{\omega^2 - i\omega\gamma} \quad 1.1$$

The function ϵ_p is a material's complex dielectric function, ϵ_∞ is the high frequency dielectric constant, γ is the damping constant, and ω_p is the plasma frequency which is a function of carrier concentration (N) and effective mass (m_e) as illustrated in Equation 1.2.

$$\omega_p = \sqrt{\frac{Ne^2}{m_e\epsilon_0}} \quad 1.2$$

The peak position of a LSPR is largely impacted by the plasma frequency, ω_p of the electron gas. Traditionally, in metals (Ag or Au) [9–11], due to high carrier concentrations, LSPR for small nanocrystals (substantially sub-wavelength) are at energies in the visible spectrum (Figure 1.1). Further, LSPR energy tuning is achieved by changing the size and morphology of the nanostructures [9,10,12–14], but this can be at the expense of other advantageous properties associated with smaller sizes, such as high packing density, bio-delivery, or facile processing.

Conductive metal oxide (CMO) materials are degenerately doped semiconductors with metal-like optical properties, a class of materials that offer an alternative to traditional metals [15–17]. They exhibit similar and, in some ways, enhanced plasmonic responses in which the LSPR frequency is controlled through chemical composition as well as shape and size of the nanocrystal. This enables physical dimensions to be optimized for the requirements of the target application. Though the behavior of conduction band electrons in metals and CMOs manifest in similar properties such as

high electronic and thermal conductivity and strong polarizability, their origins are quite different. Metals, which are metallically bonded and inherently conducting, have carrier densities on the order of 10^{23} cm^{-3} with the Fermi level well within the conduction band [18]. In contrast, metal oxides are semiconductors and need to be doped via charged impurities or crystal defects to move the Fermi level out of the bandgap and generate free carriers. Though semiconductors can be doped either p- [15] or n-type to make them metallic, most CMOs derive their conductivity from free electrons and those treated within the scope of this review are all n-type. Doping as a means of introducing electrons into the conduction band can yield electron concentrations across several orders of magnitude that can induce LSPR (10^{18}-10^{22} cm^{-3}) [15,17,19,20]. As these values are much lower than those of metals, CMOs have lower plasma frequencies and consequently lower energy LSPR. In nanostructures, CMOs sustain LSPR all across the near- and mid-infrared depending on elemental composition and dopant concentration; each material spanning a range of achievable LSPR energies [16,17,19–26] (Figure 1.1b).

Though doping is a useful tool for controlling carrier concentration in CMOs, it can lead to changes in the mobility of free electrons. High electron scattering off ionized impurity sites in metal oxide such as Sn:In_2O_3 [25,27–30] and Al:ZnO [24,31,32] broaden their LSPRs and hampers the opportunity for strong near field enhancement (NFE) in the IR spectrum. The band structure of the material strongly influences electronic properties. Impurities and defects cause changes in the band structure through the introduction of additional electronic states that differ from the pure material or even induce changes in the crystal structure [33–35]. Recently, some researchers have focused on developing metal oxide compositions such as Ce:In_2O_3 [16] and F, In codoped CdO [36] (Figure 1.1b) that have high electronic mobility developed by defect engineering, co-doping or controlling dopant distribution inside the nanocrystal. The crystal structures of metal oxides can also

vary from symmetric cubic structures like metals, resulting in the degeneracy of the LSPR, to anisotropic crystal structures that break the degeneracy as a result of unequal effective mass and electron mobilities in different crystallographic orientations [26]. The ways in which defect engineering can be applied to impact the plasmonic properties of metal oxides will be discussed in detail within this review.

As the size and shape of CMO nanocrystals (NCs) can be tuned independently of their optical response, they can easily be optimized to meet application requirements across the electromagnetic spectrum [19,37] (Figure 1.1). Metal oxides exhibiting IR LSPR as nanoscale colloids makes them uniquely suited for wide variety of applications. CMO nanomaterials such as tungsten oxide-based compositions [23,26,38], whose LSPR overlaps well with the therapeutic window [39], (Figure 1.1a) have already been applied to photothermal therapy [3,4,40–42]. Sn:In_2O_3, one of the most widely studied CMOs, has a widely tunable LSPR that has been used for enhancement of infrared vibrational spectroscopy [8] and waste heat management [43] in the mid-IR, as well as plasmon enhanced two photon upconversion in the near-infrared (NIR) [44], and other applications [28,45–47]. Not only have static applications been developed in CMOs, but electrochemical [28,48–50], photochemical [22,47,51] and redox modulation [46] of the LSPR are all easily achievable, making these materials a highly dynamic alternative to metals for applications of IR and visible plasmonics such as sensors [46], smart windows [25,28,52] and telecommunications [45,53,54].

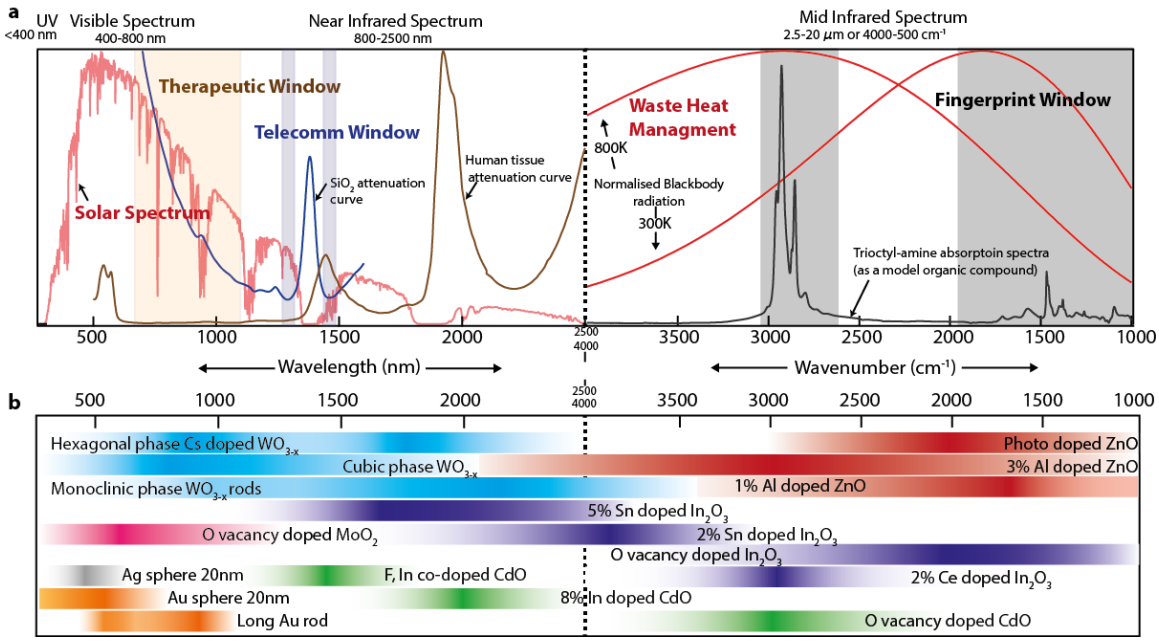

Figure 1.1 Optical Property of Metal Oxide nanocrystals and its potential applications. a) Spectral regions of interest for different plasmon-based applications. The solar spectrum (250-2500 nm AM1.5, red) is relevant for smart windows, and harnessing solar energy. The human tissue attenuation curve[39] (brown) shows greater transmission in the therapeutic window (light brown region) relevant for photothermal therapy and bio-imaging. The SiO_2 waveguide attenuation curve [55] reveals narrow regions around 1350 nm and 1500 nm most suitable for telecommunications due to low loss in these regions. Blackbody body radiation spectra at 300 K and 800 K show that doped metal oxide plasmonic materials are suitable for waste heat management applications in the mid-IR. The fingerprint region (less than 1770 cm^{-1}) and C-H vibration region (2800-3300 cm^{-1}) are noteworthy spectral windows for mid-IR plasmon-based applications such as surface enhanced infrared absorption (SEIRA).b) LSPR extinction spectra color map (Gradients express LSPR spectra with the maximum darkness corresponding to peak positon) of doped metal oxide and metal NCs spanning from visible to mid IR. All nanocrystals are spherical in shape other than hexagonal platelets of Cs_xWO_3 and gold nanorods. Metal oxides such as ZnO [21,22] (red), In_2O_3 [25] (violet), CdO [19](green), MoO_2 [4] (pink), and WO_3 [23,26,56](blue) have intrinsic oxygen vacancies leading to LSPR, which can be tuned and blue shifted via chemical doping, photodoping or through shape or crystal phase control during colloidal synthesis. Metals such as gold [9,13](yellow) and silver (grey) exhibit LSPR in the visible spectrum.

1.2 Metallic optical properties of doped metal oxides

1.2.1 Tunable plasma frequencies in degenerately doped metal oxides

As advances in the deposition and characterization of metal oxide thin films [57] led to experimentation with n-type doping, degenerately doped metal oxide films emerged as transparent conductors. As materials research entered the nanoscale new optical effects arising from the free carriers in metal oxide NCs were observed. For example, UV illumination in anaerobic conditions was found to induce Moss-Burnstien shifts consistent with stabilization of free electrons in the conduction band of ZnO NCs [58]. Upon hydrothermal synthesis of colloidal Sb:SnO_2 NCs, a common degenerately doped metal oxide thin film material, Nütz *et al.*[59] saw that the colloid exhibited a blue color and films of the NCs were observed to have a strong infrared absorption which shifted to lower energies in samples with lower concentrations of antimony dopants. This demonstrated that through control of antimony dopant concentration, the plasma frequency can be controlled in CMO NCs and consequently the LSPR energy.

Synthetic advances in CMO NCs since these early hydrothermal syntheses of irregularly shaped NCs has led to increased diversity and specificity of control. Advances in microwave syntheses led to both NCs of Sn:In_2O_3 (ITO) and doped Al:ZnO NCs, which represent the most popular transparent conducting oxide materials [29,60]. Not long after, further synthetic developments utilizing Schlenk techniques to perform aminolysis and esterolysis of metal carboxylate complexes led to better uniformity in NC geometries and sizes [24,30,31,61,62]. As sample quality improved it became possible to differentiate optical modeling of the infrared response of these materials as a LSPR while in colloidal dispersions[16,28] rather than treating the optical properties of annealed films of the NCs with a plasmon-polariton model [34]. Additionally, synthetic advances led to identification of LSPR in myriad CMO NCs such as those based on tungsten oxide [23,26,38], molybdenum

oxide (4), doped CdO [19,36,63,64], doped ZnO [24,32,60,65–68] doped TiO_2 [50,69], and vanadium oxide [70]. These materials, as illustrated in Figure 1.1b, exhibit LSPR resonance energies from the visible through the near infrared (NIR) to the mid-IR, which can be controlled through material selection and dopant concentration (Figure 1.1b). The intrinsic dielectric background and electronic band structure of each material as well as the range of dopant concentrations that the material can sustain without changing phase determines the magnitude and range of LSPR energies attainable within a material as illustrated by the different ranges achieved by WO_x, MoO_x, ZnO, CdO and In_2O_3 in Figure 1.1b.

1.2.2 Dielectric functions and corresponding LSPR

Conduction band electrons behave as a free electron gas, which typically calls for the Drude-Lorentz model [16,17,20,34,71,72] to be employed to extract the dielectric function. This model is simplistic in that it treats electrons as unbound and moving in straight lines, only being scattered by a periodic array on positive ion sites. Despite this simplicity, it is widely applicable with reasonable precision in predicting and modeling the behavior of both metal [18,73] and metal oxide LSPR. The Drude-Lorentz dielectric function [1] (Equation 1.2) is a complex function.

$$\epsilon_p(\omega) = \epsilon_1(\omega) + i\epsilon_2(\omega) \qquad 1.3$$

The real part of dielectric function, $\epsilon_1(\omega)$ determines the polarizability of the material, and loss due to the inertia of the free carriers is expressed in the imaginary part, $\epsilon_2(\omega)$.

$$\epsilon_1 = \epsilon_\infty - \frac{\omega_p^2}{\omega^2 + \gamma^2} \qquad \epsilon_2 = \frac{\omega_p^2 \gamma}{\omega(\omega + \gamma^2)} \qquad 1.4\text{-}1.5$$

While increasing the carrier concentration causes the imaginary part of the dielectric function to directly increase, and thus leads to optical loss, the damping

constant is also important for understating energy loss from an excited LSPR. There are several scattering mechanisms that impact free carriers in plasmonic systems such as electron-electron scattering (γ_{e-e}), electron-phonon scattering (γ_{e-ph}), interband transition scattering (γ_{ib}), surface scattering (γ_s), and electron-impurity scattering (γ_{e-i}) as well as material and morphologically specific scattering mechanisms. These scattering mechanisms are additive via Matthiessen's rule [20] leading to the overall scattering function of the material [Equation 1. 6].

$$\gamma = \sum \gamma_i = \gamma_{e-e} + \gamma_{e-ph} + \gamma_{ib} + \gamma_s + \gamma_{e-i} + \cdots \quad 1.6$$

Often, loss due to scattering is undesirable as it leads to low efficiency of light propagation in photonic systems, shorter lived local electric fields, and broader LSPR peaks, which decreases interactions with other oscillators and lessens the sensitivity of plasmonic sensors. Some loss processes are intrinsic, such as the case of the d-d transition interband gap scattering characteristic of gold [18,73]. On the other hand, silver does not have significant interband scattering due to there being little overlap between such transitions and the LSPR frequency. Metal oxides typically have a wide bandgap and low energy LSPR and so they exhibit very little interband scattering. Electron- phonon scattering is strongly temperature dependent and plays an important role only at high temperatures [20]. Electron-electron scattering is a minor contributor due to minimal interaction between electrons. Conversely, in metal oxides, dopants and crystal defects can lead to significant defect scattering, which can be an important source of damping [74]. The optical properties of commonly studied metal oxide systems such as In_2O_3 , ZnO, and CdO depend upon the choice of dopant type, carrier concentration, and scattering values leading to distinct dispersive properties. These material properties result in changes of important optical parameters such as the crossover frequency where the real part of

dielectric constant becomes negative (Figure 1.2a-top), LSPR frequency, absorption coefficient (Figure 1.2a, b-bottom), and refractive index (Figure 1.2b-top) of the material. For example, even though Al:ZnO and Ce:In_2O_3 have similar carrier concentration, due to their vastly different damping constants, we observe huge differences in their absorption coefficient and imaginary dielectric values.

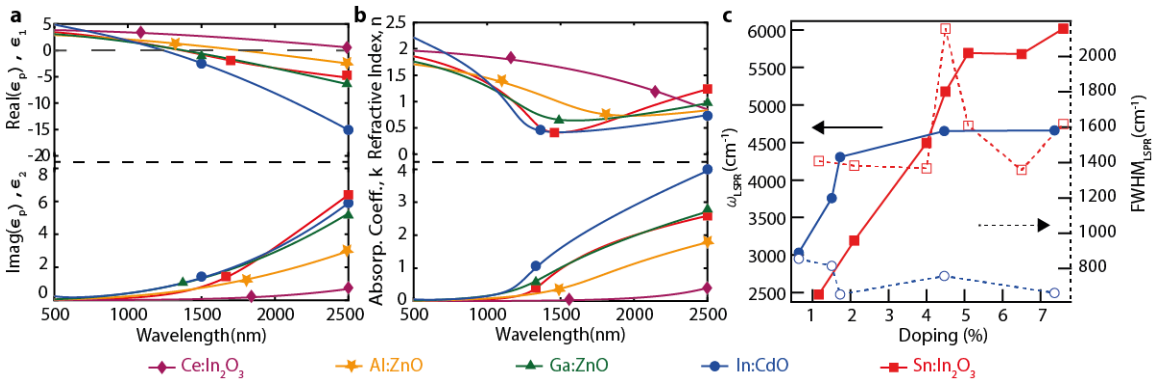

Figure 1.2 **Dielectric functions of metal oxides** a) Real (top) and imaginary (bottom) part of complex dielectric function for different metal oxide systems. b) Corresponding complex refractive index (top) and absorption coefficient (bottom) derived from complex dielectric functions shown in part a. The real part of the dielectric function shows that depending upon the metal oxide we have different crossover frequency from positive to negative values (dashed line). Both a and b show strong dependence upon material properties like electron scattering and carrier concentration. Metal oxide system discussed here are Ce:In2O3 16 (violet), Al:ZnO 75 (yellow), Ga:ZnO 76 (green), In:CdO 34 (blue), and Sn:In2O3 77 (red) c) $\boldsymbol{\omega_{LSPR}}$ (solid lines) and FWHMLSPR (dashed lines) vs doping for both In:CdO and Sn:In2O3. As dopant concentration increases there is a blue-shifts the LSPR frequency. FWHM shows strong host dependence due to different electron scattering mechanism in these materials.

Using the Drude-Lorentz dielectric function, LSPR spectra of spherical nanocrystals can be modeled through the application of Mie theory. While the LSPR of small NCs will primarily lead to absorption of light, above a diameter threshold of

approximately d=λ_{LSPR}/20 LSPR will begin to scatter light with increasing efficiency at larger sizes. This distinction is important in understanding optical properties of CMO NCs as the resonance is often at wavelengths longer than 1 μm, typically between 1.5-10 μm, which means NCs must be larger than 75 nm to begin to show size effects or significant scattering, unlike metals, which hit this threshold around 20 nm. The full response for the LSPR absorption and scattering (Equation 1.7-8) accounts for the dielectric constant of the medium as well as the dielectric function of the material since these polarizabilities both contribute to how light interacts with the material. For example, spherical NCs (with d<λ_{LSPR}/20), will exhibit maximum LSPR absorption and scattering where the dielectric function and the dielectric constant of the surroundings (ϵ_H) follow the relationship of the $\epsilon_p = -2\epsilon_H$ according to Mie theory (Equation 1.7-8). For non-spherical nanocrystals, LSPR can be theoretically simulated by computationally solving the Maxwell equations over a bounded nanocrystal-surrounding control volume. This causes LSPR to be highly sensitive to small changes in the dielectric environment, as well as interactions with other nearby polarizable components like vibrational, electronic or plasmonic resonances.

$$C_{abs}(\omega) = 4\pi R^2 (k(\epsilon_H)^{1/2} R) \mathrm{Im}\left\{\frac{\epsilon_p(\omega) - \epsilon_H}{\epsilon_p(\omega) + 2\epsilon_H}\right\} \quad 1.7$$

$$C_{sca}(\omega) = 4\pi R^2 (k(\epsilon_H)^{1/2} R)^4 \left|\frac{\epsilon_{\mathrm{p}}(\omega) - \epsilon_{\mathrm{H}}}{\epsilon_{\mathrm{p}}(\omega) + 2\epsilon_{\mathrm{H}}}\right|^2 \quad 1.8$$

Here, k represents the wavevector, R the NC radius, and ϵ_H is the dielectric constant of the NCs surroundings.

Measurement of the full dielectric response of plasmonic materials, which is correlated directly to the complex refractive index ($n + ik = \sqrt{\epsilon_1 + i\epsilon_2}$), requires

probing both the real and imaginary portion of the dielectric function. Normally, this is achieved through ellipsometry in thin films or films of NCs [34] (Figure 1.2a-b). Extracting the electronic properties of these films is important for many device applications; these properties can be measured directly using impedance spectroscopy [78], resistivity measurements [63] and compared with those deduced by analyzing optical spectral. For example, the LSPR linewidth ($FWHM_{LSPR}$) scales with damping (Figure 1.2c –dashed lines) and thus can be used to measure carrier mobility. This analysis is especially useful for NCs since measuring inherent electronic properties directly is not possible, while LSPR spectra of single NCs can be collected using scanning near-field optical microscopy (s-SNOM) to deduce their complex dielectric function [79,80]. Material properties derived from the optical response such as LSPR frequency (ω_{LSPR}) and FWHM of Sn:In_2O_3 and In:CdO nanocrystal (Figure 1.2c) indicate differing degrees of dopant activation and carrier scattering. These values greatly depend upon defect type and concentration, the host material background dielectric constant, as well as hybridization of dopant atomic orbitals with the host band structure.

1.3 Influence of Defects on LSPR

1.3.1 Carrier donating defects in metal oxides

Using defects to generate free carriers in metal oxides demands consideration of how different defect equilibria influence one another. For example, substitutional doping of Sn in Sn:In_2O_3 donates charge carriers, but also impacts the thermodynamic driving force for creating other defects such as oxygen vacancies, another electron donor. Additionally, all types of defects will introduce some degree of strain into the lattice of the material, which can make it synthetically challenging to incorporate dopants into NCs. Several types of defects occur in CMOs, each with their own impact on the

dielectric function of the material (and consequently the LSPR). In particular, the defects that donate free carriers and those that significantly impact the mobility of free carriers within the material are of interest when considering plasmonic properties. Intrinsic doping by vacancies, mainly oxygen vacancies and cation vacancies [16,23,38,81], extrinsic aliovalent substitutional doping to introduce free carriers [16,19,24,30–32,36,63,67,77], and extrinsic interstitial doping compensated by free carriers [20,23] have all been discussed in the literature (Figure 1.3a).

Metal oxides [57] can have equilibrium oxygen vacancies, the concentration of which is governed by the thermodynamics of defect formation energy, with the entropic driving force for forming vacancy defects balanced by the enthalpic cost of each vacancy. Equilibrium oxygen vacancy concentration can be controlled by adjusting oxygen partial pressure while at sufficiently high temperature to enable diffusion [82], then vacancies can be kinetically trapped by cooling. Since oxygen vacancies are each compensated by two free electrons in order to maintain charge neutrality, these defects can generate carrier densities on the order of 10^{19} cm^{-3}, rendering even undoped metal oxide NCs plasmonic. Though these LSPRs will be lost when NCs are annealed in oxygen rich environments [41,48,82], often times as-synthesized NCs will present a plasmonic absorption peak at energies as high as 2500 cm^{-1} (0.3 eV) without the addition of any extrinsic dopants.

Aliovalent doping is a deliberate synthetic approach for tuning the electronic properties of a semiconductor. Here, a lattice atom is substituted for a higher or lower valence atom to raise or lower the Fermi level. Depending on the energetic overlap of the dopant orbitals with the bands of the metal oxide, free carriers can result, i.e. the dopants are activated, or they can be compensated by other defects such as cation vacancies or interstitial oxygen. NCs are typically doped such that 0.5-15% of the lattice sites are

substituted, which is more than enough to reach degeneracy yielding metallic behavior in the case of shallow charge donors.

Agoston *et al.* [83] and Hwang *et al.* [84], studied Sn:In_2O_3 defect chemistry to elucidate the interplay between Sn doping and other defect compensation (Figure 1.3b). They showed that carrier concentration depends upon the relative contribution of substitutional Sn^{4+} atoms, oxygen vacancies and oxygen interstitial atoms which compensate for Sn by forming ($2Sn_{In}^{\cdot} - O_i^{''}$) defect complexes. This leads to intrinsic, extrinsic and compensation regimes of defect chemistry depending upon the dopant concentration which can lead to saturation effects in which Sn no longer donates free electrons at high dopant concentration. These regimes are apparent in observing the LSPR energy as a function of Sn concentration. Undoped In_2O_3 NCs exhibit a low energy LSPR that blue shifts with the addition of Sn, but eventually even adding more Sn cannot blue the shift the LSPR further or even leads to a red shift (Figure 1.3d). Similar behavior has been reported by Sachet *et al.* [85] for Dy:CdO thin films. They proposed the following defect reaction mechanism to understand these changes.

$$Cd_{Cd}^{x} + O_o^{x} \Leftrightarrow Cd_{Cd}^{x} + V_O^{\cdot\cdot} + 2n + \frac{1}{2}O_2(g) \quad 1.9$$

$$Dy_2O_3 \xrightarrow{CdO} 2Dy_{Cd}^{\cdot} + O_o^{x} + 2n + \frac{1}{2}O_2(g) \quad 1.10$$

They argued that intrinsic cadmium oxide is an n-type semiconductor; in which electrons originate from doubly ionized O vacancies (Equation 1.9). By changing oxygen partial pressure one can modulate O vacancy concentration. Further doping with aliovalent cations, here Dy, will act as an extrinsic donor (Equation 1.10). By Le Chatelier's principle, increasing the Dy concentration will drive the oxygen vacancy equilibrium backwards. At high concentrations of Dy, clustering of dopants is favored in

CdO. These parameters have important impacts on the dielectric function as the $Dy_{Cd}^{\cdot}$ and $V_O^{\cdot\cdot}$ concentrations will shift the plasma frequency of the CMO, but certain defect types can also change the damping constant of the material. The charge of the donor sites (Z) dictates the ionized impurity scattering. The impurity or defect scattering potential scales with Z^2. As a result of this, dianion oxygen vacancy sites contributing two electrons will scatter more than two singly ionized aliovalent sites. Depending upon the relative defect equilibria, tunable carrier concentration and low scattering can be achieved by an optimal ratio of extrinsic and intrinsic doping.

Sachet *et al.* [85] have also discussed the role of strain in scattering and mobility within the metal oxides. Since Dy^{3+} and Cd^{2+} have similar ionic radii, CdO experiences less lattice perturbation from Dy doping than from O vacancies. Runnerstrom *et al.* [16] have recently substantiated on this concept in NCs of In_2O_3. Using density functional theory, the induced lattice strain due to the presence of different dopant ions (Ce, Sn and O vacancy) was calculated for the In_2O_3 unit cell. Lattice strain around O vacancy sites was found to be three times greater than around Ce^{4+} sites. They have further discovered that defect formation energy of substitutional Ce is 3.5 eV lower than substitutional Sn which is attributed to cation size mismatch in Sn^{4+} compared to Ce^{4+} and the corresponding difference in relative ionic radius compared to In^{3+}.

Though strain impacts mobility, doping can lead to changes in the band structure that even more significantly impact the resulting LSPR. Using Ce instead of Sn as a dopant results in a decrease in LSPR linewidth of 30%, though the LSPR saturated in energy in the mid-IR while Sn can lead to higher carrier concentrations resulting in a NIR resonance. Similar results were earlier postulated by Bhachu *et al.* [86] for Mo:In_2O_3 thin films. Electronic structure calculations showed that states near the bottom of conduction band are primarily of In 5s and O 2p character (Figure 1.3e). This means that if the

dopant orbitals do not have good energy overlap with these orbitals they will not hybridize well near the conduction band minimum (CBM) resulting in free carriers being effectively electrostatically screened from significant dopant based ionized impurity scattering. Compared to $Sn:In_2O_3$ which hybridizes well near the CBM and has high overall scattering Mo and Ce orbitals hybridize with states much higher in energy than the CBM and indeed, scattering in these materials is less prevalent resulting in a substantial decrease in LSPR linewidth.

Incorporating multiple types of substitutional doping in the same material can lead to opening a large dynamic range for the carrier concentration. In the case of CdO, both In^{3+} and F^- substitutional dopants are defects that contribute one electron to the conduction band [36]. Interestingly though even after In doping saturates at high dopant concentrations (~20%) co-doping with F can lead to a substantially higher carrier concentration beyond that point (Figure 1.3c) accompanied by a decrease in linewidth at similar dopant concentrations. This effect shows that using multiple dopants in the same material can introduce multiple benefits, not only multiple electron sources that can boost the carrier concentration, but also, some defects can be used to both enhance carrier mobility in addition to changing carrier concentration like in the case of F in CdO.

Extrinsic interstitial doping can also introduce electrons into the conduction band of metal oxides. Some metal oxides like M_xWO_3 (M=Cs, K, Li, Na, etc.) due to a relatively open crystal lattice allow intercalation of ions, resulting in a broad LSPR spanning the near IR and tailing into the visible. Mattox *et al.* [23] achieved Cs incorporation into tungstate oxide NCs with a hexagonal crystal structure. Several researchers have shown that lithiation of crystalline tungstate materials enhances light absorption [48,87]. Yang *et al.* [88] demonstrated with density functional theory (DFT) that lithiation of tungsten oxide leads to substantial free carrier density.

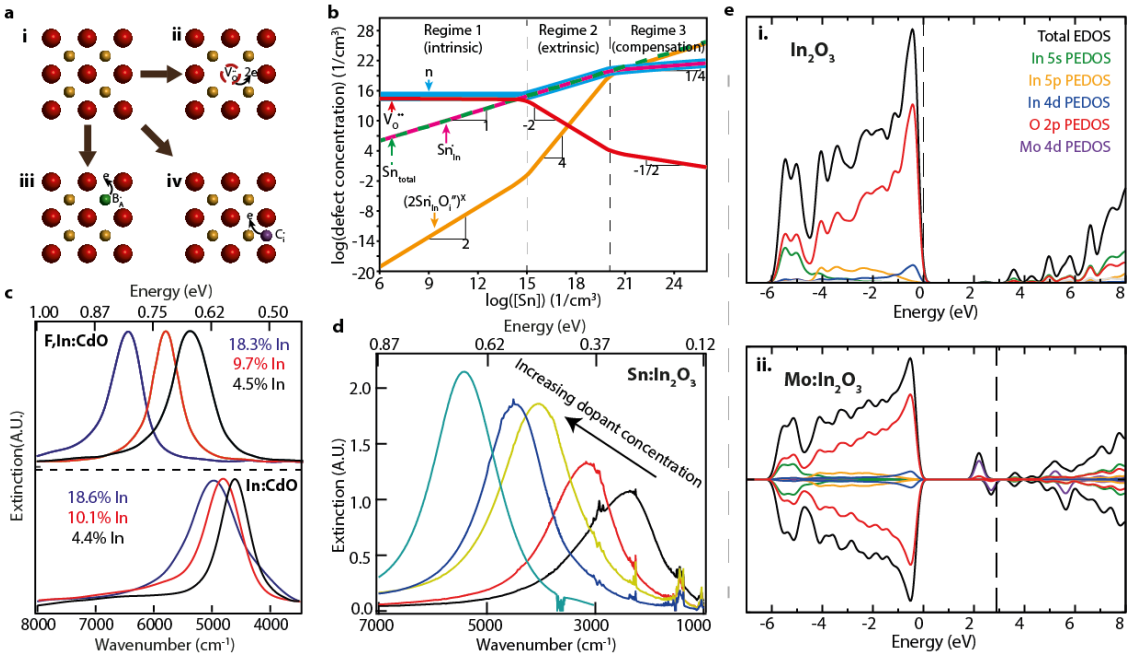

Figure 1.3 Defect chemistry and its impact on metal oxide plasmon. a) Schemes of common doping mechanisms (i) with host cation (orange spheres) and oxygen anions (red sphere). Three common donor doping types are (ii) oxygen vacancies, (iii) aliovalent substitutional impurities and (iv) interstitial impurities. Reprinted with permission from 17 © 2014 American Chemical Society. b) Brouwer defect equilibrium diagram for [Sn] and oxygen vacancies in In2O3 at fixed partial pressure of O2. Free electron concentration depends upon the relative concentration of $\boldsymbol{Sn_{In}^{\cdot}}$, oxygen vacancies, $\boldsymbol{V_O^{\cdot\cdot}}$, and $(2\boldsymbol{Sn_{In}^{\cdot}} - \boldsymbol{O_i''})$ complexes. As [Sn] is increased this leads leads to intrinsic, extrinsic, and compensating regimes. Reprinted adapted version with permission from 17 © 2014 American Chemical Society, based on the 84 © 2000 version with permission from Elsevier c) UV-Vis-NIR spectra of spherical F,In:CdO NCs (top) and In:CdO NCs (bottom) having similar dopant concentrations. Incorporation of F in In:CdO lattice leads to higher carrier concentration and lower scattering resulting in a LSPR blue-shift and decrease in FWHM. Reprinted with permission from 36 © 2014 American Chemical Society. d) FTIR spectra of Sn:In2O3 NCs at various dopant concentrations (0-5%) oxygen vacancies in In2O3 lead to a LSPR around 2000cm-1 (black). Increasing Sn concentration (spectra in color) lead to higher energy LSPR which saturates at around 5500 cm-1. e) Calculated total and partial density of states for (a) pure In2O3 and (b) one Mo dopant on the 8b site in a 40 atom primitive cell. The dashed lines indicate the highest occupied states. Absence of Mo 4d state above the highest occupied state in Mo:In2O3 EDOS curve signifies low scattering of free electron from $\boldsymbol{Mo_{In}^{\cdot}}$defect site. Reprinted with permission from 86 © 2015 American Chemical Society.

1.3.2 Dopant integration and dopant choice effects on LSPR

Control over dopant integration into NCs is a non-trivial aspect of understanding LSPR in CMOs. Depending upon the synthetic method utilized the dopant concentration, the dopant spatial distribution, and dopant activation are greatly impacted. Due to interactions between delocalized carriers and dopants, these effects make a substantial impact on the final LSPR properties of the nanocrystals. Free electrons in photo-doped ZnO NCs behave similarly to compositionally doped Al:ZnO NCs by EPR indicating metallic behavior of both [89,90]. However, both theoretical [33] and experimental studies [24] have indicated that the presence of the Al^{3+} ion changes the LSPR damping and selection rules significantly [32,63]. Also, incorporation of different dopants into the same lattice can lead to very different energies and peak shapes in the LSPR within the same material like in the case of CdO [63] (Figure 1.4a). Understanding both the electronic structure via the dielectric function of these materials but also the physical structure through careful materials characterization is crucial to obtain an accurate understanding of the ways LSPR are influenced by the unique dielectric environments of CMOs compared to metals.

One common example of dopant ions changing the scattering response of carriers in metal oxide is ionized impurity scattering observed in thin films of $Sn:In_2O_3$. Hamberg and Granquist [72] applied the method developed by Gerlach and Goose [91] to calculate the frequency dependence of ionized impurity scattering. In this method, scattering interactions are calculated assuming scattering centers oscillate relative to a stationary sea of electrons. When assessing the complex dynamical resistivity, the real part of this function takes on a constant value at low frequencies which is roughly equivalent to the DC resistivity of the material since the electrons are able to screen ionized impurities during the relatively large amplitude of oscillation. At high frequencies, the electrons are

no longer able to fully screen scattering centers and the total ionized impurity scattering value decreases as the frequency continues to increase. One can think of this effect as the amplitude of oscillation decreases at higher frequencies, causing electrons to sample less of the material before they change direction, decreasing the probability of scattering events, this frequency dependence leads to an asymmetrical peak shape in the LSPR. Empirical functions can be employed in fitting Sn:In_2O_3 LSPR to assess the constant low frequency damping constant expected from such a model. This low frequency damping constant (γ_L), is used to calculate DC resistivity of NCs obtained by fitting the LSPR spectrum using Equation 1.11.

$$\gamma = \gamma_L - \frac{\gamma_L - \gamma_H}{\pi}\left(atan\left(\frac{\omega - \gamma_x}{\gamma_w}\right) + \frac{\pi}{2}\right) \qquad 1.11$$

This function has γ_L as the low frequency damping, γ_H is high frequency damping, γ_X is a crossover frequency, and γ_W is the crossover width (depicted in Figure 1.4b inset).

As dopants can cause substantial scattering through ionized impurity scattering it's important to understand how dopant placement within a NC effects dopant induced scattering of carriers. (Figure 1.4b.) Lounis *et al.* [17,77] demonstrated that two common synthetic methods for making Sn:In_2O_3 NCs leads to homogenous dopant distributions versus surface segregation of dopants by energy dependent XPS [77]. In the case of homogenously doped particles, the LSPR exhibits strong frequency dependence of its scattering, conversely, surface doped NCs exhibit no significant frequency dependence of scattering. This suggests that dopants when located near the surface of NCs can contribute electrons stably but be separated enough spatially from where those carriers

are moving in the NCs that they do not damp the LSPR. Since minimizing scattering in these materials is crucial to most applications, surface segregation of dopants may help minimize scattering. Yet, NCs with their dopants near the surface have a lower carrier-to-dopant ratio, indicating that it is easier for other defects to compensate aliovalent dopants that are near the surface, making doping less efficient and stable.

The frequency dependent scattering model is a simplistic model and is not necessarily applicable to all metal oxide systems. For example for In:CdO, Mendelsberg *et al.*[34] found that for $\omega > \omega_p$, a high background dielectric value of the host crystal led to impurities being screened efficiently. Ce doping instead of Sn doping in In_2O_3 leads to effectively no frequency dependent scattering in the material [16]. It's important to take into account the very different values of ω_p observed throughout the different CMO materials and consider not only which dopants will hybridize with the CBM in way that causes them to introduce ionized impurity scattering, but also which energy regimes are relevant for screening effects changing appreciably across the linewidth of the LSPR.

Indeed, thinking of dopants as simple free carrier donors that can have their impact on carrier mobility mitigated by spatial distribution within the NC is not a complete picture of how dopants change the electronic properties. For example, comparing photo- doped In_2O_3 and Sn:In_2O_3 NCs indicated that Sn is lowering the CBM of In_2O_3 keeping the Fermi level more or less fixed in oxygen rich environments [47]. Some dopants that would appear to aliovalently dope their host, for example Fe^{3+}:ZnO, do not cause any substantial free carriers to appear within the conduction band as the Fe orbitals are too deep of donors to hybridize with the CBM. In this case another negatively charged defect must compensate the charge on the Fe^{3+} ions. Despite this, the Fe sites will still accept charges upon co-doping with other charge donating dopants (Figure 1.4d-e). In ZnO both Sn dopants as well as photodoping (see Section 4 for description of

photodoping) have been shown to convert Fe^{3+} to Fe^{2+} before starting to add charge carriers to the conduction band [92,93] despite other charge compensating defects already being present in the material.

Improving methods for controlled dopant integration into NCs will enable meaningful research into the effect of dopants on scattering in NCs. Many observations of ensemble linewidths in NCs of CMOs indicated much lower carrier mobilities than expected. Though the introduction of surface and interfacial scattering are significant here when comparing NCs to bulk, these observations of substantial broadening were surprising. Interrogating single NC optical responses is required to understand this effect, as homogenous linewidths are the best indicator of the physical process at play. In IR responsive materials, it is challenging to make single NC optical measurements as the diffraction limit is so much larger than small sized NCs. Standard techniques for optical characterization of single NC LSPR such as dark field scattering [94,95] and acoustic modulation [96,97] are not easily adapted to IR light. Johns *et al.* demonstrated that through the use of near-field optics single NC measurements can be made with a light source that is adequately bright and spectrally broad to probe the full LSPR lineshape [80]. One such option is the use of IR synchrotron radiation as the light source of s-SNOM, a technique known as synchrotron infrared nano-spectroscopy (SINS) [98]. Extreme particle to particle variability in LSPR energy as well as linewidth and lineshape were observed in Al:ZnO NCs. The single nanocrystal LSPR linewidth (Figure 1.4f) is less than half the linewidth of ensembles indicating that dopant integration is quite heterogeneous in CMO NCs with some synthetic methods. These single particle measurements can be used to obtain a more accurate value for the NC dielectric function without the contribution of ensemble broadening, which can be used to model the pure response of the material without contribution from its surroundings (Figure 1.4g) [16].

Better control over dopant integration is already possible for some doping schemes such as using plasma synthesis to make Al:ZnO NCs [21] to ensure dopants are integrated homogenously rather than only at the surface. An even higher degree of control (doping, particle monodispersity, and colloidal stability) has been achieved through layer by layer growth of $Sn:In_2O_3$ at such a slow rate that dopants can be selectively introduced at any point during the growth by merely changing if a doped or undoped metal precursor solution is used during different points in the reaction [99]. Expanding similar levels of control over size, shape and dopant distribution across a range of plasmonic CMO NC compositions is crucial for further advances in this field. It's worth noting that in addition to better control over dopant location, there is still significant variation in literature reports regarding the apparent dopant activation. For example, in $Sn:In_2O_3$ NCs LSPR energies are often reported across the mid-IR and up to, but never higher than ~0.8 eV. While this tuning range has been demonstrated over dopant ranges from 0-5% Sn in some cases [100] in others it required more than 10% Sn to reach this same high energy limit of the LSPR [30].

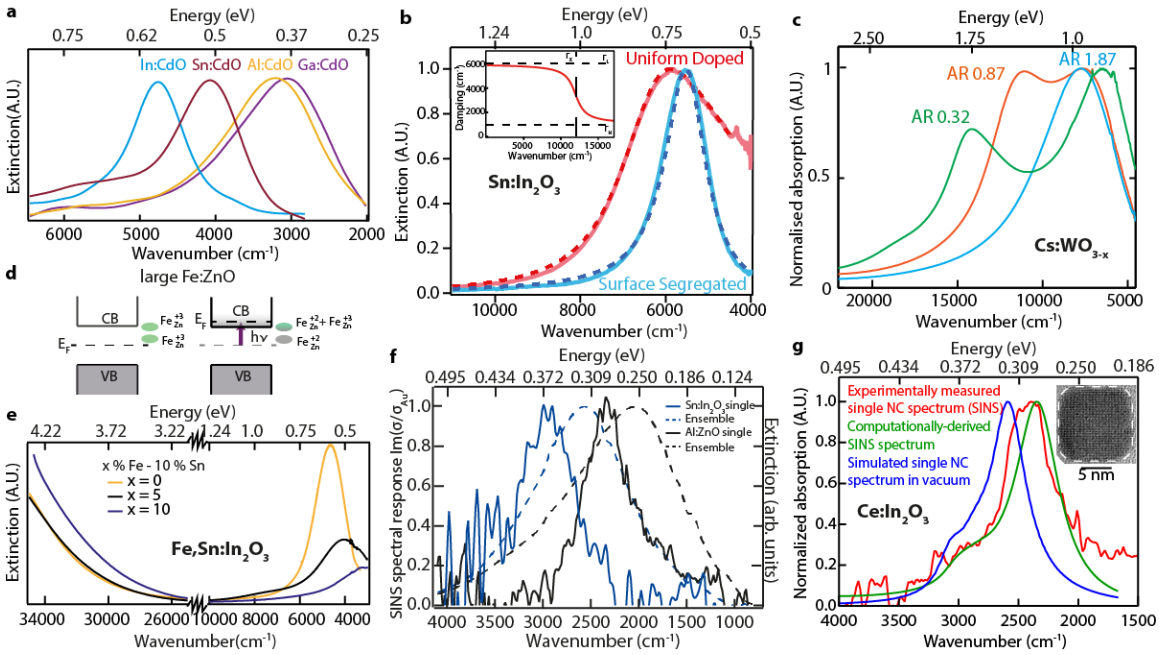
a
Energy (eV)
0.75 0.62 0.5 0.37 0.25
In:CdO Sn:CdO Al:CdO Ga:CdO
Extinction(A.U.)
6000 5000 4000 3000 2000
Wavenumber (cm-1)
b
Energy (eV)
1.24 1.0 0.75 0.5
Uniform Doped
Surface Segregated
Sn:In2O3
Extinction (A.U.)
Damping (cm-1)
Wavenumber (cm-1)
10000 8000 6000 4000
Wavenumber (cm-1)
c
Energy (eV)
2.50 1.75 1.0
AR 1.87
AR 0.87
AR 0.32
Cs:WO3-x
Normalised absorption (A.U.)
20000 15000 10000 5000
Wavenumber (cm-1)
d
large Fe:ZnO
CB
VB
CB
VB
hν
e
Energy (eV)
4.22 3.72 3.22 1.24 1.0 0.75 0.5
x % Fe - 10 % Sn
x = 0
x = 5
x = 10
Fe,Sn:In2O3
Extinction (A.U.)
34000 30000 26000 10000 8000 6000 4000
Wavenumber(cm-1)
f
Energy (eV)
0.495 0.434 0.372 0.309 0.250 0.186 0.124
SnIn2O3 single
Ensemble
AlZnO single
Ensemble
SINS spectral response Im(σ/σAu)
Extinction (arb. units)
4000 3500 3000 2500 2000 1500 1000
Wavenumber (cm-1)
g
Energy (eV)
0.495 0.434 0.372 0.309 0.250 0.186
Experimentally measured
single NC spectrum (SINS)
Computationally-derived
SINS spectrum
Simulated single NC
spectrum in vacuum
5 nm
Ce:In2O3
Normalized absorption (A.U.)
4000 3500 3000 2500 2000 1500
Wavenumber (cm-1)

Figure 1.4

Figure 1.4 Doping strategies and resultant metal oxide LSPR properties a) Normalized FTIR extinction spectra of doped CdO NCs dispersed in tetrachloroethylene (TCE). Due to different extent to which dopants are incorporated and activated, different dopants such as In (blue), Sn (brown), Al (yellow), and Ga (violet) show LSPR saturation at different frequencies. Adapted with permission from [63] © 2014 American Chemical Society b) Optical extinction (solid lines) and extended Drude fit (dashed lines) for surface segregated (blue) and uniform doped Sn:In_2O_3 NCs. Higher frequency dependent scattering (inset) due to [Sn] defect sites leads to broader FWHM in uniform doped NCs. Adapted with permission from [77] © 2014 American Chemical Society c) Normalized optical absorption spectra of hexagonal Cs:WO3 nanocrystal samples of platelets (green), isoprisms (orange), and rods (blue) dispersed in TCE. Spectra show strong aspect ratio dependence on LSPR response which could only be explained via consideration of both shape and crystalline anisotropy in these NCs Reprinted with permission from [26] © 2016 American Chemical Society d) Schematic band diagram for Fe-doped ZnO QDs before and after raising the Fermi level by photodoping. Incorporation of Fe in ZnO lattice leads to deep trap states, which effectively reduces overall photo induced free electron concentration. Schematic is adapted from [93], published by The Royal Society of Chemistry. e) Reduction of overall free electron concentration resulted from codoping Fe with Sn in In_2O_3 NC. Incorporation of Fe leads to red shift of plasmon absorbance spectra denoting decrease in free carrier density as electrons localize on Fe sites. Figure 1.is adapted with permission from [92] © 2014 American Chemical Society. f) Comparison between ensemble spectra measured by conventional transmission FTIR on KBr substrates (dashed lines) to single nanocrystal spectra of Al:ZnO and Sn:In_2O_3 shows substantial decrease in FWHM in single NC measurement due to NC-to-NC variations in LSPR frequency within a batch. Reprinted with permission from [80] © 2016 Nature Publishing Group g) Dielectric function evaluation of Ce:In_2O_3 NCs (Inset) via fitting SINS spectrum (red line) using electromagnetic simulations of SINS experimental setup (green line). Obtained dielectric function was used to simulate absorption spectra of single isolated NC. Reprinted with permission from [16] © 2016 American Chemical Society.

1.4 Material and morphological influences on near field enhancement

Though doping is certainly a powerful tool for tuning plasmonic properties in CMOs it is not the only factor that changes the LSPR response. NC shape, crystal structure, and orientation in space can all lead to substantial changes in the optical response. Depending on the reactivity of dopant precursors, ligand chemistry and reaction mechanism NCs with very different structures and degrees of heterogeneity can be formed. Radovanovic *et al.* [101,102] observed two products from a single reaction; NCs 5 nm in diameter trapped in the metastable corundum (rh-Sn:In_2O_3) phase and larger (>10 nm) NCs in the cubic bixbyite phase (bcc-Sn:In_2O_3). These phases have distinctly different dopant dependence of their optical responses. While bcc-Sn:In_2O_3 nanocrystals have strong dopant concentration dependence of LSPR frequency, bcc-Sn:In_2O_3 has a small free carrier density and does not exhibit a plasmonic response at any dopant concentration. Differences in the CBM versus the Sn^{+4} donor state lead to differing degrees of donor activation.

Further, Kim *et al.* [26] have shown that depending upon synthetic conditions Cs_y:WO_{3-x} can be formed in the hexagonal (Cs doped) phase, which differs significantly from the cubic or monoclinic phases of WO_{3-x} that are not Cs doped (Figure 1.1b). In contrast to the symmetric cubic phase, optical spectra of hexagonal phase tungsten oxide can only be explained via a cooperative influence of crystalline and shape anisotropies. The role that intrinsic crystalline anisotropy plays in breaking the degeneracy of LSPR directionality is substantial and can cause peak splitting in LSPR as a result of the crystallographic orientation. This effect also occurs in cesium tungstate nanocrystals by synthetically varying NC aspect ratios. Integration of spectroscopic observations (Figure 1.4c) and electromagnetic near-field simulations (Figure 1.5b) revealed that unlike classical metal platelets or rods in which one resonance mode dominates based on the NC

shape, here cesium tungstate nanocrystals sustain strong dipolar LSPR modes both along the c-axis and parallel to the basal plane despite physical aspect ratio. Simulations of LSPR must account for anisotropic crystal structures as well as shape in order to properly model spectra in some CMO materials.

In addition to the optical response, the localization of electromagnetic radiation into near-field electronic polarization via plasmonic resonances is a major topic of research in plasmonic materials. Applications in chemical sensing [97], imaging [3,96], surface enhanced Raman spectroscopy [8,65,103], enhanced luminescence [44,104] and opto-electronics [105] all rely on coupling to high intensity local near fields produced. Such enhancement depends primarily upon NC electron density, electron scattering and surface curvature. Metallic nanoparticles have high carrier density and have been made with complex sharp-cornered shapes such as nano-stars [12], nano-rice [14], and multipod structures [9] each demonstrating efficient near-field enhancement. For nanostar tips, enhancement on the order of 10^5 was shown upon illumination with 700-800 nm light [12]. To reach infrared light enhancement metal structures are increased in size, such as hollow spheres, or long nanorods at the cost of reduced near field intensity [10,13]. These drawbacks of metal nanoparticles for IR applications make metal oxide NCs a promising alternative candidate.

Demonstrating the potential of CMO NCs for near-field enhancement, Agrawal *et al.* [37] used the discrete dipole approximation to simulate enhancement by In:CdO NCs. Despite the lower carrier concentration compared to metals, suppressed electron scattering in CdO allows these NCs to efficiently concentrate IR light. Near field intensity enhancement (NFE) was calculated for sharp cornered cubes and octahedra of In:CdO (Figure 1.5a-b) for dipolar modes along the corners, edges, and faces. A maximum NFE of 10^5 was calculated, and was shown to be significantly reduced with

rounding of sharp corners and edges. Shape control is very important to NFE, and can be controlled somewhat through choice of precursors in NC synthesis[106]. Runnerstrom *et al.* [16] demonstrated the shape of Ce:In_2O_3 can be tuned between spherical and cubic through choice of precursor. Further, Gaspera *et al.* [32]. showed that even the dopant element choice can impact the shape of doped ZnO nanocrystal ranging from pseudo-spherical with Ga and In to elongated pyramids with Al. Other shape induced LSPR properties have been demonstrated in Cs doped WO_3, [26] which supports almost equal NFE for both longitudinal and transverse polarization (Figure 1.5c). This result is noteworthy as in metal nanorods, high NFE is only observed along the longitudinal mode. Certainly, the intricate interplay between shape and crystalline anisotropy in CMOs can be leveraged for precise peak splitting for applications such as imaging, SERS spectroscopy and photonics. Better shape and size control, as well as dopant choice and distribution warrant further research for improved CMO NFE.

Plasmon coupling between adjacent NCs and films to induce plasmon gap modes is another approach to improving NFE. Computations of hot spot formation in between coupled In:CdO NC dimers indicated that coupling can lead to an order of magnitude improvement in NFE [37]. Moreover, Li *et al.* [27] studied the effect of inter-particle spacing on the optical response of random and periodic assemblies of Sn:In_2O_3 nanorods. The periodic Sn:In_2O_3 nanorod array demonstrated a narrower plasmon peak and several small features in the p-polarized reflection spectrum, indicative of coupling between dipole (multipole) modes and standing waves in the Sn:In_2O_3 nanorods (Figure 1.5d) Due to the generation of mid-IR plasmons in CMO NCs at small sizes, Kuznetsov [107] was able to demonstrate that despite the lower NFE of single CMO nano-antennas compared to metallic ones, their small size allowed more closely packed arrays of nano-antennas. This provides a 30-fold increase in the density of the hotspots compared to a metallic array,

indicated device scale enhancement substrates are more likely to be successful in CMOs in the mid-IR. Finally, Gordon *et al.* [19] showed that via self-assembly of metal oxide NCs into large scale periodic structures, inter-particle spacing is controllable *via* the packing structure. With promising NFE in both single NCs and periodic structures, metal oxide plasmon are attracting more attention for a diverse range of application taking advantage of their light absorption as well as their near field enhancement.

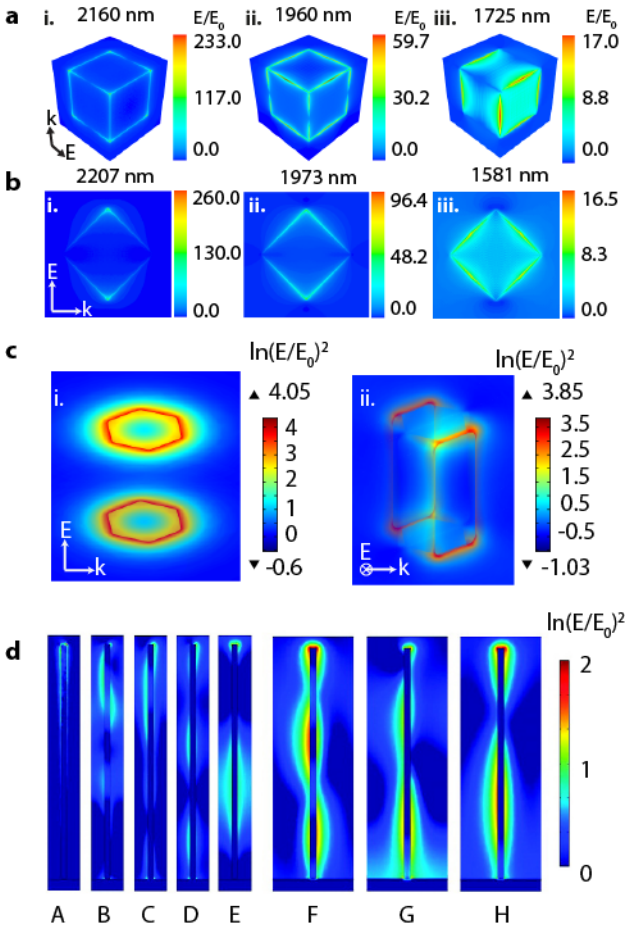

Figure 1.5

Figure 1.5 **Near field enhancement in plasmonic metal oxide nanocrystals** Near field enhancement (NFE) map of a In:CdO cube (a) and octahedron (b) using the discrete dipole approximation. For both shapes fundamentalcorner, edge and face geometrical modes were observed (from left to right). For the cube at the highest intensity peak (2207 nm), the enhanced field is strongly localized at the corners of the cube, reaching field enhancement factors of up to 233, while for the octahedron at highest intensity peak (2160 nm), NFE of up to 260 was observed. Reprinted with permission from [37] © 2015 American Chemical Society c) Near field intensity map on log scale for a rod excited at the two LSPR peak frequencies of $CsWO_3$ nanorods. Due to strong crystalline anisotropy in h-$CsWO_3$ almost equal enhancement could be sustained along both transverse and longitudinal plasmon modes. Reprinted with permission from [26] © 2016 American Chemical Society d) Near field enhancement in periodic structure of Sn:In_2O_3 nanorods with inter-particle spacing of 600nm (A-E) and 1500nm (F-H). Inter-particle dependent coupling between standing waves and dipolar plasmon modes lead to different near field profiles. Reprinted with permission from [27] © 2011 American Chemical Society

1.5 Active modulation of metal oxide plasmonics

Carrier concentration in CMO nano-structures have been post-synthetically varied, leading to dynamic modulation of their plasmonic properties across a technologically relevant dynamic range. Their ability to respond to external stimuli has led to proposed applications in smart windows [25,48–50,87,108–113], redox sensors [26,46], and electro-optical modulators for all photonic circuitry [45,53,105,114–116]. Since the LSPR of nano-materials can be induced to shift over wide energy ranges upon changes in free electron concentration, controlling carrier concentration dynamically leads to control over the optical properties. Several approaches can be taken to shift the carrier concentration whether electrochemically (electrochromism), photoelectrochemically (photochromism), or through direct chemical redox processes (chemochromism). Each of these approaches not only shows the versatility of CMO plasmonics but also helps to elucidate the electronic and chemical properties of these materials in ways that static observation cannot fully resolve.

Though modulation has been demonstrated in metals such as Au and Ag, [117,118], generally very small optical modulations have been achieved. For example, Mulvaney *et al.* [117,118] showed that for both Au and Ag, a nominal shift of their LSPR of only around 30 meV (about 10nm at 680 nm) can be induced using an external applied voltage. Alternatively, several researchers [28,49,52,119] have shown that metal oxide NCs can exhibit LSPR modulation over more than 200meV (about 450 nm at 1800nm) due to the substantially larger debye lengths of semiconductors compared to metals and the fact that at and lower carrier concentration the change per electrons added is proportionally larger. The sensitivity to modulation strongly depends upon the material, NC size and morphology, dopant characteristics, and charging method.

1.5.1 Electrochromism

Changing the free carrier concentration in a material via an externally applied voltage leads to accumulation or depletion of electrons compared to equilibrium conditions. This approach to modulating the optical properties of NCs can be achieved through both electrical (capacitor configuration) and electrochemical (supercapacitor or battery configuration) methods for disrupting the equilibrium charge states of a material [110,113]. One prolific example of such electrochromism is in developing 'smart' windows where one can modulate NIR solar transmission by inducing large shifts in the absorption maximum of the LSPR of metal oxide NCs. Motivated by the potential for energy savings via control over light and heat transmission through windows, researchers have developed ways to separately modulate visible transmission of a colored host material and NIR transmission of embedded plasmonic CMO NCs. The approach in such devices is a "battery type" multi-layer electrochromic device consisting of an active electrochromic electrode layer, a counter electrode, an electrolyte layer separating the two electrodes, and two transparent conducting oxide coated supporting substrates which serve as back electrical contacts. The device operates through Faradaic (intercalation of cations such as Li^+ or H^+) or capacitive processes, and depending upon the potential applied electrons are stabilized or removed from the electrochromic electrode. As electrons are added or removed from the material the carrier concentration can vary by so much as to see changes in transmission of over 80% across the solar NIR (Figure 1.6a-b).

Electrodes made from NC films can exhibit unique electrochromic performance [78]. Garcia et.al. [25] demonstrated that such capacitive charge injection is possible when porous ITO nanocrystal films are made. The NCs must be stripped of their native ligands and annealed so as to minimize barriers for electron conduction through the NC network. If the interconnected NC network is too resistive problems arise such as requiring

voltages that exceed electrolyte stability or extremely slow charge percolation through the film. Porous networks of $Sn:In_2O_3$ NCs were first employed because in addition to enabling electron conduction through the NC network, the open pores of the film allowed for a high active surface area of compensating counter ions to adsorb onto the NC surfaces for charge compensation. This approach to forming efficient electrochromic layers of metal oxide NCs has now been demonstrated in $Sn:In_2O_3$[25,49,108], Al:ZnO [24], $Nb:TiO_2$ [50], as well as in WO_{3-x} [48,87] and $Cs:WO_{3-x}$ [26]. In order to achieve dual-band visible and NIR electrochromism, Llordes *et al.* [49] demonstrated that by replacing the native ligands of $Sn:In_2O_3$ NCs with polyniobate clusters before annealing a NbO_x matrix NC composite film can be made, which, is capable of controlling both visible and NIR light independently. At a low cathodic voltage, the LSPR of the NCs in NIR is modulated but at higher potentials reduction of NbO_x gives polaronic electrochromic response in the visible spectrum. Building upon this work, Kim *et al.* [48] used architectured WO_3-NbO_x composite films to achieve even faster switching kinetics, as well as enhanced charge capacity and durability. Further advances are certainly possible in such systems when it comes to color neutrality, switching speeds, and understanding new methods for pre-charging NC films.

1.5.2. Chemochromism

Applications of metal nanoparticle LSPRs in sensing applications usually relies upon detecting changes in the peak energy either due to a change in the dielectric constant of the particle surroundings due to a change in chemical composition of the medium, [10,11,97,120] or due to changes in interparticle LSPR coupling, which is distance dependent [103,121,122]. In these applications, nanoparticles act as chemically passive observers; they do not participate in processes taking place around it. Recent studies have

shown that metal oxide NCs could act as sensors by reacting with local species via chemical interaction. Mendelsberg *et al.* [46] demonstrated that Sn:In_2O_3 NCs mediated as well as monitored the electron transfer during chemical conversion of CytC oxidase (o-CytC) to CytC reductase (r-CytC). Based on optical modeling it is possible to quantify the number of such electrons transferred (Figure 1.6c-d). It was also possible to detect electrons transferred to the NCs from bacteria, which could be used as an electrode-less monitor of conditions under which biological agents are electrochemically active in their metabolism. CMOs are well suited to tasks in which they are needed to generate a measurable optical shift based on charge transfer processes due to the fact that a change in less than 1 electron per NC is still quite substantial in terms of carrier concentration in these small particles at low initial carrier concentrations.

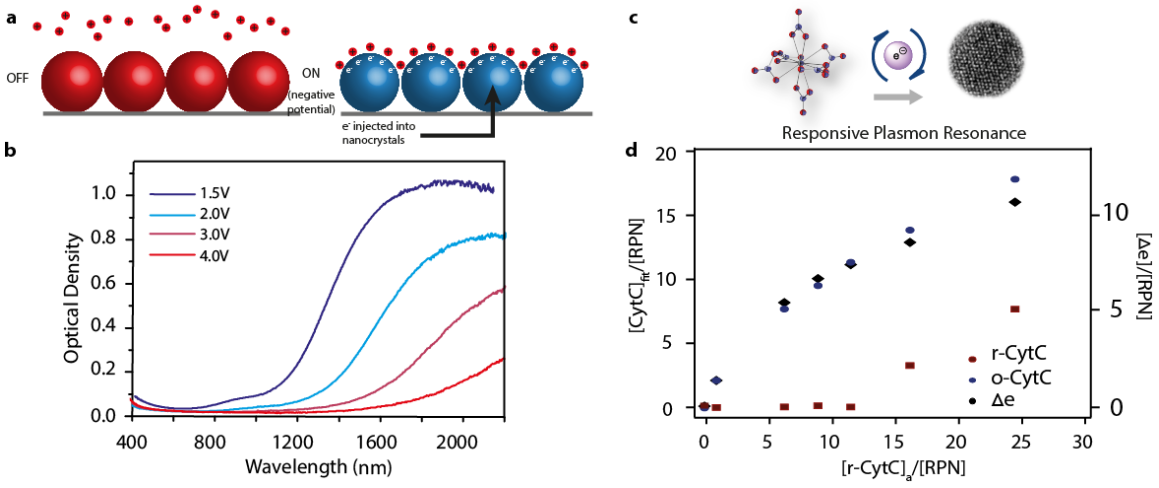

Figure 1.6 **Dynamic Modulation of metal oxide LSPR.** Schematic (a) illustrates the capacitive charging mechanism of electrochromic smart widows and corresponding optical changes (b). When oxidizing potentials (+3V, +4V) are applied to the NCs, they are depleted of electrons and the NCs do not interact strongly with the electrolyte resulting in a red shift and decrease of absorbance of the NC film (red lines). At reducing potential (+1.5V, +2.0V) electrons are injected into the NCs and lithium ions capacity compensate the injected charge at the NC surface, leading to a LSPR blue (blue lines). Schematic (a) is reprinted from [110], published by The Royal Society of Chemistry and Figure 1.(b) is reprinted with permission from [25] © 2011 American Chemical Society. c-d) Tracking electron transfer events during oxidation of r-CytC using buffered $Sn:In_2O_3$ NCs. Electron concentration extracted via quantitative modeling of absorption spectra shows the number of transferred electrons follows the amount of r-CytC converted to o-CytC, with [r-CytC] a being the concentration of r-CytC added and $[CytC]_{fit}$ being the optically determined concentration of either form of CytC. Reprinted with permission from [46] © John Wiley & Sons, Inc.

1.6 Applications of Metal oxide LSPR

Achieving a plasmonic response in the near- and mid- IR while still maintaining a high degree of control over size has made metal oxides a compelling choice for many applications of plasmonics. Due to the high absorption cross section of LSPR these materials have been applied to photothermal therapy [3,4,40–42,123,124], perfect IR absorbers [125], IR imaging [3,4,40], near field enhancement of photovoltaics [43,104,126–128], electrochromic windows [25,49,50] and more. The potential for strong near field enhancement can also lead to coupling between LSPR and other resonators such as molecular vibrations, electronic transitions, phonons, and photonic modes. This has enabled application in SEIRA, sensing, solar cells, telecommunications, and optoelectronics. Metal oxides can improve upon performance over metals for many of these application, though not without some challenges.

1.6.1 Photothermal therapy and imaging

LSPR-based diagnostics and treatment of diseases have been demonstrated at the lab scale using Au nanoparticles that can generate concentrated heat and simultaneously scatter light for imaging. As discussed by Soo Choi *et al.* [42], gold has an X-ray attenuation coefficient 150-fold higher than bone and can interfere with accurate computed tomographic (CT) scanning in organs such as the liver where nanoparticles can eventually accumulate. In order to avoid such accumulation within human body and to promote efficient renal clearance, it has been shown that plasmonic NCs smaller than 4.5 nm are optimal. In this size regime, gold invariably has a plasmon in the visible spectrum, which is outside the biological transparency window (700-950 nm). As metal oxide NCs do not depend upon complex shape or size control to determine plasmon energy they can be made at small sizes with an LSPR in the biological transparency window in the IR. Doped tungsten oxide [3,23,38,43] and molybdenum oxide [41] demonstrate plasmons between

500 nm to 1000 nm and thus are promising for such applications. Zhou *et al.* [3] and Deng *et al.* [40] have recently demonstrated that PEGylated WO_{3-x} rods act as a dual-functionality materials; simultaneously functioning as a CT imaging agent, a photothermal imaging agent, as well as for photothermal therapy purposes. Deng *et al.* [40] demonstrated photothermal therapeutic tungsten oxide nanorods responding to 808 nm night with intensity of 1.5 W/cm^2 can lead to a local temperature of up to 49 C within 4 minutes which causes apoptosis in tumor cells, killing them (Figure 1.7a). Zhou *et al.* [3] additionally imaged xenografted HeLa tumors in a mouse with a dosage of 20 mg/kg of body weight; the tumor signal was enhanced 60 times in presence of WO_{3-x} NCs. Tumor cell viability tests showed a promising decrease in cancer cells by more than 80% at moderately low laser power (Figure 1.7b). Studies also found WO_3 to be non-toxic in the short term, though the long-term implications and lifetime inside the human body is still unknown.

1.6.2 Coupling with other resonant processes

Coupling between plasmonic phenomena and other resonant processes such as molecular vibrations, and electronic transitions has been demonstrated for LSPR of metal nanoparticles. Improving such coupling of lower energy processes such molecular vibrations, phonon resonance modes, or low energy electronic transitions of excitonic material such as GaAs using metal oxides is an exciting direction for future research on CMO LSPRs as more control is gained over the characteristics of their plasmonic resonances, colloidal stability, shaapes, and sizes. Already, low frequency phonon modes and excition modes of NCs have been theoretically predicted to couple with IR plasmon supporting materials such graphene [6] or CMO NCs [8,44] .

The interaction between a molecular vibration and a plasmon resonance is essentially the interference of two oscillating electric dipoles [129,130]. The electromagnetic interference between the plasmon near field and a molecular bond resonance leads to a Fano resonance, which can be observed in molecular vibration lineshapes on the top of the broader plasmon feature. Strong plasmon induced near fields can enhance this interaction, which can be maximized through low loss LSPR (metal oxides can be very low loss compared to metals) and through sharp surface curvature, which synthetic developments are beginning to yield. Indeed, metal oxide nanostructures have already been used to couple to molecular vibrations by Abb *et al.* [8]. Lithographically patterned $Sn:In_2O_3$ nanorods with controlled inter-rod spacing and rod length were coated with PMMA and the effect on the C=O molecular vibration was monitored. Indeed, the Fano resonance line shape strongly depends upon the size and resonance frequency of the nanorods (Figure 1.7c-d). These promising interactions as well as the fabrication of optical structures [131] utilizing a metal-insulator-metal resonator will be able to offer more sensitive detection capabilities as well as the potential for directing energy into specific molecular bonds via near field coupling.

Another important optical process that LSPR can enhance is two photon absorption and upconversion, particularly in increasing the efficiency of light harvesting processes. Two photon processes occur more efficiently when within strong electromagnetic fields. Furube *et al.* [44] studied the transient absorption of a dye coated onto a $Sn:In_2O_3$ NC film. The near-IR absorbing laser dye IR26 was coated homogenously over the 100-150 nm NC film with a LSPR maximum around 2140 nm. By pumping at 2200 nm, a strong transient bleach in the dye absorption occurred in the presence of the NCs compared to no signal from only IR 26 film (Figure 1.7e-f). This observation confirmed the NFE of the NCs was inducing a two photon absorption in the

dye that non-plasmon enhanced light of the same power could not induce. On the basis of pump power dependence on bleaching amplitude they quantified the NFE factor of around 6, Matsui *et al.* [132] showed similar enhancement behavior with Er light emission enhanced by Sn:In_2O_3 NC films.

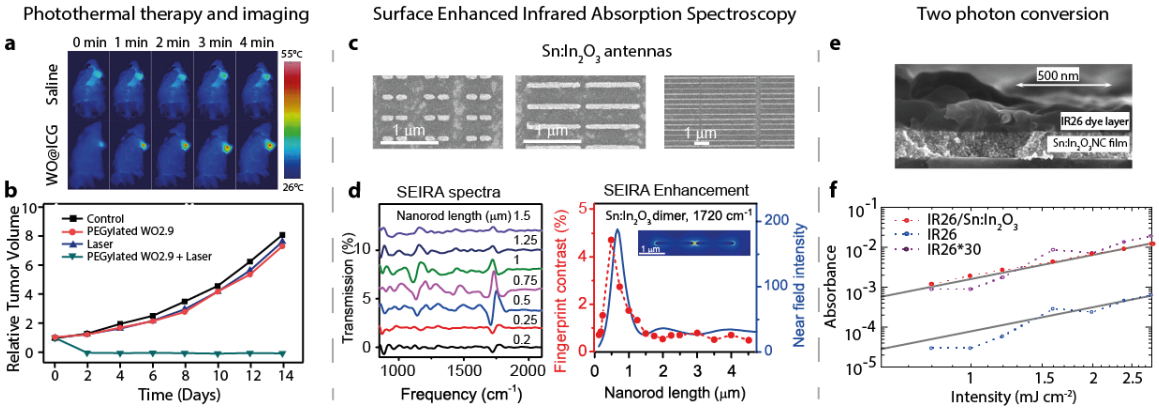

Figure 1.7 **Static applications on metal oxide LSPR** (a) Photothermal imaging demonstrated with an IR heat map of a tumor with (bottom row) and without (top row) tungsten oxide NCs at different durations of irradiation shows a sharp in increase in local temperature around the tumor due to strong plasmon induced local heating. Reprinted from [40] © John Wiley & Sons, Inc (b) The high local heat kills the infected tumor (green) compared to continuous tumor volume expansion in non NC treated cases. Reprinted with permission from [3] © 2014 Nature Publishing Group (c-d) Demonstration of SEIRA in nano-antennas of Sn:In_2O_3. (c) SEM images of lithographically printed Sn:In_2O_3 dimer nanorods of various length (d-left) Vibrational spectral features and intensity illustrate strong nanorod length dependence on the degree of LSPR-vibration coupling. (d-right) Nanorod length dependence on vibrational absorbance can be directly mapped on to the near field strength in such coupled system. Reprinted from [8] © 2014 American Chemical Society (e-f) Plasmon enhanced two photon upconversion. (e) SEM cross-sectional image of IR dye (IR26) on a layer of Sn:In_2O_3 NCs. (f) This system showed 30-fold enhancement in dye absorption in presence of Sn:In_2O_3 layer. This could be attribute to plasmon induced near field enhancement at the dye-NC film interface Reprinted from [44] © John Wiley & Sons, Inc.

1.7 Conclusion

NCs of CMOs have been used to demonstrate that through deliberate control over the carrier concentration and electronic structure near the Fermi level, LSPRs are tunable both in resonance energy and also in quality factor across two orders of magnitude of energy independent of NC size or shape. The fact that these properties can lead to modulation of the optical response means that the size and morphology of NCs can be optimized for applications of interest. Significant synthetic advances that would enhance the potential of CMO NCs would be to achieve NCs that are stably doped at high carrier concentrations even at smaller sizes, to control the distribution of dopants within and between NCs in an ensemble, NCs with sharper faceting for the sake of enabling assembly and achieving high NFE, and NCs that are highly monodisperse in more complex morphologies. Additionally, the ways in which the surface and strain within the nanocrystals interact with the electronic doping process should be further studied, as defect compensation mechanisms are still poorly understood in these materials. Doping leads to carrier concentrations substantially lower than the dopant concentration, which is still largely unresolved. Finally, taking full advantage of the tunability of LSPR in CMOs in order to enhance and modulate plasmonic coupling is yet to be demonstrated and could lead to technologically relevant performance that surpasses metal nanoparticles. This field and class of materials demonstrate great promise and through further investigation will yield substantial technological advances in controlling light interactions in nanoscale volumes.

Chapter 2

Shape-Dependent Field Enhancement and Plasmon Resonance of Oxide Nanocrystals

This chapter is adapted from the work "Ankit Agrawal, Ilka Kriegel, Delia J. Milliron. Shape-Dependent Field Enhancement and Plasmon Resonance of Oxide Nanocrystals. *J. Phys. Chem. C*, **2015**, 119(11).". My contribution to this work included the all the simulations of metal oxide LSPR.

2.1 Introduction

The ability to localize electromagnetic waves to the size of the nano-object through localized surface plasmon resonances (LSPRs) gives rise to a manifold of applications and biology-related challenges, such as sensing,[133–139] enhanced spectroscopies[140–14517], or photothermal therapy.[4,22,23] In metallic nanocrystals (NCs), the LSPR is mostly limited to the visible part of the spectrum and determined at the stage of synthesis. The LSPR frequency range of metallic nanostructures can be further extended to the near infrared (NIR) but this requires larger sized particles with complex shapes such as nanorods[148](> 50 nm in length) or nanoshells[149,150](> 60 nm in diameter). The ability to modify the plasmon resonance of NCs less than 20 nm in size to precise resonant absorption lines and with resonances within the biological window in the NIR[151] would be beneficial for numerous applications, such as enhancement spectroscopies in the near infrared,[137,138,152] sensing, or photothermal therapies.[153,154]

More recently, intense interest has been focused on a new type of plasmonic nanomaterials offering exactly these tunable properties, namely doped semiconductor NCs.[155,156] These are comprised of vacancy doped semiconductors such as copper

chalcogenides,[157–159] tungsten oxides,[160,161] or doped metal oxide nanocrystals.[155,156,162–164] The greatest advantage is however, the possibility to tune their plasmonic absorption through a careful choice of the dopant concentration, which establishes the number of carriers and, thus the spectral position of the LSPR.[156,165] In metal oxides, synthetic control over doping has been made possible by balancing the reactivity of precursors for the dopant and host crystal. Controlled synthetic doping with precise shape control[155,156,166] leads to carrier densities in the range of 10^{20}-10^{21} cm^{-3} and plasmon resonances covering a broad range of frequencies from the red to the infrared spectral range.[156,167] Moreover, the possibility to post-synthetically modify the LSPR by applying a voltage to conducting films of such NCs has been demonstrated[165,168–171] and successfully applied to electrochromic devices.[170,171] More recent work has triggered the implementation of such NCs as sensors for chemical redox reactions, where an electron transfer event can be detected as a shift in the LSPR on a single electron level.[172] Moreover, in photo-redox chemistry, a shift of the plasmon resonance is triggered by photochemical addition of electrons, which can be reversed by the addition of mild oxidants.[173]

Indium doped cadmium oxide (ICO) is an interesting candidate of such material.[162] The great advantage of ICO is that its spectral characteristics can be well-understood by a simple Drude-like free electron model, as demonstrated by analysis of optical spectra of thin films of ICO with different doping levels.[174,175] Unlike in other doped metal oxides, where impurity scattering results in a frequency dependent damping[176] or vacancies in the crystal result in localization effects,[177] the carriers in this material can be considered as essentially free and thus can be treated like a Drude metal.[174] ICO nanoparticles have been demonstrated to provide a tunable LSPR by varying the doping level, and to be synthesized in various shapes such as spheres or

octahedra.[162] However, many open questions remain in particular regarding the plasmonic properties of ICO nanoparticles, their shape-, size- and doping-dependent near- and far-field properties, their sensitivity to the surrounding medium, the possible effects of coupling plasmons in adjacent nanoparticles, and the potential for local heat production by dissipating energy from plasmon excitations. In this work, we explore these characteristics and simulate plasmonic far- and near-field properties of ICO nanoparticles under different constraints.

A powerful tool to unlock these plasmonic properties of ICO NCs is the discrete dipole approximation (DDA).[178–181] The NC volume is discretized into a finite array of polarizable points on a cubic lattice and the polarizability is calculated by taking into account the electric field arising from the surrounding induced dipoles.[178,179] Thus, the extinction (absorption and scattering) cross section of a single NC of arbitrary shape or the electric field surrounding the nanostructure can be calculated.

Here, we have done numerical calculations using the DDA and an analytical solution based on the Mie theory in order to calculate for the first time the plasmonic properties of metal oxide nanostructures, and in particular ICO NCs of varying carrier concentration, shape and size. The near- and far-field optical responses of differently shaped ICO NCs have been studied, taking advantage of the experimentally determined dielectric function of ICO at various doping levels. Our results demonstrate that such NCs are interesting candidates for infrared plasmonics with the benefit of synthesis and post-synthesis control over their LSPR allowing a precise tailoring of their plasmonic properties, which demonstrate a high sensitivity to the carrier concentration and shape.

2.2 Methods

2.2.1 Lorentz-Mie Theory

The Mie solution is an analytical solution to the Maxwell's equations to obtain light scattering from a spherical particle. It is a general solution for any spherical size, and has been simplified under sub wavelength conditions ($a_{eff} << \lambda$). In this quasi-static limit, Mie theory assumes that the phase retardation and effect of higher multipoles are neglected and field can be considered as constant throughout the volume of the particle. Under this assumption, absorption coefficient is given by the following equation,

$$C_{abs}(\mathrm{w}) = 4\pi \mathrm{k}(\varepsilon_H)^{1/2} R^3 \,\mathrm{Im}\left\{\frac{\varepsilon_p(w)-\varepsilon_H}{\varepsilon_p(w)+2\varepsilon_H}\right\} \qquad 2.1$$

where k is the wavevector in vaccum, $\varepsilon_p(\omega)$ is the dielectric function of the particle, ε_H is the dielectric function of the medium and R is radius of particle.

2.2.2 Discrete Dipole Approximation

The Mie solution is only applicable for spherical particles and for ellipsoids or rods applying certain corrections. But in order to simulate extinction spectra for any general shape and size a numerical method is required. In this work, our computational results are based on a numerical solution of the Maxwell's equations. The Discrete Dipole Approximation (DDA) was employed as a numerical method for its solution[178,179] and an open source program DDSCAT 7.2[178,179] was employed for the calculation. The DDA technique allows the calculation of the optical absorption and scattering of NCs of arbitrary shape. In practice, the continuum target is approximated by an array of polarizable points located on a cubic lattice with an interdipole distance, d given by $V=N\cdot d^3$, where V is the volume of the particle and N the number of polarizable points. The size of the particle is determined by the effective radius $r_{eff} = \left(3V/4\pi\right)^{1/3}$, representing

the radius of a sphere of equal volume. The differently shaped NCs are discretized into an N×N×N array of interacting spherical dipoles. In order to get converged numerical results, a sufficient number of discrete dipoles needs to be considered, which is chosen to satisfy the convergence condition

$$|\varepsilon|\kappa d < 0.5 \tag{2.2}$$

where ε is the complex dielectric function, $\kappa = 2\pi/\lambda$ is wave number. Then, the polarization for each dipole is determined by solving 3N equations for

$$\sum_{k=1}^{N} A_{jk}\vec{P}_j = \vec{E}_{inc,j} \tag{2.3}$$

with $\vec{E}_{inc,j}$ the incident electric field and $\vec{P}_j$ the polarization of the j^{th} dipole. The inter-dipole interaction term A_{jk} ($j \neq k$) is a 3×3 matrix given by

$$A_{jk} = \frac{e^{i\kappa r_{jk}}}{r_{jk}}\left[\kappa^2(\hat{r}_{jk}\hat{r}_{jk} - \tilde{I}) + \frac{i\kappa r_{jk} - 1}{r_{jk}}(3\hat{r}_{jk}\hat{r}_{jk} - \tilde{I})\right],\ j \neq k \tag{2.4}$$

where r_{jk} is the distance between j and k dipole, $\hat{r}_{jk}$ is the unit vector along r_{jk} and $\tilde{I}$ is the identity matrix. The self-interacting term A_{jj} is given by

$$A_{jj} = \alpha_j^{-1} \tag{2.5}$$

where α_j is the complex polarizabitlity of the dipole, which depends upon the material's dielectric function (ε_j), the radius of each dipole r_{eff} and the surrounding dielectric medium (ε_H). It is given by the corrected discretized Clausius-Mossotti equation. It has been found that accuracy of this mathematical formulation can be improved for high dielectric value materials by filtering out the high spatial frequency component. This new corrected dipole is known as Filtered Couple Dipole. Convergence of different numerical method is compared to analytical Mie solution in Figure 2.1.

$$\alpha_j = \frac{\alpha^{(CM)}}{1 + D} \tag{2.6}$$

where, $\alpha^{(CM)}$ is Claussius Mossotti term given by

$$\alpha^{(CM)} = \frac{3d^3(\varepsilon_j^2 - 1)}{4\pi(\varepsilon_j^2 + 1)} \qquad 2.7$$

and D is the correction term given by

$$D = \frac{\alpha^{(CM)}}{d^3}\left[\frac{4}{3}(\kappa d)^2 - \frac{2}{3\pi}\ln\left[\frac{\pi - \kappa d}{\pi + \kappa d}\right] + \frac{2}{3}i(\kappa d)^3\right] \quad . \qquad 2.8$$

Extinction, absorption and scattering cross sections can by calculated using the polarizability obtained from eq 2.6 through,

$$C_{ext} = \frac{4\pi\kappa}{|E_0|^2}\sum_{j=1}^{N}\mathrm{Im}(\vec{E}^*_{inc,j}.\vec{P}_j) \qquad 2.9$$

$$C_{abs} = \frac{4\pi\kappa}{|E_0|^2}\sum_{j=1}^{N}\left[\mathrm{Im}\left\{\vec{P}_j.(\vec{\alpha}_j^{-1})^*\vec{P}_j^*\right\} - \frac{2}{3}\kappa^3(\vec{P}_j.\vec{P}_j^*)\right] \qquad 2.10$$

$$C_{ext} = C_{abs} + C_{sca} \qquad 2.11$$

Now, Near Electric Field and Internal Electric Field can be calculated through,

$$\vec{E} = \vec{E}_{inc} + \vec{E}_{scat} = \begin{cases} \alpha_j^{-1}P_j & dipole,\ j \\ E_{inc,i} - \sum_{j\in\ dipoles} A_{ij}P_j & i \in \ surrounding\ discretization \end{cases} \qquad 2.12$$

Extinction, absorption and scattering efficiency, which is directly calculated from DDSCAT is defined as $Q_i = \frac{C_i}{\pi a_{eff}^2}$, *where i = ext, scat, abs* 2. 13

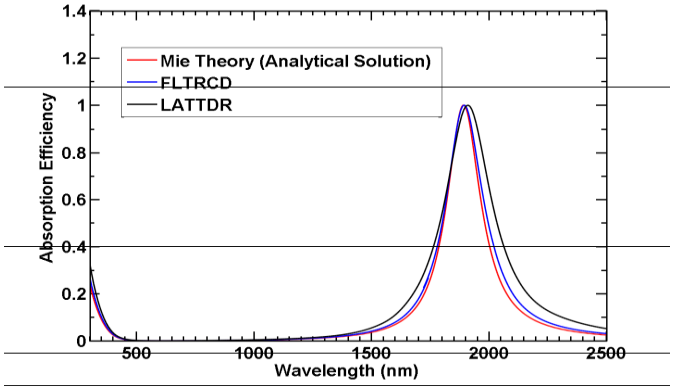

Figure 2.1 **Numerical Convergence of DDSCAT methodology** Convergence of DDA compared to the analytical solution from Mie theory. Comparison of performance of different method of discretization of Maxwell equation available in DDSCAT package

2.2.3 Plasmon Heating

The NC absorption of energy due to the plasmon resonance will give rise to a temperature increase of and around the NC. The heat is considered to be localized in close vicinity of the NCs. Since its dimensions are in the nanometer range the temperature gradient inside the particle can be considered as static and a steady state is reached within a few picoseconds. Here, we therefore estimate only the steady state temperature profile. At steady state, heat is absorbed by the NC (Q_{abs}) and dissipated to the surrounding (Q_{dis}). For the calculation of the absorbed heat the absorption cross section C_{abs} of the NC is considered. Then Q_{abs} is given as

$$Q_{abs} = C_{abs} I = C_{abs} \frac{(\varepsilon_H)^{1/2} c\varepsilon_0}{2} |E_0|^2 \qquad 2.14$$

with *c* being the speed of light, and Q_{dis} as

$$Q_{dis} = ha(T_{nanoparticle} - T_{bulk}), \qquad 2.15$$

where *h* is the heat transfer coefficient, *a* is the surface area and T_{bulk} determines the temperature in the surrounding medium. The heat transfer coefficient for a spherical particle immersed in a pool of surrounding medium is given by $h = \frac{k_s}{R}$, where k_s is the thermal conductivity of the medium and *R* is the radius of the particle. Taken together, this results in the following equation

$$(T_{nanoparticle} - T_{bulk}) = \frac{C_{abs}}{ha} \frac{(\varepsilon_H)^{1/2} c\varepsilon_0}{2} |E_0|^2, \qquad 2.16$$

Substituting C_{abs} from Mie theory for the spherical particle we get:

$$(T_{nanoparticle} - T_{bulk}) = \frac{\mathrm{k}\,\varepsilon_H R^2}{k_s} \frac{c\varepsilon_0}{2} |E_0|^2 \,\mathrm{Im}\left\{ \frac{\varepsilon_p(w) - \varepsilon_H}{\varepsilon_p(w) + 2\varepsilon_H} \right\} \qquad 2.17$$

which determines the temperature change in the surrounding medium as a function of the NC radius *R*. It shows that temperature difference is proportional to the

square of the radius of the particle and directly proportional to the intensity of the incoming wave.

2.3 Results and discussion

A major differentiation of plasmonic semiconductor NCs versus metallic nanoparticles is the possibility to change the free carrier concentration inside the particle over a wide range, which can be pre- and post-synthetically controlled. This plasmon characteristic, which is unique to this class of materials, allows dynamic modulation of the plasmonic response. Here, we investigated the effect of varying carrier concentration via doping on the optical near- and far-field properties of ICO NCs. We simulated the extinction spectra of 10 nm diameter spherical ICO NCs for carrier concentrations varying from 0.81 to $1.33 \cdot 10^{21}$ cm^{-3} (Figure 2.2a). The strong resonance in the near infrared (NIR) is ascribed to the localized surface plasmon resonance (LSPR), which can be tuned from 2250 to 1600 nm depending upon the carrier concentration. A blue shift of the LSPR is observed with increasing carrier concentration. This result can be understood from the Mie theory where the absorption cross section is given as:

$$C_{abs}(\omega) = 4\pi \mathrm{k}(\varepsilon_H)^{1/2} R^3 \,\mathrm{Im}\left\{\frac{\varepsilon_p(\omega) - \varepsilon_H}{\varepsilon_p(\omega) + 2\varepsilon_H}\right\} \qquad 2.18$$

with k being the wavevector, R the NC radius, ε_H the host dielectric constant, and $\varepsilon_p(\omega)$ the material dielectric function. Taking the resonance condition $\varepsilon_r = -2\varepsilon_H$ and the Drude dielectric function the LSPR peak position can be found as

$$\omega_{LSPR} = \sqrt{\frac{\omega_p^2}{1 + 2\varepsilon_H} - \gamma^2} \qquad 2.19$$

where, γ is the damping constant and ω_p, the plasma frequency that relates the carrier density $N_{c:}$ to the LSPR peak position ω_{LSPR}, is:

$$\omega_p = \sqrt{\frac{N_c e^2}{m_e^* \varepsilon_0}} \,. \qquad 2.20$$

where e is the electron charge, m_e^* is effective electron mass, and ε_0 is the vacuum permittivity.

\

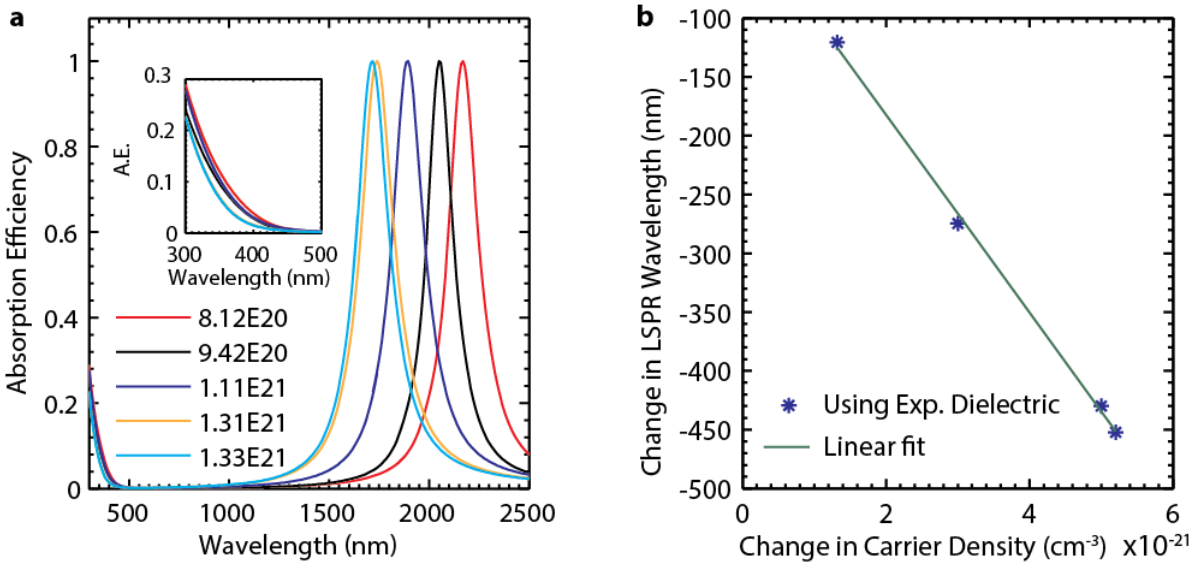

Figure 2.2 Dopant concentration effect on LSPR properties of ICO nanocrystals. a) Extinction coefficient of ICO NCs of 10 nm diameter at different levels of doping ranging from $8.1 \cdot 10^{20}$ To $1.33 \cdot 10^{21}$ cm^{-3}. Inset: interband region illustrating the Moss-Burstein shift with increasing carrier density. b) Change in LSPR peak wavelength versus change in carrier concentration assuming an initial carrier concentration of $8.12 \cdot 10^{20}$ cm^{-3}. The slope of the linear relationship is defined by us as the carrier concentration sensitivity factor.

Thus, an increase in carrier density directly explains the strong blue shift of the plasmon peak position. In line with this, it has been shown in a recent work by Mendelsberg *et al*,[172] that using the carrier dependent plasmon peak shift, it is possible to track, model and quantify electron transfer events from organic, inorganic, biogenic, and even living species to the doped semiconductor NC. To quantify the sensitivity of the

plasmon peak to the actual carrier concentration N_c, we have derived the carrier concentration sensitivity factor (S_{N_c}) using the Drude model and the Mie theory (the derivation is given in the Appendix 1). The carrier concentration sensitivity factor linearly correlates the change in the LSPR peak ($\Delta\lambda$) to the change in free carrier concentration (ΔN_c) as shown below.

$$\Delta\lambda = -S_{N_c}\Delta N_c, \qquad 2.21$$

where

$$S_{N_c} = \frac{\lambda_i^3 e^2}{2m_e^* \varepsilon_o (\varepsilon_\infty + 2*\varepsilon_H) c^2}. \qquad 2.22$$

λ_i is the initial plasmon peak, ε_∞ is the bulk high frequency dielectric constant and *c* is the speed of light (all in SI units). ICO NCs with an initial carrier density of $0.81 \cdot 10^{21}$ cm^{-3} follow this correlation precisely having a sensitivity factor of 20 $nm/10^{20} cm^{-3}$ (Figure 2.2b). This means that for a spherical ICO NC of 5 nm in diameter the addition of 100 electrons would lead to a shift of the plasmon resonance of 38 nm. The addition of even one electron would give an easily detectable shift of 3.8 nm, underscoring the potential of these NCs as highly sensitive redox sensors.

Since our calculations have been performed using an experimentally measured dielectric function[41] which inherently includes the contribution of interband transitions, we can see the onset of the interband absorption in all spectra at around 450 nm, which is blue shifted with respect to the bulk bandgap of undoped CdO at around 570 nm (2.16 eV)[182]. The blue shift of the interband absorption increases progressively with increasing carrier density (Figure 2.2a, inset). This shift is understood in terms of the Moss-Burstein effect of heavily doped semiconductors, where the optical band gap is shifted to higher energy due to the filling of states near the conduction band edge with increasing doping level.[183]

Another very important characteristic of plasmonic NCs is the ability to efficiently scatter light resonant with the plasmon frequency. We calculated the extinction spectra of ICO NCs of varying size ranging from 10 to 300 nm in diameter (Figure 2.3a). In the far-field response with increasing size up to around 100 nm in diameter, no change in the plasmon peak position is observed and a change in peak intensity is consistent with the increase in absorption with the volume change. In this size regime, absorption is the dominant mechanism contributing to the extinction and scattering is almost completely absent. These calculations are consistent with the dipolar approximation of the Mie theory for particles very small in comparison to the incoming wavelength.[184] From particles of 100 nm to 300 nm in diameter we observe a red shifted plasmon resonance and the contribution of scattering increases rapidly, so that scattering is stronger than absorption for the 300 nm diameter particles (Figure 2.3b). This very strong plasmon scattering in the infrared is a distinguishing characteristic of doped semiconductor NCs and is envisaged to be very useful for application such as infrared microscopy,[185] imaging,[136] or enhanced solar conversion.[186] As sizes increase toward the electromagnetic field decay length, asymmetry in the extinction spectrum is observed and multi-mode absorption arises (Figure 2.3b). The origin of these modes is explored by calculating the spatial distribution of the electric near field.

Maps of the enhanced electric near-field under variable single-wavelength excitation are calculated for NCs of 10 nm, 200 nm, and 300 nm diameter to reveal the plasmon modes responsible for the far-field resonance peaks (Figure 2.3c). Below 100 nm, isolated spherical NCs have dipolar modes with modest near field enhancement (NFE) factors up to 24. The NFE is independent of the NC size for sizes up to 100 nm, consistent with the Mie theory in the dipolar regime (Figure 2.3c (i,ii)) [138] As scattering makes a stronger contribution for the 200 nm diameter particle, the NFE starts to

decrease (Figure 2.3c (iii)). We can also clearly see the effect of electric field decay along the wave-vector in the 300 nm particle spectra and that the higher intensity peak is due to dipolar mode and the lower intensity peak is due to the quadruple mode (Figure 2.3c (iv),(v)). These results show that plasmonic modes are size dependent above 100 nm and the relative contribution of absorption and scattering to the total extinction cross section can be tuned by changing the size of the NC.

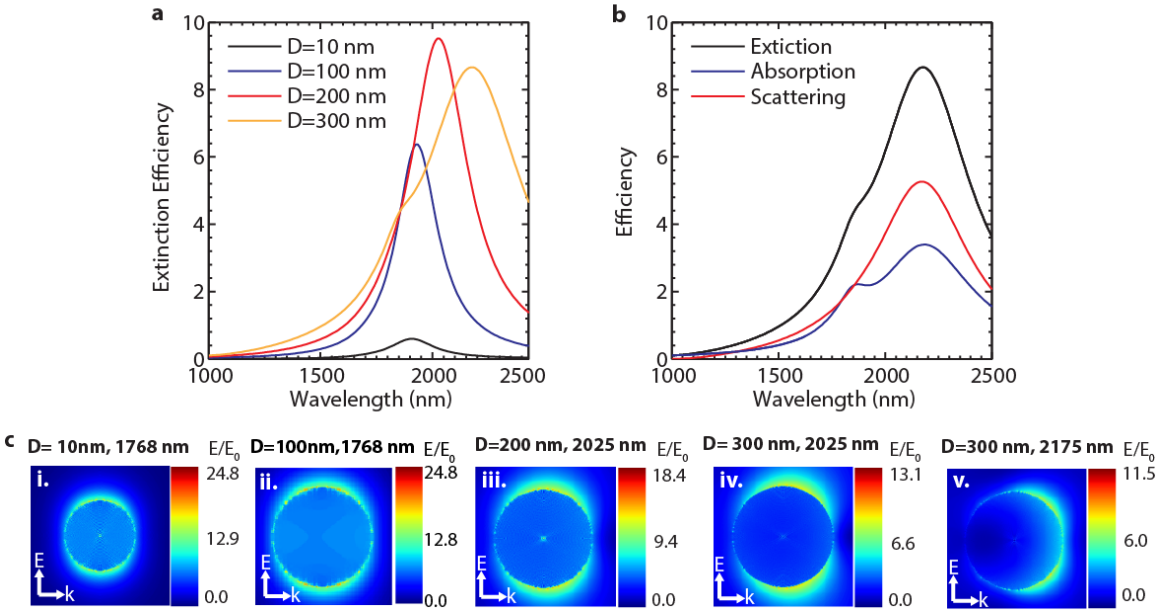

Figure 2.3 **Nanocrystal size effect on ICO LSPR** a) Extinction spectra of spherical ICO NCs of increasing diameters ranging from 10 to 300 nm. b) The scattering (red) and absorption (blue) contribution to the extinction of a 150 nm diameter sphere. For sizes of less than 100 nm, the scattering becomes negligible (not shown here). c) NFE maps for the same NCs with increasing size. (i,ii) The NFE factors are not influenced by size in a range from 10 nm to 100 nm in diameter. iii) the NFE becomes lower because scattering and multipolar modes start to play a major role for 200 nm diameter particles, iv), v) NFE maps illustrating the multipolar modes for the 300 nm sized .

By varying the growth conditions, differently shaped NCs of the same material can be synthesized. Shape is known to strongly influence the near and far field properties

of conventional plasmonic nanomaterials.[136,144,160,162] In a recent work by Gordon *et al.* ICO NCs have been successfully synthesized in different shapes such as octahedron, and a shape dependent optical response has been demonstrated.[162] Similarly, Mattox *et al.* reported shape-dependent far-field spectra for Cs_xWO_3 NCs.[160] We calculated the shape dependent extinction spectra for spheres, cubes and octahedra (Figure 2.4a). As we move from the spherical to the sharp cornered or edged particles such as the octahedron or cube, the plasmon peak red shifts, becomes broader, and substantially decreases in peak intensity. Moreover, the spectra are characterized by secondary peaks and shoulders corresponding to multipolar excitations.

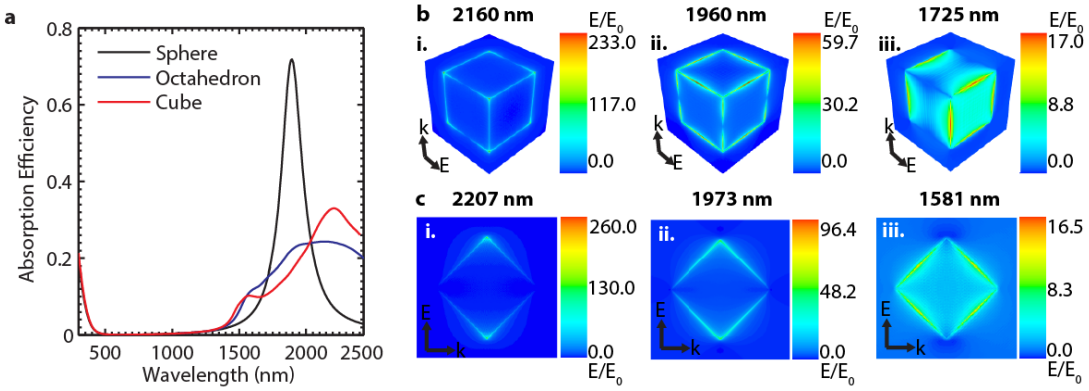

Figure 2.4 **Nanocrystal shape effect on ICO LSPR**. a) Extinction spectra of differently shaped ICO NCs with a carrier density of 1.11E21 cm^{-3}: All shapes have volume equivalent to volume of 10 nm of spherical particle. The spectra of cube and octahedron are dominated by multiple peaks. b) NFE map of cube excited at 2160 nm, 1960 nm and 1725 nm demonstrating the multipolar excitation. For the highest intensity peak (2207 nm) the enhanced field is strongly localized at the corners of the cube, reaching field enhancement factors of up to 233, while for the lower intensity peaks the field enhancement is spread over the edges (1960 nm) and faces (1725 nm) leading to decreased enhancement factors. c) NFE map of octahedron excited at 2207 nm, 1973 nm and 1581 demonstrating the multipolar modes. For the highest intensity peak (2160 nm) the enhanced field is strongly localized at the corners of the octahedron, reaching field enhancement factors of up to 260 while for the lower intensity peaks the field enhancement is spreading over the edges (1973 nm) and faces (1581 nm) leading to decreased enhancement factors.

The origin of the multiple peaks can be explained using near-field calculations on faceted NCs. In the calculations, the plasmon resonance is excited at the different peak or shoulder wavelengths with light polarized in y-direction and the NFE of the electric field is calculated. The NFE maps of the octahedron show multipolar modes mostly distributed over the faces, the edges and the corners (Figure 2.4c). The distribution of the near field is primarily over the faces when exciting the lowest intensity peak (1725 nm), over the edges when exciting the mid-intensity peak (1960 m), and over the corners for the highest intensity peak (2160 nm), leading to NFE factors between 15.5 and 260. The strong

differences in intensity are understood by the different distributions of the field. The strong accumulation of field intensity at the corners for excitation with the highest intensity peak leads to the highest NFE factors of up to 260. Very similar results are observed for the cubic particle, where the shift of the accumulated near field from the faces to the corners results in increased NFE factors of up to 233 (Figure 2.4b). The higher NFE factor in the octahedron with respect to the cube is due to excitation polarization along tip-tip diagonal. These strongly localized field distributions are responsible for high sensitivity of the plasmon resonance to the refractive index of the surrounding medium and this sensitivity is exploited for various applications such as sensing of single molecules or mass spectrometry.[137,138,54] An advantage that our semiconducting nanoparticles hold over metallic ones is their surface chemistry that supports surfactants of various functional groups and coordination chemistry for specific binding to certain facets in the crystal. The surface chemistry of semiconducting nanoparticles has been studied in detail and is widely understood, resulting in the possibility to fine tune and precisely control the shape and size of such nanoparticles.[187,188,189] Thus, a direct attachment of various functional groups to specific facets is given in semiconducting NCs, which can be exploited for sensing application or surface enhanced spectroscopies with site specific detection.[190]

To analyze the sensitivity of our nanostructures to their surrounding medium, we have calculated the plasmon resonance of ICO nanoparticles with different surrounding refractive index, thereby taking into account differently shaped particles, such as sharp cornered octahedra, cubes or spherical particles. First, we have calculated the plasmonic response for a 10 nm diameter spherical particle to the medium refractive index (Figure 2.5a) using the Mie theory, which in the dipolar limit gives similar results to the DDA. Equation 2.23 demonstrates the dependence of the absorption to the surrounding medium:

$$\Delta\lambda = m \cdot \Delta n \qquad 2.23$$

where m is the sensitivity factor per refractive index unit, Δn is the change in refractive index and $\Delta\lambda$ is the corresponding wavelength shift.[137] The calculated extinction spectra for the sphere (Figure 2.5a) show an increase in peak intensity and a red shift with increasing refractive index. For sensing application, it has been found that sharp edges or corners in the plasmonic nanoparticles give a stronger response to changes in the surrounding environment.[191] Thus, we calculated the shape dependent response of the ICO octahedron to changes in the surrounding medium (Figure 2.5b). A redshift in plasmon peak is observed with increasing refractive index of the medium, which is greater in magnitude compared to the spherical particle (Figure 2.5d). Using equation 22 and from Figure 2.5d, we have calculated the sensitivity factor per refractive index unit for both spherical and octahedron particles at their highest intensity peaks to be 560 nm and 804 nm per refractive index unit (RIU^{-1}), respectively, demonstrating the stronger sensitivity of the ICO octahedron and spherical particle to the medium refractive index when compared to a typical RIU of around 300nm for gold nanorods.[192] This sensitivity in turn affects the NFE factors as summarized for the three peaks of the octahedron in Figure 2.5c, demonstrating an increase of NFE with increasing refractive index. This is understood due to the weaker electric field in a medium with higher refractive index. Generally, our results demonstrate that each mode separately shows sensitivity to the medium refractive index, which implicates that a control over specific binding to the NC surface is of great importance for molecular sensing applications or enhanced spectroscopies in the infrared.

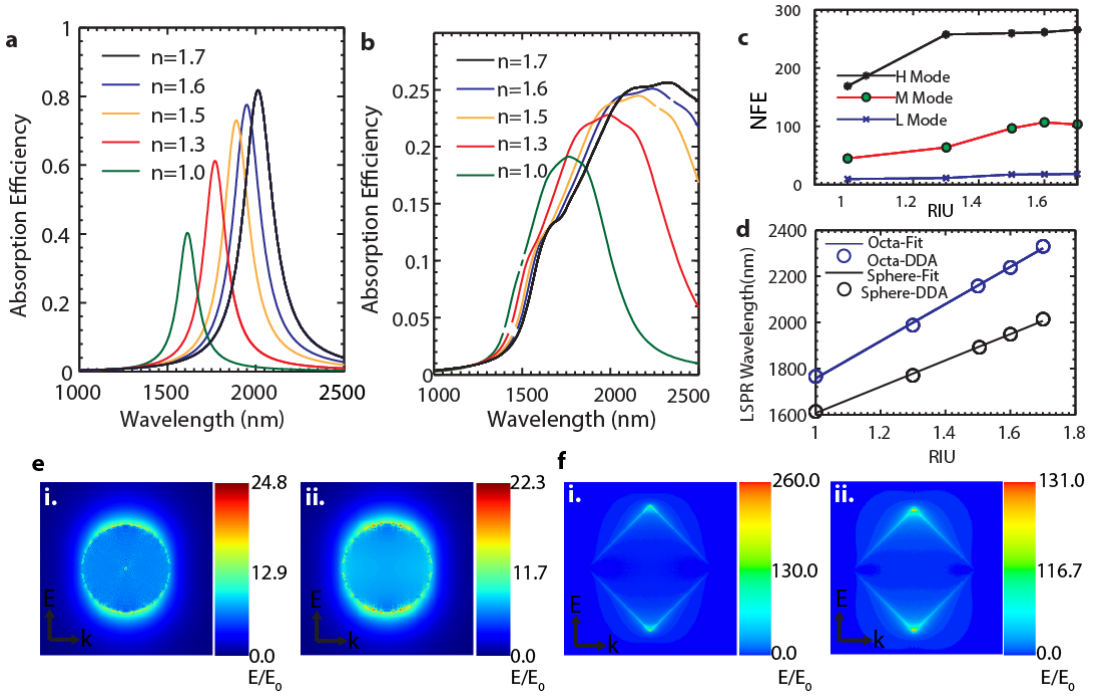

Figure 2.5 **Effect of the surrounding on ICO LSPR.** Extinction spectra of (a) sphere of 10 nm diameter and (b) octahedron with volume equivalent to volume of 10 nm spherical particle and a carrier density of $1.11 \cdot 10^{21}$ in different medium refractive index. A red shift and increase in intensity is observed with increasing surrounding refractive index. c) NFE factors excited at the highest intensity absorption peak (H Mode), mid intensity peak (M mode) and low intensity peak (L mode) versus refractive index of the medium. d) LSPR peak wavelength versus refractive index for both spherical and octahedron particle. All calculations were performed with the experimental dielectric functions and the fits show linear correlation as expected from the sensitivity relation (eq. 6) and (f) NFE maps for different carrier densities of i) $9.42 \cdot 10^{20}$, ii) $1.11 \cdot 10^{21}$ for the sphere (e) and the octahedron (f). With increasing carrier density the NFE is increasing.

The NFE is also strongly dependent on the carrier concentration. Therefore we calculated the NFE maps for both the sphere and the octahedron (Figure 4e and f) for two different carrier densities of $9.42 \cdot 10^{20}$ cm^{-3}(i) and $1.11 \cdot 10^{21}$ cm^{-3}(ii). As we increase the free carrier density, the NFE factor increases. While this effect is minor in the sphere it is very strong for the octahedron (from around 130 to around 260). This result goes in hand

with a stronger sensitivity of the plasmon resonance to the surrounding medium of the NC (due to the higher fields). We envisage that *in situ* tuning of the NC carrier density could modify the sensitivity of the plasmon resonance to its surrounding. Thus, a variation of the NFE through the control of the carrier concentration in the NCs, offers a way to switch on, off and fine tune its sensitivity to the surrounding, supplying an additional parameter for resonance specific sensing. Taken together, the carrier density, size, shape and refractive index deliver a broad variety of parameters to tune the near and far field properties of ICO NCs in the near infrared, with a more complex shape, and higher carrier density delivering higher NFEs.

Thus far, perfectly shaped NCs have been considered, however realistic NCs have rounded edges that may influence plasmonic properties. To explore the impact of such shape perturbations in ICO NCs, we compared the ensemble extinction spectra of synthesized ICO octahedra NCs with our calculations. By transmission and scanning electron microscopy (TEM and SEM) of the octahedral NCs (Figure 2.6a, inset), it is observed that the 10 - 20 nm sized particles show a strong deviation from a perfect shape, in that the edges and corners are rounded in most cases. The experimental absorption spectrum is qualitatively similar to the calculated spectrum for an isolated, perfect octahedron, but the experimental spectrum is not as broad as the simulated one (Figure 2.6a). This difference motivated us to study with the DDA the effect of rounding of the corners and edges on the absorption spectra and NFE. This study was performed on a cubic particle of 8 nm side length. To study this effect, the corners and edges of a perfect cube (Figure 2.6b, (i)) are rounded to a different extent (Figure 2.6b (ii)). The rounding has been described using a rounding factor (a) as the ratio between the radius of curvature (R) to the side length of the perfect cube (L).

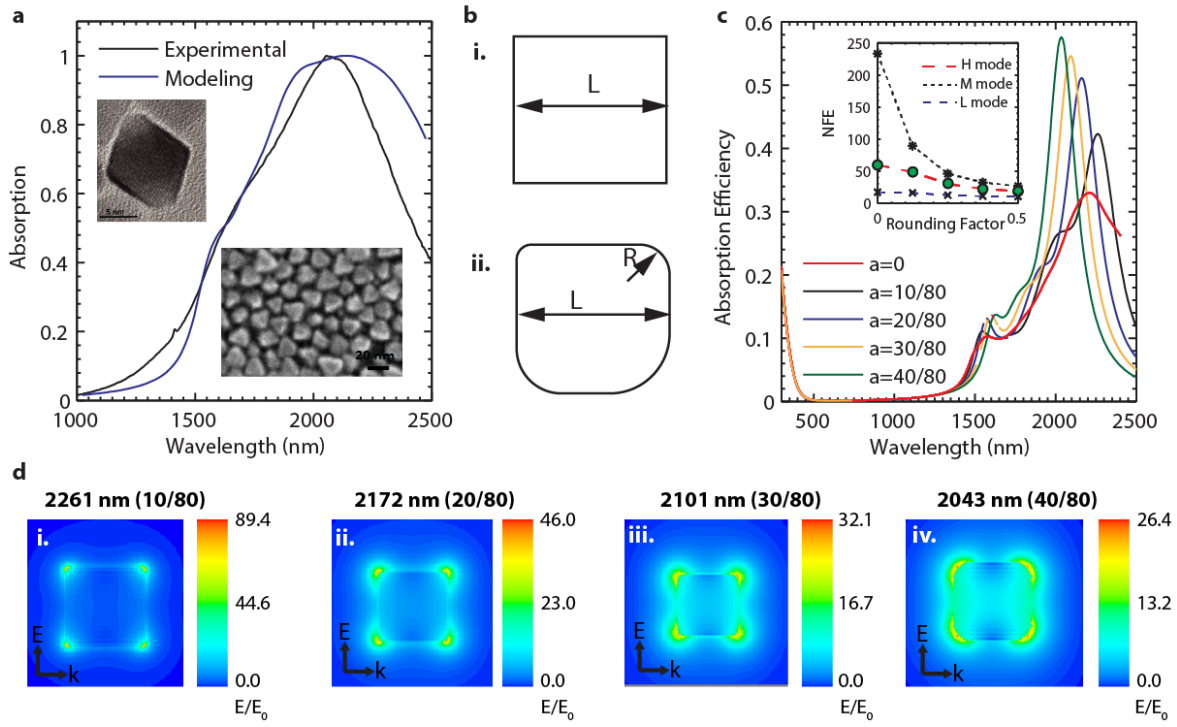

Figure 2.6 **Implication of non-ideal rounded shape on ICO LSPR.** a) Experimental and theoretical absorption spectra of around 10 nm ICO octahedron particle (insets)TEM and SEM images of synthesized octahedral particles show a deviation from the perfect octahedron shape due to rounding of the edges and corners. b) Illustration of rounding of the edges and corners of a perfect cube (i) to different extents as illustrated by the different rounding of the four corners (ii). The value of a defines the rounding as is calculated by a = R/L c) Effect of rounding the edges and corners of a cube with a carrier density of 1.11E21 on the absorption spectrum. Volume of all the shape is equivalent to volume of 10 nm spherical particle Inset: the NFE factor versus rounding. With increasing rounding the different modes merge together to reach an unresolved broad band, along with a dramatic decrease in NFE factors.

The calculated extinction spectra for the perfect cube of 8 nm dimension is shown in Figure 2.6c, together with four rounded edge cubes. As we increase the rounding, the highest intensity peak blue shifts and the spectrum becomes narrower. Lower and higher order modes move towards each other as rounding increases and the most intense dipolar

mode[193] dominates the absorption spectra approaching the single dipolar mode of a perfect sphere. These simulations are consistent with the experimental observation for the 10 - 20 nm sized octahedra (Inset, Figure 2.6a), where a more narrow resonance was found in the synthesized NCs, with lower and higher energy modes that are closer in energy compared to the spectrum calculated for the perfect octahedron. From NFE calculations, we can see that as we increase the rounding, there is a significant decrease in the enhancement from 233 for the perfect cube (highest intensity mode) to 69.4 for a rounding of 1/8 (Figure 2.6d). These results demonstrate that for any application based on near field enhancement, the synthetic route should be optimized to have maximally precise shape control.

Other than developing new synthetic routes, coupling of plasmonic particles arranged in assemblies may offer another option to reach higher enhancement factors. Indeed, in our calculations a sharp increase in the NFE occurs via the formation of hot spots in between proximal particles (see below). A major application taking advantage of the high NFE factors is surface enhanced Raman spectroscopy (SERS). It has been found that as a molecule is adsorbed onto a plasmonic nanoparticle or come close to it, the Raman scattering gets enhanced by factors ranging from 10^8 to 10^{14}.[138,141,142] This leads to specific and sensitive detection of molecules. To get the maximum enhancement, it is ideal to have the plasmon wavelength close in energy to both the incident wave frequency and the Stokes shifted Raman frequency.[138] Another way to enhance the Raman signal is resonance Raman spectroscopy, where the Raman signal is enhanced at least by five orders of magnitude (SERRS), when exciting with a laser in resonance to an electronic transition of the molecule.[194] In addition, surface enhanced infrared spectroscopy leads to enhanced infrared absorption signals of molecules covering islands of plasmonic nanostructures that show plasmonic absorption up to the infrared.[195] Plasmonic

semiconductor NCs have plasmonic resonances in the infrared tunable over a broad range of wavelengths. This might deliver a new approach to enhanced spectroscopies in the infrared through a pre or post-synthetic fine tuning of the LSPR peak to the frequencies of interest, such as the molecular resonance of a certain molecule of desire.

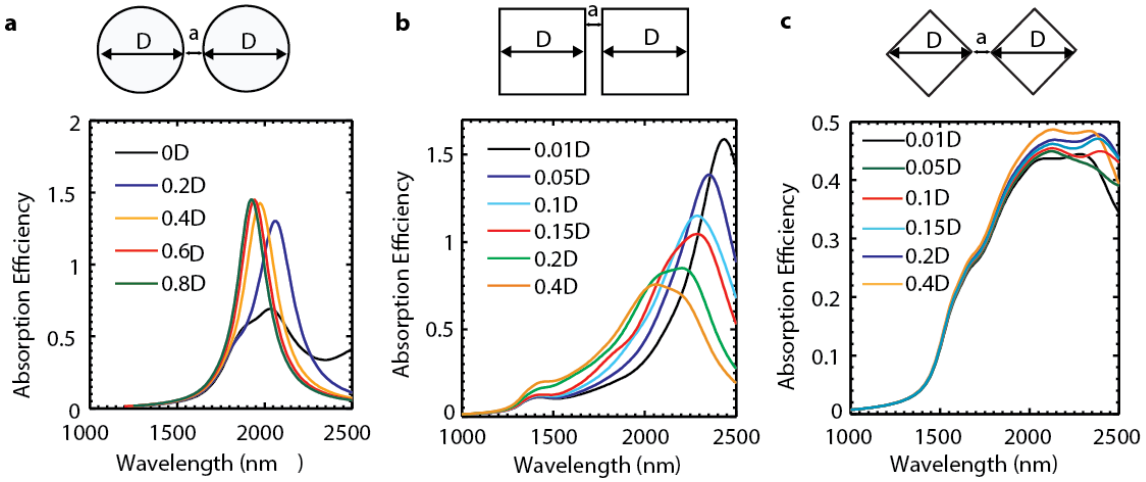

Figure 2.7 LSPR coupling effect on optical spectra. a) Absorption spectra for the dimers of (a) sphere, (b) cube and (c) octahedron for different interparticle distances a and a carrier density of $1.11 \cdot 10^{21}$ for sphere and octahedron and $1.3 \cdot 10^{21}$ for cube dimer. Volume of single particle in all the dimer are equivalent to volume of 10nm spherical particle. The LSPR shifts due to interparticle plasmon coupling the closer the particles get. This effect is the strongest in the cube dimer with face to face orientation.

Thus, we investigated the field enhancement between adjacent plasmonic ICO NCs with spherical shape, tip to tip enhancement in octahedron NCs and face to face enhancement in cubic NCs. These orientations could plausibly be formed during assembly of NCs. Absorption spectra were calculated for a polarization parallel (x-polarized) and perpendicular (y-polarized) to the center to center axis of the dimer (here the x-axis). The effect of coupling was studied for different interparticle distances *a*, defined as factor of the maximum particle dimension D along the x-axis, as illustrated in

Figure 2.7 a-c, upper panel. The calculated absorption spectra vary with the value of *a* for the spherical, octahedron and cubic NC dimers excited with x-polarization (along the dimer axis, Figure 2.7a-c). As the inter-particle distance decreases and the coupling becomes stronger, the major plasmon peak red shifts for all shapes, which becomes very pronounced with an inter particle distance of 0.2D and less. For particles in direct contact (a = 0), or nearly so (a = 0.01D) a stronger effect is observed: in the sphere and the cube dimer, the absorption spectrum changes drastically with strong multimodal peaks appearing (Figure 2.7a). This is attributed to the occurrence of new plasmon modes distributed over the entire NC dimer. Since in the case of the tip-to-tip octahedron dimer the plasmon coupling region is very small, we do not observe a very pronounced effect on its spectra, even for near-direct contact.[196]

The strong plasmon coupling in NC dimers also leads to the generation of hot spots in the NC dimer gap. The NFE factors are increased multifold in the zone between the particles and are increasing with decreasing interparticle distance. The maximum enhancement was found for interparticle ratios between a = 0.05 and 0.2. A coupling analysis for the ratios from 0 to 0.05 has been omitted, as the classical Maxwell treatment fails in this zone and quantum tunneling effects take over.[196] NFE maps were calculated for sphere, cube and octahedron dimers for different interparticle distances (Figure 2.8a-c). The closer the NCs the higher the NFE factors become (Figure 2.8a). In the sphere and octahedron dimers a clear hot spot between the two particles is observed (Figure 7c (i) and (ii), respectively). In the case of the cube dimer, the location of the maximum field enhancement is strongly dependent on the distance between the particles (Figure 2.8b).

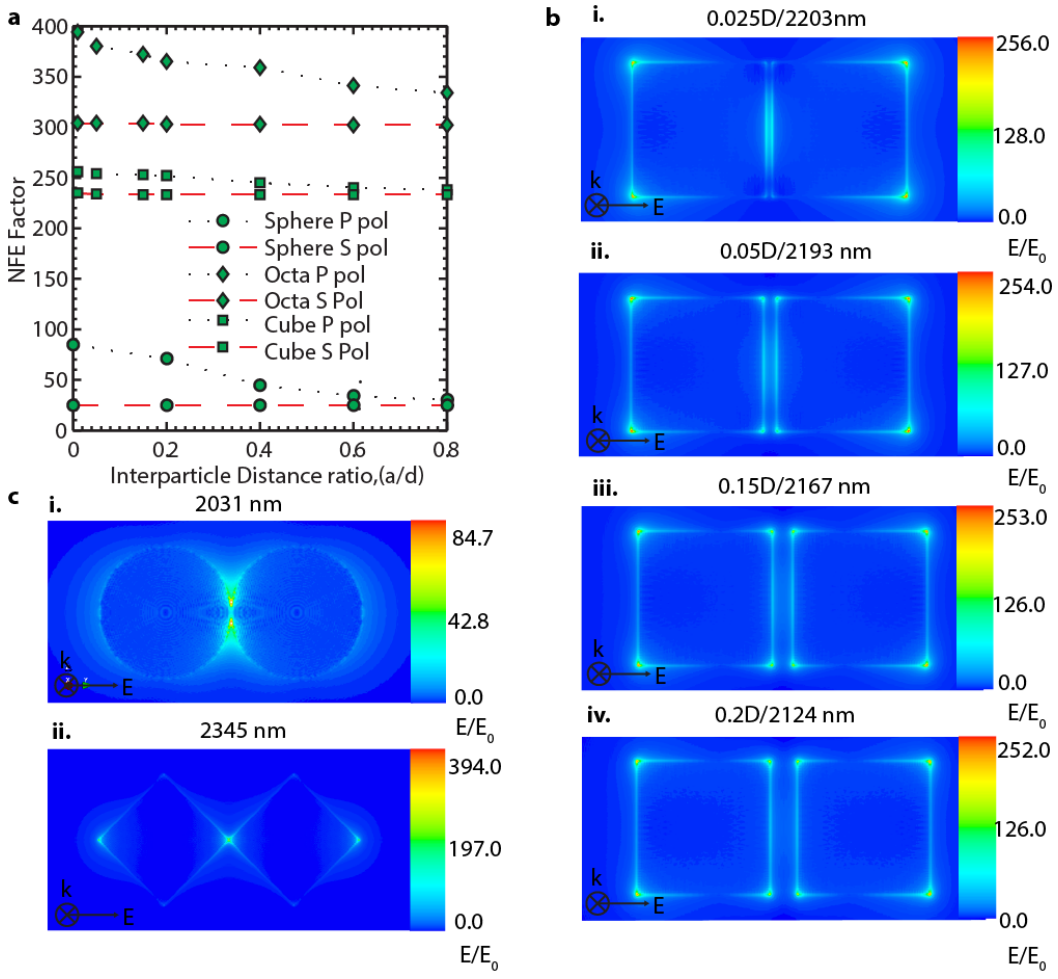

Figure 2.8 **Near field enhancement map of ICO dimers.** a) Maximum NFE values versus interparticle separation for the sphere, octahedron and cube dimers. With decreasing separation the NFE increases. The highest values of 394 is obtained for the octahedron dimer due to the strong localization of the field between the tips. B) Coupling in the cube dimer for different interparticle distance ranging from 0.05D (top panel) to 2D (bottom panel). The position of the hot spot shifts from between the faces to the corners with increasing distance. C) Field enhancement map of the (i) sphere and (ii) octahedron dimer with an interparticle distance of 0D excited at 2031 nm and 2345 nm, respectively. Hot spots in between the particles are observed, which are strongly localized in the octahedron dimer.

For cubes very close to each other, i.e. less than 0.1D, the enhancement is very much localized in between the faces, while the enhancement shifts towards the corners as

the distance increases. Similar results were observed previously for the case of gold nanoparticles.[180] For the excitation of the dimer we chose the highest intensity peak in all cases, while we note that the enhancement at the lower energy plasmon peak in the cube dimer is very similar to that of the higher energy peak (Figure 2.9d). For y-polarized light (perpendicular to the dimer axis), coupling was very weak and minor changes to the absorption spectra were observed for all the shapes (Figure2.9e, f). For distances greater than 1D the NC plasmon characteristics approach those of isolated NCs, indicating that for a pronounced coupling effect the inter-particle distance ratio needs to be less than 0.2. Summarizing the maximum NFE versus interparticle distance for all three shapes (Figure 2.8a), a maximum enhancement of 400 is found in the octahedron case with an interparticle distance of 0.01D due to the very localized fields between the tips of the octahedron corners. In the small size range investigated here the spectra and the NFE of the dimers were found to be independent of the size of the NCs and only depended on the relative interparticle distance (Figure S2.9a). This scale-independence has been found previously also for noble metal NCs.[196] Nevertheless, our results demonstrated that with a clever choice of shape and interparticle distance, we can design a system where field enhancement is obtained at the corners, faces or in between the spheres, which we predict will allow an enhancement of molecules located at specific facets of plasmonic semiconductor NCs.

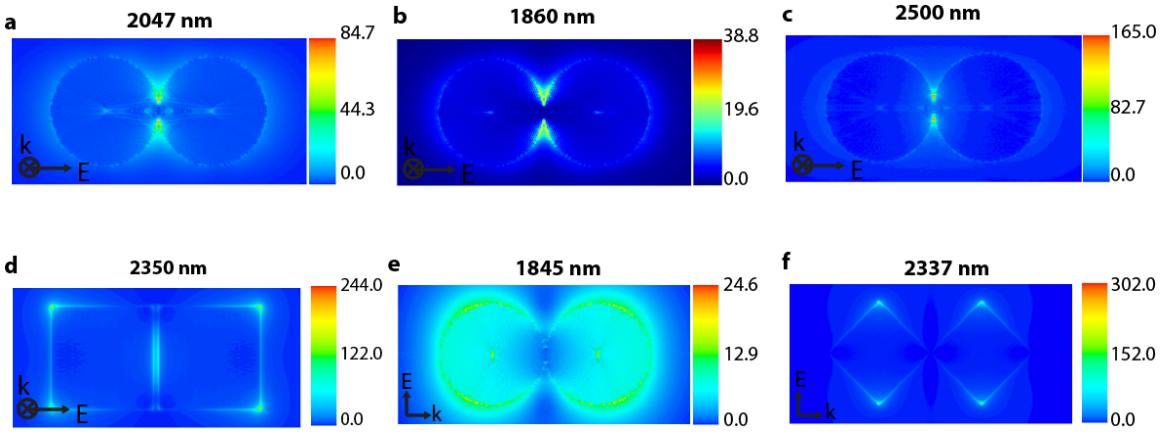

Figure 2.9 **Polarisation dependent NFE map of coupled ICO dimers.** a) NFE map at 2047 nm showing coupling between spherical particles of diameter 40nm. This figure shows that the NFE factor is independent of size of the nanocrystal in the region where we can neglect the scattering contributuion and NFE is only dependent on the relative interparticle distance b), c) NFE map at 1860 nm and 2500 nm showing the development of different mode of absorption for spherical particles in contact, each having 10nm diameter.d) NFE map for a cube dimer with spacing 0.05D at the higher wavelength peak. This map shows that the NFE factor in the case of a cube dimer is not very different from the highest NFE obtained at 2193 nm e) f) NFE maps for sphere and octahedron dimers at 1845 nm and 2337 nm, respectively, for electric field traveling along dimer axis and polarization perpendicular to it.

Plasmon resonances in NCs are known to decay through the emission of phonons to the surrounding medium and the efficient generation of heat in the local environment.[137,197,198] Currently, plasmonic NCs made of noble metals are being explored for their use in tumor cell cancer treatment[146,147], where the heat transfer from the excited NC is used to destroy the cancer cell. To reduce the absorption of the excitation light by the biological medium and associated non-targeted heating effects, researchers are currently trying to shift the plasmon resonances of noble metal NCs toward the infrared zone and into the biological window through synthesis of complex shapes such as gold rods[199] or nanoshells[200]. Here, semiconductor NCs are an attractive alternative due to

their plasmon resonance inherently in the infrared zone and easily tunable over a wide range of frequencies without resorting to large sizes that can limit biological targeting opportunities. Due to these reasons, semiconductor plasmonic NCs may hold immense potential for biological applications. Important parameters essential in photothermal application are the temperature at the surface of the NC and the light scattering from the NC for possible simultaneous bio-imaging. Therefore, we have studied the effect of the NC size and intensity of a monochromatic laser with a frequency equal to the LSPR on the surface temperature of ICO NCs. All the calculations have been performed in steady state. A detailed calculation of the surface temperature can be found in the theory section of this paper. The surface temperature is proportional to the square of the particle radius and to the intensity of the incoming laser light (Equation 2.24, below).

$$(T_{nanoparticle} - T_{bulk}) = \frac{\mathrm{k}\,\varepsilon_H R^2}{k_s}\frac{c\varepsilon_0}{2}\left|E_0\right|^2 \mathrm{Im}\left\{\frac{\varepsilon_p(w)-\varepsilon_H}{\varepsilon_p(w)+2\varepsilon_H}\right\} \qquad 2.24$$

where $T_{nanoparticle}$ is the surface temperature of the nanoparticle, T_{bulk} is the surrounding temperature, k_s is the thermal conductivity of surrounding medium, and E_0 is the incident electric field.

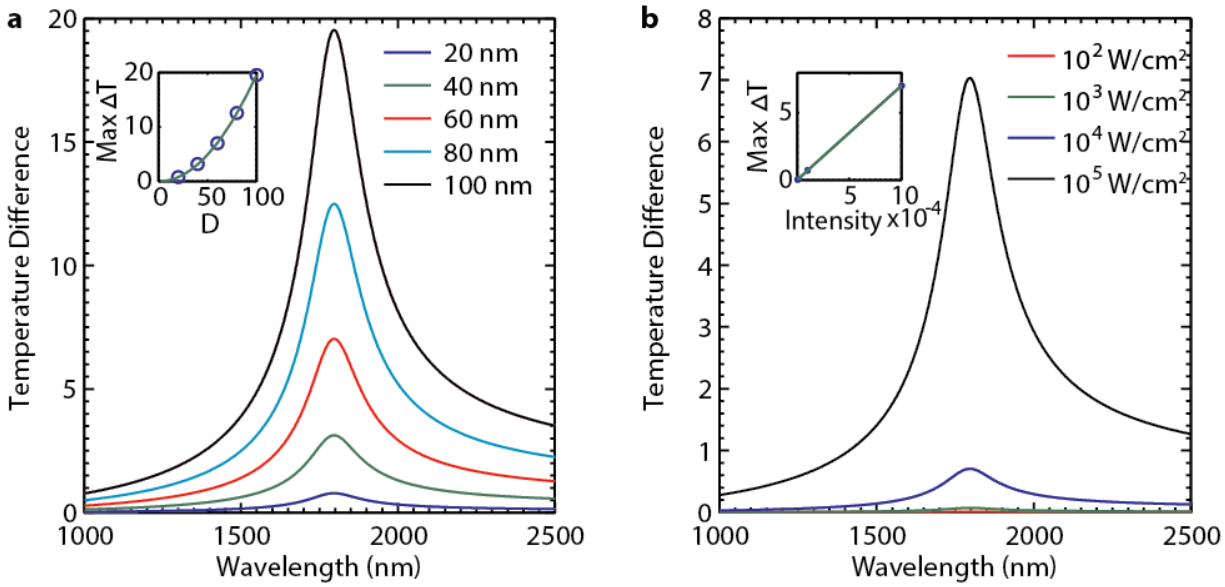

Figure 2.10 Photo-thermal properties on single ICO nanocrystal. (a) Maximum temperature difference plotted against wavelength for different diameters of spheres ranging from 20 nm to 100 nm for an excitation density of 10^4 W/cm^2 and a carrier density of $1.11 \cdot 10^{21}$ Inset: The maximum peak temperature difference Max ΔT is directly proportional to the square of the radius of particle b) for different intensities of the incoming light ranging from 10^2 W/cm^2 to 10^5 W/cm^2 for a NC radius of 60 nm. Inset: The maximum peak temperature difference Max ΔT is directly proportional to the intensity of the incident light. With increasing NC size and excitation density higher temperatures are reached.

For particles of diameter 20 to 100 nm and an incoming laser intensity of 10^5 W/cm^2 a local temperature increase of 1 to 20 Kelvin can be reached (Figure 2.10a). This temperature difference can be strongly influenced by choosing the proper laser intensity, as demonstrated in Figure 8b for a 60 nm diameter spherical NC. Our results show that the generation of heat in semiconductor NCs can compete with the properties of noble metal nanoparticles. Semiconductor NCs produce slightly less temperature increase compared to metal nanoparticles which can create temperature rises up to 50 K for similar shapes and sizes.[197] However, doped metal oxide NCs deliver the unique

opportunity of carrying an LSPR in the near infrared spectral region, even in very small particles, which helps in minimizing light extinction by intrinsic chromophores in tissue[148] and presents an opportunity to design an optimal system for photothermal applications.

2.4 Conclusions

In summary, we have shown that the near- and far-field infrared plasmonic properties of semiconducting ICO NCs are tunable by size and shape, but more importantly through the variation of the free carrier concentration, a characteristic unique to doped metal oxide NCs. Thus, for sensors and new optical technologies particularly located in the infrared these heavily doped semiconductor nanostructures provide an extra degree of freedom for their design and optical integration.This opens the entire new realm of opportunities for an on-device tunability of the infrared LSPR. To quantify this effect and facilitate comparisons between emerging plasmonic materials we have defined the carrier concentration sensitivity factor relating the LSPR shift to the change in carrier concentration. In ICO, this factor predicts a peak shift of 3.8 nm upon addition or removal of one electron from a 5 nm NC.

Although metal nanostructures can be designed to have infrared resonance, this has required the use of complex shapes such as nanoholes[201] or nanoshells[150] and large particles (>100nm), which has been a major bottleneck for the development of infrared plasmonics. Applications such surface enhanced infrared absorption (SEIRA),[195] a spectroscopy technique used for applications ranging from studies of catalytic processes to molecular sensing, are limited currently by the limitations in concentrating infrared light into highly localized near fields, which we have now shown is feasible with plasmonic semiconductor NCs. Unlike nanofabricated complex patterns, these NCs are

simple to fabricate on large scale using solution phase synthesis and our calculations predict that they can offer substantial near field enhancement of up to 260 times and high sensitivity to the surrounding medium of up to 800 nm per RIU, all from a very small octahedron nanocrystal (10nm) and in the infrared regime. These LSPR characteristics represent a substantial opportunity not afforded by conventional metals.

We furthermore found a very strong plasmon scattering contribution of ICO NCs in the infrared from sizes of 100 nm, which is an important parameter for scattering based application. Taking a cue from experimentally synthesized ICO NCs and their absorption spectra, a study of the edge and corner rounding of cubic NCs showed a tremendous decrease in their NFE properties upon rounding, signifying that for single molecule detection and identification, a precise control over the shape is desired to reach the NFE factors of up to 260 as calculated for perfect octahedra. We demonstrated that “hot spot” dimer based applications, such as enhanced spectroscopies, as well as photothermal heat transfer, can be extended well in the infrared zone using ICO NCs. For both isolated NCs as well as in dimers high NFE factors of up to 400 have been found, directly correlating with the spectroscopy enhancement effectiveness of these infrared plasmonic NCs. While we demonstrated the potential of ICO NCs for infrared plasmonic applications, there are further contributions likely to affect the plasmonic near- and far-field properties, such as the dopant distribution within the particle or the anisotropy of the underlying crystal structure, which are features unique to semiconductor NCs. But nevertheless, with semiconductor plasmonics, we are no more restricted to sub-micron length scale for infrared plasmonics based applications and instead can concentrate long wavelength far field light into very small regions. Taken together, we believe that with the developing and increasing interest of the scientific community in infrared semiconductor NC

plasmonics, breakthrough inventions in the field of sensing, imaging and spectroscopy in the infrared spectral region will advance rapidly.

Chapter 3

The Interplay of Shape and Crystalline Anisotropies in Plasmonic Semiconductor Nanocrystals

This chapter is adapted from the work "Jongwook Kim, Ankit Agrawal, Franziska Krieg, Amy Bergerud, Delia J. Milliron. The interplay of Shape and Crystalline Anisotropies in Plasmonic Semiconductor Nanocyrstals. *Nano Lett.*, **2016**, 16(6).". My contribution to this work included the simulations and spectroscopy of metal oxide LSPR.

3.1 Introduction

Localized surface plasmon resonance (LSPR) in metal nanoparticles or nanostructures has been extensively studied and utilized practically for sensing and manipulation of light[97,202–204]. Gold and silver are typical LSPR host materials as their high free electron densities (~10^{23}/cm^3) create resonances in the visible region[205]. Employing an anisotropic particle shape allows for tuning of the LSPR, giving rise to variable resonance frequency (ω_{lsp}) via LSPR band-splitting that is inaccessible with (pseudo-) spherical particles[206]. For instance, by changing the aspect ratio (*AR*) of gold nanorods, the longitudinal LSPR mode can be shifted to the near-infrared (NIR) while the transverse mode remains in the visible[207].

In doped semiconductor nanocrystals, highly variable carrier density, *N*, (10^{18}~10^{22}/cm^3) enables ω_{lsp} over the entire infrared region[208–210]. However, the connections between LSPR properties and materials composition and structure are still being established for this novel class of plasmonic materials. Especially as a broad range of doped semiconductor nanocrystal compositions (*e.g.*, group IV elements, metal oxides, metal chalcogenides, and nitrides) are studied for plasmonic applications, there is a

pressing need to rationalize and control the widely tunable LSPR in the infrared range. So far, the primary means to tune the ω_{lsp} of these nanocrystals has been to vary the doping level by controlling the concentration of vacancies (*e.g.*, $Cu_{2-x}S$, InN, WO_{3-x})[56,208,211–214]or extrinsic dopants (*e.g.*, Sb:SnO_2, Sn:InO_2, Al:ZnO, P-doped Si)[30,59,215,216]. *N* can thus be varied by two orders of magnitude, a tunability that has no parallel in classical metal plasmonics. What's more, *N* and therefore ω_{lsp} can be modulated post-synthetically by chemical, electrochemical[25,78], or photoelectrochemical[47,217] charging and discharging. Photoelectrochemical charging, or photodoping, in which photoexcited holes are scavenged to stabilize conduction band electrons, was used to compare the ω_{lsp} in Sn:In_2O_3 with different Sn doping levels that had been post-synthetically adjusted to have comparable *N*. The ω_{lsp} varied with Sn concentration, highlighting that composition impacts LSPR properties beyond the role of dopants in balancing the charge of free carriers.

While rapid progress has been made to understand how variable doping influences LSPR of semiconductor nanocrystals, the effect of anisotropic particle shape has been inconsistently reported and has only rarely been quantitatively rationalized[218,219]. As stated above, shape anisotropy is well established as a dominant means of tuning LSPR in metal nanoparticles, which motivates investigation of shape effects in plasmonic semiconductor nanocrystals. Faceted octahedral In:CdO nanocrystals exhibited multiband LSPR that were well matched by simulated spectra in which deconvoluted dipolar spatial modes contributed to the lineshape[19,219], whereas WO_{3-x} nanorods and $Cu_{2-x}Te$ platelets, rods, and tetrapods have not shown LSPR band-splitting despite their highly anisotropic morphologies[56,220]. In the case of $Cu_{2-x}S$ nanodisks, two widely separated peaks were observed and assigned to in-plane and out-of-plane modes, though the peak shifts with changing *AR* were unexpectedly small[221]. Meanwhile, only

one AR-dependent resonance peak was observed for covellite CuS nanoplatelets, which was assigned to the in-plane mode. To rationalize the literature on copper chalcogenide nanocrystal LSPR, the question of how the anisotropic (layered) crystal structure influences LSPR properties has been raised. After all, unlike classical plasmonic metals, which are typically isotropic, compound semiconductors commonly exhibit anisotropic crystal structures. Hence, we sought to understand how nanocrystal shape anisotropy and the underlying crystalline anisotropy might collaborate to produce the observed optical properties of these emerging plasmonic nanomaterials.

3.2 Methods

3.2.1 Nanocrystal synthesis

We used standard Schlenk line techniques under nitrogen atmosphere to synthesize h-Cs:WO_3 nanocrystals. 55 mg (0.17 mmol) of W(IV)Cl_4 (Alfa Aesar) was mixed with 5 mL of oleic acid (Sigma-Aldrich). 18 mg (0.11 mm) of CsCl (Sigma-Aldrich) was mixed with 13.3 mL of oleic acid and 0.7 mL of oleylamine (Aldrich). Both solutions were degassed separately at 120°C to prepare active precursors of tungsten and cesium. The degassed W(IV)Cl_4 solution was then injected into the degassed CsCl solution that was pre-heated to ~300°C and held for 9 minutes before cooling. The nanocrystal aspect ratio was controlled by varying the reaction temperature and the tungsten precursor degassing time, as well as the addition of acetic acid in the W(IV)Cl_4 solution. The featured samples were prepared with the following details. *Platelets*: 0.1 mL of acetic acid was added to W(IV)Cl_4 solution and then degassed for 2 hours. The reaction temperature was 300°C. *Iso-prisms*: W(IV)Cl_4 solution was degassed for 2 hours and aged for 24 hours before reaction. The reaction temperature was 310°C. *Rods*: W(IV)Cl_4 solution was degassed for 5 hours. The reaction temperature was 300°C.

3.2.2 Transmission electron microscopy (TEM)

The TEM images were acquired on a JEOL-2010F with samples prepared by drying a drop of diluted nanocrystal solution in hexane on the surface of a carbon-coated copper grid. The nanocrystal sizes (height, width, and aspect ratio) were counted from 118, 81, and 227 particles lying 'on-edge' on the TEM grid respectively for platelet, isoprism, and rod samples.

3.2.3 X-ray diffraction (XRD) and size analysis by Scherrer analysis

The XRD samples were prepared by drying several drops of concentrated nanocrystal solution in toluene on a silicon wafer substrate. The standard XRD patterns were acquired on a Rigaku R-axis Rapid II diffractometer with Cu K-α ray in a reflection configuration. The high-resolution XRD patterns for Scherrer analysis were obtained using a Rigaku Miniflex 600 diffractometer with a Cu K-α X-ray source operating at 40 kV and 15 mA with a graphite monochromator. Multiple scans were collected between $2\theta = 15°$ and 65° with a step size of 0.02° and scan speed of 2°/min, then averaged to reduce noise. Lattice parameters were refined using the program TOPAS in order to determine peak positions. To account for shape anisotropy leading to differences in peak broadening, a multiple peak fit was performed in the area between 20° and 32°, containing the (002), (111), and (020) peaks, along with two smaller peaks which were omitted in the fit. The positions of the peaks were fixed to the values obtained by Rietveld refinement while peak area and FWHM were allowed to vary. The corresponding crystallite sizes along the <002> and <020> directions were computed using the Scherrer equation then divided to calculate the aspect ratio of each sample. Crystal structure images were produced using the VESTA visualization program[222].

3.2.4 Vis-NIR spectroscopy

The absorbance spectra of h-Cs:WO_3 nanocrystals were collected on an Agilent-Cary5000 spectrophotometer with samples prepared by dispersing nanocrystals in tetrachloroethylene in a quartz cuvette with 1 cm path length.

LSPR modulation by oxidation and reduction – An Agilent-Cary5000 spectrophotometer equipped with a diffuse reflectance accessory was used for this experiment. 3 mL of a dilute platelet sample solution was prepared in a quartz cuvette with an airtight screw cap. Initially, the absorption spectrum was taken in the air-free condition. For the oxidation, the sample was exposed to air by opening the cap for a couple of seconds and then stirring the cuvette. The absorption spectra were collected after each time of air exposure, which was repeated until the decay of peak intensity was saturated. For the reduction, hydrazine was incrementally added (0.8 μL for each step) into the cuvette and the absorption spectra were collected at each step until the increase of the peak intensity was saturated.

3.2.5 Computational Modeling

Cs:WO_3 nanocrystals with varying aspect ratio derived from XRD and physical dimensions derived from TEM were designed using the Design module in COMSOL. The sharp cornered hexagonal prisms were then rounded to depict realistic shape as well as to ensure fast numerical convergence. This structure was then surrounded by a sphere representing the surrounding medium (i.e. tetrachloroethylene (n=1.475), which was used for all experimental measurements). This whole system was then surrounded by a perfect index matching layer which prevented unwanted reflections from the outside boundary. The maximum and minimum mesh size in the nanocrystal was set to 10 nm and 0.1 nm, respectively (Figure 3.1). This ensures fine meshing, yielding typically 2 million degrees of freedom, which corresponds to 3 – 15 GB of RAM when using the direct PARDISO or

MUMPS solver. The hexagonal phase of $Cs:WO_3$ is described by an anisotropic frequency dependent dielectric function which was expressed using the Lorentz-Drude dispersion model. Dielectric parameters are listed in Table 3.1. The hexagonal phase of $Cs:WO_3$ is described by an anisotropic frequency dependent dielectric function which was expressed using the Lorentz-Drude dispersion model. Dielectric parameters are listed below in Table 3.1. Dielectric parameters such as plasma frequency, scattering constant and high frequency dielectric constant were estimated based upon the work of Hussain et al and our experimental spectra. As reported in Hussain et al[223], the relative values of the in-plane versus out-of-plane high frequency dielectric constant and that relative values of the damping constant and effective mass were almost constant irrespective of the amount of cesium doping. In-plane Drude parameter were averaged over the xy- crossection plane and did not take into account the slight anisotropy along x direction compared to y direction. For our simulations, we have assumed these values correspond to that of 25% doping level. Furthermore, based on the fact that free carrier density and damping constant values may differ between film and nanocrystal morphologies, the absolute values were adjusted based upon our spectra peak position while keeping the relative values in different crystallographic directions fixed.

The refractive index of the surrounding medium was set to that of tetrachloroethylene (n=1.475), which was used for all experimental measurements.

Dielectric Function Parameters	Along c-axis	Along a-axis
ω_p, plasma frequency (cm^{-1})	37610	25650
m_e, effective mass (relative to free electron mass)	0.75	1.6125
ε_∞, high frequency dielectric constant	5.3	4.8
γ, scattering constant (cm^{-1})	1750	2700

Table 3.1 Dielectric parameters used in modeling plasmonic properties of h-Cs:WO3 nanocrystals

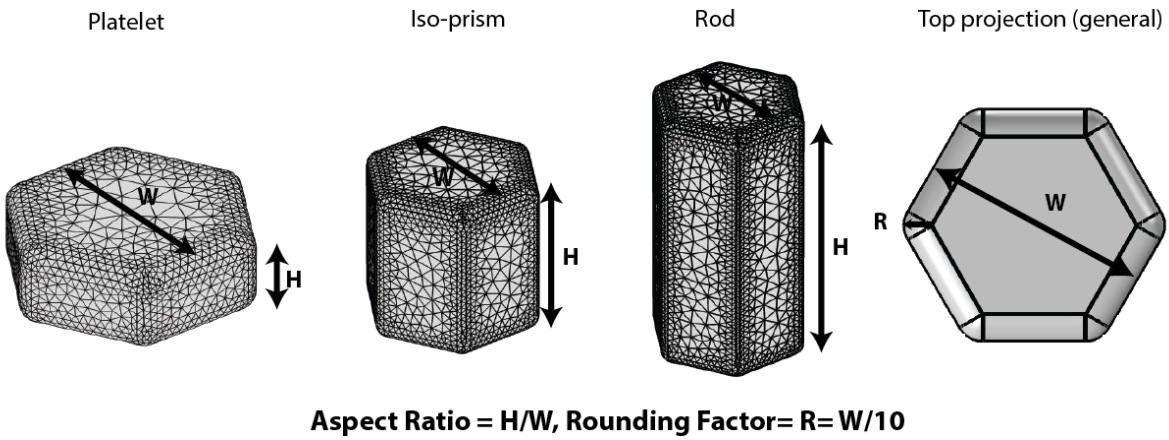

Figure 3.1 Geometry and meshing of platelet, iso-prism and rod.

3.3 Result and Discussion

In this study, h-Cs:WO_3 nanocrystals were investigated as a prototypical material since the hexagonal structure exhibits strong crystalline anisotropy. We modified our previously reported synthesis of h-Cs:WO_3 nanocrystals[224] to gain control over *AR*, producing hexagonal prisms with *AR* from 0.3 to 2. Figure 3.2a-c displays the transmission electron microscopy (TEM) images for three representative samples, namely, platelets, *iso*-prisms, and rods with an *AR* of 0.32, 0.87, and 1.69, respectively.

XRD patterns (Figure 3.2d-f) verify that they share the same hexagonal crystal phase (ICSD number 56223). *AR* is defined as the height (*H*) of the prism divided by the in-plane width (*W*) parallel to the basal (002) plane (Figure 3.2g-i). For each sample, *W*, *H*, and *AR* values of individual nanocrystals were assessed from multiple TEM images. The histograms of *W* and *H* (insets in Figure 3.2a-c) clearly show the distinct morphology of each sample, despite the obvious size heterogeneity. *AR*s were also calculated via the Scherrer formula[225], with the (002) and (020) XRD peaks exhibiting size-dependent broadening corresponding to *H* and *W*, respectively, and found to be generally consistent with the results of TEM analysis (insets in Figure 3.2, Table 3.2, and Table 3.3). The Scherrer-derived *AR* was employed in all subsequent analysis considering the possible statistical errors from the limited number of nanocrystals measured by TEM.

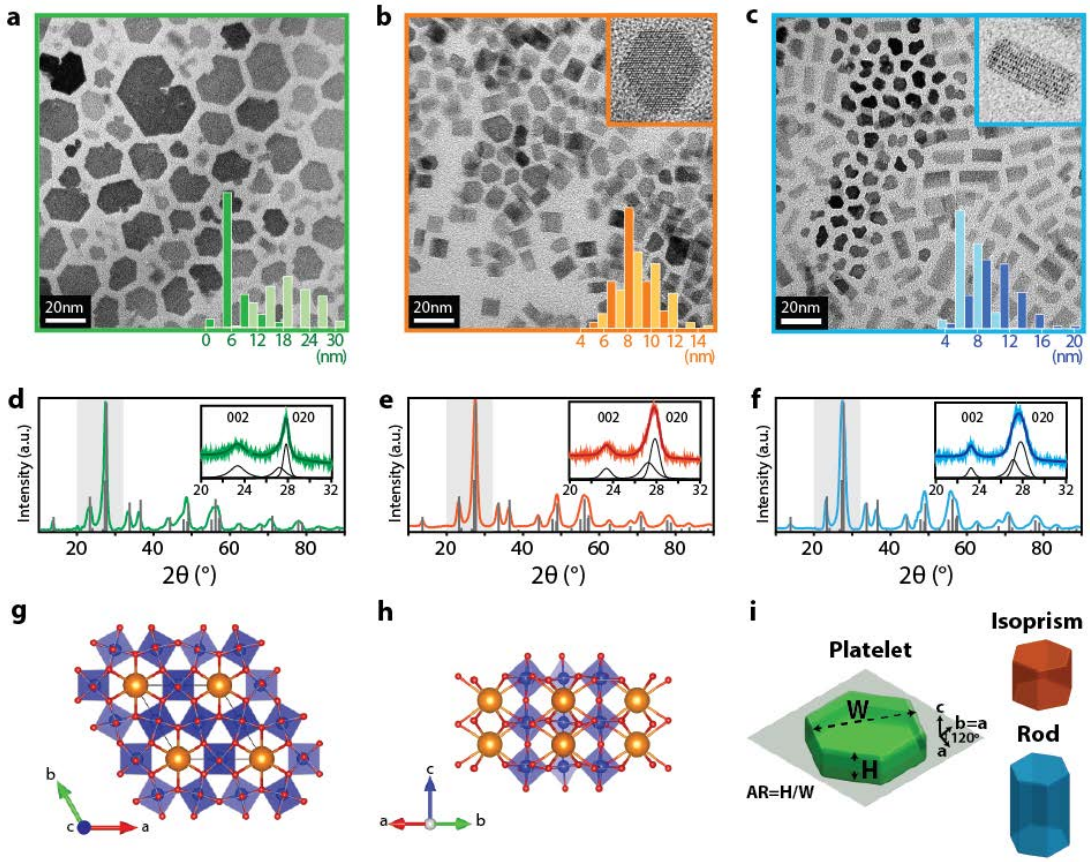

Figure 3.2 **Hexagonal cesium-doped tungsten oxide (h-Cs:WO3) nanocrystals with different aspect ratios.** a-c) Transmission electron micrographs (TEM) of h-Cs:WO3 nanocrystals in the shape of a) platelets, b) iso-prisms, and c) rods. The bottom right insets in a-c) are size distribution histograms for the average height (dark color bars) and width (light color bars) of nanocrystals. Average sizes are listed in Table 1. d-f) Powder x-ray diffraction (XRD) patterns for the h-Cs:WO3 nanocrystal samples corresponding to a-c). The insets in d-f) are high-resolution XRD patterns of the grey regions, containing the (002) and (020) peaks that exhibit size-dependent broadening corresponding, respectively, to the height and width of nanocrystals. g-h) Illustration of the h-Cs:WO3 lattice structure projection on g) basal plane and h) prismatic plane: Cs (gold), W (blue) and O (red). i) Schematic illustration of nanocrystal shape corresponding to a-c) showing the conventions used in this chapter.

Sample	Peak	Position (°)	Area	FWHM	Crystallite Size (nm)	aspect ratio
Platelet	(002)	23.29	2.69	1.60	10.32	0.32
	(111)	27.18	2.52	1.22	13.70	
	(020)	27.78	3.12	0.54	32.27	
Iso-Prism	(002)	23.30	2.78	1.04	14.99	0.87
	(111)	27.17	5.85	1.32	12.66	
	(020)	27.79	10.91	0.92	18.42	
Rod	(002)	23.26	3.00	0.70	24.09	1.69
	(111)	27.15	4.85	0.83	20.53	
	(020)	27.84	15.16	1.18	14.21	

Sample	a (Å)	c (Å)
Platelet	7.413	7.630
Iso-prism	7.404	7.626
Rod	7.387	7.630

Table 3.2 (Top) Fitting parameters and aspect ratio obtained by Scherrer analysis XRD pattern, (Bottom) Hexagonal phase lattice parameters obtained by Rietveld refinement.

Nanocrystal Sample	Size analysis by TEM			Scherrer Analysis of XRD data
	Height (*H*) (nm)	Width (*W*) (nm)	Aspect Ratio (*AR*)	Aspect Ratio (*AR*)
Platelet	7.0±3.0	21.4±4.3	0.46±0.17	0.32
Iso-prism	9.8±1.8	9.0±1.3	0.94±0.17	0.87
Rod	11.3±3.0	4.5±1.5	2.10±0.44	1.69

Table 3.3 Nanocrystal dimensions obtained by analyzing TEM images and XRD patterns.

The optical absorption spectra of the three representative colloidal samples vary systematically with *AR* (Figure 3.3a). The platelet spectrum (*AR* = 0.32) contains two

peaks- a high frequency peak (ω_{lsp1}) at 14140 cm^{-1} and a low-frequency peak (ω_{lsp2}) at 6480 cm^{-1}. The resulting peak separation ($\Delta\omega_{lsp}$) of 7660 cm^{-1} is quite large. As *AR* increases, ω_{lsp1} redshifts while ω_{lsp2} blueshifts, resulting is a decrease in $\Delta\omega_{lsp}$ (orange and blue lines, green circles in Figure 3.3b). According to the established model for LSPR band-splitting developed in the context of classical metal nanoparticles[226], ω_{lsp1} of the platelets is expected to be the longitudinal LSPR (out-of-plane) mode and ω_{lsp2} is to be the transverse (in-plane) mode. Assuming dielectric isotropy, as in conventional plasmonic metals, the two peaks are expected to coincide ($\Delta\omega_{lsp} = 0$) when $AR \approx 1$, and to crossover and separate once again when $AR > 1$ (blue stars in Figure 3.3b). Instead, we observe a striking deviation from this expectation, with $\Delta\omega_{lsp}$ continuously decreasing, without crossover, even as the *AR* increases to well over 1 (Figure 3.3a, green circles in Figure 3.3b). This result suggests that intrinsic crystalline anisotropy may strongly modify the expectations for LSPR of anisotropically shaped nanocrystals, even qualitatively changing the interpretation and assignment of multi-peaked spectra. According to the Drude model,

$$\vec{\epsilon_D}(\omega) = \vec{\epsilon_\infty}(\omega) - \frac{\vec{\omega_p}^2}{\omega^2 - \omega\vec{\gamma}}, \quad \vec{\omega_p} = \sqrt{\frac{Ne^2}{\epsilon_0 \vec{m_e}}} \qquad 3.1$$

dielectric permittivity ($\vec{\epsilon_D}$) and bulk plasma frequency ($\vec{\omega_p}$) are determined by free carrier concentration (*N*), elementary electronic charge (*e*), the permittivity of free space (ε_0), high frequency permittivity ($\vec{\epsilon_\infty}$), damping ($\vec{\gamma}$), and electron effective mass ($\vec{m_e}$), the last three of which can vary with direction in crystals with anisotropic structures. In case of bulk h-Cs:WO_3, density functional theory calculations[227] and reflection spectroscopic measurements[223] have shown that $\vec{m_e}$, $\vec{\epsilon_\infty}$, $\vec{\gamma}$ and are all strongly dependent upon the lattice direction. In particular, the significantly lower m_e along the c-

axis compared to that parallel to the basal plane results in the longitudinal ω_p being 1.5 times higher than the transverse ω_p. LSPR of h-Cs:WO_3 nanocrystals should accordingly exhibit a similar anisotropy in ω_{lsp} in addition to the effect of shape anisotropy. The unexpected observation of a substantial peak splitting ($\Delta\omega_{lsp}$ = 4000 cm^{-1}) when $AR \approx 1$ (Figure 3.3b) is thus a natural consequence of the strong crystalline anisotropy of h-Cs:WO_3. The revised calculation of $\Delta\omega_{lsp}$ *vs.* *AR*, employing an anisotropic $\overrightarrow{\omega_p}$, (pink stars in Figure 3.3b) matches well with the experimental data (green circles in Figure 3.3b).

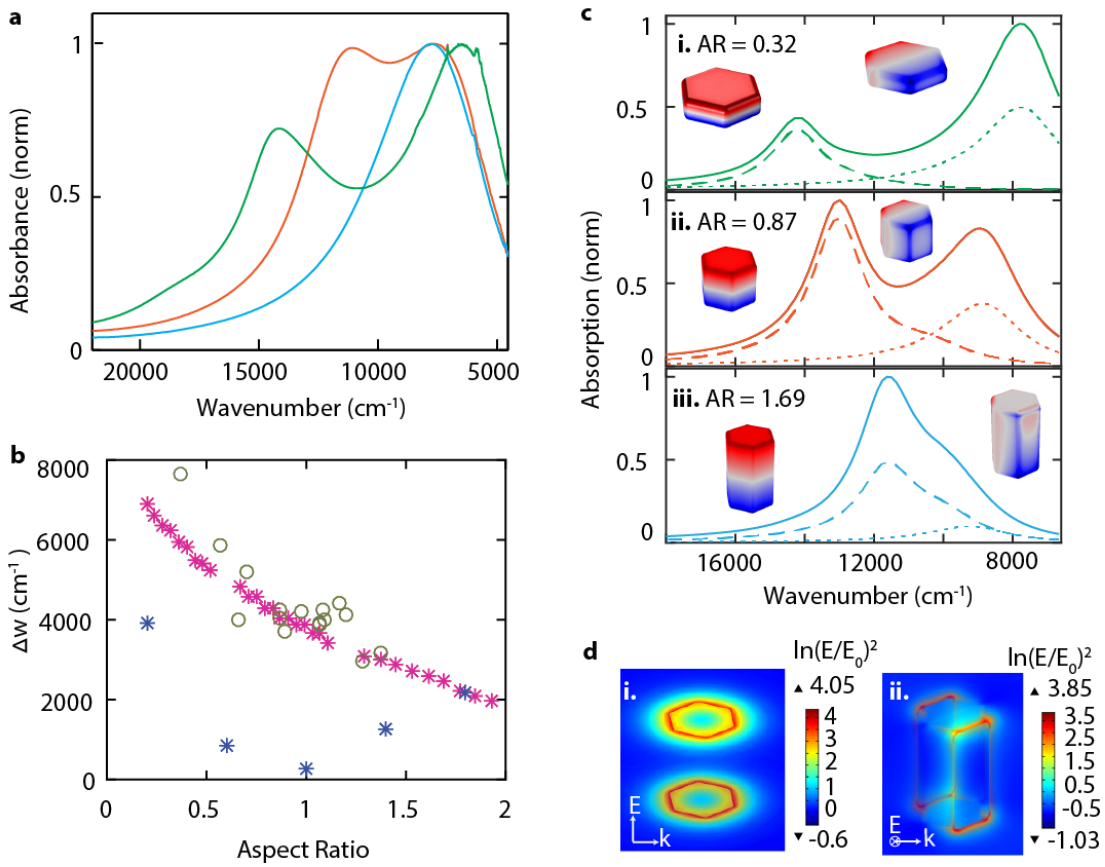

Figure 3.3 **LSPR of h-Cs:WO3 nanocrystals.** a) Experimental optical absorption spectra of h-Cs:WO3 nanocrystal samples of platelets (green), iso-prisms (orange), and rods (blue) dispersed in tetrachloroethylene showing the aspect ratio-dependence of LSPR. b) Plot of LSPR peak splitting (Δωlsp) vs. particle aspect ratio obtained experimentally with synthesized nanocrystals (open circles) and by theoretical modeling assuming isotropic (blue stars) or anisotropic (Pink stars) dielectric functions. c) Theoretically simulated LSPR spectra for platelet-, iso-prism-, and rod-shaped nanocrystals (top to bottom) using the anisotropic dielectric function of h-Cs:WO3. Solid lines show the overall absorption profiles, summing one longitudinal mode (dashed lines) and two identical transverse modes (dotted lines). The insets show the simulated dipolar surface charge distributions at each peak frequency of the longitudinal and transverse modes. d) Color map of the simulated near field enhancement for a rod excited at the two LSPR peak frequencies.

Spectra of the cesium-doped tungsten oxide sample with a platelet shape (AR=0.32) show two absorption peaks. In order to validate that both of these peaks can be attributed to LSPR, we observed the shift in absorption peak position with change in solvent refractive index. LSPR absorption peaks are known to be sensitive to surrounding media, with LSPR red shifting linearly with increasing solvent refractive index, according to the following equation,

$$\lambda_{LSPR}^2 = \lambda_p^2(2n^2+1) \qquad 3.2$$

Where λ_p plasma wavelength which is directly proportional to effective mass, *n* is the solvent refractive index and λ_{LSPR} is the LSPR wavelength.

Optical spectra of the platelet sample were taken in hexane (*n*=1.37), chloroform (*n*=1.44), TCE (*n*=1.48) and toluene (*n*=1.50). Peak maxima (Figure 3.4) were found to shift linearly with solvent refractive index. Moreover, it was seen that the high energy peak is less sensitive to change in dielectric medium compared to the low energy peak. This observation could be explained by looking at the plasmon sensitivity factor derived in literature which shows that sensitivity factor is directly proportional to plasma wavelength[224]. The dielectric function of hexagonal phase Cs:WO_3 is anisotropic and the properties that carry this anisotropy are plasma wavelength and frequency via different effective masses. It is evident that high energy plasmon peaks correspond to lower plasma wavelengths and low energy plasmon peaks correspond to high plasma wavelengths, and thus low energy peaks are more sensitive to environment compared to higher energy peaks. This observation also supports our claim that the high energy peak corresponds to longitudinal plasmon excitation and the low energy peak corresponds to transverse plasmon excitation.

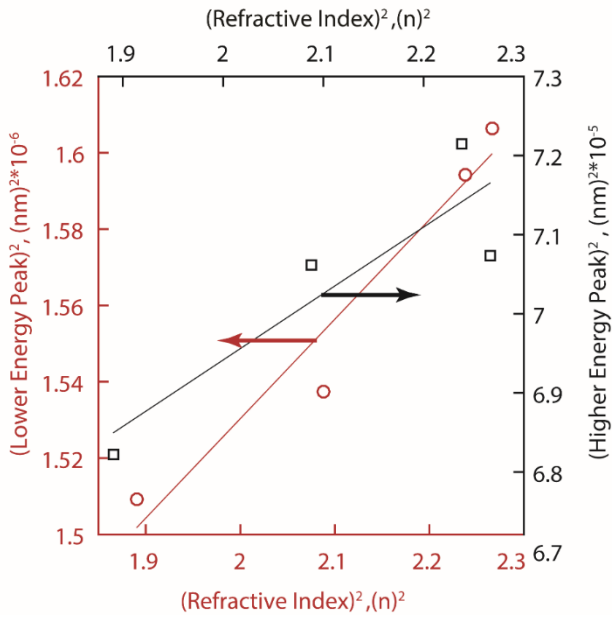

Figure 3.4 Low energy (Red) and high energy (black) peak position dependence on solvent refractive index.

In order to theoretically investigate the implications of such an interplay of shape and crystalline anisotropies, electromagnetic field simulations were performed by setting anisotropic dielectric functions along different lattice directions and varying the *AR* of the nanocrystal (Figure 3.1). In the simulated LSPR spectra (Figure 3.3c) the longitudinal and transverse modes are visibly separated when *AR* = 0.32 and 0.87 and overlay only when *AR* = 1.69, which is in good agreement with the experimental data (Figure 3.3a). By contrast, simulated spectra for an isotropic dielectric function (Figure 3.5) exhibit two modes that overlap over the entire range of *AR* (from 0.2 to 1.8) due to smaller $\Delta\omega_{lsp}$ and that have strongly divergent peak intensities at low or high *AR*, yielding a single strong peak and a shoulder. These results confirm that crystalline anisotropy is a major contributor to the LSPR band-splitting and overall lineshape in h-Cs:WO_3.

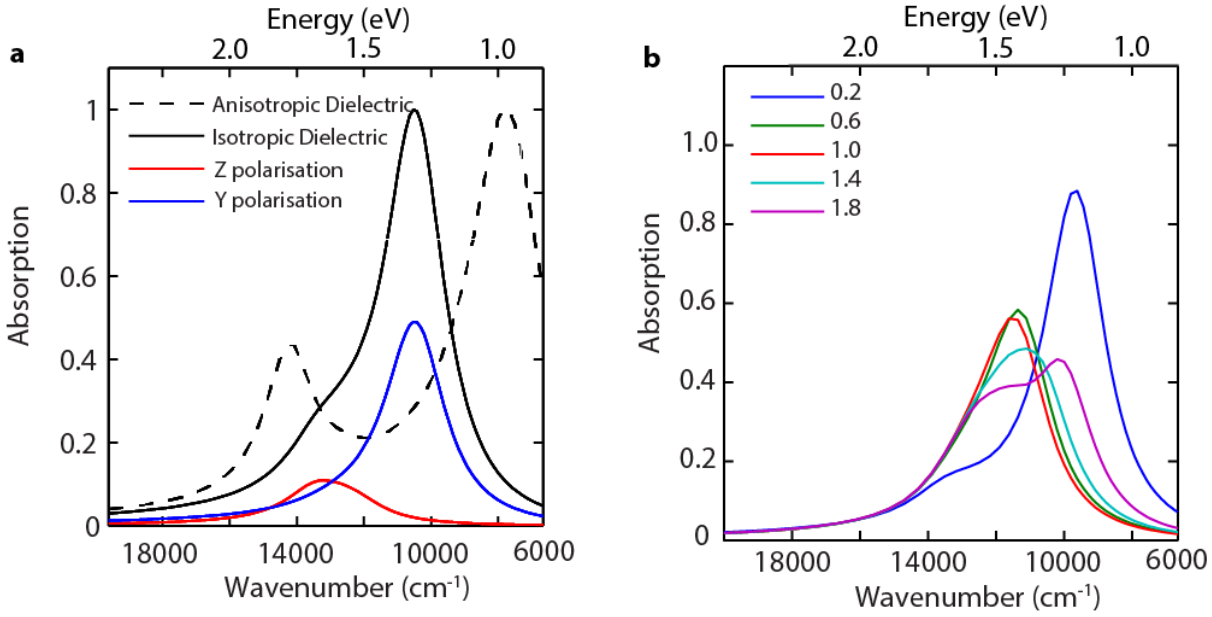

Figure 3.5 Comparison betweeen isotropic and anisotrpic crystal structure plasmon properties. a) Decovolution of isotropic spectra along different polarization directions and comparison with anisotropic dielectric function absorption spectra. b) Absorption spectra for hexagonal nanocrystal with different aspect ratios calculated with isotropic dielectric function.

Studying the near field enhancement around plasmonic nanocrystals is essential to evaluate their potential applications in sensing, enhanced spectroscopy, and energy transfer processes. Equally important is to know how the surface charge is distributed on the nanocrystal for applications such as waveguides and optical tweezers. The deconvoluted spectra showing each LSPR mode (dashed and dotted lines in Figure 3.3c) and the surface charge distribution profiles reveal that each peak corresponds to a distinct dipolar mode (Figure 3.3c-insets and Figure 3.6).Surface charge distribution on a Cs:WO_3 platelet nanocrystal was simulated for at peak absorption frequency and frequencies around it for both longitudinal and transverse polarizations. As frequency is

decreased, a shift of the resonance charge distribution was observed from faces to edges to corners (Figure 3.6) in accordance with the reported behavior in metal nanoparticles [228] and semiconductor nanocrystals lacking crystalline anisotropy[219]. The difference in h-Cs:WO_3 is the splitting of each geometric mode into two different frequencies for each polarization mode due to the anisotropic dielectric function. Each of these geometric modes contain a superposition of fundamental dipolar, quadrupole, and higher order eigenmodes. This split of geometric modes into polarization-dependent modes could potentially be leveraged in applications such as switchable optical tweezer or waveguides.

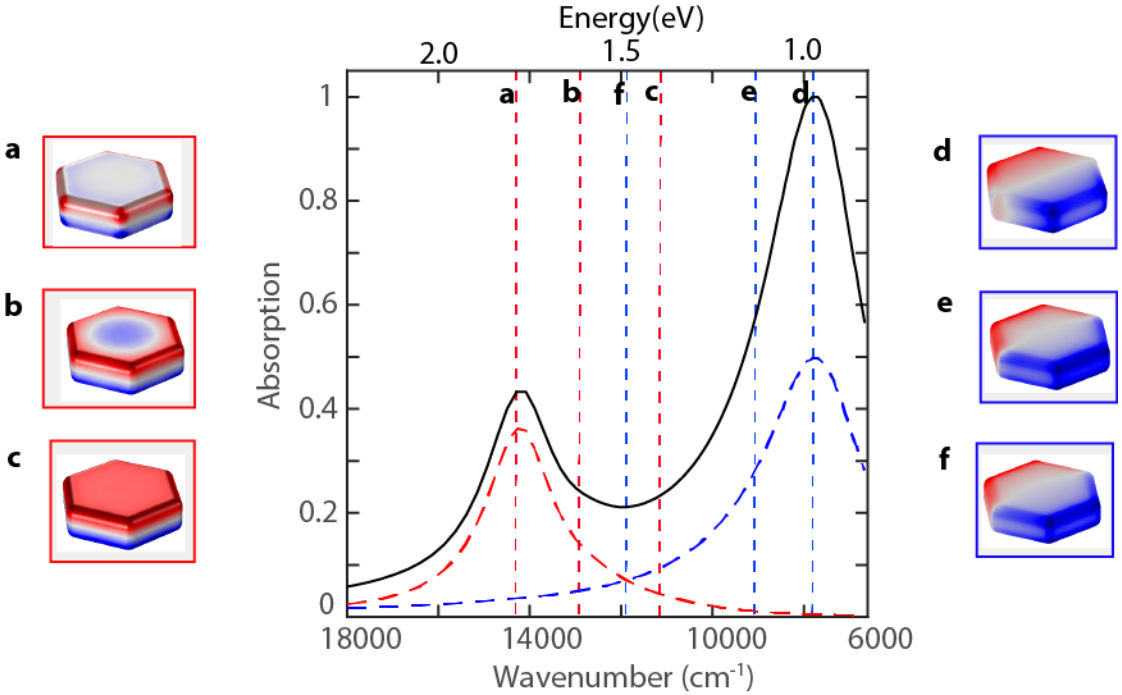

Figure 3.6 Surface charge distribution at different frequencies under transverse (blue boxes) and longitudinal (red boxes) polarization.

Furthermore, the near field intensity maps (Figure 3.7) illustrate that up to 400-fold enhancement is achievable for both longitudinal and transverse modes in a given

anisotropic h-Cs:WO_3 nanocrystal. This is a unique attribute of anisotropic crystalline hosts as isotropic hosts inevitably give rise to unbalanced field enhancement for the different modes. This balanced dual-mode LSPR property enables effective concentration of infrared light over a broad energy range and through a substantial region of space spanning all solid angles around the nanocrystal.

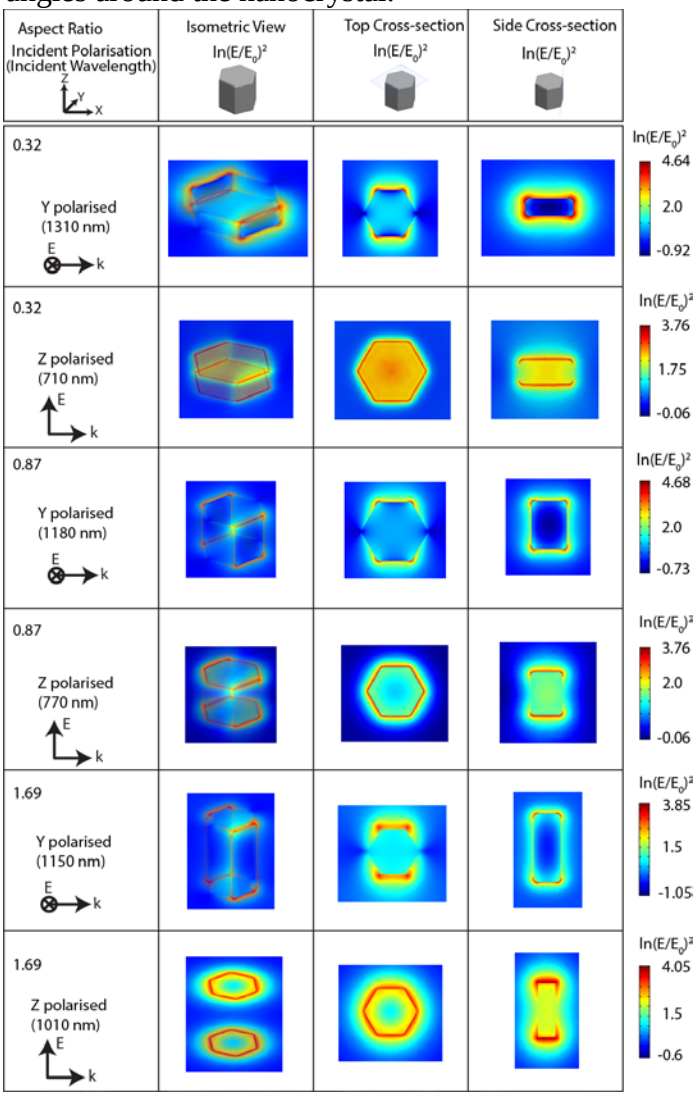

Figure 3.7 Near field maps in 3D, top, and side views for a platelet, iso-prism and rod under different polarization illumination.

One can recognize that the experimental spectra (Figure 3.3a) are broader than the simulated ones (Figure 3.3c) and that the relative peak intensities are not precisely reproduced. A possible reason for these discrepancies is the polydispersity in the size and shape of nanocrystals that is obvious from TEM images (Figure 3.2a-c). Simulation parameters were thus adjusted to examine the validity of our model to describe these non-ideal ensembles of nanocrystals. First, a Gaussian average of the nanocrystal *AR* (with fixed volume) was applied using the measured standard deviations from TEM (Table 3.2), resulting in broadened LSPR spectra for all the three shapes (platelets, *iso*-prisms, rods) (Figure 3.8). It was also found that the longitudinal mode, corresponding to the lower m_e, varies non-linearly and more rapidly with changing *AR* in both intensity and peak position compared to the transverse mode, resulting in a higher relative intensity at the longitudinal peak (Figure 3.8). Second, the experimentally realized morphologies exhibit substantial "bites" taken out of the lateral facets, especially in the platelets. This morphology was mimicked by simulating the LSPR spectrum of a distinctively shaped platelet. Compared to the pristine shape, there was no noticeable change in the peak positions while a broadening of the transverse mode peak was observed (Figure 3.9). Therefore, the minor differences between experimental and simulated spectra can be accounted for by size and shape heterogeneity within each nanocrystal sample.

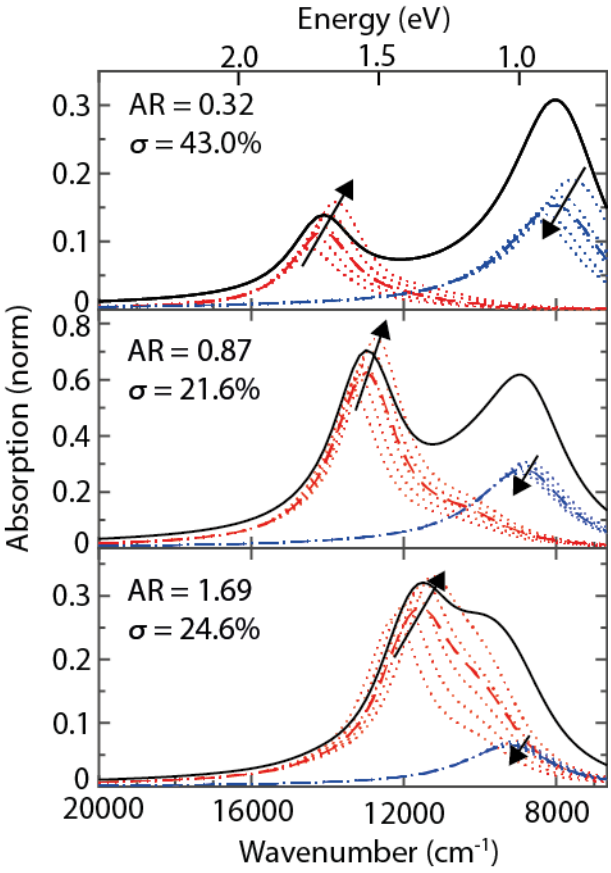

Figure 3.8 **Gaussian broadning of plasmonic spectra**. Dotted red and blue lines denote the aspect ratio dependent absorption spectrum under longitudinal and transverse polarization, respectively. Dashed red and blue line shows the Gaussian averaged spectra. The direction of the arrows in each of panel indicate the direction of increasing aspect ratio. All Gaussian parameters are obtained from TEM analysis with the mean deviation for each listed on the panels. Black spectra show the total ensemble calculated absorption spectra for platelets, iso-prisms and rods, which are broader than spectra calculated assuming monodisperse sizes.

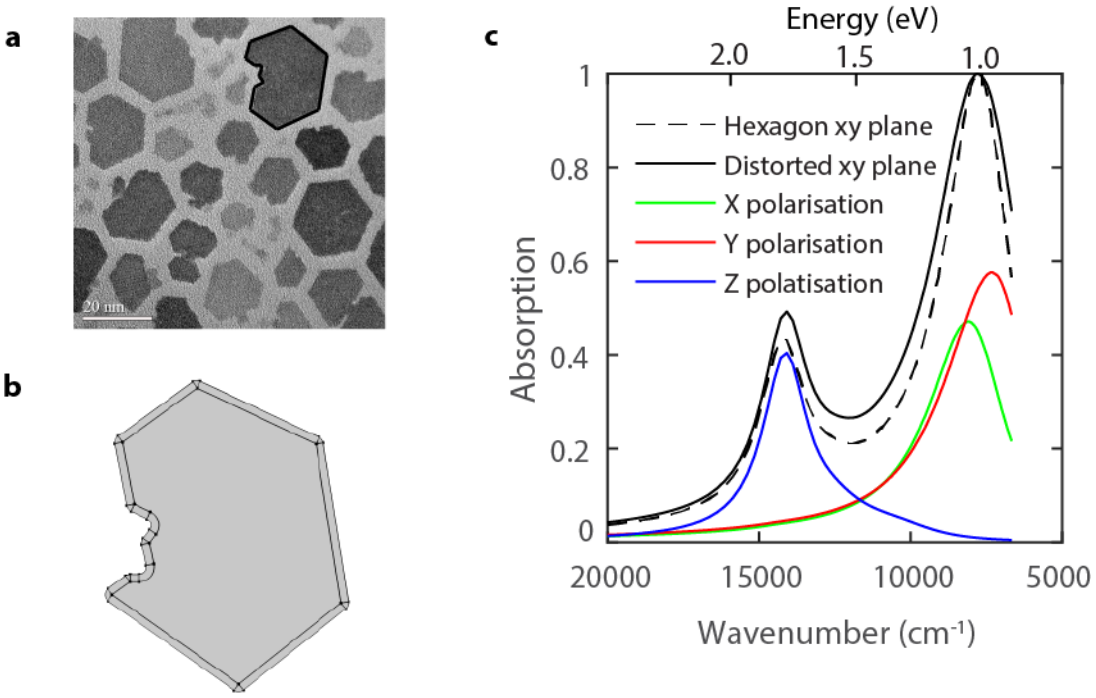

Figure 3.9 Effect of distortion from perfect hexagonal pyramid (a, b) on absorption spectrum (c) under different incident polarization.

Considering that post-synthetic modulation of LSPR is a key feature of plasmonic semiconductor nanocrystals, we sought to understand how shape and crystalline anisotropy influence the spectra evolution of h-Cs:WO_3 nanocrystals subjected to oxidation and reduction. It is well-known that free carriers in vacancy doped tungsten oxides are highly sensitive to oxygen partial pressure, where high levels of atmospheric oxygen can drive the insertion of oxygen, thus diminishing the free electron population. This effect, usually limited to the near-surf[56,229] ace regime in bulk materials, has been shown to overwhelm the entire volume of small WO_3 nanocrystals, and therefore the LSPR may be greatly diminished in intensity in oxidative conditions.

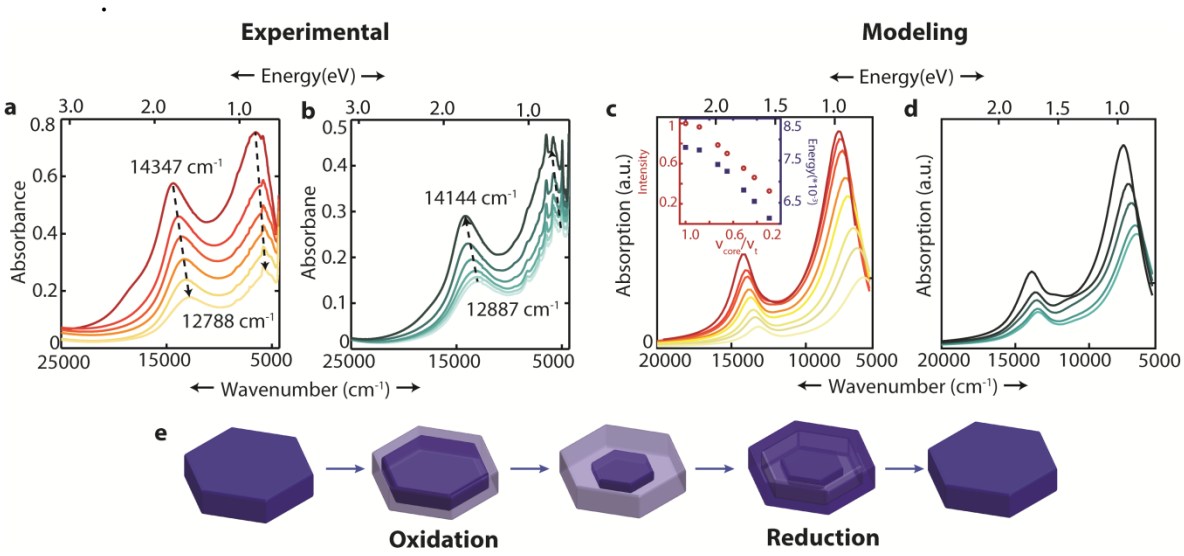

Figure 3.10 Redox-mediated modulation of LSPR. a-b) Dynamic optical absorption spectra of h-Cs:WO_3 platelets undergoing a) oxidation by exposure to air for up to 24 hours and b) reduction by incremental addition of hydrazine. c-d) Simulated evolution of LSPR for c) oxidation and d) reduction. e) The simulation was performed assuming oxidation proceeds by the growth of a fully oxidized shell with unchanged carrier density in the core, and reduction by the growth of fully reduced shell upon the previously oxidized volume. The inset in c) is a plot of the longitudinal mode peak intensity (red dots) and peak position (black squares) vs. unoxidized core volume during simulated oxidation, both showing approximately linear relationship.

We tracked the oxidation-induced quenching and redshift of LSPR in h-Cs:WO_3 nanocrystals as a function of air exposure (Figure 3.10a). Moreover, by addition of hydrazine as a reducing agent, the oxidized nanocrystals could be reduced again, recovering the original line shape and peak positions (Figure 3.10b). The correlated response of the two peaks supports our description of the spectra as two distinct LSPR modes originating from the same free carriers; by contrast, if the two peaks reflected distinct electronic states they would have differing responses to the oxidation and reduction processes. The moderate peak shifts while the peak intensities are strongly

modulated are inconsistent with a homogeneous depletion of *N* (Figure 3.11a), but can be reproduced instead by assuming that oxidation proceeds from the surface. This was modeled by creating an oxidized, fully depleted shell and a shrinking core with unchanged carrier density, as depicted in Figure 3e. Similarly, the reduction process was modeled with a reduced shell growing progressively inwards from the surface (Figure 3.10e). The simulated evolution of the LSPR spectra based on this redox mechanism (Figure 3.10c-d), in which peaks experience a moderate linear shift due to the dielectric environment imposed by the growing shell (Figure 3.10c-inset), is highly consistent with the experimental observations (Figure 3.10a-b). Although the redox-mediated LSPR evolution in semiconductor nanocrystals has typically been described as a homogeneous modulation of *N*, our results suggest this model should be revisited to ensure a realistic view of the electronic changes within the nanocrystals that underlie observed LSPR modulation.

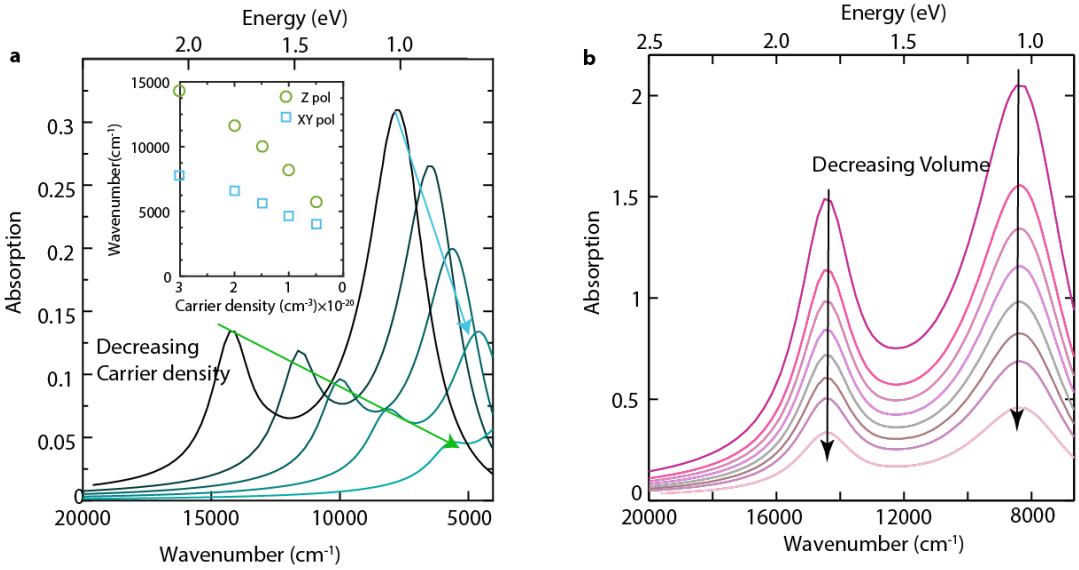

Figure 3.11 a) Effect of free carrier density on absorption spectra, Inset: Change in peak position with free carrier density. b) Effect of volume decrease on plasmon absorption characteristics.

3.4 Conclusion

To conclude, colloidally synthesized hexagonal phase Cs:WO_3 nanocrystals exhibit strong aspect ratio-dependent LSPR absorption peaks that can only be explained via a cooperative influence of crystalline and shape anisotropies. This finding highlights the limitations of conventional treatments of LSPR that assume isotropic dielectric constants and attribute multimodal peaks uniquely to shape anisotropy effects. This understanding extends our ability to rationally tune LSPR lineshape and near-field enhancement via synthetic control of shape and crystalline anisotropies of semiconductor nanocrystals. Such control may prove useful by enhancing light-matter interactions across a broad spectral and spatial region, leading to the advances in developing switchable optical devices, sensors, and waveguides. In particular, the demonstrated multimodal LSPR with near-equal intensities of h-Cs:WO_3 nanocrystals covers the near-infrared (NIR) region of great importance in photonic, solar, and clinical applications while maintaining high visible transparency due to its wide band gap. Such an optical performance with the additional functionality of dynamic, reversible modulability is promising for sensing applications[46] and for energy saving NIR-selective electrochromic windows[49], which also motivates the additional study of the optical response of this doubly anisotropic nanomaterial to chemical or electrochemical stimuli.

Chapter 4

Resonant Coupling between Molecular Vibrations and Localized Surface Plasmon Resonance of Faceted Metal Oxide Nanocrystals

This chapter is adapted from the work "Ankit Agrawal, Ajay Singh, Sadegh Yazdi, Amita Singh, Gary K. Ong, Karen Bustillo, Robert W. Johns, Emilie Ringe, Delia J. Milliron. Resonant Coupling between Molecular Vibrations and Localized Surface Plasmon Resonance of Faceted Metal Oxide Nanocrystals. *Nano Lett.*, **2017**, 17(4)." My contribution to this work included the simulations and spectroscopy of metal oxide LSPR.

4.1 Introduction

Plasmonic nanocrystals (NCs) are promising optical elements for a wide variety of applications owing to their ability to enhance and localize electric fields at an interface at the nanoscale, well below the diffraction limit[230]. This enhanced electric near field can couple to other optical transitions such as excitons, vibrations and interband transitions to enhance the efficiency of various optical processes such as photoluminescence[231,232], photon upconversion[44,233,234], solar energy conversion[235–237] and vibrational spectroscopy[8,238,239]. Specifically, coupling between localized surface plasmon resonances (LSPRs) and molecular vibrations can improve the sensitivity for detecting vibrational signatures, giving rise to techniques such as surface enhanced Raman spectroscopy (SERS)[238,239] and surface enhanced infrared absorption spectroscopy (SEIRA)[8,240]. SERS has been extensively studied using Au[103,238] and Ag[14] NC LSPRs which conveniently appear in the visible spectral region. To demonstrate SEIRA however, LSPRs must be located in the mid-IR which has been achieved primarily with

micron-scale lithographically deposited Au[241,242], Ag[243], and recently Sn:In_2O_3[8] structures. While limited, this work on plasmonic metal oxide SEIRA[8] has already suggested that metal oxide systems can exhibit significantly less long range coupling effects than classical metals, indicating that these materials can be organized or patterned at higher packing density to produce a higher spatial density of near field hot spots.

To achieve a higher spatial density of hot spots, one approach is to utilize small colloidal NCs as has been demonstrated with Au nanoparticles for SERS applications. However, to access the mid-IR LSPR regime for SEIRA applications while preserving small NC sizes, we must consider plasmonic systems beyond that of Au and Ag. Recent development in colloidal metal oxide NC synthesis and doping have introduced a library of plasmonic materials systems such as Sn:In_2O_3[28,101,244,245], In:CdO[19,37,71], Al:ZnO[32,246], etc. that exhibit LSPRs over the entire infrared region. These materials derive their plasmonic properties from degenerate doping and are therefore easily tuned to the desired resonance frequency (ω_{LSPR}) using ionizable defects such as oxygen vacancies and aliovalent dopants[23,26,246], redox and photochemical charging[47,90,247] or electrochemical modulation in NC films[25,28,48,52]. Furthermore, the optical properties of metal oxide NCs can be tuned separately from their morphology. This synthetic and post-synthetic tunability opens an opportunity to develop new high density, scalable and *electrically tunable* or *chemically responsive* SEIRA substrates for application such as molecular sensing and catalysis. However, this is contingent upon first understanding the coupling behavior between molecular vibrations and metal oxide NC LSPRs. Such phenomena have yet to be reported and are studied here by a combined experimental and theoretical approach.

In general, coupled molecular vibration - LSPR systems can be modeled using a coupled harmonic oscillator system[129,130,241,242,248], assuming the vibrational resonances

behave as Lorentzian resonators. This approach, as applied to a lithographically defined gold model system[241], has shown that depending upon the relative cross sections for scattering and absorption, and relative resonance frequencies of the LSPR and vibrational resonances, coupling between the two resonances can lead to different Fano lineshapes in the vibrational spectrum ranging from enhanced absorption, to the more typical Fano derivative lineshape or induced transparency. However, for metal oxide systems, this response is expected to differ owing to plasmonic metal oxides being low loss materials that are semi-transparent in the IR. Furthermore, in the case of NC films, the interplay of size, shape, and arrangement in determining all the aforementioned optical parameters must be addressed.

Coupling to vibrational modes is enabled by the concentration of IR light around a plasmonic nanostructure when molecules with resonant modes are present in the adjacent space. Qualitatively, the strength of light concentration adjacent to plasmonic nanostructures, or near field enhancement (NFE), depends upon many factors including carrier concentration[37], electron scattering[16,37,85,86,249], and corner sharpness[8,16,26,37] (shape). Higher NFE can even be obtained upon coupling plasmonic nanostructures, in narrow gaps between structures where these "hot spots" can exhibit at least an order of magnitude stronger electric fields compared to those surrounding isolated nanostructures[250–252]. Summarizing our current knowledge of how NFE could manifest in plasmonic metal oxide NC systems, we expect maximum NFE for systems with high carrier concentration but low carrier scattering combined with a shape with sharp edges, preferably assembled into an extended array, creating inter-NC hot spots. Having outlined these considerations, we synthesized cubic codoped Sn,F:In_2O_3 as an ideal model system to study the coupling behavior between a metal oxide NC LSPR and molecular vibrations, specifically the C-H vibrations of native oleate ligands.

In this work, we demonstrate that the NFE around doped indium oxide NCs is substantial and it facilitates coupling between NCs in self-assembled arrays, and further between NC LSPRs and molecular vibrations. Specifically, we share the synthetic protocol for variable-sized colloidal cubes of fluorine (F) and tin (Sn) co-doped In_2O_3 (FITO), and characterize the presence and influence of the near field around these highly faceted NCs. Incorporation of F^- dopant into $Sn:In_2O_3$ was found to yield more cubic NCs and to decrease electron scattering, which improves the quality factor of the LSPR compared to $Sn:In_2O_3$. We report the size dependent LSPR spectra of FITO, map the NFE around a single cubic NC via scanning tunneling electron microscopy-electron energy loss spectroscopy (STEM-EELS) and compare these results with far field and near field electromagnetic simulations. Interactions between LSPR modes of adjacent NCs in a chain and in a 2x2 array give rise to coupled modes that are mapped via EELS. Molecular vibrations, specifically C-H stretching modes of the surface-bound ligands, are shown to couple to the coupled LSPR modes in NC arrays. The dependence of coupling on the carrier concentration and NC size is apparent in systematic changes in the Fano lineshape observed by Fourier transform infrared spectroscopy (FTIR). The interpretation of these results is bolstered by modeling and electromagnetic simulations, which enables us to delineate the convoluted dependence of Fano lineshape on several parameters such as size of the NC, coupling strength, and LSPR frequency. For this purpose, temporal coupled mode theory (TCMT) was developed in this work as applied to a coupled system of metal oxide LSPRs and multiple molecular vibrational modes.

4.2 Methods

4.2.1 Synthesis

Indium (III) acetylacetonate (0.97 mmol), Tin (IV) fluoride (0.03 mmol—0.06 mmol), Oleic acid (3.0 mmol), Tri-octylamine (8.0 mmol), Octylamine (3.0 mmol) were loaded in a 3-neck flask. This mixture was degassed at room temperature and 120 °C for 15-30 min to form the indium oleate complex. After that the solution was ramped to 290-310 °C under N_2/Ar environment. When the temperature reached around 285-295 °C (depending on the dopant concentration), the reaction turns from a brownish-yellow to a deep blue/green color (depending on dopant concentration) indicating nanocrystal nucleation. The nanocrystals were further allowed to grow for 3-7 minute under heating. After that the reaction was cooled quickly and the nanocrystal are washed with a non-polar/polar solvent mixture (Toluene/Ethanol) and further redispersed in toluene or tetrachlroethylene (TCE) for further characterization. Here, Fluorine not only caused the shape of the nanocrystal to be cubic, but also co-doped the In_2O_3 nanocrystal alongside Sn. Halogens have been used as shape directing agents previously in the colloidal synthesis of metal and semiconductor nanocrystals.

4.2.2 FTIR spectroscopy

Fourier transform infrared spectroscopy was performed using a Bruker Vertex 70 FTIR. Solution ensemble measurements were performed using a FTIR liquid cell with a 0.25 mm path length. Solid state measurement for LSPR-molecular vibration coupling experiments were done on CaF_2 substrates in normal incidence geometry.

4.2.3 Electron microscopy

FITO nanocrystal were characterized by angular dark-filed scanning transmission electron microscopy (ADF-STEM) by using a FEI-TitanX, operated at 200kV. HRSTEM

images were acquired with the double aberration- corrected TEAM 0.5 microscope operated at 300kV. Low-resolution STEM and SEM images were obtained using a Hitachi S5500 scanning electron microscope operating in STEM mode at 30 kV accelerating voltage.

4.2.4 X-ray diffraction (XRD)

The sample for XRD analysis was prepared by drop-casting the as-synthesized FITO nanocrystal solution on a silicon substrate. XRD patterns were collected using a Rigaku MiniFlex 600 with a Cu Kα x-ray source, operating in Bragg-Bretano geometry.

4.2.5 Isolated Nanocrystal Simulation

Doped In_2O_3 nanocrystals with varying sizes designed using the design module in COMSOL. The sharp cornered shapes were then rounded to depict a realistic shape as well as to ensure fast numerical convergence. These structures were then surrounded by a sphere representing the surrounding medium (i.e. tetrachloroethylene (n=1.475), which was used for all experimental measurements). This whole system was then surrounded by a perfect index matching layer which prevented unwanted reflections from the outside boundary. The maximum and minimum mesh size in the nanocrystal was set to 10 nm and 0.1 nm, respectively (Figure 4.1). This ensures fine meshing, yielding typically 2 million degrees of freedom, which corresponds to 3 – 15 GB of RAM when using the direct PARDISO or MUMPS solver. Maxwell equation were solved in scattered field formulation with the background electric field propagating along Z axis and polarized along X axis.

The dielectric function of $Sn:In_2O_3$ is described by a frequency dependent dielectric function, which was expressed using the Extended Drude model.

$$\epsilon_p = \epsilon_\infty - \frac{\omega_p^2}{\omega^2 - \gamma\omega} \quad (4.1)$$

$$\gamma = \gamma_L - \frac{\gamma_L - \gamma_H}{\pi}\left[arctan\left(\frac{\omega - \gamma_X}{\gamma_W}\right) + \frac{\pi}{2}\right] \quad (4.2)$$

Dielectric parameters for ITO are used here were derived in our previous work[77]. To obtain the dielectric function of FITO, spectra of 20 nm cubes were fitted using Mie theory. This derived dielectric function was then iteratively modified computationally to match the simulated extinction spectrum with the experimentally obtained spectrum. The dielectric function obtained through the iterative process with 20 nm cubic nanocrystals was then used to calculate the optical properties of larger sized cubes and periodic assembled films. The dielectric functions used for both ITO and FITO are tabulated in the table below.

	Plasma frequency, $\boldsymbol{\omega_p}, \mathbf{cm^{-1}}$	Low frequency damping, $\boldsymbol{\gamma_L}, \mathbf{cm^{-1}}$	High frequency damping, $\boldsymbol{\gamma_H}, \mathbf{cm^{-1}}$	Crossover frequency, $\boldsymbol{\gamma_X}, \mathbf{cm^{-1}}$	Crossover width, $\boldsymbol{\gamma_W}, \mathbf{cm^{-1}}$
ITO	16000	5000	200	4000	4000
FITO	16000	2250	1500	4500	3000

Table 4.1 Dielectric parameter for ITO and FITO metal oxides.

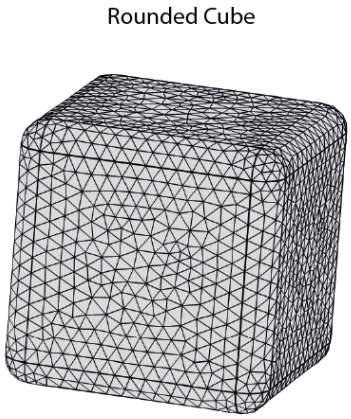

Figure 4.1 Geometry and Meshing. A rounded cube was designed using the Design module in COMSOL and was finely meshed to ensure convergence.

4.2.6 Molecular vibration optical data

Molecular vibrational modes were modelled as the sum of the contribution from indium oleate (80%) and octyl amine (20%) (Figure 4.2). The vibrational profile was modelled as the sum over several harmonic oscillators, each modelled as Lorentzian functions with strength A^2, centered at ω_v, and having line width, γ_v.

The overall dielectric function of such a system can be expressed based on Lorentian functions as,

$$\epsilon_v = 1 - \sum_i \frac{A_i^2}{(\omega^2 - \omega_{v,i}^2) - i\gamma_{v,i}\omega} \quad 4.3$$

Number	ω_v, vibration central frequency (cm^{-1})	γ_v, line width (cm^{-1})	A^2, Vibration strength
1	2794.97697	47.21519	0.01248
2	2854.51954	15.5833	0.08256
3	2872.69632	8.20294	0.01585
4	2899.48843	24.2066	0.01547
5	2927.97829	28.0525	0.15365
6	2958.4874	15.94813	0.05625

Table 4.2 Dielectric parameters for different molecular vibrations.

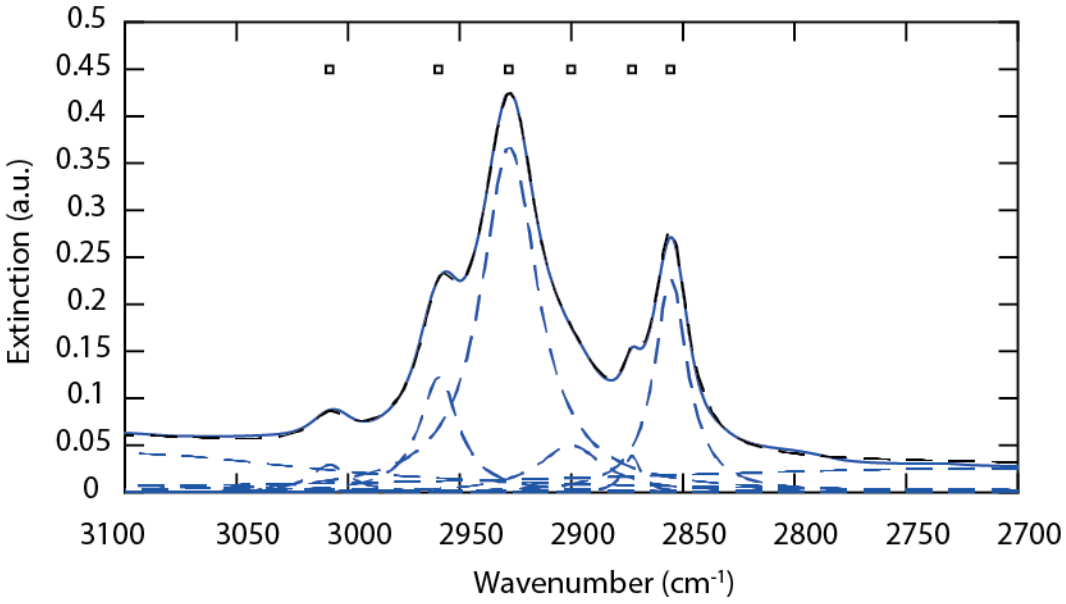

Figure 4.2 **Molecular vibration dielectric function**. Vibrational extinction spectrum of a 80% oleic acid-20% indium oleate liquid mixture. This spectrum was decomposed into several primary molecular vibrations which were then used to formulate the dielectric function of molecular vibrations to be used in simulation and theory work.

4.2.7 Electron Energy Loss Spectroscopy (EELS)

EELS images were acquired at 80 keV in STEM mode in an FEI Titan Themis (S)TEM equipped with a monochromator, probe spherical aberration corrector and Gatan

Quantum ERS electron spectrometer. Zero loss peak (ZLP) full width at half maximum (FWHM) was measured to be 0.15±0.01 eV in the vacuum region, and the energy dispersion per channel and pixel dwell time were set to be 0.01 eV and 5 ms, respectively. For acquiring spectrum images, the 105 nm FITO nanocrystals were drop casted on 10 nm thick silicon nitride TEM grids from TEM windows (TEMwindows.com). The method of non-negative matrix factorization (NMF) was applied to the spectrum images in HYPERSPY (open source software available at hyperspy.com) for extracting LSPR peaks and their spatial distribution[253]. The number of spectral components is a user input in this method and can affect the identification of LSPR peaks and their spatial distribution.

4.2.8 Periodic Boundary Simulation

To simulate the LSPR – LSPR coupling and LSPR – vibration coupling in periodic arrays of NCs, the Maxwell equations were solved in full field mode. As illustrated in Figure S6, a monolayer of cubic NCs on a substrate was modeled using periodic boundary conditions in 2 dimensions. Nanocrystal LSPR is excited via normal incident light from Port 1 and transmitted light collected at Port 2. For size-dependent LSPR-LSPR coupling (Figure 4.3-left), interparticle spacing was kept constant (3 nm) while varying the size of the nanocrystals. In LSPR-vibration coupling simulations, the nanocrystals are surrounded by a 1.5 nm layer of oleic acid molecules (Red box in Figure 4.3-right).

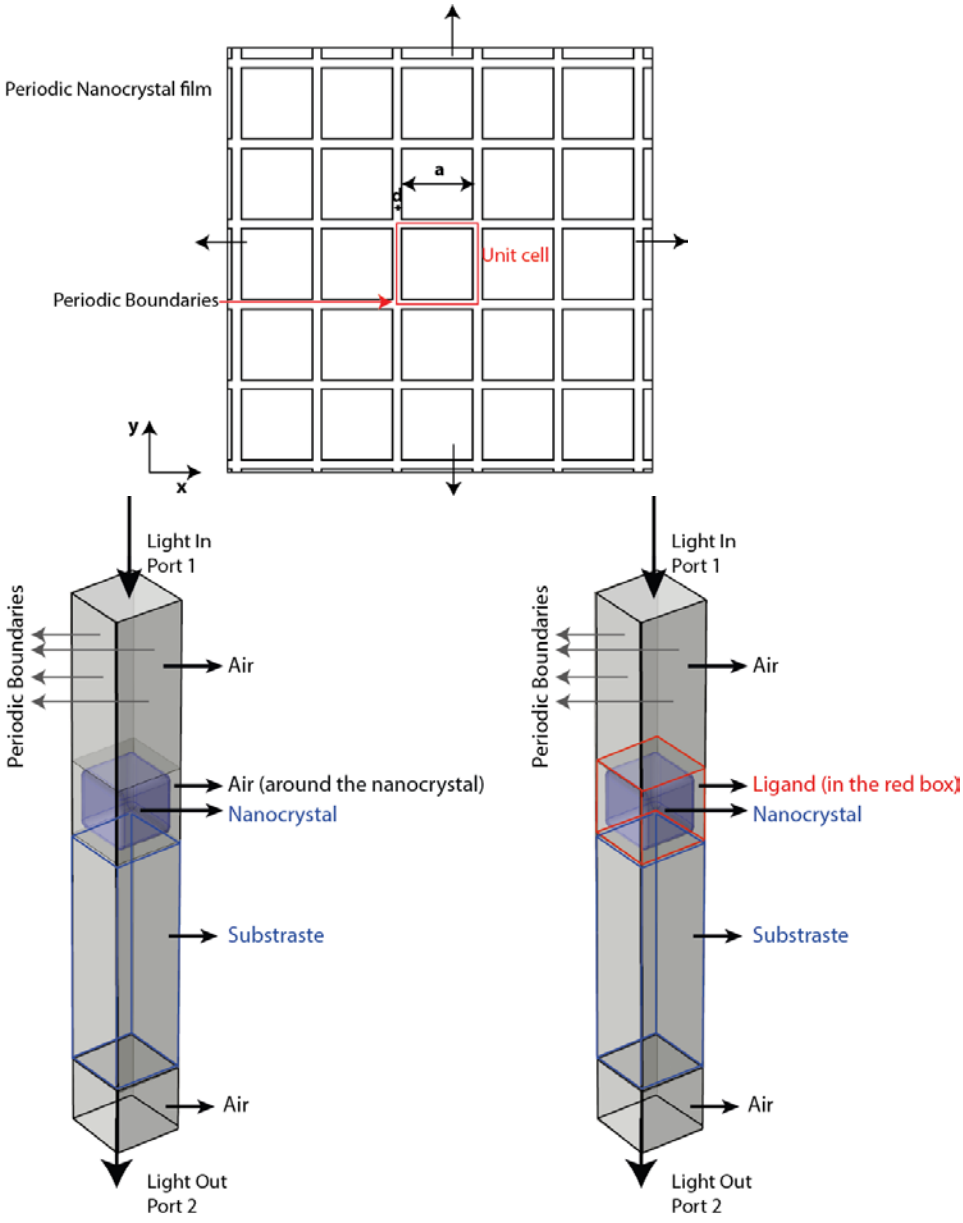

Figure 4.3 **Periodic boundary simulation setup.** LSPR-LSPR coupling study (left) computational setup where light is incident from port 1 and collected at port 2. Periodic boundary conditions are applied in 2 dimensions to model a monolayer of assembled nanocrystal film (top). For the LSPR - vibration coupling simulation (Right) the nanocrystal is surrounded by a 1.5 nm thick layer of oleic acid molecules.

4.2.9 Temporal Coupled Mode Theory

Both LSPR and molecular vibrations can be expressed as harmonic oscillators with corresponding resonance frequencies and decay rates. In a coupled LSPR-vibrational mode system, the LSPR mode is excited via incident light and it is considered as a bright mode. To first approximation, the response of an uncoupled molecular vibration is very weak compared to that of the LSPR, so it is approximated as a dark mode in our system. Full derivation and method is described in Appendix 2

4.3 Result and discussion

Doped In_2O_3 NCs were synthesized using standard Schlenk line air-free colloidal synthesis techniques with a synthetic protocol based upon the decomposition of a metal oleate at high temperatures in an organic solvent and in the presence of mixed primary and tertiary amine to yield the metal oxide. In Figure 4.5 and 4.6, scanning transmission electron microscopy (STEM) of different sizes of doped In_2O_3 NCs are shown, illustrating the tight control on size (edge length) of the cubic FITO (Figure 4.5). The average size (20-120 nm) of the NCs can be tuned by varying the ratio of primary and tertiary amines and the growth time (See SI for details). X-ray diffraction (XRD) shows (Figure 4.6b) that FITO NCs possess the cubic bixbyite structure typical of In_2O_3, with a strong (100) texture arising from preferential orientation of nanocubes with their square faces lying flat on the substrate.

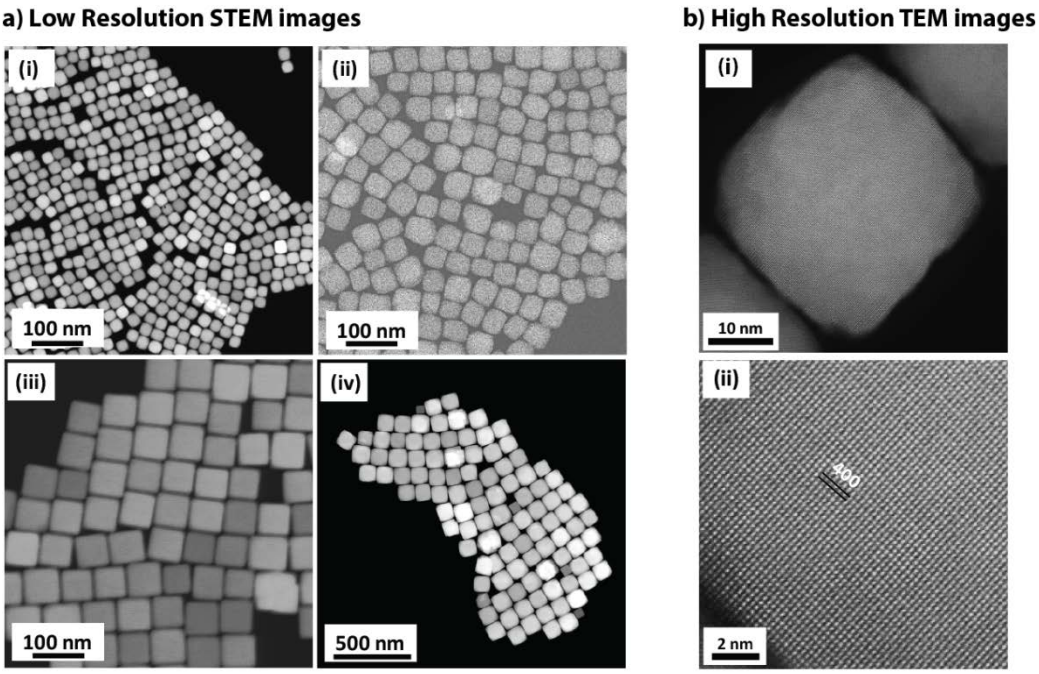

Figure 4.5 **STEM imaging of FITO nanocrystals**. a) Additional STEM images of the nanocrystals shown in figure 1 in main text i) 20 nm, ii) 40 nm, iii) 65 nm, iv) 105 nm. b) High Resolution TEM images of 40 nm cubes showing the single crystalline nature of each nanocrystal.

The optical extinction spectra of the four representative samples as colloidal dispersions do not vary significantly with the size of the NCs (Figure 1c) because the NCs are isolated from one another. Note that the secondary peak at lower energy for the 105 nm sample is due to coupling between NCs as a result of slight NC aggregation in tetrachloroethylene (TCE). These NCs are all sufficiently small that we expect the electric field inside the NCs to be largely size invariant per the quasi-static approximation[1] that is valid for particle sizes well below the excitation wavelength (here, approximately 2500 nm). In electromagnetic simulations of the optical response (Figure S2 and S3), we found that in this size regime, absorption is dominant and size

independent, while scattering contributes little to the extinction spectra. However, NC size was found to strongly influence coupling, as discussed below.

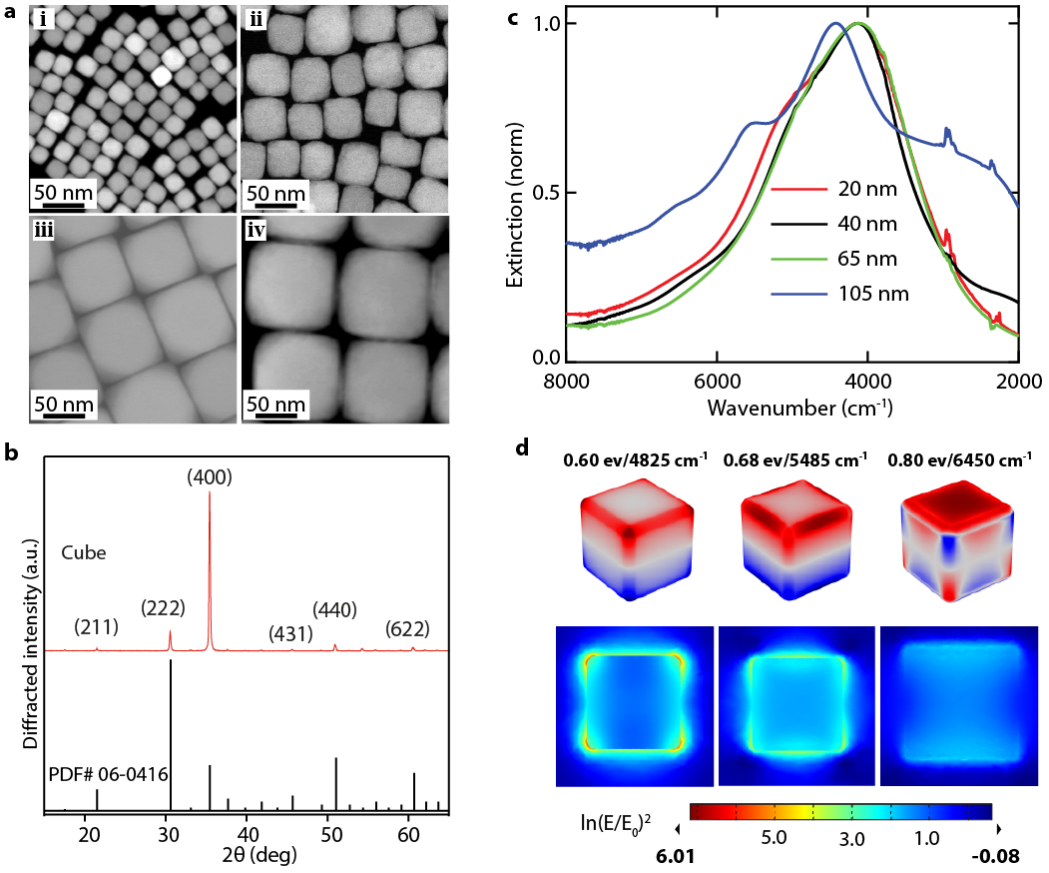

Figure 4.6 **Characterization of FITO cubes**. a) STEM images of different sized cubic F, Sn- codoped In_2O_3 NCs with average size (edge length) of i) 20nm, ii) 40 nm, iii) 65 nm, and iv) 105 nm. b) XRD pattern for 105 nm FITO cubes compared to the reference pattern for bixbyite In_2O_3. c) Optical spectra of different sized cubic dispersed in TCE. c), d) The fundamental modes are verified using optical simulation of an isolated FITO NC, which also suggests high NFE (shown on a log scale).

Dopant type and distribution inside each NC can significantly impact LSPR spectra and near field properties. In the case of $Sn:In_2O_3$, carrier mobility and hence LSPR damping are substantially influenced by ionized impurity scattering at dopant sites and oxygen vacancy defects ($Sn_{In}^{\cdot}$ and $V_O^{\cdot\cdot}$ in Kröger-Vink notation). It was recently

shown that defect engineering by doping In_2O_3 NCs with cerium can greatly reduce dopant related ionized impurity scattering, but the achievable carrier concentrations were much lower than those attainable with tin doping[16]. Here, we have instead incorporated fluorine as a co-dopant with tin in the In_2O_3 NCs. Fluorine ions likely occupy oxygen sites ($F_O^{\cdot}$), contribute free electrons, and can decrease the oxygen vacancy concentration. Since the cross section for ionized impurity scattering is proportional to the square of ionic charge (Z^2), $F_O^{\cdot}$ defects will scatter electrons more weakly than oxygen vacancies ($V_O^{\cdot\cdot}$) with the overall effect being that fluorine co-doping can reduce LSPR damping while maintaining a high carrier concentration. To understand the effect of fluorine incorporation on far field optical properties, the full-width half maximum (FWHM) of the LSPR was used to quantify damping. We compared the simulated extinction spectrum of FITO cubes (Figure 4.8), with that of Sn:In_2O_3 (ITO) cubes, using the same geometry for each (Figure 4.1) to isolate the impact of differences in scattering. The dielectric function of ITO was taken from previously published work[77], while the FITO dielectric function was determined by fitting spectra of the 20 nm cubes reported here. The reduction of damping upon incorporation of fluorine is apparent in the narrower LSPR peak of the FITO cubes, as expected. The reduction of ionized impurity scattering in FITO also suggests that higher NFE may be achievable under resonant excitation of these NCs.

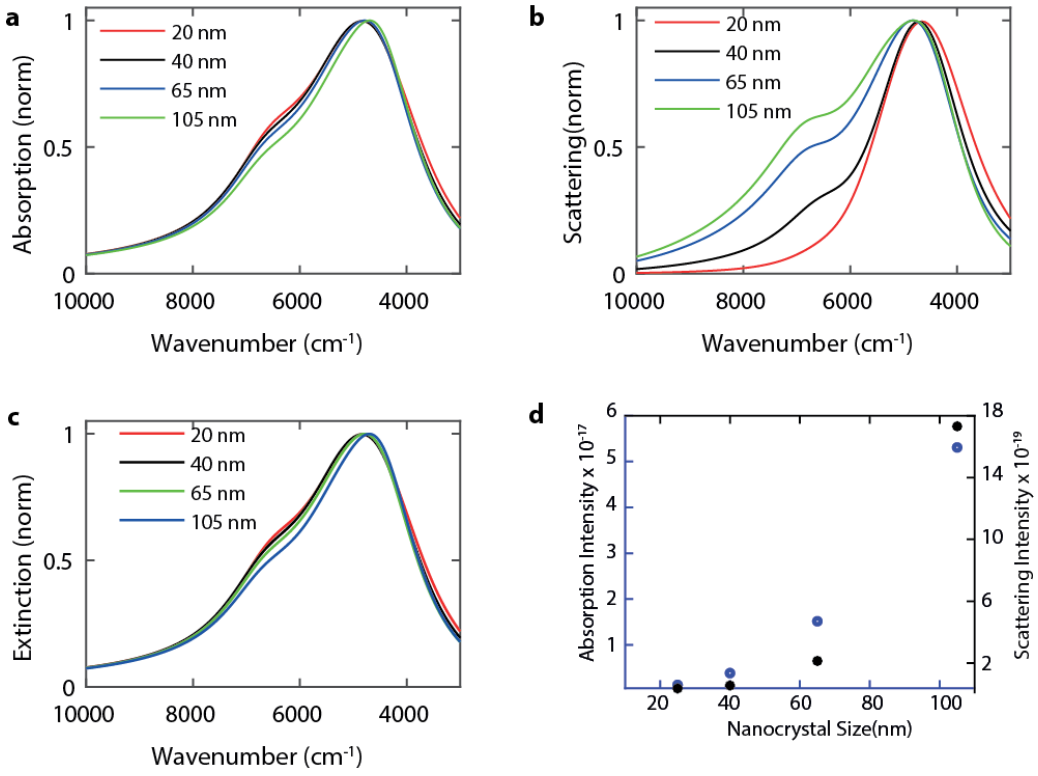

Figure 4.7 **Size Dependent optical properties.** Simulated size dependent normalized absorption (a), normalized scattering (b), and normalized extinction (c) spectra. As the size of the nanocrystals is very small compared to the wavelength of light, under the quasi-static limit extinction should not have any size dependence. This behavior is reflected well in the absorption and extinction spectra. At such a small sizes, scattering is expected to be very small compared to absorption. This is well reflected in the intensities of the peak absorption and scattering for all sizes as plotted in d).

The optical spectra (Figure 1c) reflect the convolution of three fundamental geometric eigenmodes, i.e. corner, edge, and face-centered modes from low to higher energy, respectively. Simulated surface charge maps of a 20 nm and 100nm FITO NC under excitation at different energies, (Figure 4.6d and 4.9), show that all the geometrical modes are of dipolar nature. The NFE maps (Figure 4.6d-bottom) show that the sharp edges and reduced ionized impurity scattering in FITO results into larger NFE (>400) than previously reported values for spherical (~10)[44] and rod-like ITO (150-160)[8].

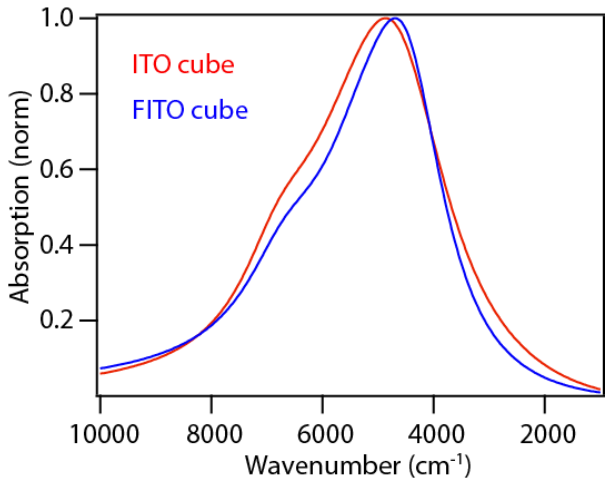

Figure 4.8 **Comparing ITO cubes with FITO cubes**. Due to lower electron scattering in FITO compared to ITO nanocrystals, the simulated absorption spectrum of an FITO cube (blue) has a smaller FWHM compared to the simulated spectrum of an ITO cube (red).

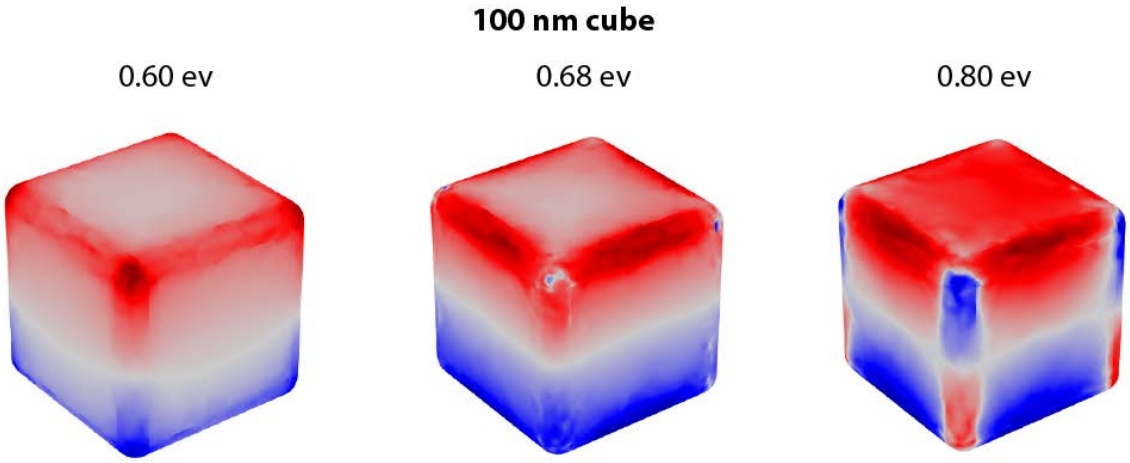

Figure 4.9 **LSPR modes for a 100 nm cube.** These mode profiles are very similar to those of the 20 nm nanocube. This further confirms our hypothesis that in the size range studied (20 -100 nm) we are still under the quasi-static limit leading to no size dependence.

To observe the expected LSPR modes experimentally, we mapped the plasmon-induced near field properties of FITO cubes with high spatial resolution using monochromated STEM-EELS (zero-loss peak FWHM of 0.15 eV), performed in an FEI Titan Themis[3] equipped with a Gatan Quantum ERS electron spectrometer. To extract the LSPRs' spatial and spectral distribution, the global fitting technique of non-negative matrix factorization (NMF)[253–259] was applied to the recorded spectrum images (Figure 4.10a and 4.11). Figure 4.10b shows the three distinct LSPR modes at (0.62 eV/5000 cm^{-1}, 0.73 eV/5888 cm^{-1}, 0.85 eV/6855 cm^{-1}) of a single FITO cube on a 10 nm thick SiN substrate. Even though the excitation mechanism in experimental EELS and optical simulation are different (electrons and photons, respectively), the plasmon peak energies in the EEL spectra are similar to that obtained via experimental FTIR and simulated spectra. EEL spectra thereby verify the presence of different geometric modes (Figure 4.10b) in metal oxide NCs, in good agreement with the simulated near field map (Figure 4.6b). In agreement with current and previous simulations[255], these EELS maps are the first direct evidence establishing that plasmonic metal oxide NCs exhibit near field modes similar to those in faceted gold and silver nanoparticles, which have been the key to developing numerous applications of plasmonic materials.

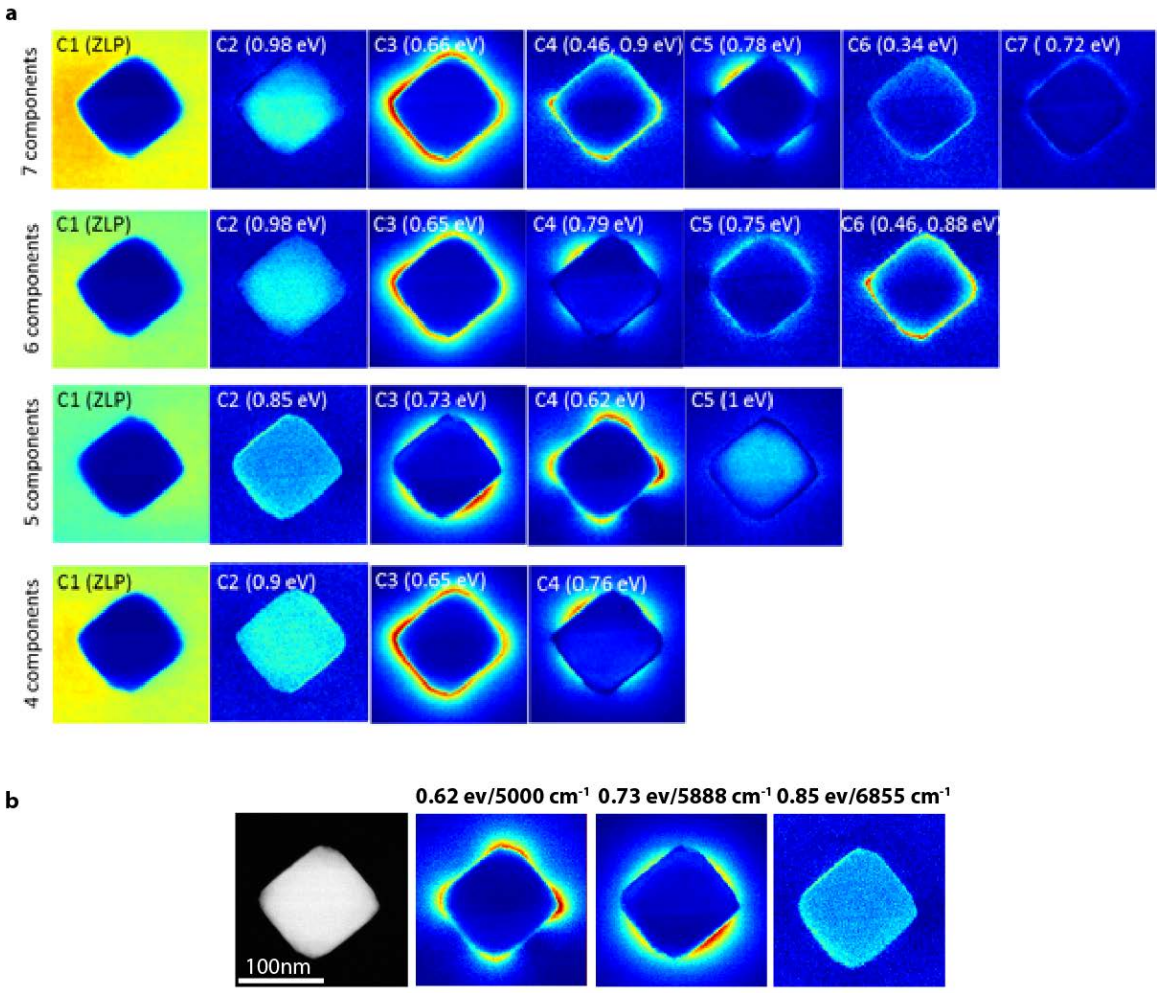

Figure 4.10 EELS map of isolated FITO nanocrystal. (a) Systematic study of the effect of the number of components on NMF analysis for the single FITO nanocube in Figure 2a. Decomposing the spectrum image using 5 components results in the corner, edge and face geometrical LSPR eigenmodes at 0.62 eV, 0.73 eV and 0.85 eV, respectively. Although the appearance of 0.46 eV peak at the cube corners for NMF analysis with larger than 5 spectral components suggests the presence of an LSPR peak at 0.46 eV, its contribution to the spectrum is not significant. The amount of shift in the peak position by increasing the number of spectral components is negligible. (b)

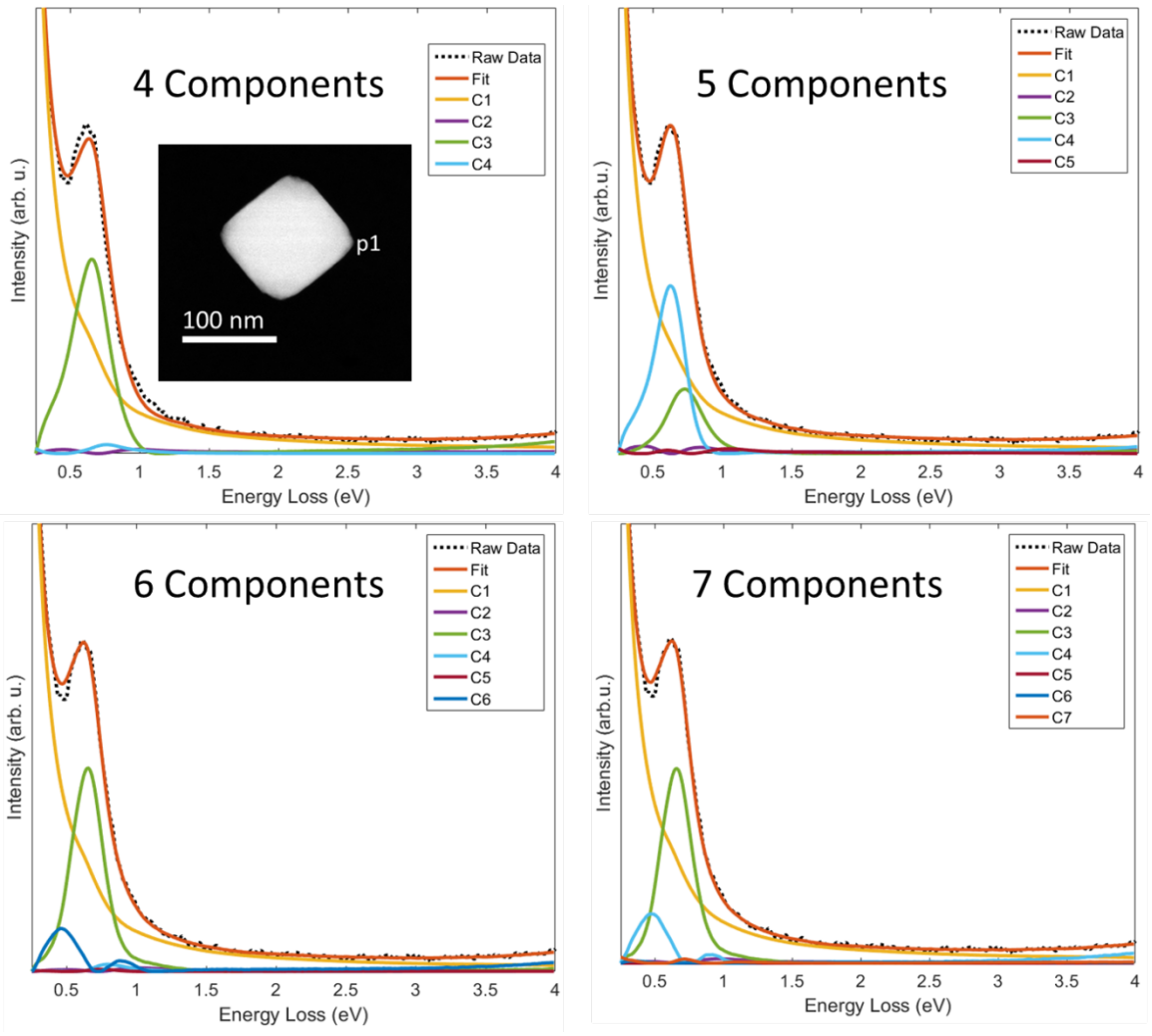

Figure 4.11 NMF decomposition of EELS spectrum of isolated FITO nanocrystal. Spectral components for NMF analysis with 4, 5, 6, and 7 components and comparison of corresponding fitted spectrum with as-acquired spectrum at position p1, marked on the inset HAADF-STEM image, for each sets of components.

Assembling NCs into extended structures leads to LSPR modes arising from NC-NC coupling, which causes both more intense and a higher density of near field hotspots[250,260,261]. Recently, Kuznetsov[262] demonstrated computationally that although

individual metal oxide NCs have weaker NFE than metal nanoparticles, due to higher spatial hot spot density coupled metal oxide structures have higher volumetrically average NFE than similar metallic nanostructures. We examined the LSPR coupling of FITO NCs, first by mapping the LSPR modes of small NC clusters on SiN substrates and then by extending our study to mesoscale film of self-assembled NCs. The LSPR modes of both a linear chain of three NCs and a 2×2 square array of NC cubes were observed by EELS (Figure 4.12-4.15). In both cases, the lowest energy modes spanned the cluster as a single entity and shifts towards lower energy compared to isolated NC due to strong LSPR-LSPR coupling (Figure 4.12b and 4.14b). For instance, in the linear structure, the modes at 0.43 ev/3468 cm^{-1} and 0.68 eV/5484 cm^{-1}, respectively, are localized at the geometrical corners and edges of the overall chain structure. Similarly, for the 2×2 structure, the mode at 0.57 eV/4597 cm^{-1} is localized at the corners of the overall structure. Prior literature[253,255,263] on plasmon coupling in clusters of Au nanoparticles has shown that for closely spaced particles, clusters of NCs behave as a single entity with LSPR modes that extend across the overall structure. Since our system of 105 nm cubes had an average 3 nm face to face separation due to surface bound ligands, which is very small compared to the size of the NC, our observation appears consistent with this expectation. However, alongside the expected assembly-spanning modes, we also observed localized internal modes such as one at 0.8 eV, which produces a hot spot localized at the center of the (2x2) array. Overall, the EELS maps of these NC clusters prove that coupled and individual metal oxide NCs support the formation of LSPR modes and hot spots, just as for noble metals, so these materials offer a new alternative for applications based on near field enhancement of infrared light.

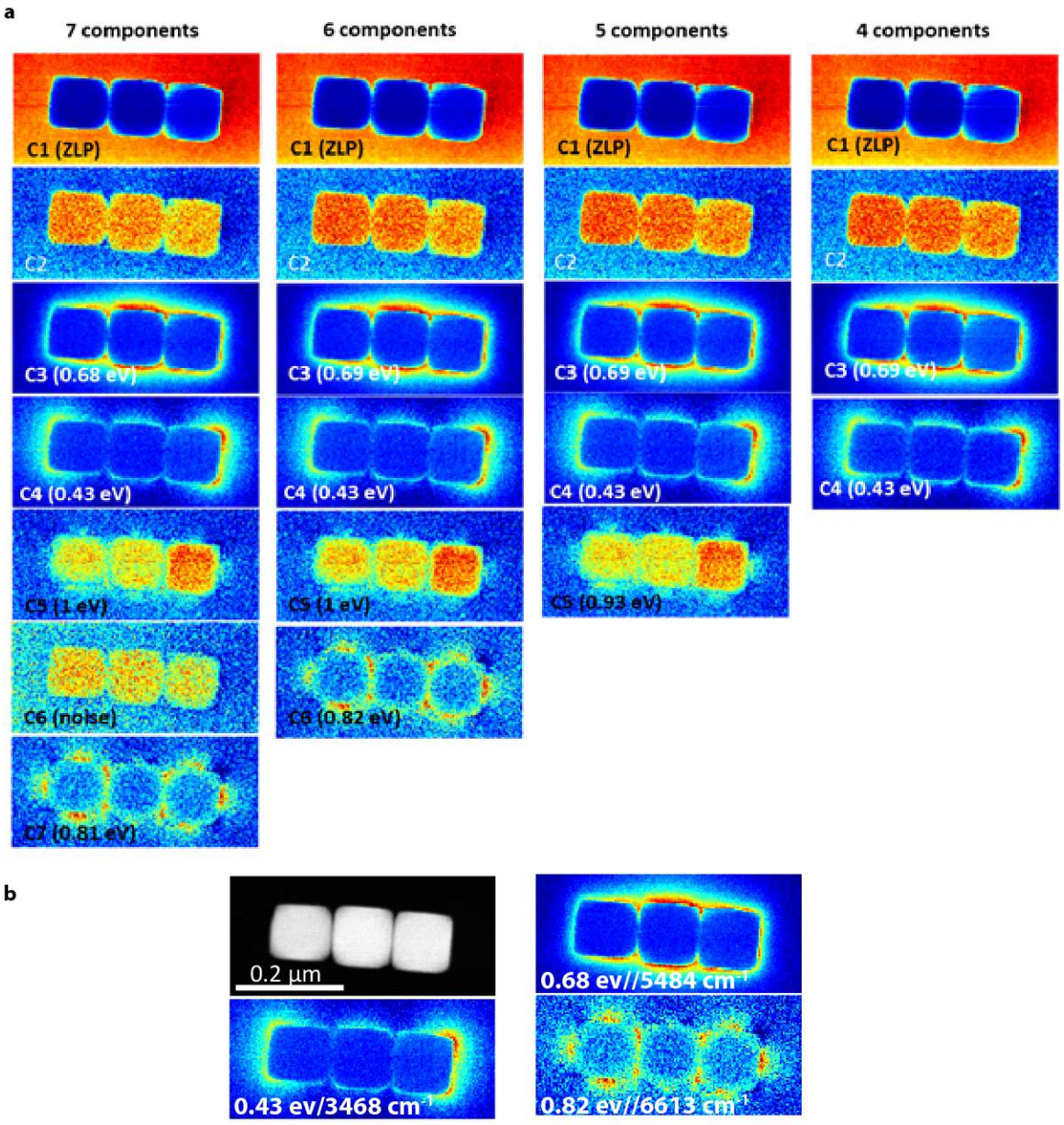

Figure 4.12 EELS map of 1D chain of FITO nanocrystal (a) Systematic study of the effect of the number of components on NMF analysis for the 1D chain of FITO nanocubes in Figures 2b. The change in the peak position and spatial distribution of LSPRs with the number of spectral components is negligible. All LSPR peaks are extracted with the choice of 6 or 7 components in NMF analysis. (b)

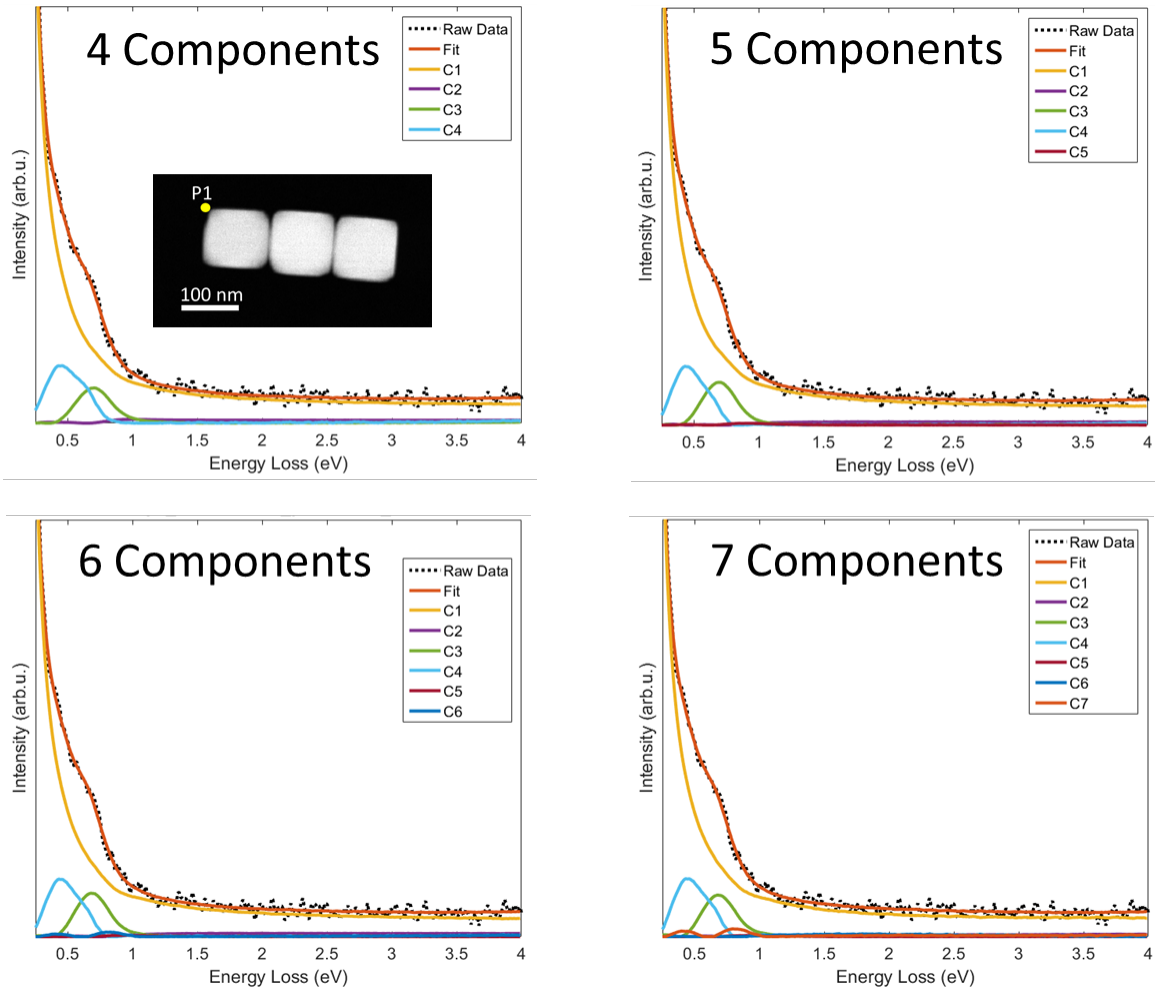

Figure 4.13 NMF decomposition of EELS spectrum of 1D chain of FITO nanocrystals. Spectral components for NMF analysis with 4, 5, 6, and 7 components and comparison of corresponding fitted spectrum with as-acquired spectrum at position p1, marked with a yellow circle on the inset HAADF-STEM image, for each sets of components.

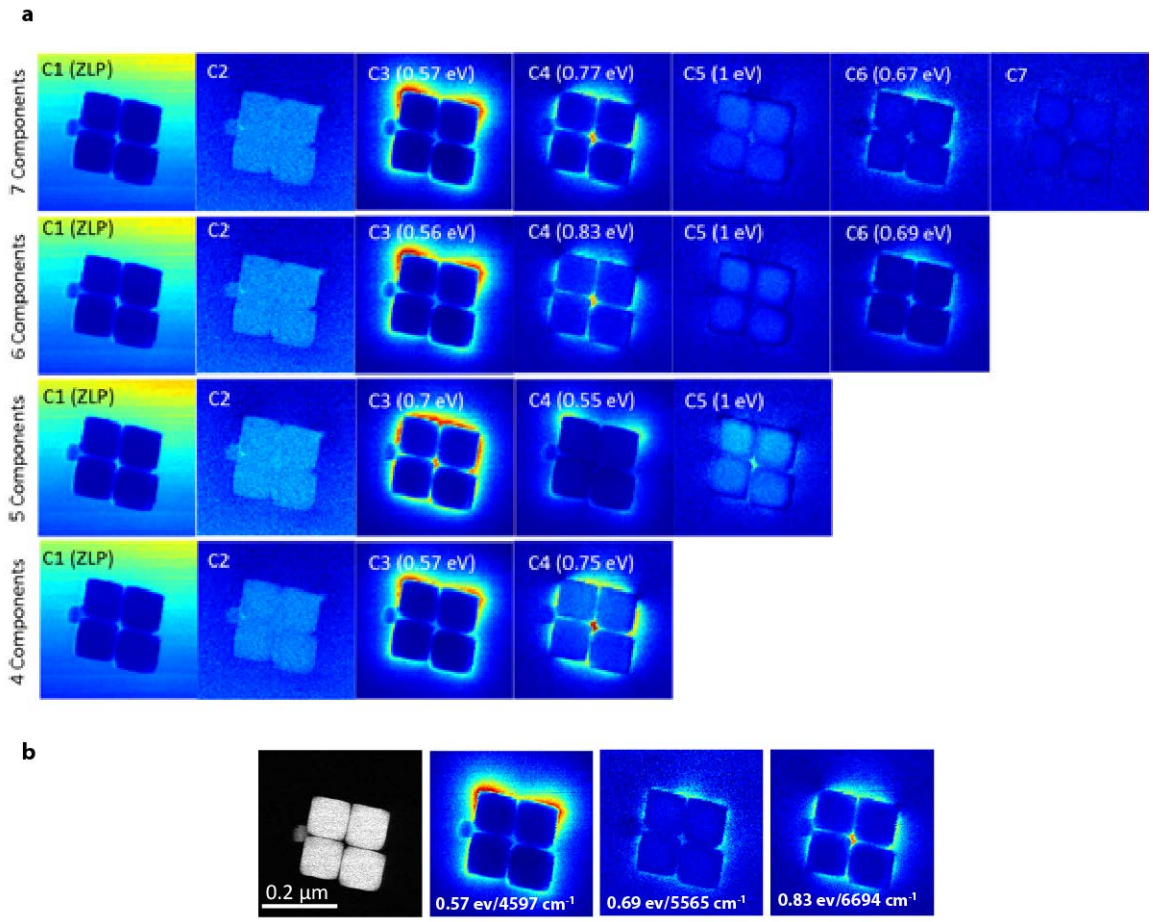

Figure 4.14 EELS map of 2D cluster of FITO nanocrystal (a) Systematic study of the effect of the number of components on NMF analysis for the 2×2 array of FITO nanocubes in Figure 2c. The change in the peak position and spatial distribution of LSPRs with the number of spectral components is negligible. All LSPR peaks are extracted with the choice of 6 or 7 components in NMF analysis. (b)

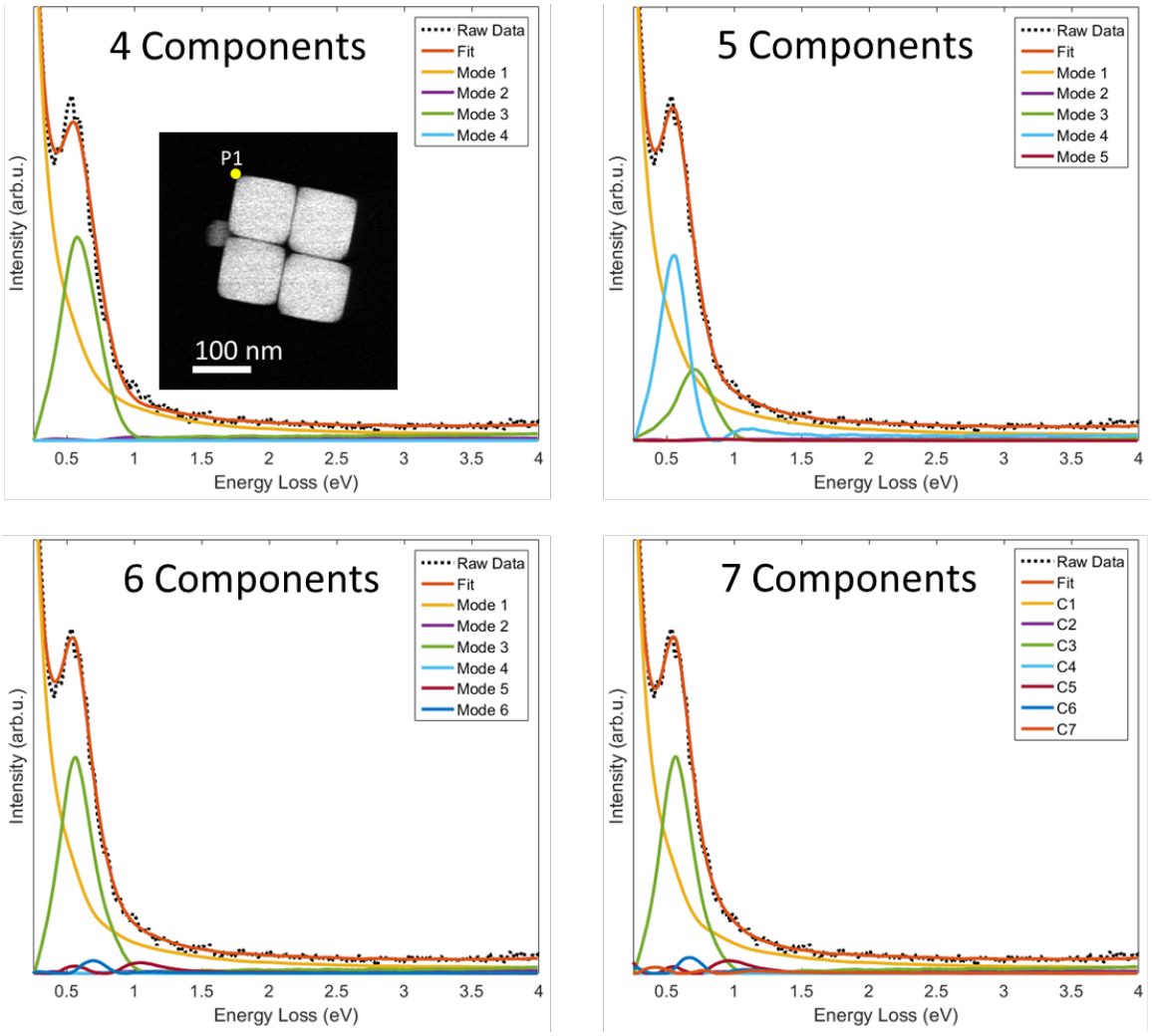

Figure 4.15 NMF decomposition of EELS spectrum of 2D cluster of FITO nanocrystal. Spectral components for NMF analysis with 4, 5, 6, and 7 components and comparison of corresponding fitted spectrum with as-acquired spectrum at position p1, marked with a yellow circle on the inset HAADF-STEM image, for each sets of components.

For SEIRA in particular, maximizing the effective optical density of a molecular vibration is desired, which is best achieved by assembling NCs over a large substrate area to create a high density of hot spots with strong NFE. Extended close-packed assemblies

of FITO cubes were prepared by drop casting NC solutions on a CaF_2 substrates and drying slowly to yield close-packed layers (Figure 4.16a).

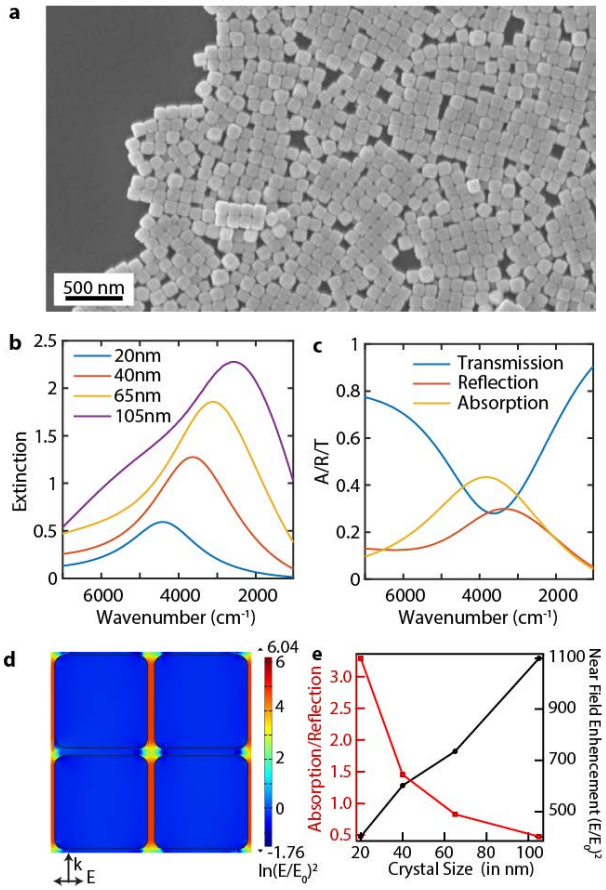

Figure 4.16 Optical properties of coupled NC assemblies. a) Scanning electron microscopy (SEM) image of a slowly dried drop cast film of 105 nm FITO NCs. b) Simulated extinction spectra of periodic monolayer film of closed packed FITO NCs of different sizes. The distance (*d*) between the NCs was kept fixed while changing their size (*a*). As the size increases, the ratio R=*d/a* decreases, resulting in stronger LSPR-LSPR coupling; increased coupling shifts the LSPR towards lower energy. c) Simulated reflection, transmission and absorption spectra of a 40 nm NC assembly. d) Simulated NFE map at the extinction peak for a 105 nm NC assembly with light polarized laterally. Formation of hot spots in between the NCs leads to an order of magnitude increase in NFE compared to an isolated NC. e) The ratio of absorption to reflection decreases (red line) and maximum NFE increases (black line) with the increasing size.

The optical response of extended arrays of FITO cubes was simulated for each sample size and then compared to the experimental spectra. The simulation employs periodic boundary conditions in two dimensions for a monolayer of NCs on a CaF_2 substrate to approximate the experimental conditions (Figure 4.3). Spectra were calculated using the COMSOL wave optics module while varying the size of the NCs keeping the interparticle distance constant. As the ratio ($R=d/a$) between inter-particle distance (d) and NC size (a) decreases, coupling between the LSPR of neighboring NCs becomes stronger, resulting in a redshift of the LSPR in the extinction spectrum toward lower energy (Figure 4.16b). In the experimental extinction spectra, a similar trend is observed as NC size increases (Figure 4.17). This result demonstrates that in contrast to size independent optical extinction in solution where the interparticle coupling is very weak; in assembled films, the size of the NCs governs the extent of LSPR-LSPR coupling. Moreover, at first look, the decrease in transmittance for larger NCs could be rationalized by an increase in the amount of material in a NC monolayer. However, a closer view of the simulation results shows that losses due to both reflection and absorption contribute to this change in the extinction (Figure 4.16c). As R decreases, the effective refractive index approaches that of continuous TCO film and the larger NC films are substantially reflective. In the simulated spectra, the LSPR absorbance and reflectance redshift as R decreases, while the reflectance monotonically increases in intensity (Figure 4.18). The absorption is predicted to peak at around 40% of the incident light for 40 nm NC (Figure 4.18).

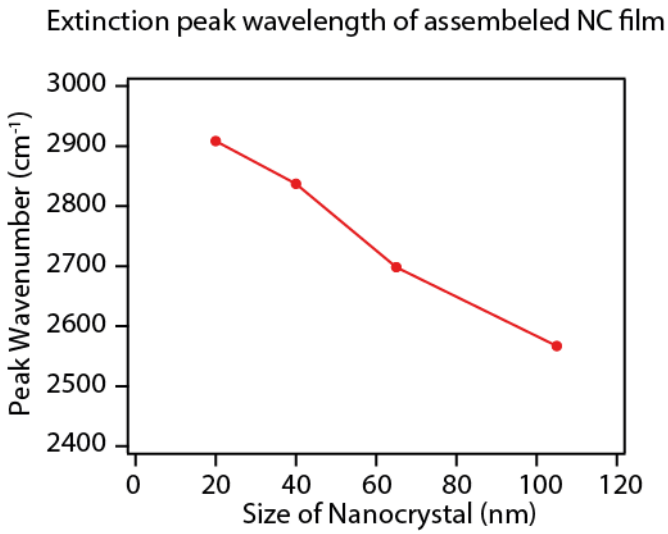

Figure 4.17 Peak position in wavenumbers from extinction spectra of close packed cubic FITO NC films. LSPR coupling between the nanocrystals strengthens as the size of the nanocrystals increases thereby red shifting the LSPR.

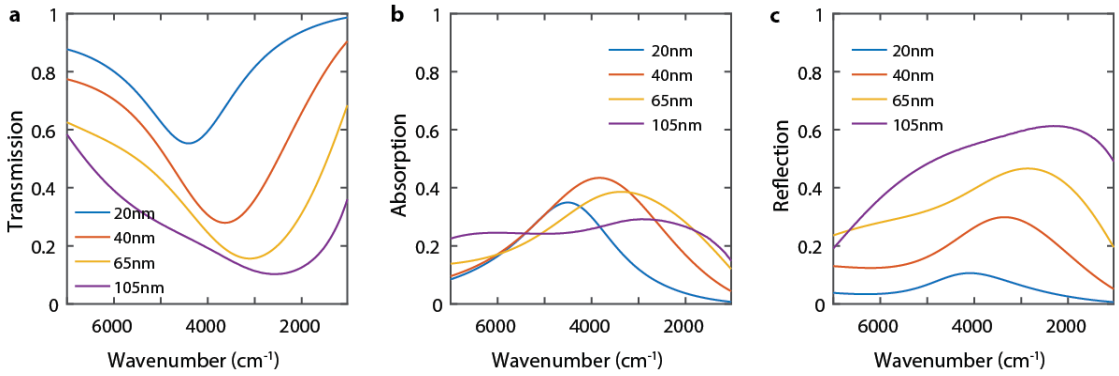

Figure 4.18 Simulated spectra of periodic nanocrystal film. Simulated transmission (a), absorption (b) and reflection (c) spectra of a 2-D periodic structure of different sized FITO NCs.

Simulations of the NFE of infrared light at the energy where extinction is strongest show that the strongest enhancement is in hot spots between assembled NCs (Figure 4.16d). As R decreases, the NFE increases (Figure 4.16e-black). The influence of NC size on LSPR-LSPR coupling in films is an increase in reflection intensity compared to absorption intensity at larger sizes, and increased near field coupling as NC size increases (Figure 4.16e). Next, we will examine the influence of both of these factors on coupling between the LSPR of assembled NC films and the vibrational resonance of C-H bonds in adsorbed molecules.

Coupling between relatively broad plasmonic resonances and sharp vibrational resonances of molecular bonds can result in Fano-type interference as well as plasmon-induced transparency or plasmon-enhanced absorption[129,130,241]. Such resonant coupling effects have been studied using 2D-graphene structures[264], gold nanorods[241] and other metallic structures[265,266] with infrared resonances. In most of these previous studies, a reflective gold substrate is used and spectra are collected in reflection geometry. For the plasmonic system consisting of gold nanorods separated from a gold substrate by a thin layer of PMMA, Altug et.al.[241] observed that if the LSPR frequency is resonant with the molecular vibration frequency, the coupling behavior between them qualitatively changes depending upon the ratio of plasmon decay rate to scattering and absorption. If this ratio is less than one, coupling gives rise to plasmon-induced transparency of the vibrational signal and if it is greater than one, enhanced absorption is observed. In related works, Altug et.al.[129,130] and Shvet et.al.[242] have shown that off resonant coupling results in a Fano-like derivative line shape. All of these observations can be rationalized using coupled harmonic oscillators as a model of TCMT[241,242,267] (Figure 4.19 a,b).

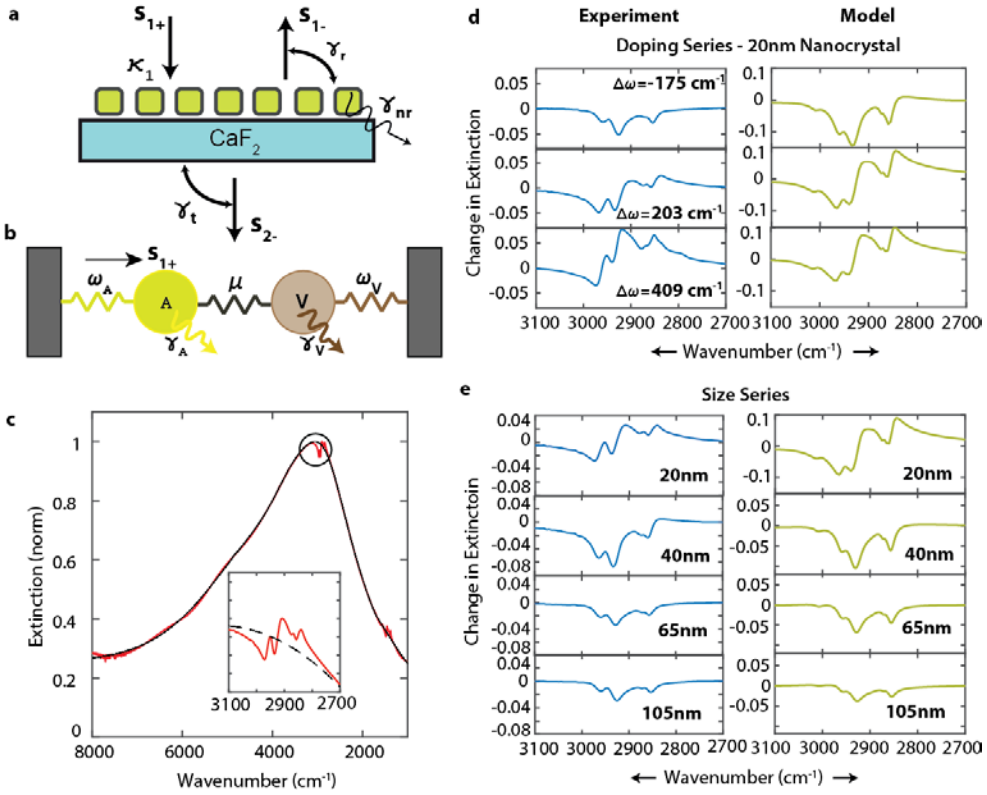

Figure 4.19 Plasmon – Vibrational Mode Coupling: a) Schematic depicting the interaction between the incident light (s_{1+}) and periodic film of cubic NCs with the coupling constant (κ_1). Plasmon excitation decays through both radiative and non-radiative pathways. It couples with reflected and transmitted light at plasmon decay rate γ_r and γ_t, respectively. The non-radiative decay rate (γ_{nr}) determines the absorption in the film. b) Schematic illustrates the coupling between LSPR and vibrational resonance, describing both as harmonic oscillator. c) Measured extinction spectrum of a film of 20 nm ligand capped NCs. Inset: Zoom in on the coupling zone showing the Fano resonant coupling signature d) Left Panel - Background subtracted vibrational signal changes from plasmon induced transparency to Fano interference with increase in detuning between the LSPR and the vibrational resonances. The NCs were 20 nm in all cases. Right Panel - Simulation of transmittance for periodic structures of ligand bound NCs reproduces the same coupling behavior as observed in experimental spectra. e) Left Panel - Coupling between different sized NCs in a film with vibrational resonance changes from Fano resonance for 20 nm to plasmon-induced transparency for larger sizes. Right Panel – Simulation of transmittance for periodic structures of ligand-bounded NCs of different size with fixed inter-particle distance reproduces the observed behavior.

Here, we have studied the coupling between semi-transparent (in the IR spectral range) films of 20 nm FITO NCs on CaF_2 substrates and different C-H stretching modes of NC-bound oleate molecules, which are sharp resonances in the range of (2800-3100 cm^{-1}) (Figure 4.20). Oleic acid is bound to the NC surfaces during colloidal synthesis and a monolayer remains adsorbed following isolation of the NCs, which allows us to prepare thin films from solvent dispersions. FTIR transmission spectra are recorded at a perpendicular angle of incidence relative to the substrate and reported as extinction (Figure 4.19c). The oleic acid vibrational signature is observed on top of an intense LSPR signal (Figure 4.19c, inset). To isolate the vibration signal and investigate coupling between the resonators, the transmittance was divided by a polynomial fit to the plasmon line shape (Figure 4.19c, red). The derivative shape of the vibrational signal is Fano-like and indicative of coupling. Hence, we anticipate dependence of this lineshape on two main parameters, namely the NC size and the detuning of the LSPR frequency with respect to the vibrational resonance ($\Delta\omega = \omega_{LSPR} - \omega_{vib,avg}$).

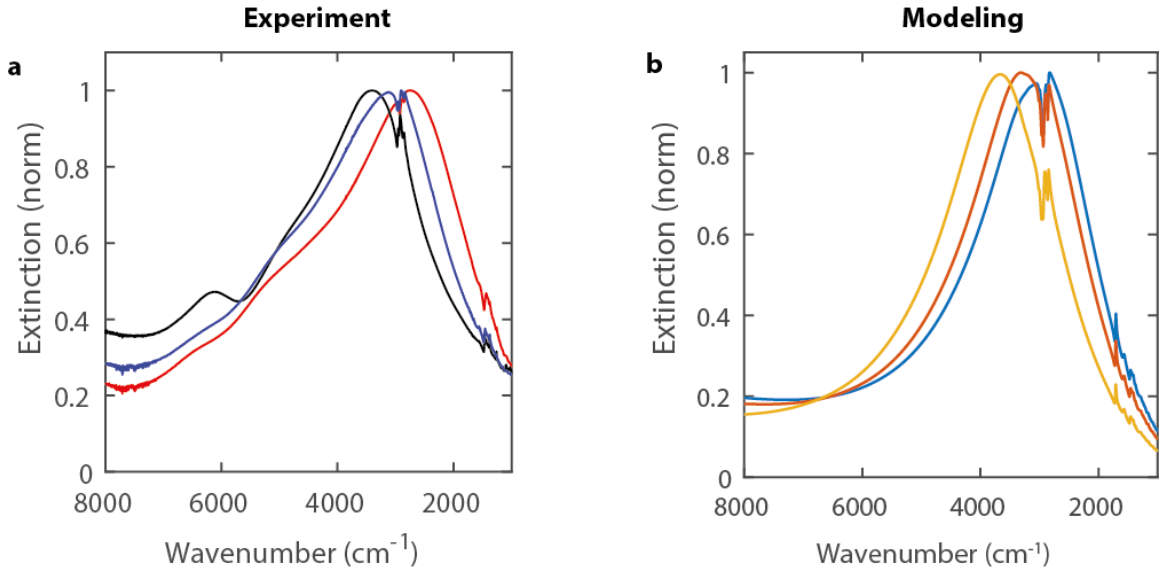

Figure 4.20 Effect of doping on coupling between NCs and ligand vibrations. Experimental spectra (left) of ligand coated nanocrystal films show the Fano resonance interference signature on top of the broad LSPR peak. As the average vibrational resonance frequency shifts red of the LSPR frequency, the coupling behavior changes from an LSPR-induced dip to derivative-like Fano resonance. This coupling behavior was reproduced in periodic structure simulations (right).

To examine the spectral changes induced by detuning, we varied the LSPR frequency by synthetically changing the tin dopant concentration in 20 nm NCs. As the free electron concentration increases with doping, the LSPR peak shifts from lower to higher energy relative to the vibrational resonance (Figure 4.20 and Figure 4.19d). For the lowest energy LSPR, each vibrational band appears as a dip in extinction, indicating plasmon-induced transparency, while for higher energy LSPR the asymmetric Fano-like lineshape appears. This indicates that indeed, the FITO LSPR is coupling to the oleic acid molecular vibrations. We compare this trend to numerical simulations of the coupled optical response (Figure 4.20 and Figure 4.19d). In the numerical simulation, a two-dimensional periodic structure consisting of a monolayer of ligand coated 20 nm NCs was excited at normal incidence. The simulated extinction spectra were background

subtracted in the same way as the experimental spectra to obtain the vibration signature. The LSPRs in the simulations were chosen to match the range of experimental detuning. The simulated spectral profiles matched the experimental results, although the strength of the vibrational signals seems to be over-estimated by the simulations, which will be discussed below. The variations in vibrational lineshapes resulting from LSPR-vibrational coupling are attributed to changes in frequency detuning since we do not expect substantial differences in NFE or relative value of reflection to absorption over this narrow energy range.

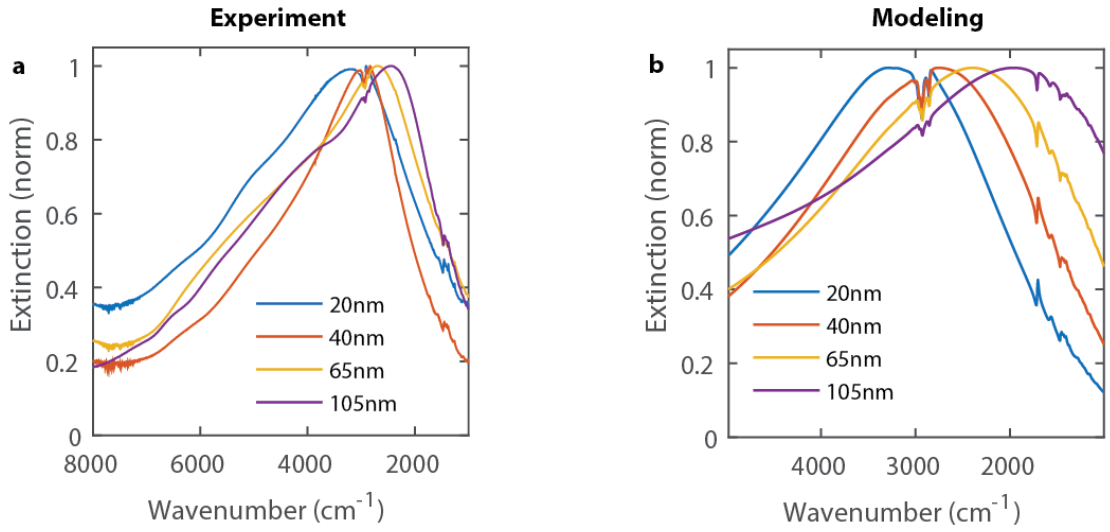

Figure 4.21 Effect of size of NCs on coupling between NCs and ligand vibrations. Experimental spectra of monolayers of close packed ligand coated nanocrystals. Coupling signatures on top of broad LSPR peaks show strong size dependence. This behavior is in agreement with modeled extinction spectra (right).

We expect NC size to alter the observed vibrational lineshape owing to its influence on far field reflection, transmission and absorption in organized NC films. As observed, the vibrational signal has a Fano-like line shape for a film of 20 nm NCs,

which evolves towards plasmon-induced transparency for 40 nm, 65 nm, and 105 nm NCs due to a progressive red shift of the plasmon resonance from positive to negative detuning with increasing size, due to stronger LSPR-LSPR coupling of larger NCs (Figure 4.21, Figure 4.19e). These trends are counterintuitive relative to the understanding outlined in literature regarding LSPR in conventional metal nanostructures. From prior literature on coupling in classical metal plasmonic systems[130,241], we expect a recovery of an asymmetric Fano lineshape once the LSPR frequency is red-shifted away from the molecular vibration, such as the case of 65 nm and 100 nm NC films. Indeed, as explained earlier, the derivative-like Fano lineshape did appear when we detuned the LSPR by varying doping (at constant 20 nm size). This contrast between the size dependence and dopant dependence on the lineshape suggests that some other size-dependent properties of the NCs, rather than only detuning are responsible for the persistence of the plasmon-induced transparency in the self-assembled films of larger NCs. A closer analysis utilizing numerical simulation is required to explain the trends and is discussed below.

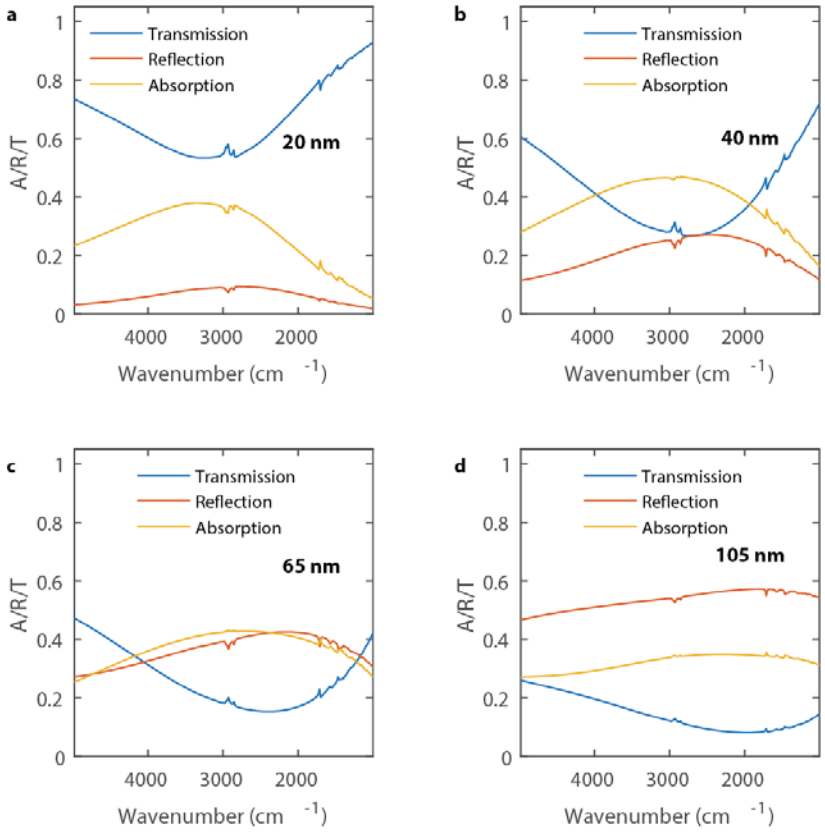

Figure 4.22 Vibration coupling signature in in different optical decay pathways. Coupling signatures differ in reflection, transmission and absorption spectra for all sizes of nanocrystals. It depends upon the relative LSPR decay rates through respective processes.

Energy stored in a resonant process like an LSPR gets dissipated to its surrounding via both radiative and non-radiative processes. Here, in the case of a periodic film, the available non-radiative channel would be absorption and the radiative channels would include both reflection and transmission. In a coupled resonance system, coupling would be exhibited differently in each decay channel. As expected, simulations show that the signatures of coupling in absorption, reflection and transmission differ from each other and depend strongly on the size of the NCs (Figure 4.22). Background subtracted molecular vibration spectra (Figure 4.23) show that with increasing NC size, the coupling

profile in absorption spectra changes from asymmetric Fano-like resonance (20 nm) to a complete induced transparency (40 nm) and then to enhanced absorption (65 nm and 105 nm). In contrast, the reflection spectra always show a plasmon-induced transparency irrespective of NC size. So, as the relative contributions of reflection and absorption to the measured transmittance spectra change with NC size, the lineshape changes from asymmetric (20 and 40 nm) to a plasmon-induced transparency (65 and 100 nm). For 20 nm NC films (for all dopant concentrations), where absorption is dominant over reflection, the absorption spectrum determines the shape of the vibrational resonances in extinction spectra. At the other size extreme, in a 100 nm NC film, it is the vibrational signature in reflection that is dominant in the extinction spectrum. Simulated near field maps also show that even though there is higher NFE at the peak LSPR energy with increasing size, the NFE decreases at the actual vibration frequency (2850 cm^{-1}) (Figure 4.24) because the detuning between the LSPR and vibration increases as the larger NCs couple more to each other. This trend explains our observation of a decrease in vibrational signal strength with increasing NC size. That said, the trends in vibrational lineshape observed here differ from those in the literature on classical metal systems. To understand this behavior in greater depth, taking inspiration from the works of Altug et.al.[241], Haus et.al.[268] and Fan et. al.[267,269], we developed a theoretical model to further explain our results.

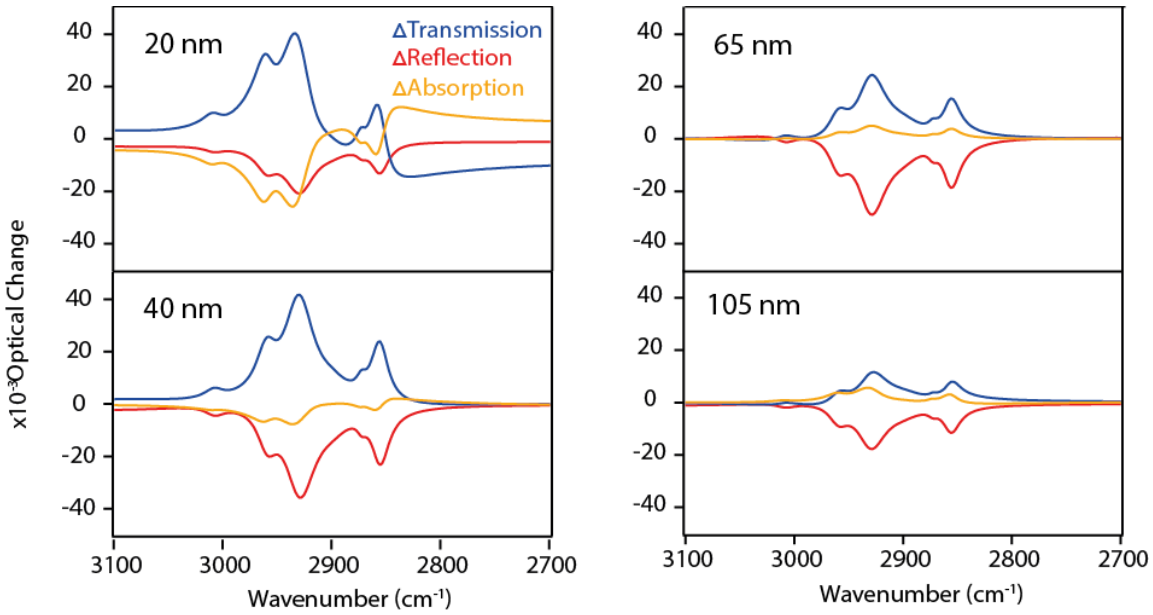

Figure 4.23 Background subtracted simulated vibrational signals in different decay pathways. Background subtracted simulated reflectance (red), absorption (yellow) and transmission (blue) spectra showing the dependence of lineshape of molecular vibrations on the size of the nanocrystals.

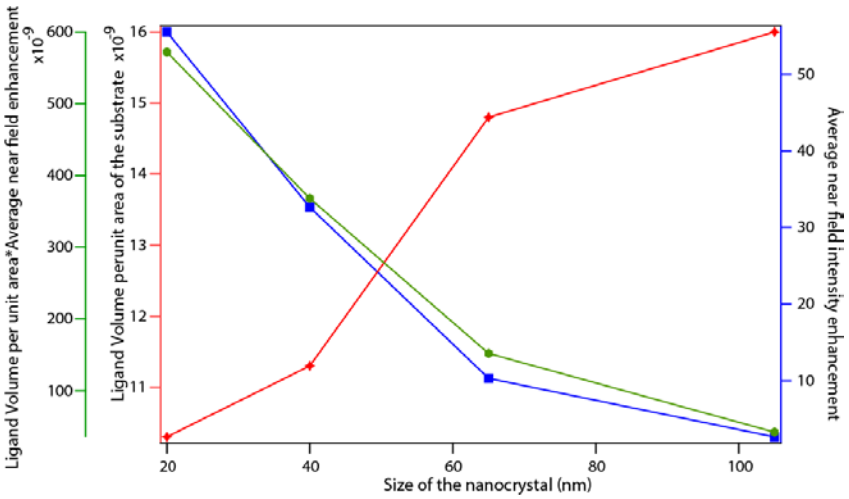

Figure 4.24 Volume average electric field enhancement at average vibrational frequency (2900 cm^{-1}) (blue-right) and ligand volume fraction as a function of the size of the NC (red-left). Although, these two trends runs counter to each other, the product of the two quantities (green-left) effectively determines the intensity of the coupled molecular vibration signal.

TCMT analysis used previously to rationalize coupling effects in plasmonic systems based on classical metals cannot be directly applied as it assumes only one optical port with incident and reflected light. For semi-transparent (in the IR range) metal oxide films, we need to consider all three components of electromagnetic waves, that is, reflected, transmitted, and absorbed light. With this consideration, we developed a theoretical model to explain the optical properties using two port coupled mode theory.

As shown schematically in Figure 4.19a, the plasmonic resonators are coupled to incident (s_{1+}) and reflected (s_{1-}) light through port 1, and transmitted light (s_{2-}) through port 2, where the +/- sign signifies an incoming or outgoing wave. LSPR and vibrational resonators are modeled as simple harmonic oscillators. Energy exchange between these resonators occurs due to interaction between the LSPR-induced near field and the

vibrational oscillators with a magnitude determined by the coupling rate, μ. This coupled harmonic oscillator system is represented as,

$$\frac{d}{dt}\phi(t) = [j\omega_{LSPR} - (\gamma_r + \gamma_t + \gamma_{nr})]\phi(t) + \kappa_1 s_{1+} + j\sum \mu_i P_i \quad 4.1$$

$$\frac{d}{dt}P_i(t) = [j\omega_v^i - \gamma_v^i]P_i(t) + j\mu_i\phi(t) \quad 4.2$$

Where, in equation 4.1, $|\phi(t)|^2$ is the energy stored in LSPR resonator, ω_{LSPR} is LSPR frequency of the resonator, γ_r is the energy loss rate in reflection, γ_t is the energy loss rate in transmission, γ_{nr} is non-radiative energy loss rate, κ_1 is the coupling coefficient to incoming light s_{1+}, and μ_i is the coupling coefficient to *i*th vibration resonance, P_i. In equation 4.2, $|P_i(t)|^2$is the energy stored in the *i*th vibration resonance, ω_v^i and γ_v^i are the central frequency and linewidth of *i*th vibrational resonance, respectively.

The energy balance between incoming and outgoing waves is represented by,

$$s_- = Cs_+ + K\phi(t) \quad 4.3$$

where *C* is the non-resonant scattering matrix and *K* is $[(2\gamma_r)^{\frac{1}{2}}\ (2\gamma_t)^{\frac{1}{2}}\ ]^T$.

These equations can then be simplified (For the detailed mathematical derivation, see section S6 in SI) to derive transmission and reflection intensity as,

$$T(\omega) = \left| t_D - \left\{ \frac{\sqrt{4\gamma_r\gamma_t}}{j(\omega - \omega_{LSPR} - \sum\omega_\mu^i) - (\gamma_{tot} + \sum\gamma_\mu^i)} e^{j\theta} \right\} \right|^2 \quad 4.4$$

$$R(\omega) = \left| r_1 - \left\{ \frac{2\gamma_r}{j(\omega - \omega_{LSPR} - \sum\omega_\mu^i) - (\gamma_{tot} + \sum\gamma_\mu^i)} e^{j\theta_1} \right\} \right|^2 \quad 4.5$$

where, t_D and r_1 are non-resonant transmission and reflection, γ_{tot} is the net plasmon loss which equals $\gamma_r + \gamma_t + \gamma_{nr}$, θ is transmission phase, θ_1 is reflection phase, γ_μ^i and ω_μ^i expressed as

$$\omega_{\mu}^{i} = \frac{\mu^2(\omega - \omega_v^i)}{[(\omega - \omega_v^i)^2 + (\gamma_v^i)^2]} \quad 4.6$$

$$\gamma_{\mu}^{i} = \frac{\mu^2 \gamma_v^i}{[(\omega - \omega_v^i)^2 + (\gamma_v^i)^2]} \quad 4.7$$

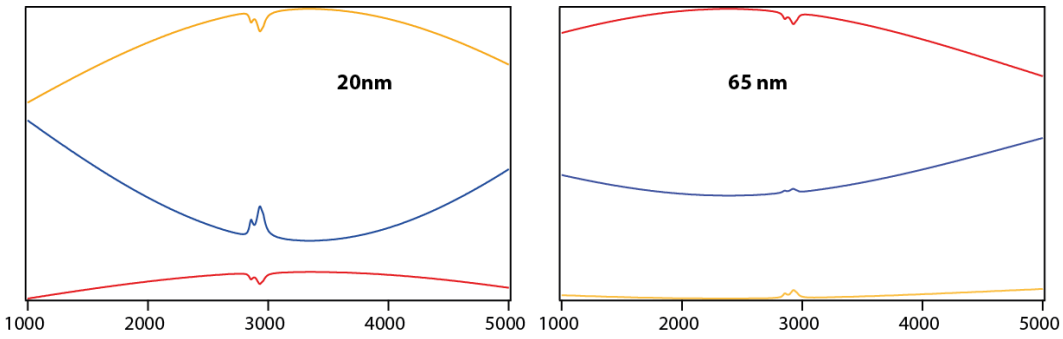

Figure 4.25 TCMT size dependence. Using the electric field enhancement and decay rates from the modeling, TCMT qualitatively predicts the size dependence following the trends seen from computational and experimental results. Theoretical reflection (red), absorption (yellow) and transmission (blue) spectra show the dependence of lineshape of molecular vibrations on the size of the nanocrystals.

Applying TCMT (Equation 4.4, 4.5 and Figure 4.25), the lineshapes of the vibrational signal in reflection, transmission and absorption spectra agree between our experimental and modeling results. Derived Reflection and Transmission equations (Equation 4.4 and 4.5), were used to deconvolute the effect of various contributing factors such as plasmon resonance energy decay rates in reflection (γ_r), transmission (γ_t) and absorption (γ_{nr}) as well as LSPR frequency and coupling constant (μ), in determining the lineshape of the coupled vibrational signals. The sensitivity of the coupled vibrational signal lineshape to each of the factors was determined by changing one parameter at a time while keeping all others fixed. Our results show that as we increase γ_t, the coupled vibration signal intensity increases with no change in the lineshape of either the reflection or transmission spectrum (Figure 4.26). Similar behavior was observed when only ω_{LSPR} (Figure 4.27) or μ (Figure 4.28) were changed. These

trends suggest that the change in vibrational lineshape with increasing NC size is due to the synergistic effects of simultaneous changes in decay rates ($\gamma_r, \gamma_a,$ and γ_t). To verify this hypothesis, the impact of simultaneous changes in relative decay rates γ_r/γ_t and γ_a/γ_t while keeping other parameters such as ω_{LSPR} and NFE fixed was examined. This prediction was done for 20 nm and 65 nm NC films, where the differences in decay rates were maximized. The results of this theoretical prediction reproduced the similar coupling lineshapes as observed in experiments with some difference in signal intensity (Figure 4.29). This conclusively shows that the vibrational lineshapes are governed by the plasmon decay dynamics. The relative decay rates γ_r/γ_t and γ_a/γ_t determine the Fano lineshapes of coupled vibrational-LSPR spectra and vibrational signal intensity is determined by several factors such as ω_{LSPR}, NFE, and ligand volume fraction. Our experimental observations, unraveled by both simulations and TCMT, indicate that for semi-transparent metal oxide NC films, coupling between the LSPR and molecular vibrations depends not only on the NFE; it also depends on the relative far field resonance decay rates in reflection, transmission and absorption spectrum. For applications such as SEIRA, sensing, or catalysis, where it is crucial to maximize the interaction between the LSPR and the vibrational resonance, thinking of the system as a whole is crucial. Not only the NC properties matter, but how they are arranged impacts the coupling interactions achievable in the system. Since size and shape impact self-assembly in NC systems changing one must account for how they impact the final coupled NC spectral properties, which can be strongly dependent on the assembled mesoscale structure.

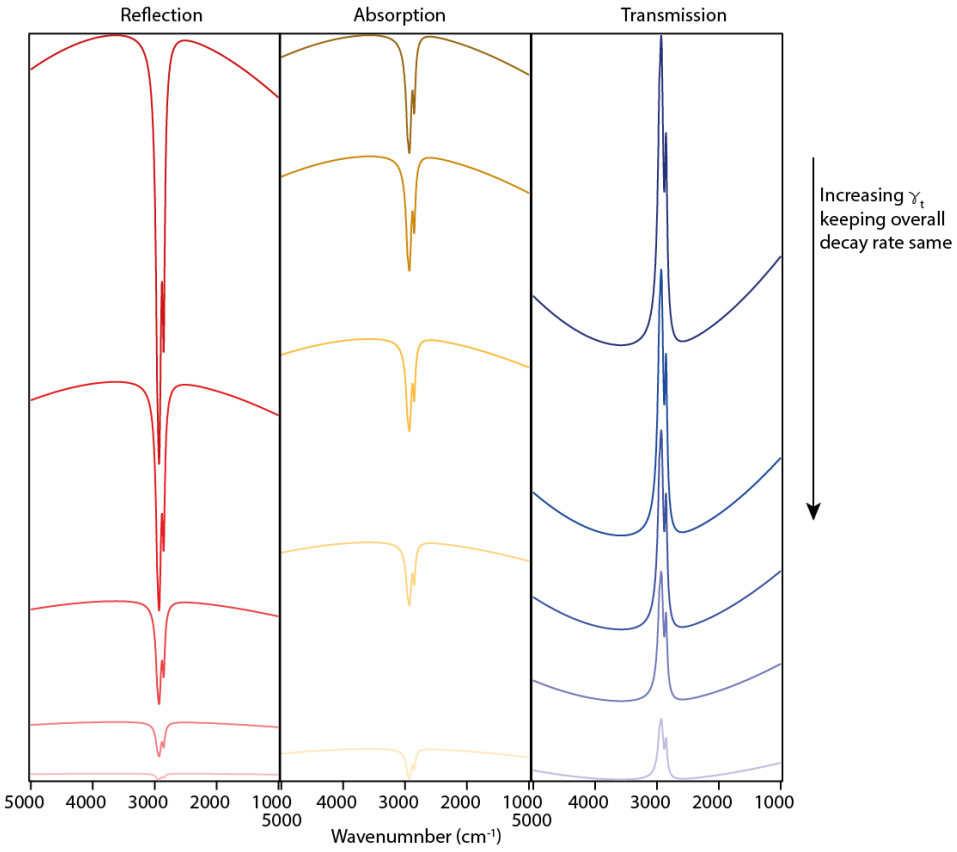

Figure 4.26 Transmission decay rate parametric study. Keeping total decay rate and relative decay rate in reflection and transmission as well as all other coupling variables constant and the same as those from simulation of a 20 nm NC periodic film, changes in transmission decay rate do not change the lineshape of molecular vibrations over the LSPR resonance in any of the reflection, transmission, or absorption spectra. Changes in transmission decay rate do change the intensity of the vibrational signal.

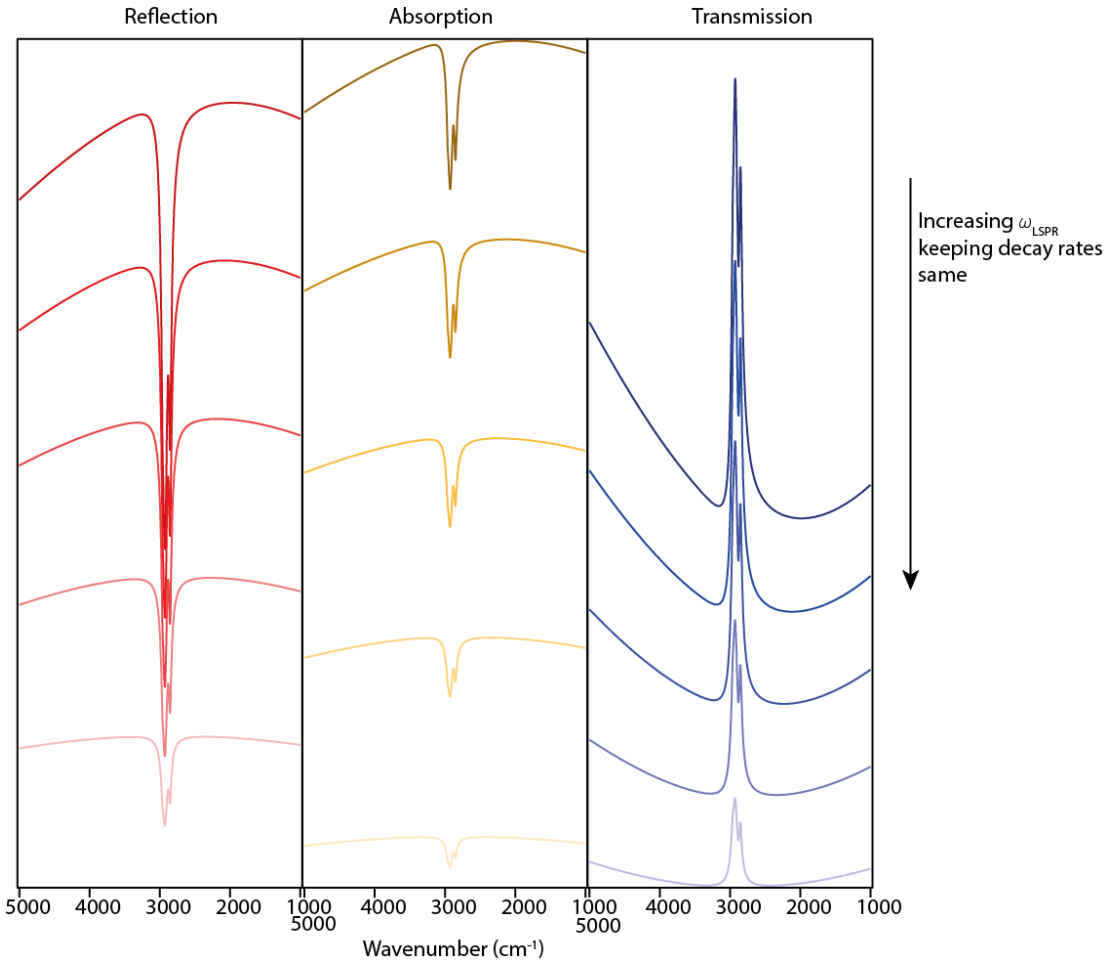

Figure 4.27 LSPR frequency parametric study. Keeping all the decay rates and other coupling variables constant and the same as those from the simulation of a 20 nm NC periodic film, changes in LSPR frequency also do not change the lineshape of molecular vibrations over the plasmon resonance in any of the reflection, transmission, or absorption spectra. Change in LSPR frequency do change the intensity of the vibrational signal.

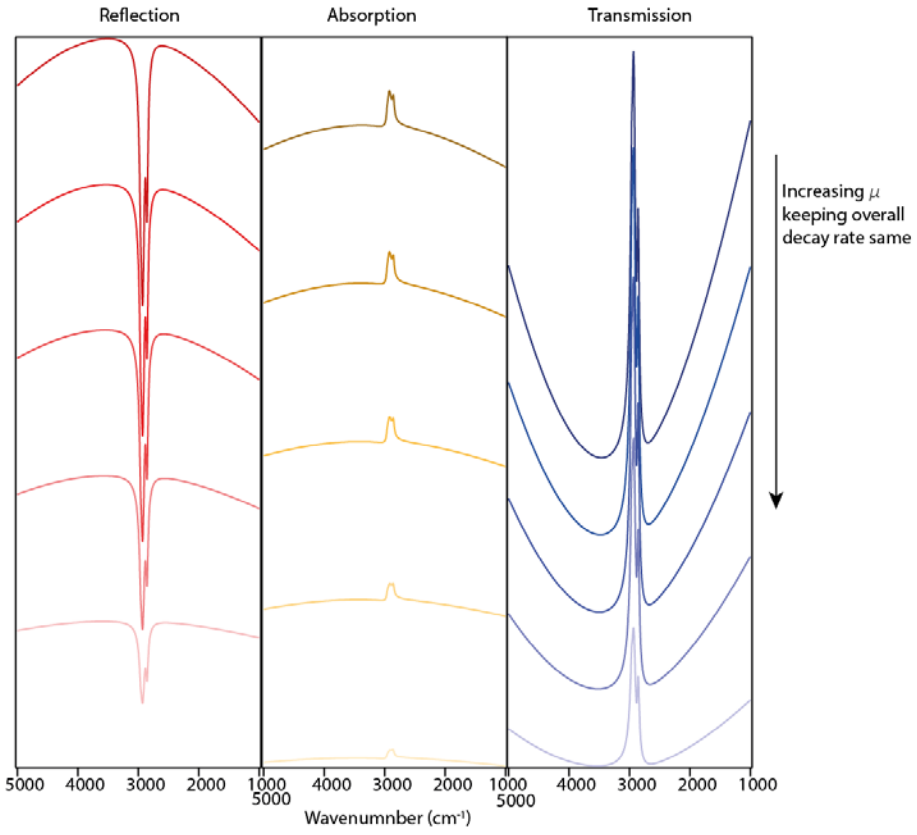

Figure 4.28 Electric field enhancement parametric study. Keeping all decay rates and LSPR frequency constant and the same as those from simulation of a 65 nm NC periodic film, changes in electric field enhancement (equivalently coupling strength, μ) changes the intensity of vibrational signal. Similar trend was also observed for 20nm NC periodic film.

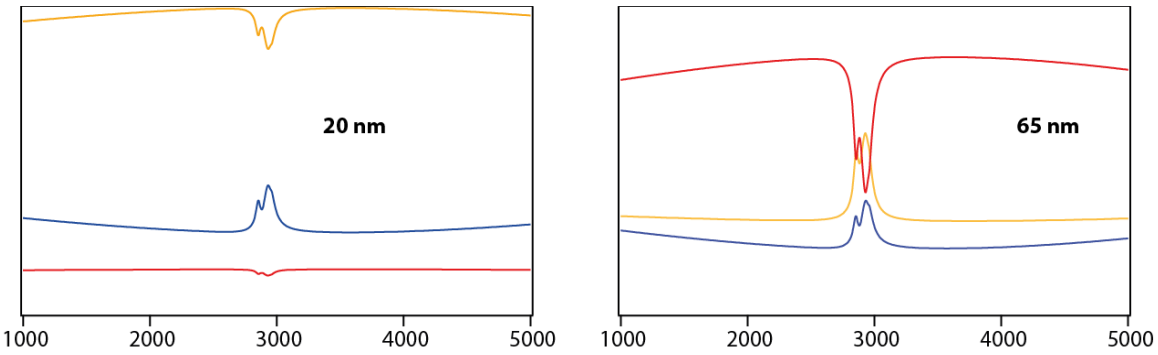

Figure 4.29 Simultaneous decay rate dictates the coupled signature lineshape. Using the decay rates obtained from simulation for 20 nm and 65 nm NC films, and keeping all the other parameters the same as those for the 20 nm case, molecular vibration lineshape remains the same as the case in Figure 4.24. The only change here is in the intensity of the molecular vibration signal in the left figure, due to the higher spatially averaged electric field enhancement in the 20 nm case.

4.4 Conclusion

In conclusion, we discerned the nature of coupling between molecular vibrational modes of the native ligands and metal oxide plasmonic NCs. This was achieved by using colloidially synthesized F-Sn co-doped In_2O_3 cubic NCs of variable size (20-110 nm), which enabled efficient localization of electric fields around the NCs due to low ionized impurity scattering. This study highlights that an innovative synthetic strategy such as co-doping can substantially improve the quality factor of metal oxide NCs, providing a favorable alternative to metallic systems. Using EELS, we experimentally mapped the fundamental geometrical LSPR modes in single NCs as well as in small NC clusters, which were previously hypothesized to exist in computational studies. Exploiting the promising NFE properties, these materials were employed to demonstrate and understand the nature of plasmon-molecular vibration coupling for metal oxide systems. Specifically, we investigated the coupling between C-H stretches of native oleate ligands and NC films

and showed that the Fano lineshape is highly dependent upon the optical decay rates of available pathways, i.e., reflection, transmission and absorption. This finding is contrary to the popular belief that NFE and optical detuning are the sole factors governing the coupling signature of the interaction between an LSPR and molecular vibrations. Furthermore, the computational model and theoretical TCMT as applied to metal oxide systems developed in this work could be easily extended to other material systems and will facilitate the study of metal oxides in greater depth. Although this study showcases the promise of metal oxide systems for coupling applications, it does not take into account the potential effects of dopant distribution, dopant activation and molecular vibration orientation relative to the NC surface on the coupling between NC LSPR and molecular vibrations. However, future studies addressing the aforementioned effects will be improvements upon the foundational work presented here that may be already of relevance to potential applications ranging from catalysis, SEIRA, and integrated optoelectronics. We hope that this study will motivate researchers to investigate metal oxide systems towards developing electrically, or photo(chemically) tunable substrates for various mid-IR optical applications.

Chapter 5

Impacts of Surface Depletion on the Plasmonic Properties of Doped Semiconductor Nanocrystals

5.1 Introduction

Degenerately doped semiconductor nanocrystals (NCs) display unique localized surface plasmon resonance (LSPR) properties, where unlike metals, the carrier density is tunable by several orders of magnitude ($10E^{18}$–$10E^{21}$)[15,208,230]. Such flexibility over carrier concentrations allows the LSPR frequency (ω_{LSPR}) to be varied broadly in the visible to mid-IR spectral window. Tunability of ω_{LSPR} in semiconductor NCs originates from changing band structure parameter such as band gap (E_G) and Fermi level (E_F) by introducing ionizable defects such as oxygen vacancies[38,86] and aliovalent dopants[16,19,244,246], redox and photochemical charging[90,270], or electrochemical modulation[28,78,113,229] in NC films. Such LSPR properties have been leveraged for numerous applications such as in smart windows[49,113,271], optoelectronics[45,272], sensing[97], and catalysis[273].

The LSPR is semiconductor NCs is commonly treated as Drude response of free carriers as in metals[34,71,274]. The underlying assumption behind such treatment is that once the semiconductor is degenerately doped, the effects of the band structure modifications on the LSPR properties are minimal. Even though, this is a reasonable assumption for expressing the optical property such as the dielectric function of bulk material, near-surface properties of semiconductors are greatly modified due to the presence of surface defects, surface trap states, and interaction with surface ligands. It has been demonstrated that presence of surface traps changes the optical transitions such as exciton and interband transitions for applications such as photo-luminescence and two-photon conversion[275–277]. Native surface states or an externally applied potential pins Fermi level

at the surface potential leading to the formation of the depletion or accumulation layer near the surface of the NC[278,279]. Surface depletion or accumulation results in spatial gradient in carrier concentration, leading to spatially changing dielectric function. Such behavior and its effect on plasmonic property has been studied in semiconductor thin films such as Sn:In_2O_3 (ITO) but not been analyzed in NC system[280]. In NCs, due to high surface to volume ratio, influence of surface perturbation on LSPR property is expected to be much more severe.

Colloidally synthesized NCs such as Sn:In_2O_3[244], CuTe[281], or CuS[213] are some of the many semiconductor systems that have been studied for LSPR based application such as sensing[282], catalysis[273], surface enhanced infrared absorption spectroscopy (SEIRA)[8], or smart windows[113]. Efficacy of a NC for applications such as smart window or photodoping, where the dynamic LSPR modulation is achieved by electrochemically or photochemically changing the E_F, will greatly be affected by extend of surface depletion as a function of nanocrystal size and doping level. Contradictory reports in literature on dynamic modulation using metal oxide NCs, thus, either offer a qualitative description of LSPR frequency modulation based on Drude model[28,47,51], ignoring any depletion affects, or oversimplify the consequence of depletion on LSPR property to explain subtle changes observed in the ω_{LSPR}[78,109]. Similarly, for applications such as sensing, with semiconductor NC, much lower sensitivity compared to expected value is often reported [283]. Presence of a depletion layer on the surface is expected to reduce the sensitivity of NC plasmon to the changes in surrounding, but this effect is often ignored while analyzing such systems. Surface depletion also strongly impacts carrier dynamics in NC-based transparent conductors by imposing a potential barrier at NC-NC interface[284].

In this work, we have thoroughly investigated the effect of NCs surface depletion on the plasmonic property of doped semiconductor NCs by systematically changing the

extent of band bending ($V_{bb} = E_F - E_{app}$) through electrochemical charging/discharging of NC films and in situ monitoring of the LSPR modulation. For this purpose, ITO, a well-studied plasmonic NCs system, was chosen as a model system for the following reasons. First, the chemistry of ITO synthesis is relatively well established which enabled us to systematically vary the doping level and size of the NCs. Second, ITO is a technologically relevant material for applications such as opto-electronics[45], smart windows[28,52], and sensing[8,282]. Additionally, metal oxide NCs are well known to possess surface defects states due to the presence of surface hydroxyl groups that define the Fermi level at the surface[78,280]. Using a combination of in situ FTIR spectroelectrochemistry (FTIR SEC), solvent dielectric sensitivity, and computational modeling of electron distribution and LSPR modulation, we were able to establish a systematic relationship between the V_{bb} and the LSPR modulation behavior. We find that by varying the size and doping level of the ITO NCs the LSPR modulation can be clearly explained by the formation of depletion layer on the NC surfaces. Electrochemical charging of a partially depleted NC thus does not increase the carrier concentration as the injected electrons are consumed to charge the depleted layer resulting in a net increase in the LSPR intensity but no ω_{LSPR} shift. Further, we demonstrate, for first time in a plasmonic semiconductor system, that the NC plasmon sensitivity tracks the depletion width, being least sensitive to the surrounding for largely depleted NCs. These finding reconciles the previous literature contradiction regarding the LSPR modulation and establishes a general ground to rationally design efficient plasmonic NCs for near-field enhancement, electrochromic, catalysis, and transport applications.

5.2 Methods

5.2.1 Synthesis Protocol

Sn-doped In2O3 nanocrystals (NCs) were synthesized using a slow injection method (slow growth) recently reported by the Hutchison group99. Briefly, a desired composition of In(ac)3 and Sn(ac)4 were dissolved in 7.5 mL of oleic acid at 150 °C for 2h. In another flask 13 mL of oleyl alcohol was heated to 290 °C under a gentle flow of N2. A desired volume of metal oleate solution was slowly injected to the oleyl alcohol bath using an automated syringe pump at the rate of 0.2 mL/min. Three needles (packed with a piece Kimwipes paper) were inserted in one of the rubber stoppers as gas outlet. Upon injection, the alcohol bath turned light green-bluish color with the color intensity depended on the dopant level. After injection, the reaction was hold at 290 °C for 20 min before quenching to room temperature. The NCs were washed multiple times using hexane/ethanol solvent/anti-solvents and finally dispersed in hexane for further use.

The NCs nominal doping level was adjusted by varying the Sn/In ratio in the precursor solution while the NC size was controlled by varying the injection volume. Typically 1 mL injection volume resulted in NCs of about 6-7 nm while for larger NCs (~13-14 nm) 4 mL injection was required. The size of the NCs were analyzed from the TEM images. XRD spectra were collected for ITO NCs using a Rigako Miniflex 600 with a Cu K alpha radiation source

5.2.2 Device Film preparation

Uniform thin films of ITO NCs were deposited on commercial glass/ITO (50nm) for in situ measurements as well as on Si chips for characterization using a spin-coating method. For spin-coating substrates was submerged with an adequate volume of NCs dispersion in hexane/octane (1:1 V/V) and spun at 2000 rpm for 1 min, followed by 3000

rpm for 30 s. The NCs assembly were further ligand exchanged with formic acid driven by mass action; films were immersed in 0.1 M formic acid in MeCN for 30 min followed by rising multiple times with a mixture of 1:1 MeCN/CHCl3. At the next step, the formic acid ligands were removed by annealing the films at 120 °C for 20 min in a tube furnace under 50 sccm flow of Ar.

5.2.3 Device assembly

The NCs films were assembled in an in situ FTIR spectroelectrochemistry (SEC) device for spectroelectrochemical measurements. The devices were composed of a working electrode (the ITO NCs film) and a counter electrode consisted of a glass/ITO substrate coated with Pt nanoclusters. Pt clusters, which served to increase the capacitance of the working electrode, were deposited by drop-casting Platisol (Solaronix) on the substrates followed by heating in air at 350 °C for 20 min. Electrodes were fused together using a thermoforming Surlyn film (60 μm, Solaronix). A 1.0 cm2 hole in the Surlyn spacer provided a compartment which was further filled with electrolyte (1.5 M tetramethylammonium bis(trifluoromethanesulfonyl)imide (TBATFSI) in tetraglyme). A photograph of the final device is shown in Figure 5.1.

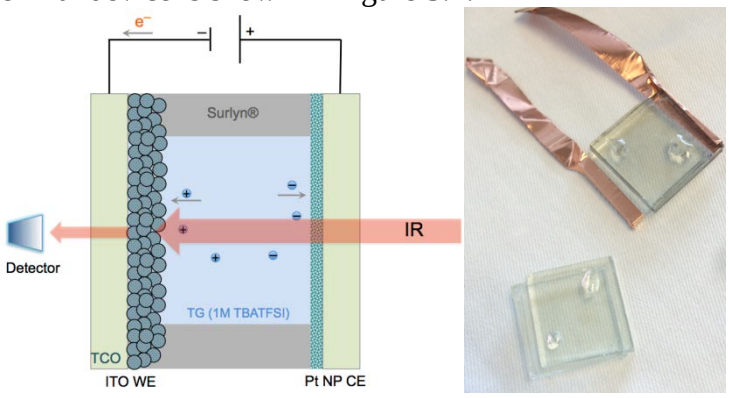

Figure 5.1 Schematic design and a photograph of the in situ FTIR SEC device.

5.2.4 Electrochemistry

Electrochemical measurement were made using a S200 Biologic potentiostat. Three cycles of cyclic voltammetry (CV) were run before the in situ FTIR measurements. Capacitive CV profiles indicated the high capacitance of the working and counter electrodes (Figure 5.2a).

5.2.5 FTIR Spectroscopy

Optical spectra were measured using a Bruker Vertex 70 FTIR. For the in situ FTIR SEC, the device were attached to a holder with an aperture of ~ 1.1 cm2. The device was titled to a 20 ° angle in order to avoid the internal refection patterns from reaching the detector. A typical in situ FTIR spectrum was acquired by backgrounding the detector versus ambient air, then applying a constant potential for 3 min before recording the spectra. A series of sample spectra (raw in situ FTIR SEC data) are shown in Figure 5.2b

Solution FTIR spectra for sensitivity analysis were recorded suing a thin layer liquid cell attachment. Background spectra were collected using the blank solvents before the NCs dispersion spectral acquisition.

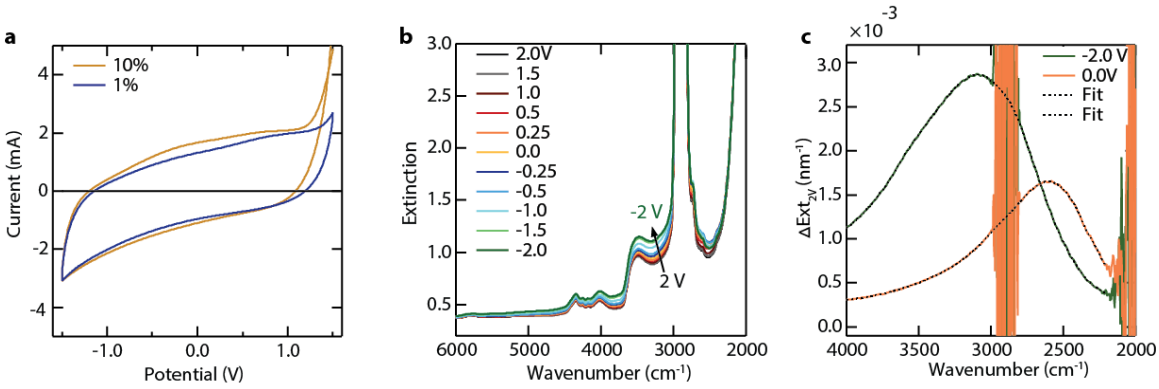

Figure 5.2 **Electrochemical device operation** a) CV curves of ITO NC films scanned at 20 mV/min. b) A series of in situ FTIR spectra for 1% doped-6nm NCs collected at the indicated potentials. For further analysis, the individual spectra were corrected versus that at 2V (the oxidized state). Two representative spectra overlapped with the fit curves are shown in (c).

5.2.6 Experimental Data Analysis

The in situ FTIR SEC spectra were further analyzed by correcting for the background and extracting the peak positions and absorption intensity. The spectra were first corrected for that recorded at 2 V. At 2 V the LSPR of the NC is largely bleached providing a reliable and reproducible background correction procedure. Using this method, absorption at 2 V is thus zero, and as the potential is stepped negatively a net LSPR absorption appears that is due to injected electrons (Figure 5.2c).

In order to extract the LSPR peak positions, the data were fit using a smoothing function from which the peak positions were extracted. Sample fits are shown in Figure 5.2c.

5.2.7 Poisson's Equation

Poisson's equation was solved numerically over the spherical nanocrystals under the assumption of uniform dopant concentration and surface potential, ES, using finite element method.

The charge density at any point inside the nanocrystal is made up of mobile electrons, holes and immobile ionized impurity centers.

Here, we have shown the potentials used to solve the Poisson's equation (Figure S8). EF is the Fermi energy level, ECB is the conduction band minima, EVB is the valence band maxima, EI is the reference potential and center of the band gap.

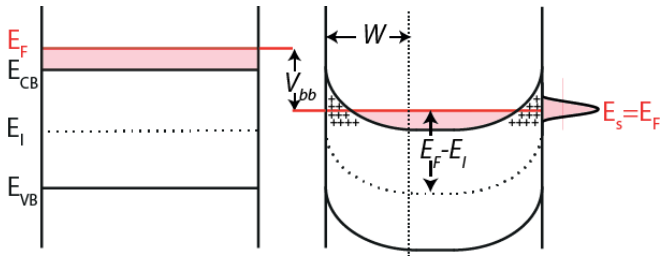

Figure 5.3 **Band structure and band bending**. The band energetics of a NC under flat band, and band bending conditions where E_S represents the surface states potential, E_I is the reference potential, V_{bb} is the band bending potential, and E_{CB} and E_{VB} are the conduction band edge and valence band edge potentials, respectively.

Here, we adapted the dimensionless form of Poisson's equation derived by Seiwatz and Green[285] to solve numerically for spherical nanoparticle in Cartesian coordinates as,

$$\nabla^2 u = -\frac{e^2 \rho}{\varepsilon \varepsilon_0 kT} \qquad 5.1$$

The non-dimensional potential is defined as, $u = \frac{E_F - E_I}{kT}$, and k is the Boltzmann constant and T is temperature. ε_0 is the vacuum permittivity, ε is the static dielectric constant, and ρ is the charge density.

$$\rho = \left\{ \rho_D - \rho_A + p - n \right\} \qquad 5.2$$

where, ρ_D is the donor dopant density, ρ_A is the acceptor dopant density, p is hole density, n is electron density. Here, since we only have aliovalent donor dopants, $\rho_A = 0$

Free electron concentration in the parabolic conduction band is equal to,

$$n = 4\pi\left[\frac{2m_e kT}{h^2}\right]^{\frac{3}{2}}\left[F_{\frac{1}{2}}\left(u - w_{c,l}\right)\right], \qquad 5.3$$

where $F_{\frac{1}{2}}\left(\eta\right) = \int_0^\infty \frac{x^{\frac{1}{2}}dx}{1+\exp(x-\eta)}, w_{c,l} = \frac{E_{CB} - E_l}{kT}$

Similarly, hole concentration in the parabolic valence band is equal to

$$p = 4\pi\left[\frac{2m_h kT}{h^2}\right]^{\frac{3}{2}}\left[F_{\frac{1}{2}}\left(w_{v,l} - u\right)\right], \text{ where } w_{v,l} = \frac{E_{VB} - E_l}{kT} \qquad 5.4$$

If the donor energy level is E_D, activated dopant concentration could be expressed as,

$$\rho_D = \frac{N_D}{1+2\exp\left(u - w_{D,l}\right)} \text{ where } w_{D,l} = \frac{E_D - E_l}{kT} \qquad 5.5$$

Substituting all the individual term into Equation 5.1

$$\nabla^2 u = -\frac{e^2}{\varepsilon\varepsilon_0 kT}\left\{\frac{N_D}{1+2\exp\left(u - w_{D,l}\right)} + 4\pi\left[\frac{2m_h kT}{h^2}\right]^{\frac{3}{2}}\left[F_{\frac{1}{2}}\left(w_{v,l} - u\right)\right] - 4\pi\left[\frac{2m_e kT}{h^2}\right]^{\frac{3}{2}}\left[F_{\frac{1}{2}}\left(u - w_{c,l}\right)\right]\right\} \qquad 5.6$$

with the boundary condition,

$$u = u_{surf} = \frac{E_{surf} - E_l}{kT} \qquad 5.7$$

Poisson's equation (Equation 5.6) was solved in COMSOL using finite element scheme. Mesh and geometry of the control volume is demonstrated in Figure 5.4,

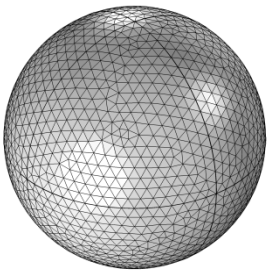

Figure 5.4 Geometery for numerical Poisson's equation solution. Meshed geometry of the spherical nanocrystal of variable radius, R. Poisson's equation was solved over this control volume using finite element method in COMSOL

5.2.8 Effective Nanocrystal Dielectric Function

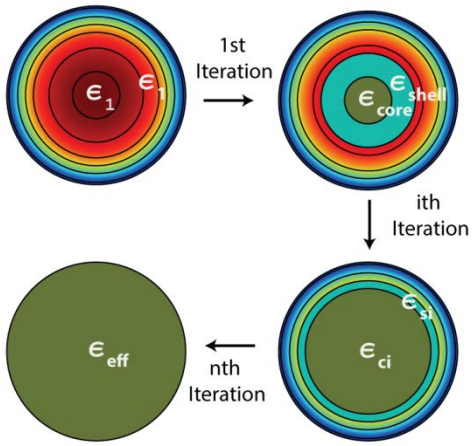

Figure 5.5 Schematic shows the iterative procedure to obtain and effective dielectric function of a depleted NC.

Here, we have developed a method to derive effective nanocrystal dielectric function. This involves applying the Maxwell-Garnet effective medium theory[286], iteratively to a finely discretized sphere into a core and multi-shell configuration (Figure S10). The detailed algorithm to obtain effective dielectric function developed in this work is listed in Appendix 3.

5.2.9 Effective film dielectric and device optical modeling

Sandwich cell designed in-house for in-situ spectroelectrochemistry was modeled using commercial SCOUT software (www.wtheiss.com) by employing several built-in optical models, including, T-matrix method to calculate extinction spectrum, Drude model to express the dielectric function of ITO thin film on glass substrate. To model the device, the steps taken are explained in detail in Appendix 4.

5.2.10 NC Plasmon Sensitivity Analysis- Experiments

Sensitivity of LSPR of ITO NCs to the changes in refractive index of the surrounding medium was measured by collecting extinction spectra of NCs dispersed in several solvent such as hexane, toluene, chloroform, and tetrachloroethylene. FTIR Spectra were collected using a Bruker Vertex 70 FTIR. Solution ensemble measurements were performed using a FTIR liquid cell with a 0.25 mm path length. LSPR peak position was extracted by fitting the spectra to sum of several Lorentian functions. As per LSPR condition from Mie theory, and substituting dielectric value using Drude function, we obtain, $\lambda_{LSPR}^2 = Sn^2$ where, λ_{LSPR} is the peak LSPR wavelength, n is the refractive index of the surrounding, and S is the sensitivity factor. This relation suggests that the slope of the curve λ_{LSPR}^2 vs. n^2 would give us the sensitivity factor. Following this equation, we plotted λ_{LSPR}^2 vs. n^2 for NC with different doping level and size and obtained the sensitivity factor for each one of them.

5.2.11 NC Plasmon Sensitivity Analysis- Model

In order to model the theoretical sensitivity of the depleted NC, we used the effective dielectric function of the nanocrystal to predict the absorption of the NC using Mie theory (Equation 5.8)

$$C_{abs}(\omega) = 4\pi R^2 (k(\epsilon_H)^{1/2} R) \mathrm{Im}\left\{ \frac{\epsilon_p(\omega) - \epsilon_H}{\epsilon_p(\omega) + 2\epsilon_H} \right\} \quad 5.8$$

Absorption profile was simulated for refractive indices varying from 1.3 and 1.6, and using these profiles, LSPR peak position was estimated as function of refractive index for various NCs. To extract the sensitivity of the NC, same procedure was followed as in experiment using theoretical LSPR peak position.

5.2.12 Near-field Enhancement.

Using the concentration profile obtained from Poisson's equation (here, we choose 1.4 eV as the surface potential), spatially varying dielectric function was derived using the Drude model. Spherical NCs surrounded by a sphere representing the surrounding medium (i.e. air (n=1)). This whole system was then surrounded by a perfect index matching layer which prevented unwanted reflections from the outside boundary. The maximum and minimum mesh size in the nanocrystal was set to 4 and 0.01 nm, respectively. This ensures fine meshing, yielding typically 2 million degrees of freedom, which corresponds to 3 – 15 GB of RAM when using the direct PARDISO or MUMPS solver. Maxwell equation were solved in scattered field formulation with the background electric field propagating along Z-axis and polarized along X-axis.

5.3 Results

Surface depletion (Figure 5.3) in semiconductors is determined by the difference between NC Fermi level and surface states energy (Vbb $= E_F - E_S$), dopant density, and shape and size of the NCs. Strong control over the NC geometry, size, and doping level is thus crucial to make reliable quantitative assessment of the effect of surface depletion on the LSPR. The first objective was thus to reproducibly synthesize monodisperse ITO NCs with various sizes and doping levels. This was achieved by adapting a slow growth

method recently developed by the Hutchison group[99]. By varying the injection volume and the relative ratio of In and Sn precursors, a series of highly monodisperse NCs with variable size (6-14 nm) and doping level (1-10% Sn) were synthesized (Figure 5.6) All the diffraction peaks can be indexed to the reference diffraction of bixbyite In_2O_3 crystal structure (PDF# 06-0416) (Figure 5.7). The optical extinction spectra (Figure 5.8) of five representative spherical NCs of diameter around ~14 nm demonstrate that LSPR blue shift with increasing dopant density (1-10%). Fitting of extinction spectrum with the Mie theory based of the dielectric function expressed using the Drude Model reveals that carrier concentration in the representative samples varies in between 3.48E20 and 1.12E21 cm^{-3}.

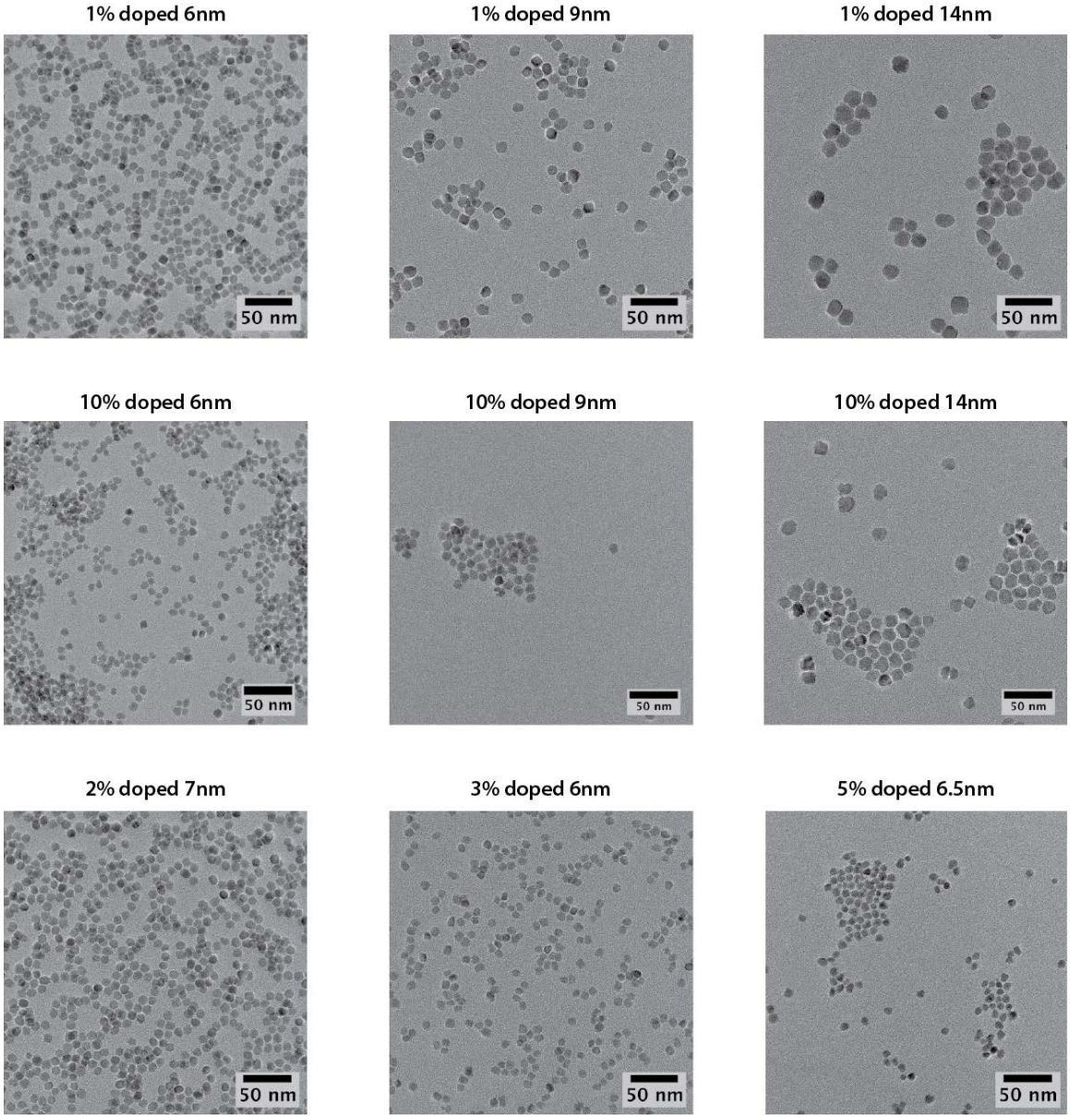

Figure 5.6 TEM images of ITO NCs

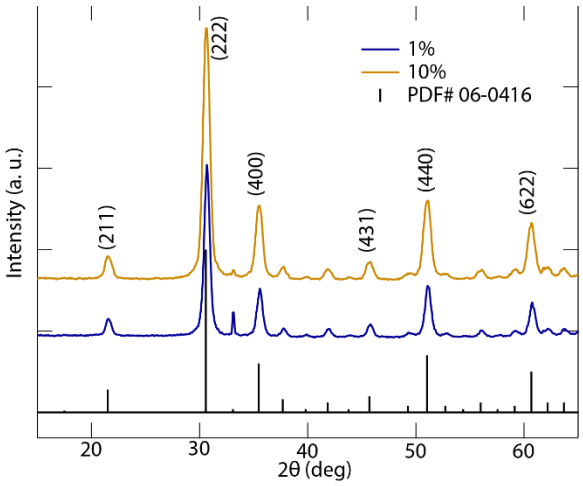

Figure 5.7 XRD spectra of 1 and 10% doped ITO NCs.

To study the role of applied potential on LSPR property, uniform thin film of NCs was spin coated from NCs dispersion on conductive ITO-coated glass substrate and assembled in a custom-made multi-layer sandwich cell for in situ FTIR SEC measurements (see the methods and Figure S3-S4). A novel design of the in-situ electrochemical cell allowed us to monitor FTIR spectra as a function of applied potential in mid-IR by minimizing the electrolyte and contacting electrodes absorption.

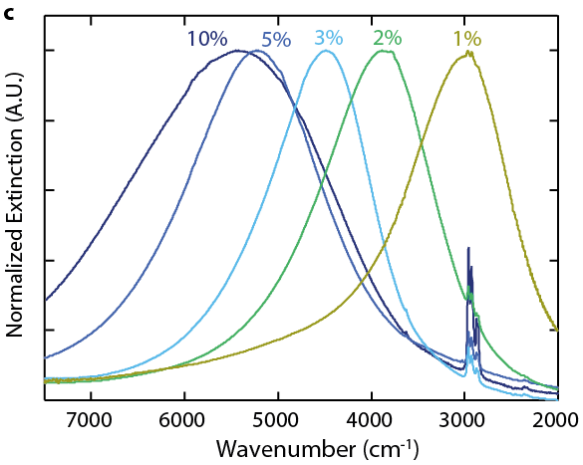

Figure 5.8 LSPR in Semiconductor NCs LSPR extinction spectra of ITO NCs with nominal doping levels ranging from 1-10% (dispersed in tetrachloroethylene).

Introducing a larger concentration of dopant in semiconductors results in significant band gap and band edge modification[287,288]. The interaction among free carriers and with ionized impurities give rise to a downward shift of the conduction band edge (E_{CB}) and an upward shift of the valence band edge (E_{VB}), resulting in a net band gap narrowing effect. The optical band gap, on the other hand, increases due to filling of the conduction band states as the E_F is raised (Burstein-Moss shift). Here, net result of two competing mechanism is summarized for the cases of low and highly doped ITO NCs (Figure 5.9a)[288]. As we elucidate below, LSPR dependence on surface potential (surface states, redox couple, or applied potential) would strongly depend on the dopant density, which determines the E_F thus the magnitude of V_{bb} (i.e. E_F–E_S) (Figure 5.9a). Downward shift of the E_{CB} thus causes a smaller V_{bb} compared to what it would have otherwise been if the E_{CB} were unchanged with doping. Therefore, the LSPR is expected to be less sensitive to changes in applied potential (i.e. varying the V_{bb}).

The in situ LSPR modulation spectra of NCs with two extreme size (6 and 14) and doping levels (nominally 1 and 10%) in response to applied potential are shown in

Figure 5.9b-e. The LSPR spectra were recorded after applying a constant potential step for 3 min to insure a steady state carrier concentration throughout the NCs assembly. Strong modulation of the LSPR extinction intensity, resulting from capacitive charging/discharging of the NCs, was observed in all cases irrespective of NCs size or dopant level. This behavior is consistent with previous studies on electrochemical modulation and is analogues to photochemical redox charging of doped metal oxide NCs[47,51,289]. Unlike the extinction intensity, the ω_{LSPR} modulation exhibited significant differences for different doping levels and NC sizes. In the case of 1% doped-6 nm NCs (Figure 5.9b) increase in the LSPR extinction is accompanied by a significant blue shift of ω_{LSPR} ($\Delta\omega$ = 704 cm^{-1}). In contrast, with 10% doped-6 nm NCs (Figure 5.9d), ω_{LSPR} shift was significantly smaller ($\Delta\omega$ = 331 cm^{-1}). Moreover, extent of modulation was not only dependent on the NCs dopant concentration but also on the size of the NCs; $\Delta\omega$ decreased to 424 and 226 cm^{-1} for 14 nm NCs-1 and 10% doped, respectively (Figure 5.9c, e). These trends can, at best, only be qualitatively explained with the hypothesis of uniform increase in carrier concentration through out the NC upon application of reducing potential. Further, no size-dependency of the LSPR is expected as the NCs sizes are much smaller than the wavelength of incident light. These observations and inconsistencies in understanding of modulation based of the prior works, motivated us to explore the effect of surface depletion on LSPR modulation in greater detail. For different NC dopant concentration and sizes, we numerically solved Poisson's equation as a function of applied surface potential (E_{app}) to evaluate radial band profile. Poisson's equation was solved in spherical coordinates under parabolic band assumption[285]. For a given surface potential, the depletion width (W) is expected to decrease with increasing dopant density and size of the NCs. Solution to Poisson's equations shows that at the most oxidizing E_{app} (0.8 eV) W, in the case of 1% doped NCs (Figure 5.9b-ii and 5.9c-ii),

is around 4 nm which decreases to less than 1 nm for 10% doped NCs (Figure 5.9d-ii and 5.9e-ii). *W* extends to the majority of the NC volume for low doped and small NCs. In contrast, for the high doped case, for all NC sizes (6 nm-14 nm), it is limited to less than 1 nm of the surface.

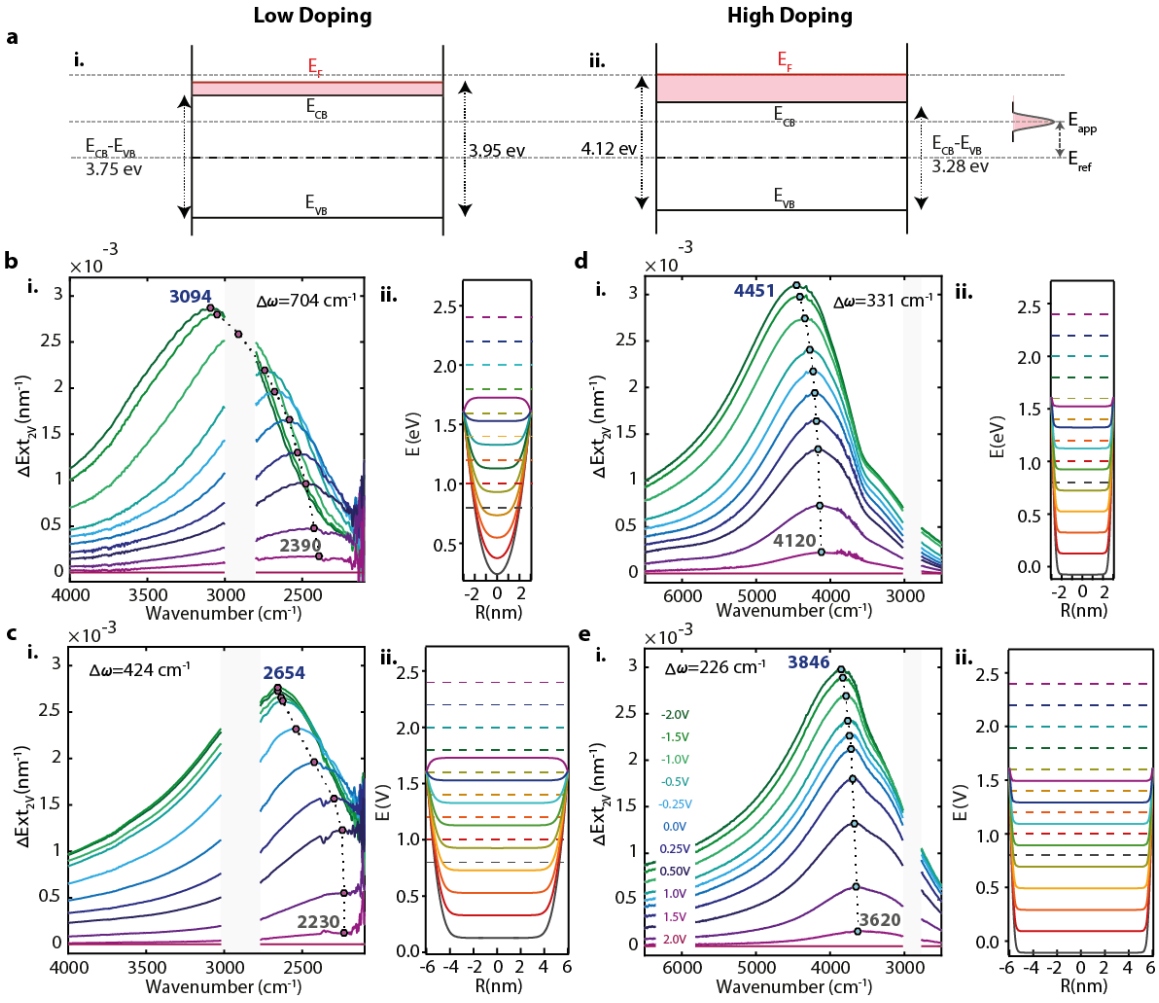

Figure 5.9

Figure 5.9 **Electrochemical LSPR Modulation.** a) Band energetics of low and highly doped NC showing the band gap narrowing and Burstein-Moss effects. b-e) In situ FTIR SEC spectra of a film of NCs collected at various applied potentials (i) along with corresponding calculated conduction band profiles (ii) for 1%-6 nm (b), 1%-14 nm (c), 10%-6 nm (d), and 10%-14 nm (e) ITO NCs. Overlapped with the LSPR spectra are the peak positions extracted from fitting the individual spectra. $\Delta\omega$ represents the maximum LSPR peak modulation going from +1.5 to -2 V. Electrochemical LSPR modulation was performed by charging the NC films via applying a more reducing potential (E_{app}) relative to the reference potential (E_{ref}). Note that E_{ref}, in the case of experimental result, is the counter electrode potential (i.e. Pt) and in the case of modeled results was taken as the mid point of the band gap where E_{ref}=0.

Applying more reducing potential decreases the *W*, which is depending upon the size and doping level of the NC. For low doped-6 nm NCs, reducing potential initially results in charging the entire NC and once the *W* is less than the radius of the NC it only increases the volume of un-depleted core. Carrier concentration profile based of Poission's equation band profile solution (Figure 5.10b-i), displays this two regime in charging of 1% doped-6 nm NC. Substantial change in carrier concentration through out the nanocrystal as a function of E_{app} explains the large observed shift in LSPR for these nanocrystals. For larger size (14 nm), where depletion thickness is already smaller than the radius, charging of such nanocrystal lies entirely in the second regime where the volume of the un-depleted core increases (Figure 5.9c). This effectively means that there is no change in carrier concentration within the un-depleted core, but it is accompanied with the substantial increase of 87.5% volume of un-depleted core and progressing towards accumulation regime at most reducing potential. Therefore, ω_{LSPR} shift for 14 nm NC is lower than 6 nm NCs, due to a smaller change in carrier concentration. The observed blue shift for 14 nm NCs is, in part, due to reduction of refractive index in the depleted layer as potential is shifted negatively.

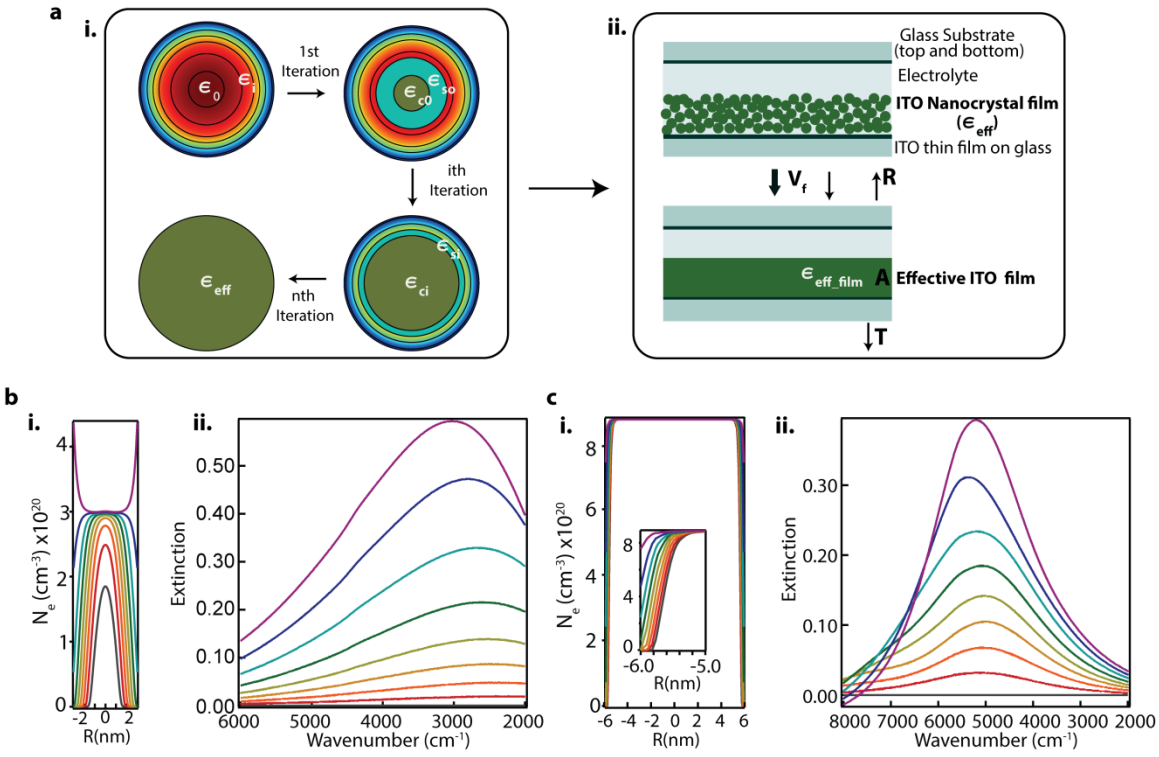

Figure 5.10 Optical Modeling of Electrochemical LSPR Modulation. a) Schematic iterative procedure used to obtain the effective dielectric function of a depleted ITO NC (i) and modeled sandwich cell configuration where ITO NCs with effective dielectric function, ε_{eff} is coated on the top of ITO thin film-coated glass substrate (ii). To model the ITO NC film optical properties, effective dielectric function of the film was calculated using Maxwell-Garnett equation. b,c) Calculated carrier concentration profiles (i.) and corresponding LSPR spectra (ii.) for 1% doped-6 nm (b) and 10% doped-12 nm (c) ITO NC films.

On the other extreme, is 10% doped NCs (Figure 5.9d and e). The *W* in the case of these highly doped NCs is less than 1 nm. The majority of the NC volume is thus remaining un-depleted at any E_{app}. As the nanocrystal is charged, the injected electrons are consumed to compensate for the depletion layer resulting in no net increase in the electron concentration. The relative volume change of un-depleted core is ~ 70 % and 42 % for 6 nm and 12 nm NCs, respectively (Figure 5.10d, e). Again small shift in the ω_{LSPR}

is attributed to the dielectric change in the depletion layer upon charging. The case of high doping is a more general picture of the behavior observed by zum Flelde *et al.*[78] for Sb: SnO_2 NCs under electrochemical charging.

To establish the direct correlation between the calculated carrier concentration profile and the optical property, we developed a multi-scale model to study optical properties of the individual NCs and that in the sandwich device. The multi-scale optical model allowed us to directly relate the expected optical modulation in the sandwich device, similar to our experimental design, to the applied potential. Optical property of the depleted nanocrystal with radial carrier concentration gradient was modeled using an effective medium theory (Figure 5.10a). Effective dielectric function of a NC (ϵ_{eff}), was calculated using iterative core-shell effective medium method. Using the ϵ_{eff} as the dielectric function of the NC, which is packed randomly in a thin film, ϵ_{eff_film} was calculated. The transmission and the reflection spectra were then calculated using T matrix method employing SCOUT optical package[274] (www.wthesis.com). Notably, the extent of LSPR modulations and $\Delta\omega_{LSPR}$ for these NCs in the modeled spectra (Figure 5.10) are in excellent agreement with observed experimental values. The consistency between the experiential and modeling results observed for various sizes and doping concentrations is indeed owing to excellent control over NCs size and morphology, and careful in situ FITR SEC analysis. Furthermore, this supports our hypothesis of surface depletion playing the crucial role in determining the LSPR property and modulation of NC film.

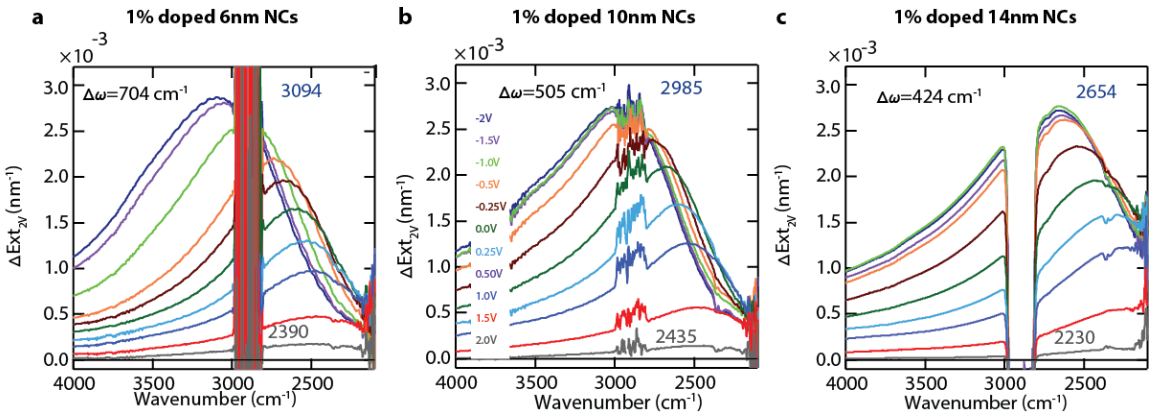

Figure 5.11 Electrochemical LSPR modulation spectra of 1% doped NCs. The peak positions at most oxidized (1.5 V) and reduced (-2 V) states are labeled.

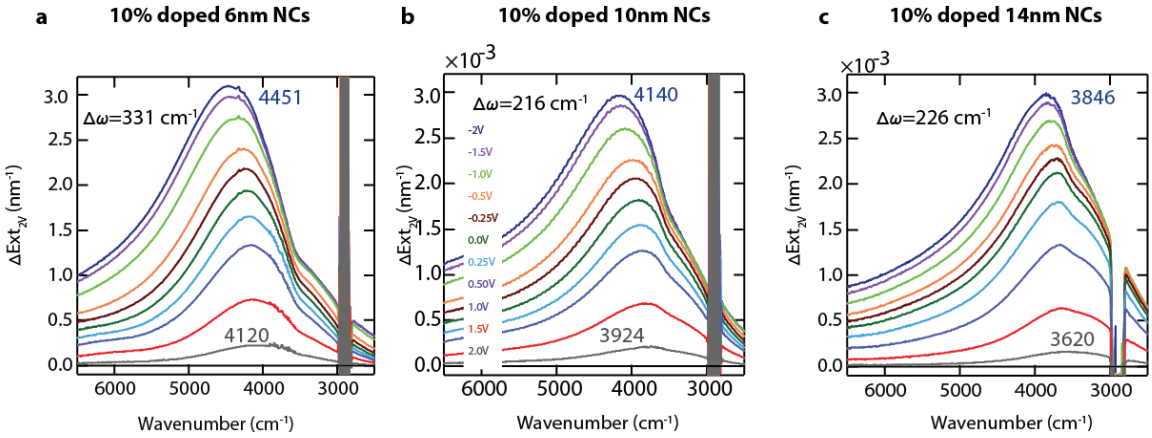

Figure 5.12 Electrochemical LSPR modulation spectra of 10% doped NCs. The peak positions at most oxidized (1.5 V) and reduced (-2 V) states are labeled.

Expanding on our discussion on the depletion layer in NCs and its dependence on size and dopant density, we systematically varied doping level and size. Systematic variation in LSPR modulation is expected as function of size and doping level, both of which would reduce the extent of *W* relative to the radius of the NC. In order to probe the

size effect, three sizes of NCs for two extreme doping levels (1 and 10%) were prepared and their in situ FTIR SEC spectra were measured. Change in LSPR peak frequency ($\Delta\omega_{LSPR}$) at different potentials versus that at 1.5 V (oxidized state) is shown in Figure 5.11-5.13. It can be clearly seen that 1% NCs overall show a larger blue shift in ω_{LSPR}, of which the 6 nm NCs exhibit the highest $\Delta\omega_{LSPR}$ of 704 cm^{-1}. As the NCs size increase, the depletion width decreases, resulting in the milder shift as elucidated before. Likewise, for the 10% NCs the largest $\Delta\omega_{LSPR}$ is observed for the 6 nm NCs. However, there is a minimal difference between 10 and 14 nm NCs, due to very small difference in *W*. To test the effect of the dopant concentration for a given size (6 nm), a series of NCs with various doping densities ranging from 1-10% were prepared. The *W*, thus the extent carrier concentration modulation within the depletion layer, decreases exponentially with increasing dopant concentration. This would lead to a systematic reduction in $\Delta\omega_{LSPR}$ as the NC dopant density increases (Figure 5.13b and Figure 5.14).

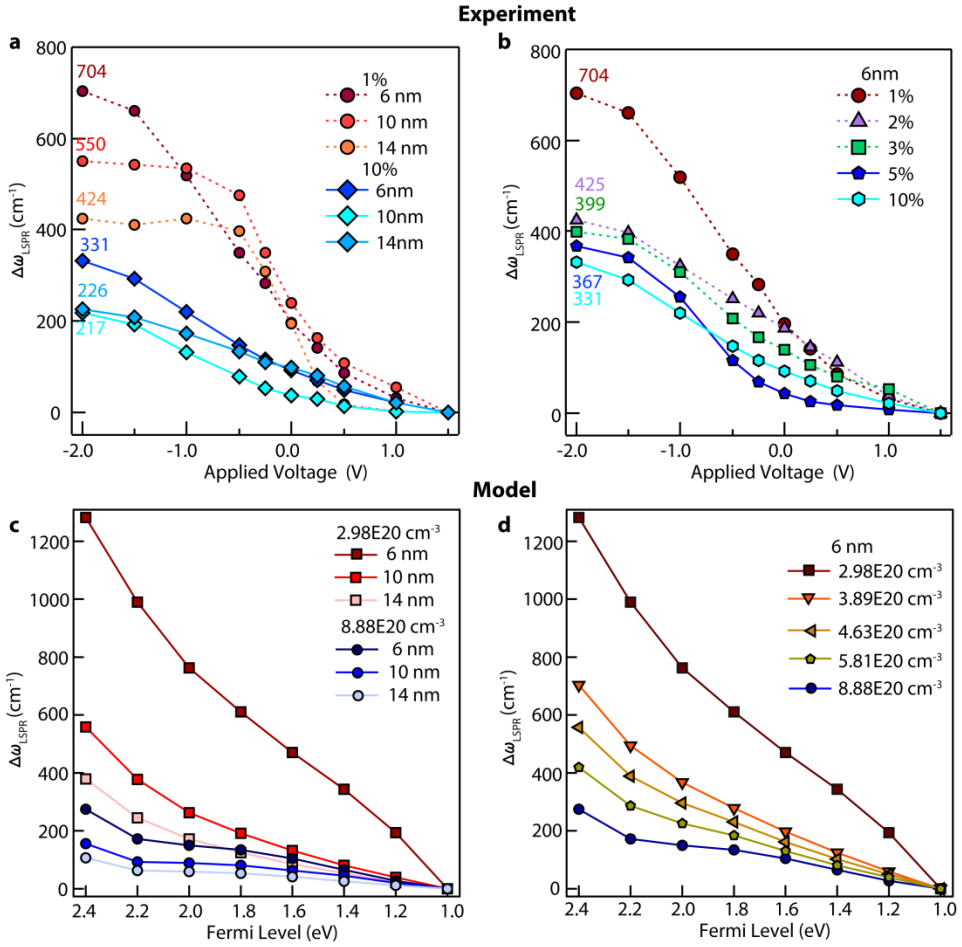

Figure 5.13 Effect of NC Size and Doping Concentration on Electrochemical LSPR modulation. LSPR peak frequency ($\Delta\omega_{LSPR}$) at different potentials versus that at 1.5 V for ITO NCs with different sizes (a) and doping concentrations (b). Modeled size and doping effects on the $\Delta\omega_{LSPR}$ of an insolated NC. Modeled shift in isolated NC, de-convoluted off the film coupling effects shows greater modulation compared to the corresponding film modulation. Modeled film data, full LSPR spectra and the details of the modeling are provided in the SI.

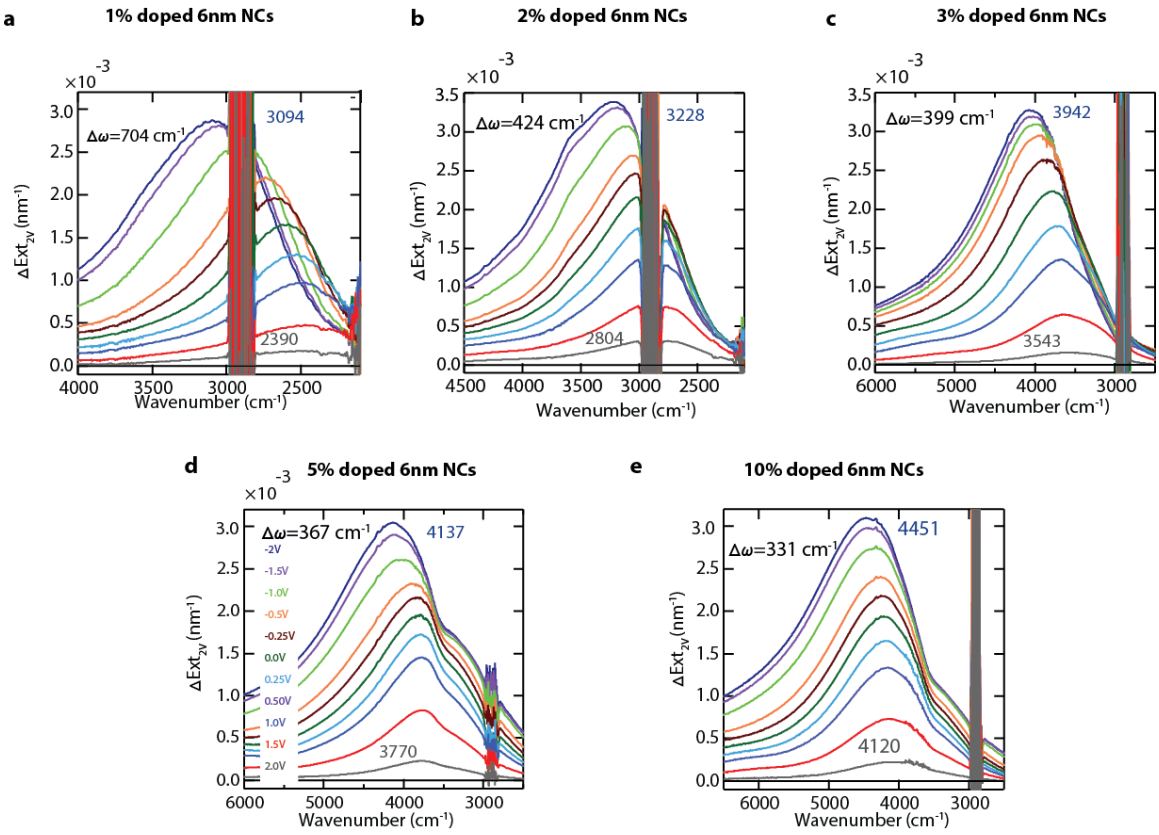

Figure 5.14 Electrochemical LSPR modulation spectra of ITO NCs with various doping levels. The peak positions at most oxidized (1.5 V) and reduced (-2 V) states are labeled.

Corresponding to these NCs, LSPR modulation spectra with comparable sizes and doping level were modeled using the method explained in the previous section. We note that the LSPR modulation behavior slightly changes going from freestanding to assembled NCs. NC-NC coupling in the film, as well as the convoluted substrate affects, complicates the direct interpretation of the experimental result on single NC scale. But one to one correspondence between the modeling and experiment in our work, allows us to study the optical modulation on single NC scale. For all sizes and doping levels, modulation at single NC scale seems to be larger than that of assembled film (Figure 5.13c,d and Figure 5.14-5.17). It also shows us the origin of absolute intensity

modulation in the experimental data. For low doping, LSPR intensity of the depleted (oxidized) NCs is very low which increases higher to higher values with reducing potential (Figure 5.14). In contrast, for high doped NCs, even the oxidized NCs retain substantial LSPR characteristic due to the presence of significant undeleted core (Figure 5.15). Single NC optical spectra clearly show case that the effect of depletion is maximum for small sized low doping level NCs which decreases with the increasing dopant concentration and size of the NC (Figure 5.17).

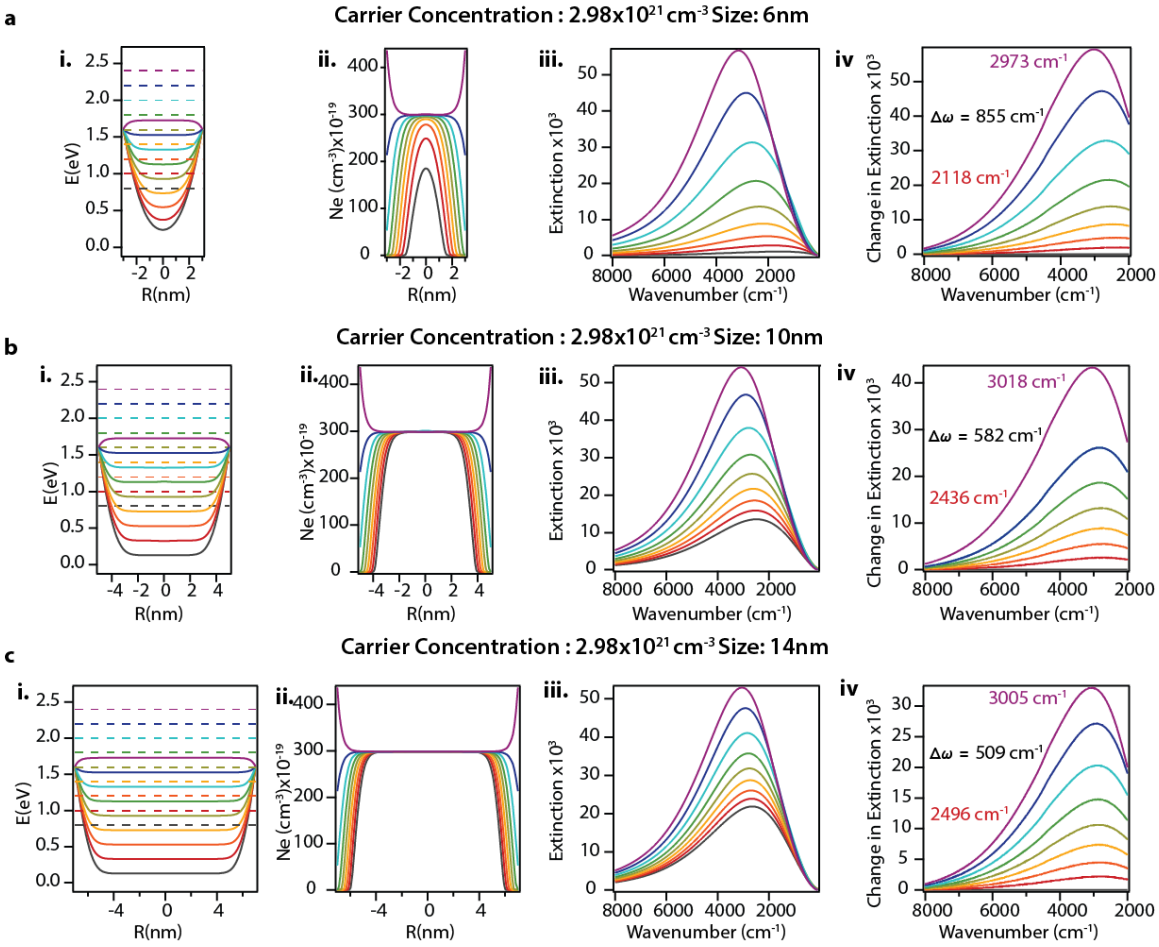

Figure 5.15 Size effect on LSPR modulation for low-doped NCs was modeled in three step. First, Poisson's equation was solved for band bending profile (i) and carrier concentration profile (ii). Radial carrier concentration profile corresponding to different surface potential was used to model the absorption spectra of single NC (iii). Taking into account the film and device effects, optical modeling of single NCs was extend to optical device (iv). Shift was maximum for low doped NCs as it is evident in carrier concentration profile, there is substantial change in carrier concentration in the core for small NCs and in the shell for the larger one.

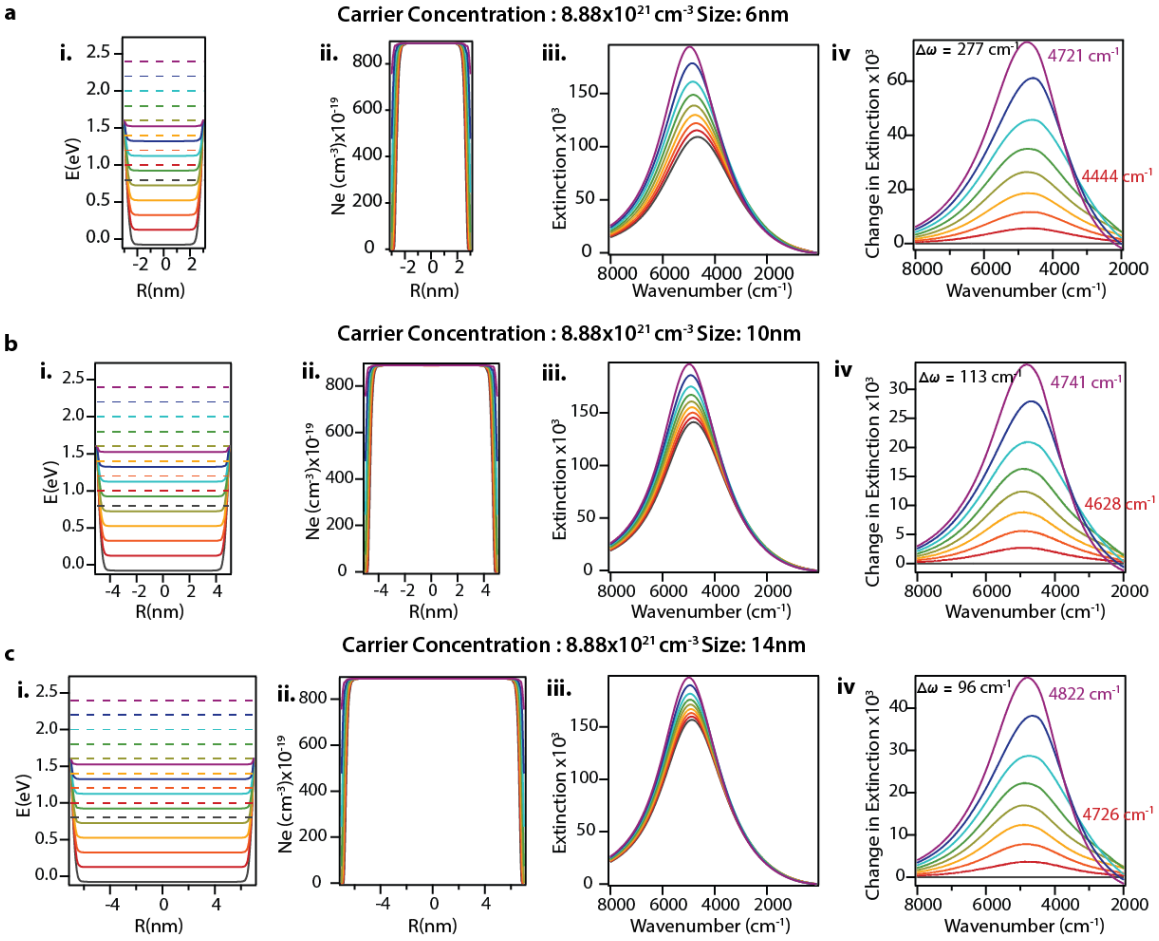

Figure 5.16 Size effect on LSPR modulation for high-doped NCs was modeled in three step. Similar procedure as described for low doped was followed for this system as well. Shift is relatively small for high doped NCs as it is evident in carrier concentration profile, the charging is limited within 1 nm of the surface of the NCs.

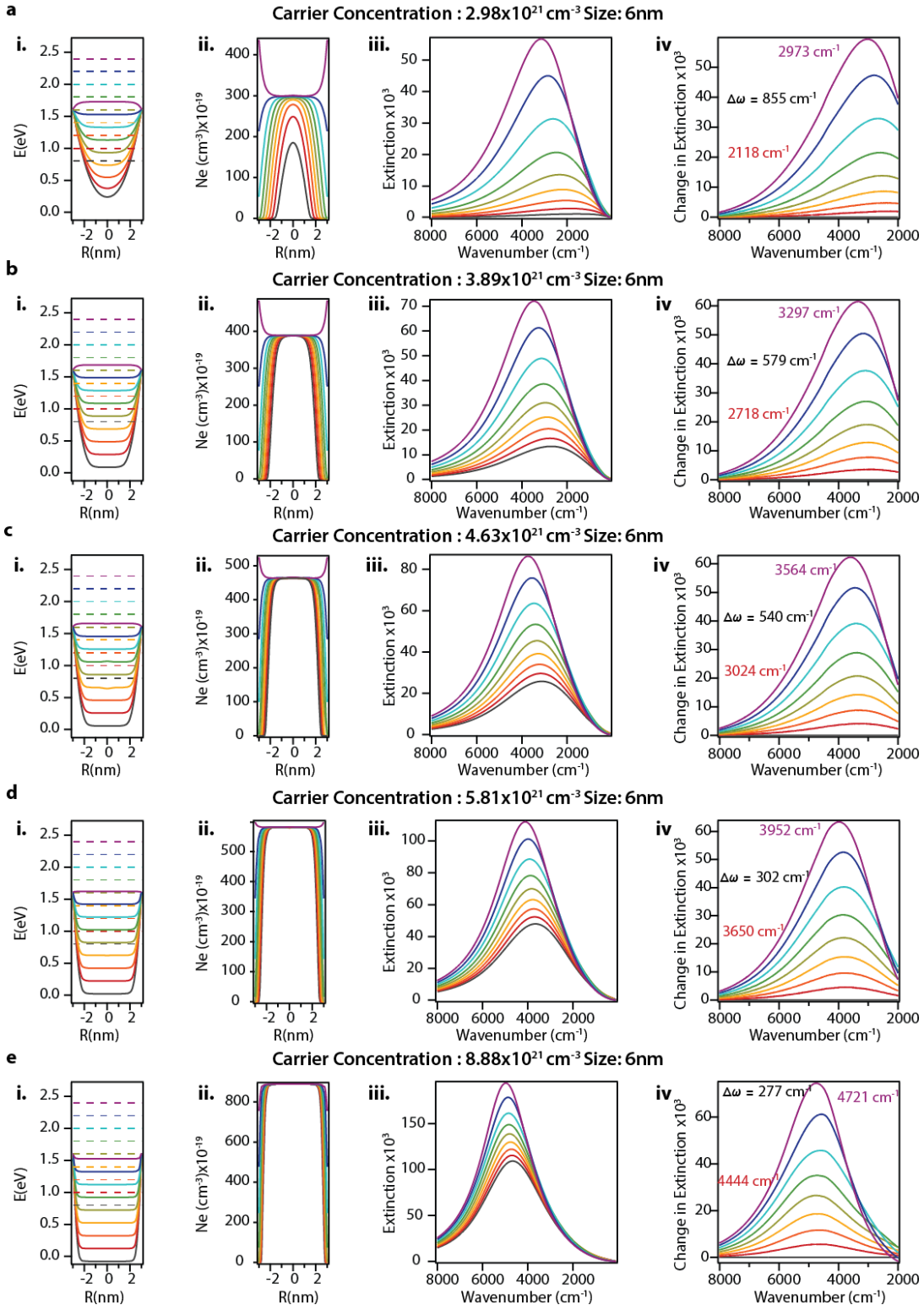
a
Carrier Concentration : 2.98x10^21 cm^-3 Size: 6nm
b
Carrier Concentration : 3.89x10^21 cm^-3 Size: 6nm
c
Carrier Concentration : 4.63x10^21 cm^-3 Size: 6nm
d
Carrier Concentration : 5.81x10^21 cm^-3 Size: 6nm
e
Carrier Concentration : 8.88x10^21 cm^-3 Size: 6nm
i.
ii.
iii.
iv
E(eV)
R(nm)
Ne (cm^-3)x10^-19
Extinction x10^3
Change in Extinction x10^3
Wavenumber (cm^-1)
2973 cm^-1
Δω = 855 cm^-1
2118 cm^-1
3297 cm^-1
Δω = 579 cm^-1
2718 cm^-1
3564 cm^-1
Δω = 540 cm^-1
3024 cm^-1
3952 cm^-1
Δω = 302 cm^-1
3650 cm^-1
Δω = 277 cm^-1
4721 cm^-1
4444 cm^-1

Figure 5.17

Figure 5.17 Doping concentration effect on LSPR modulation for 6 nm NCs. Similar procedure as described for low and high doped NCs was followed here as well. LSPR shift decreases with increasing doping concentration. From the concentration profile as function of applied surface potential, it can be seen that for low doping concentration there is substantial change in carrier concentration through out the NC, but as the doping level increases, charging is mainly limited to the NC surface layer.

A depleted surface could be imagined as a shell of a high dielectric constant, creating barrier between the active plasmonic core and the surrounding thus reducing the sensitivity of LSPR to changes in medium dielectric. This phenomenon is well-characterized in ligand capped or core-shell metallic systems[97,290,291] .The sensitivity of a NC LSPR to the surrounding refractive index unit (RIU) is defined as $(\lambda_{LSPR}/RIU)^2$ [26]. In order to evaluate NC plasmon sensitivity, NCs with various sizes and doping concentrations were dispersed in solvents with refractive indices ranging from 1.3-1.54. From the relationship (Equation 5.9) of the ω_{LSPR} versus refractive index, the sensitivity values were extracted and are plotted in Figure 5.17a for two different sizes and doping levels of 1-10%. The blue stars with connecting dashed line show the ideal case for a given carrier concentration which was calculated assuming no depletion. The experimental sensitivity data are less for all the doping levels, which is attributed to effect of surface depletion. As discussed above, the extent of depletion layer is higher for smaller NC and lower doping levels. Therefore, larger sensitivity deviation from the ideal case is expected for the smaller lightly doped NCs. Moreover, for low dopant concentration, there is maximum difference in surface depletion profile for different sizes; as expected this is mirrored in the sensitivity factor (Figure 5.17a) where the highest deviation from the ideal case is seen for 1%-6 nm. As the carrier concentration increase, this deviation and the size effect reduces reaching its minimum at 10% where the *W* is minimum. This behavior nicely tracks the trend of depletion width, and corroborates the LSPR modulation results discussed above. These results were further confirmed by calculating plasmon sensitivity for NCs of different size and carrier concentrations considering the depletion effect. The results shown in Figure 5.17b show systematic size and doping effects on the plasmon sensitivity, in excellent agreement with the experimental observations.

Ability to localize electric field at nanoscale is a unique attribute of the plasmonic NCs[37]. Here, we calculated the near-field enhancement for 1% doped- 6nm and 14nm NCs. 1% doping level was chosen as it shows the highest modulation, strong size dependence and greatest deviation from ideal sensitivity. Using the radial profile of dielectric function calculated based on carrier concentration obtained from Poisson's equation, we numerically solved for electric field using finite element method. It is clearly evident that presence of depletion layer reduces the near field enhancement (Figure 5.17c) further supporting our earlier deduction of reduced sensitivity to surrounding for such NC. Near field enhancement in the surrounding was maximum and size-invariant for an ideal case un-depleted NCs, which decreases to some degree for 14 nm NC with a thin 2 nm surface depletion layer and decreases substantially for 6nm NC due to depletion of NC to the core of the NC. Also, presence of size dependent relative depletion layer, breaks the size invariance, and induces interesting near field localization character within the depleted layer. This aspect of this study need further investigation and is a subject of our current in-depth investigation.

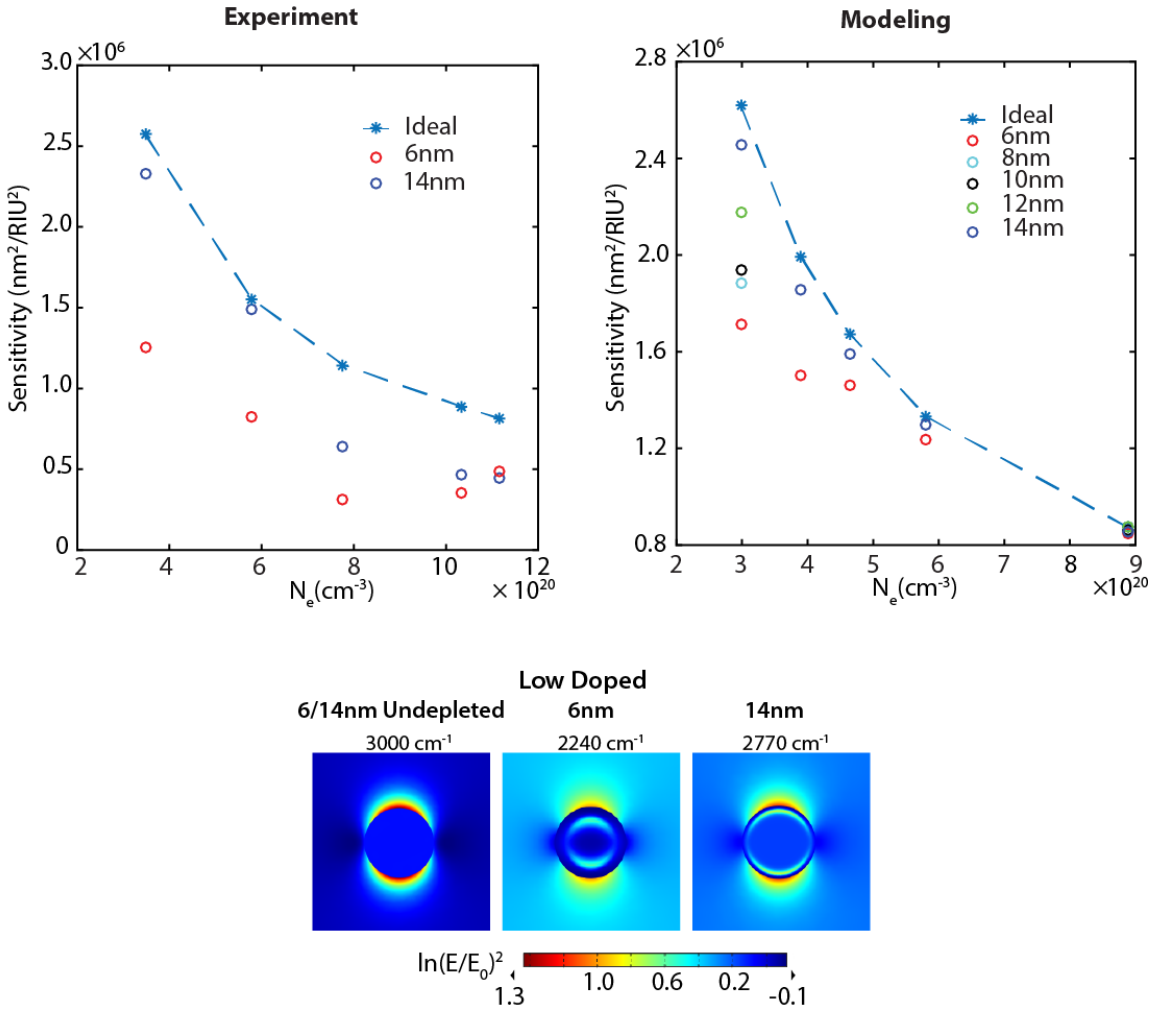

Figure 5.18 NC plasmon Sensitivity. a) Plasmon sensitivity of small and large ITO NCs with nominal doping concentrations ranging from 1-10%. The blue stars indicate the ideal case with the highest sensitivity. The NCs sensitivity factor is calculated based of the LSPR peak position in solvent with refractive indices ranging form 1.30-1.54. b) Calculated plasmon sensitivity for ITO NCs with various sizes and dopant concentrations. c) Calculated near-field enhancement maps of a spherical 1% doped ITO NC showing the effect of surface depletion. NFE is maximum for undepleted ideal NCs, which decreases for 6nm and 14 nm depleted NC. NFE decreases substantially for 6nm NC as the depletion extends to the core of the NC.

5.4 Conclusion

In conclusion, the corroborating experimental and modeling results highlight the impact of surface depletion on the plasmonic properties of doped semiconductor NCs. Here, the Fermi level was adjusted by applying a constant potential to a film of NCs. This allowed us to systematically vary the band bending (V_{bb}) and monitor its effect on electron distribution and thus the LSPR behavior. In the absence of the applied external potential (NCs dispersion or assembly) the Fermi level is defined by the surface redox potential (intrinsic surface states or a deliberately added redox couple). Regardless of their nature, surface states energetically located below the Fermi level induce a depletion layer at the NC surface Surface depletion and associated band bending potential in NCs strongly impacts their application in sensing, electro-optics, and transparent conductors.

Strong dependence of LSPR modulation, sensitivity to the surrounding, and near-field enhancement on size and doping concentration of the NCs, highlights the importance of rational choice of the NCs for a given application. For smart window application[28,113], where the maximum LSPR frequency modulation is desirable, low doped and small sized NCs are preferable. In contrast, for application such as photon upconversion[44], SEIRA[8] and sensing[291], where efficacy of the process depends on LSPR coupling to other optical processes present in the vicinity of the NC, surface depletion need to be minimized. Furthermore, the ability to modulate the sensitivity, near field enhancement, and LSPR frequency as a function of surface potential, hold a great promise for range of applications such as electro-optical modulator as well as tunable SEIRA and sensing substrate.

Appendices

Appendix A: Derivation of the Sensitivity Factor of plasmon peak to carrier concentration

The dielectric function of the material can be expressed using Drude-Lorentz model as:

$$\varepsilon_p(\omega) = \varepsilon_\infty - \frac{{\omega_p}^2}{\omega^2 + i\gamma\omega} \quad \text{A1.1}$$

Where ε_p is the frequency-dependent dielectric function, ε_∞ is high frequency dielectric constant, γ is the inverse of the bulk relaxation time and ω_p is the bulk plasma frequency given by

$$\omega_p = \sqrt{\frac{N_c e^2}{\varepsilon_0 m_{eff}}} \quad \text{A1.2}$$

Using the dielectric function obtained from equation A1.1, absorbance is calculated using Mie theory under the assumption of subwavelength particle dimensions, so that the absorption is given as:

$$C_{abs}(\omega) = 4\pi\,\mathrm{k}(\varepsilon_H)^{1/2} R^3\,\mathrm{Im}\left\{\frac{\varepsilon_p(\omega) - \varepsilon_H}{\varepsilon_p(\omega) + 2\varepsilon_H}\right\} \quad \text{A1.3}$$

Where with k being the wavevector, R the NC radius, ε_H the host dielectric constant, and $\varepsilon_p(\omega)$ the material dielectric function.

From the equation A1.3, the plasmon resonance condition can be evaluated as when

$$\mathrm{Re}\{\varepsilon_p\} = -2\cdot\varepsilon_H \quad \text{A1.4}$$

Now substituting $\mathrm{Re}\{\varepsilon_p\}$ from A1.1 in A1.4, we get,

$$\varepsilon_\infty - \frac{{\omega_p}^2}{\omega^2 + \gamma^2} = -2\varepsilon_H \quad \text{A1.5}$$

Rearranging the above equation and substituting eq A1.2 in eq A1.5, we get

$$\omega^2 + \gamma^2 = \frac{N_c e^2}{\varepsilon_0 m_{eff} (\varepsilon_\infty + 2\varepsilon_H)} \qquad \text{A1.6}$$

So, if a change in carrier concentration (ΔN_c) brings a change in frequency by $\Delta\omega$,then

$$(\omega + \Delta\omega)^2 + \gamma^2 = \frac{(N_c + \Delta N_c)e^2}{\varepsilon_0 m_{eff} (\varepsilon_\infty + 2\varepsilon_H)} \qquad \text{A1.7}$$

Now subtracting eq A1.6 from A1.7, we get

$$\Delta\omega(2\omega + \Delta\omega) = \frac{\Delta N_c e^2}{\varepsilon_0 m_{eff} (\varepsilon_\infty + 2\varepsilon_H)} \qquad \text{A1.8}$$

So if, $\Delta\omega << \omega$,

$$\omega \cdot \Delta\omega = \frac{\Delta N_c e^2}{2\varepsilon_0 m_{eff} (\varepsilon_\infty + 2\varepsilon_H)} \qquad \text{A1.9}$$

Substituting

$\omega = c / \lambda$, $\Delta\omega = (-c / \lambda^2)\Delta\lambda$

$$\Delta\lambda = \frac{-\lambda^3 e^2}{2\varepsilon_0 m_{eff} (\varepsilon_\infty + 2\varepsilon_H) \mathrm{c}^2} \Delta N_c \qquad \text{A1.10}$$

So from A1.10, we get the sensitivity factor S_{Nc} as,

$$S_{N_c} = \frac{-\lambda^3 e^2}{2\varepsilon_0 m_{eff} (\varepsilon_\infty + 2\varepsilon_H) \mathrm{c}^2} \qquad \text{A1.11}$$

Appendix B: Temporal Coupled Mode Theory

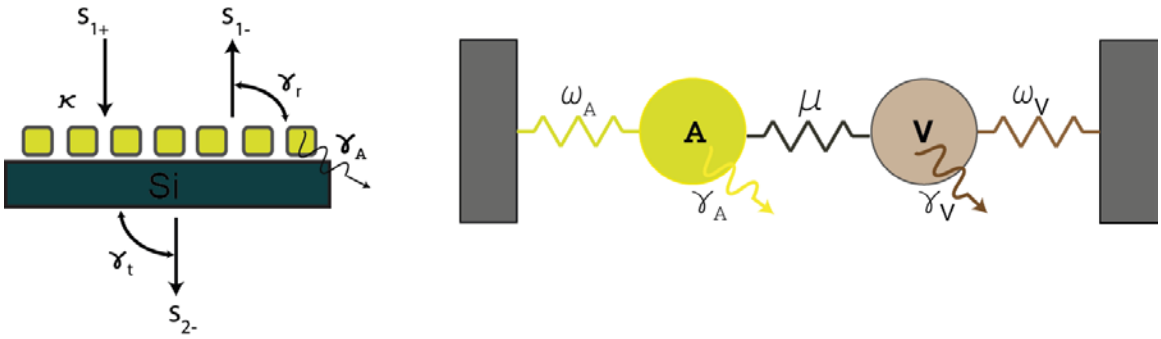

Both LSPR and molecular vibrations can be expressed as harmonic oscillators with corresponding resonance frequencies and decay rates. In a coupled LSPR-vibrational mode system, the LSPR mode is excited via incident light and it is considered as a bright mode. To first approximation, the response of an uncoupled molecular vibration is very weak compared to that of the LSPR, so it is approximated as a dark mode in our system.

Equation A2.1 expresses the LSPR as a harmonic oscillator with resonant frequency, ω_{LSPR}, and decay rate, γ_{LSPR}. The decay rate is the sum of energy decay attributed to reflected light (γ_r), transmitted light (γ_t) and non-radiative absorption decay (γ_{nr}). The LSPR harmonic oscillator is coupled with i^{th} vibrational oscillator with the coupling strength, μ_i and with external light (s_{1+}). This formulation is based upon two-port temporal coupled mode theory.

$$\frac{d}{dt}\phi(t) = [j\omega_{LSPR} - (\gamma_r + \gamma_t + \gamma_{nr})]\phi(t) + \kappa_1 s_{1+} + j\sum \mu_i P_i \qquad \text{A2.1}$$

where, $|\phi(t)|^2$ is the total energy stored in the LSPR mode. Following the work of Altug et.al[241]., Haus et.al.[268], and Fan et.al.[267], decay rates to reflected light, transmitted light

and absorption were evaluated as a ratio between the power dissipated in the relevant process to the total energy stored in the mode.

$$\gamma_r = \frac{W_r}{W}, \gamma_t = \frac{W_t}{W}, \gamma_{nr} = \frac{W_{nr}}{W} \quad \text{A2.2}$$

As derived in other works, W can be expressed as,

$$W = \frac{1}{4}\int \left[\epsilon_0 f_\epsilon(r) \left|\overrightarrow{E(r)}\right|^2 + \mu_0 \left|\overrightarrow{H}\right|^2\right] dV \quad \text{A2.3}$$

for power dissipated due to non-radiative decay in the form of absorbed light it can be expressed as

$$W_{nr} = \frac{\epsilon_0}{2}\frac{\gamma\omega_p^2}{\omega^2+\gamma^2}\int \left|\overrightarrow{E(r)}\right|^2 dV \quad \text{A2.4}$$

loss decay rate to transmitted and reflected light are calculated as

$$W_r = I\int |S_{11}|^2 dA \ , W_r = I\int |S_{21}|^2 dA \quad \text{A2.5}$$

Now, expressing the dark vibrational mode as a harmonic oscillator,

$$\frac{d}{dt}P_i(t) = [j\omega - \gamma_v^i]P_i(t) + j\mu_i\phi(t) \quad \text{A2.6}$$

Here the decay rate from each vibration is obtained by fitting a multi term Gaussian function to the absorption spectrum of the mixture of indium oleate (80%) and octyl amine (20%). The central vibrational frequency, FWHM, and mode strength corresponding to different vibrations are listed in Table 4.2.

The coupling strength between the LSPR and molecular vibrations can be calculated using the expression derived by Altug et.al.,

$$\mu^2 = \frac{1}{3}\frac{\epsilon_0 A^2 N < |E(r)|^2 >}{8W} \quad \text{A2.7}$$

where, A^2 is the vibrational mode strength, N is the number of vibrational sites, and $< |E(r)|^2 >$ is average electric field strength around the nanocrystal where the vibrational sites are present.

Balancing these equations for the incoming power and outgoing power can be expressed as,

$$s_- = Cs_+ + K\phi(t) \quad \text{A2.8}$$

where $|s_{+,-}|^2$ is the total power carried by the incoming (+) and outgoing power (-). For the two port system, $s_{+,-} = (s_{1+,-}\ s_{2+,-})^T$. Here, since there is no incidence light from port 2, s_+ equals $(s_{1+}\ 0)^T$ and s_- equals $(s_{1-}\ s_{2-}\ )^T$. C is the non-resonant scattering matrix and equals, $C = \begin{pmatrix} r & t_D \\ t_D & r \end{pmatrix}$. κ is the coupling constant between the incoming light and the resonator. As a consequence of time reversal symmetry and energy conservation, previous works[267,292] have obtained the following correlation,

$$\kappa = (\kappa_1\ \kappa_2)^T = \left(\sqrt{2\gamma_r}\ \sqrt{2\gamma_t}\right)^T \quad \text{A2.9}$$

Taking the Fourier transform of Equation A2.1 and A2.6 gives,

$$j\omega\phi(\omega) = [j\omega_{LSPR} - (\gamma_r + \gamma_t + \gamma_{nr})]\phi(\omega) + \kappa_1 s_{1+} + j\sum \mu_i P_i(\omega) \quad \text{A2.10}$$

$$j\omega P_i(\omega) = [j\omega_v^i - \gamma_v^i]P_i(\omega) + j\mu_i\phi(\omega) \quad \text{A2.11}$$

Substituting Equation A2.11 into A2.10 gives,

$$j\omega\phi(\omega) = [j\omega_{LSPR} - (\gamma_r + \gamma_t + \gamma_{nr})]\phi(\omega) + \kappa_1 s_{1+} + \sum[j\omega_\mu^i - \gamma_\mu^i]\phi(\omega) \quad \text{A2.12}$$

Where,

$$\omega_\mu^i = \frac{\mu^2(\omega - \omega_v^i)}{[(\omega - \omega_v^i)^2 + (\gamma_v^i)^2]} \quad \text{A2.13}$$

$$\gamma_\mu^i = \frac{\mu^2\gamma_v^i}{[(\omega - \omega_v^i)^2 + (\gamma_v^i)^2]} \quad \text{A2.14}$$

$$[j(\omega - \omega_{LSPR} - \sum \omega_\mu^i) - (\gamma_r + \gamma_t + \gamma_{nr} + \sum \gamma_\mu^i)]\phi(\omega) = \kappa_1 s_{1+} \quad \text{A2.15}$$

The reflection and transmission coefficients can then be defined as,

$$R = \left|\frac{s_{1-}}{s_{1+}}\right|^2, \quad T = \left|\frac{s_{2+}}{s_{1+}}\right|^2 \quad \text{A2.16}$$

substituting A2.13 into A2.8

$$R(\omega) = \left| r_1 - \left\{ \frac{2\gamma_r}{j(\omega - \omega_{LSPR} - \sum \omega_\mu^i) - (\gamma_{tot} + \sum \gamma_\mu^i)} e^{j\theta_1} \right\} \right|^2 \quad \text{A2.17}$$

$$T(\omega) = \left| t_D - \left\{ \frac{\sqrt{4\gamma_r \gamma_t}}{j(\omega - \omega_{LSPR} - \sum \omega_\mu^i) - (\gamma_{tot} + \sum \gamma_\mu^i)} e^{j\theta} \right\} \right|^2 \quad \text{A2.18}$$

Appendix C: Effective film dielectric and device optical modeling

Sandwich cell designed in-house for in-situ spectroelectrochemistry was modeled using commercial SCOUT software (www.wtheiss.com) by employing several built-in optical models, including, T-matrix method to calculate extinction spectrum, Drude model to express the dielectric function of ITO thin film on glass substrate. To model the device following steps were followed:

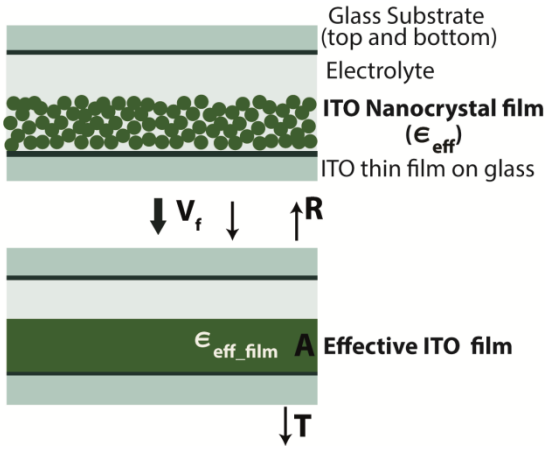

Figure C1: Schematic of the modeled sandwich device configuration. Here, ITO NCs with effective dielectric function ε_{eff} is coated on the top of ITO thin film coated glass substrate. To model the ITO NC film, effective dielectric function of the film was calculated using Maxwell-Garnett equation.

1) Building up the material library, which consists of glass substrate, ITO thin film, ITO nanocrystals and electrolyte.
2) Defining the dielectric model for each of the material.
3) Glass substrate was modeled as the sum of several Lorentian. The parameter for the lorentian was obtained by fitting the experimental extinction spectrum with modeled one. Similarly, ITO thin film on glass was fitted to obtained the Drude parameter for the background substrate used in our measurement

4) Effective dielectric function of the nanocrystals was calculated using the procedure described in the previous section and imported in the SCOUT.
5) Effective dielectric function of the nanocrystal film consisting of nanocrystal with a fixed volume fraction and the electrolyte filling the pores was calculated using built in Maxwell Garnett effective medium model.
6) Sample extinction spectra for a given doping level and size of the nanocrystal for different applied potential obtained from this procedure (Figure A3.1) is analogues to that of experimentally measured spectra (Figure A5.10). To obtain the change in spectra, similar to our experimental data analysis procedure, all spectra were background subtracted against the spectrum at the most oxidized potential.

Appendix D: Effective medium theory for single nanocrystal effective dielectric function

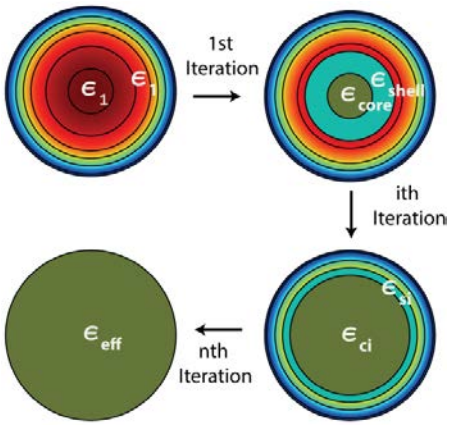

Figure D1 Schematic shows the iterative procedure to obtain and effective dielectric function of a depleted NC.

Here, we have developed a method to derive effective nanocrystal dielectric function. This involves applying the Maxwell-Garnet effective medium theory[286], iteratively to a finely discretized sphere into a core and multi-shell configuration (Figure D1). The detailed algorithm to obtain effective dielectric function developed in this work is as follows:

1) Calculated the free electron concentration from the solution of Poisson's equation.
2) Discretized the spherical geometry into a core and 4 shells. More than 4 shell was not making much difference to our solution. Discretization was based off the carrier density. Equally spaced 6 focal points in between maximum and minimum carrier density obtained of the carrier density profile was calculated

   $(n_1 = n_{\min}, n_2, \ldots, n_i, \ldots, n_5 = n_{\max})$.
3) Corresponding to those six carrier concentrations, radial distance of the center of the sphere was obtained from the carrier profile.

$(r_0 = 0, r_1, ..., r_i, ..., r_5 = R)$

4) To conserve the total number of free electron within a region (core or shell), volumetrically averaged carrier density was calculated using the following expression $N_i = \frac{\int_{r_{i-1}}^{r_i} 4\pi r^2 n_i \, dr}{\int_{r_{i-1}}^{r_i} 4\pi r^2 \, dr}$ where i =1 to 5

5) Using the value of volumetrically averaged carrier concentration obtained from 4, dielectric function of each region was determined using Drude model $\varepsilon_i = \varepsilon_\infty - \frac{\omega_{p,i}^2}{\omega^2 - \omega\gamma}$ where, $\omega_{p,i} = \sqrt{\frac{N_i e^2}{m_e \varepsilon_0}}$ and γ is the frequency dependent scattering function expressed as,

$\gamma = \gamma_L - \frac{\gamma_L - \gamma_H}{\pi}\left(\tan^{-1}\left(\frac{\omega - \gamma_X}{\gamma_W}\right) + \frac{\pi}{2}\right)$ where, γ_L is the low frequency damping, γ_H is high frequency damping, γ_X is a crossover frequency, and γ_W is the crossover width. All the parameter other than carrier concentration is uniform through out the nanocrystal.

6) Now starting from the core and first inner shell the discretized nanocrystal has the dielectric function $\varepsilon_{core} = \varepsilon_1$ and $\varepsilon_{shell} = \varepsilon_2$ (Figure D1). Using core-shell Maxwell Garnett effective medium theory, effective dielectric function ($\varepsilon_{core,i}$) of the new core is calculated. Given that core radius of a= r_1 and shell outer radius of b=r_2 ,

$$\varepsilon_{core,new} = \varepsilon_{shell} \frac{a^3(\varepsilon_{core} + 2\varepsilon_{shell}) + 2b^3(\varepsilon_{core} - \varepsilon_{shell})}{a^3(\varepsilon_{core} + 2\varepsilon_{shell}) - b^3(\varepsilon_{core} - \varepsilon_{shell})}$$

7) Above equation was applied again with the new $\varepsilon_{core,new}$ and $\varepsilon_{shell,new}$ i.e, next inner most shell to the new core (Figure A4.1). This procedure was repeated till we obtained a single effective dielectric function for the nanocrystal ($\varepsilon_{p\_effective}$).
8) Using the effective dielectric function, absorption of the single nanocrystal was calculated via Mie theory.

References

(1) *Plasmonics: Fundamentals and Applications*; Springer US: Boston, MA, 2007.

(2) Brongersma, M. L.; Halas, N. J.; Nordlander, P. Plasmon-Induced Hot Carrier Science and Technology. *Nat. Nanotechnol.* **2015**, *10*, 25–34.

(3) Zhou, Z.; Kong, B.; Yu, C.; Shi, X.; Wang, M.; Liu, W.; Sun, Y.; Zhang, Y.; Yang, H.; Yang, S. Tungsten Oxide Nanorods: An Efficient Nanoplatform for Tumor CT Imaging and Photothermal Therapy. *Sci. Rep.* **2014**, *4*.

(4) Liu, Q.; Sun, C.; He, Q.; Liu, D.; Khalil, A.; Xiang, T.; Wu, Z.; Wang, J.; Song, L. Ultrathin Carbon Layer Coated MoO2 Nanoparticles for High-Performance near-Infrared Photothermal Cancer Therapy. *Chem. Commun.* **2015**, *51*, 10054–10057.

(5) Fofang, N. T.; Park, T.-H.; Neumann, O.; Mirin, N. A.; Nordlander, P.; Halas, N. J. Plexcitonic Nanoparticles: Plasmon−Exciton Coupling in Nanoshell−J-Aggregate Complexes. *Nano Lett.* **2008**, *8*, 3481–3487.

(6) Velizhanin, K. A.; Shahbazyan, T. V. Exciton-Plasmaritons in Graphene/Semiconductor Structures. *Phys. Rev. B* **2014**, *90*, 085403.

(7) Kundu, J.; Le, F.; Nordlander, P.; Halas, N. J. Surface Enhanced Infrared Absorption (SEIRA) Spectroscopy on Nanoshell Aggregate Substrates. *Chem. Phys. Lett.* **2008**, *452*, 115–119.

(8) Abb, M.; Wang, Y.; Papasimakis, N.; de Groot, C. H.; Muskens, O. L. Surface-Enhanced Infrared Spectroscopy Using Metal Oxide Plasmonic Antenna Arrays. *Nano Lett.* **2014**, *14*, 346–352.

(9) Nehl, C. L.; Hafner, J. H. Shape-Dependent Plasmon Resonances of Gold Nanoparticles. *J. Mater. Chem.* **2008**, *18*, 2415.

(10) Chen, H.; Kou, X.; Yang, Z.; Ni, W.; Wang, J. Shape- and Size-Dependent Refractive Index Sensitivity of Gold Nanoparticles. *Langmuir* **2008**, *24*, 5233–5237.

(11) Martinsson, E.; Shahjamali, M. M.; Enander, K.; Boey, F.; Xue, C.; Aili, D.; Liedberg, B. Local Refractive Index Sensing Based on Edge Gold-Coated Silver Nanoprisms. *J. Phys. Chem. C* **2013**, *117*, 23148–23154.

(12) Nehl, C. L.; Liao, H.; Hafner, J. H. Optical Properties of Star-Shaped Gold Nanoparticles. *Nano Lett.* **2006**, *6*, 683–688.

(13) Becker, J.; Trügler, A.; Jakab, A.; Hohenester, U.; Sönnichsen, C. The Optimal Aspect Ratio of Gold Nanorods for Plasmonic Bio-Sensing. *Plasmonics* **2010**, *5*, 161–167.

(14) Wiley, B. J.; Chen, Y.; McLellan, J. M.; Xiong, Y.; Li, Z.-Y.; Ginger, D.; Xia, Y. Synthesis and Optical Properties of Silver Nanobars and Nanorice. *Nano Lett.* **2007**, *7*, 1032–1036.

(15) Mattox, T. M.; Ye, X.; Manthiram, K.; Schuck, P. J.; Alivisatos, A. P.; Urban, J. J. Chemical Control of Plasmons in Metal Chalcogenide and Metal Oxide Nanostructures. *Adv. Mater.* **2015**, *27*, 5830–5837.

(16) Runnerstrom, E. L.; Bergerud, A.; Agrawal, A.; Johns, R. W.; Dahlman, C. J.; Singh, A.; Selbach, S. M.; Milliron, D. J. Defect Engineering in Plasmonic Metal Oxide Nanocrystals. *Nano Lett.* **2016**, *16*, 3390–3398.

(17) Lounis, S. D.; Runnerstrom, E. L.; Llordés, A.; Milliron, D. J. Defect Chemistry and Plasmon Physics of Colloidal Metal Oxide Nanocrystals. *J. Phys. Chem. Lett.* **2014**, *5*, 1564–1574.

(18) Cooper, B. R.; Ehrenreich, H.; Philipp, H. R. Optical Properties of Noble Metals. II. *Phys. Rev.* **1965**, *138*, A494–A507.

(19) Gordon, T. R.; Paik, T.; Klein, D. R.; Naik, G. V.; Caglayan, H.; Boltasseva, A.; Murray, C. B. Shape-Dependent Plasmonic Response and Directed Self-Assembly in a New Semiconductor Building Block, Indium-Doped Cadmium Oxide (ICO). *Nano Lett.* **2013**, *13*, 2857–2863.

(20) Donovan, B. F.; Sachet, E.; Maria, J.-P.; Hopkins, P. E. Interplay between Mass-Impurity and Vacancy Phonon Scattering Effects on the Thermal Conductivity of Doped Cadmium Oxide. *Appl. Phys. Lett.* **2016**, *108*, 021901.

(21) Greenberg, B. L.; Ganguly, S.; Held, J. T.; Kramer, N. J.; Mkhoyan, K. A.; Aydil, E. S.; Kortshagen, U. R. Nonequilibrium-Plasma-Synthesized ZnO Nanocrystals with Plasmon Resonance Tunable via Al Doping and Quantum Confinement. *Nano Lett.* **2015**, *15*, 8162–8169.

(22) Schimpf, A. M.; Gunthardt, C. E.; Rinehart, J. D.; Mayer, J. M.; Gamelin, D. R. Controlling Carrier Densities in Photochemically Reduced Colloidal ZnO Nanocrystals: Size Dependence and Role of the Hole Quencher. *J. Am. Chem. Soc.* **2013**, *135*, 16569–16577.

(23) Mattox, T. M.; Bergerud, A.; Agrawal, A.; Milliron, D. J. Influence of Shape on the Surface Plasmon Resonance of Tungsten Bronze Nanocrystals. *Chem. Mater.* **2014**, *26*, 1779–1784.

(24) Buonsanti, R.; Llordes, A.; Aloni, S.; Helms, B. A.; Milliron, D. J. Tunable Infrared Absorption and Visible Transparency of Colloidal Aluminum-Doped Zinc Oxide Nanocrystals. *Nano Lett.* **2011**, *11*, 4706–4710.

(25) Garcia, G.; Buonsanti, R.; Runnerstrom, E. L.; Mendelsberg, R. J.; Llordes, A.; Anders, A.; Richardson, T. J.; Milliron, D. J. Dynamically Modulating the

Surface Plasmon Resonance of Doped Semiconductor Nanocrystals. *Nano Lett.* **2011**, *11*, 4415–4420.

(26) Kim, J.; Agrawal, A.; Krieg, F.; Bergerud, A.; Milliron, D. J. The Interplay of Shape and Crystalline Anisotropies in Plasmonic Semiconductor Nanocrystals. *Nano Lett.* **2016**, *16*, 3879–3884.

(27) Li, S. Q.; Guo, P.; Zhang, L.; Zhou, W.; Odom, T. W.; Seideman, T.; Ketterson, J. B.; Chang, R. P. H. Infrared Plasmonics with Indium–Tin-Oxide Nanorod Arrays. *ACS Nano* **2011**, *5*, 9161–9170.

(28) Garcia, G.; Buonsanti, R.; Llordes, A.; Runnerstrom, E. L.; Bergerud, A.; Milliron, D. J. Near-Infrared Spectrally Selective Plasmonic Electrochromic Thin Films. *Adv. Opt. Mater.* **2013**, *1*, 215–220.

(29) Bühler, G.; Thölmann, D.; Feldmann, C. One-Pot Synthesis of Highly Conductive Indium Tin Oxide Nanocrystals. *Adv. Mater.* **2007**, *19*, 2224–2227.

(30) Kanehara, M.; Koike, H.; Yoshinaga, T.; Teranishi, T. Indium Tin Oxide Nanoparticles with Compositionally Tunable Surface Plasmon Resonance Frequencies in the Near-IR Region. *J. Am. Chem. Soc.* **2009**, *131*, 17736–17737.

(31) Yang, Y.; Jin, Y.; He, H.; Wang, Q.; Tu, Y.; Lu, H.; Ye, Z. Dopant-Induced Shape Evolution of Colloidal Nanocrystals: The Case of Zinc Oxide. *J. Am. Chem. Soc.* **2010**, *132*, 13381–13394.

(32) Della Gaspera, E.; Chesman, A. S. R.; van Embden, J.; Jasieniak, J. J. Non-Injection Synthesis of Doped Zinc Oxide Plasmonic Nanocrystals. *ACS Nano* **2014**, *8*, 9154–9163.

(33) Goings, J. J.; Schimpf, A. M.; May, J. W.; Johns, R. W.; Gamelin, D. R.; Li, X. Theoretical Characterization of Conduction-Band Electrons in Photodoped and Aluminum-Doped Zinc Oxide (AZO) Quantum Dots. *J. Phys. Chem. C* **2014**, *118*, 26584–26590.

(34) Mendelsberg, R. J.; Zhu, Y.; Anders, A. Determining the Nonparabolicity Factor of the CdO Conduction Band Using Indium Doping and the Drude Theory. *J. Phys. Appl. Phys.* **2012**, *45*, 425302.

(35) Brewer, S. H.; Franzen, S. Calculation of the Electronic and Optical Properties of Indium Tin Oxide by Density Functional Theory. *Chem. Phys.* **2004**, *300*, 285–293.

(36) Ye, X.; Fei, J.; Diroll, B. T.; Paik, T.; Murray, C. B. Expanding the Spectral Tunability of Plasmonic Resonances in Doped Metal-Oxide Nanocrystals through Cooperative Cation–Anion Codoping. *J. Am. Chem. Soc.* **2014**, *136*, 11680–11686.

(37) Agrawal, A.; Kriegel, I.; Milliron, D. J. Shape-Dependent Field Enhancement and Plasmon Resonance of Oxide Nanocrystals. *J. Phys. Chem. C* **2015**, *119*, 6227–6238.

(38) Manthiram, K.; Alivisatos, A. P. Tunable Localized Surface Plasmon Resonances in Tungsten Oxide Nanocrystals. *J. Am. Chem. Soc.* **2012**, *134*, 3995–3998.

(39) Wang, L. V.; Wu, H.-I. Sensing of Optical Properties and Spectroscopy. In *Biomedical Optics*; John Wiley & Sons, Inc., 2009; pp. 135–151.

(40) Deng, K.; Hou, Z.; Deng, X.; Yang, P.; Li, C.; Lin, J. Enhanced Antitumor Efficacy by 808 Nm Laser-Induced Synergistic Photothermal and Photodynamic Therapy Based on a Indocyanine-Green-Attached W18O49 Nanostructure. *Adv. Funct. Mater.* **2015**, *25*, 7280–7290.

(41) Song, G.; Shen, J.; Jiang, F.; Hu, R.; Li, W.; An, L.; Zou, R.; Chen, Z.; Qin, Z.; Hu, J. Hydrophilic Molybdenum Oxide Nanomaterials with Controlled Morphology and Strong Plasmonic Absorption for Photothermal Ablation of Cancer Cells. *ACS Appl. Mater. Interfaces* **2014**, *6*, 3915–3922.

(42) Soo Choi, H.; Liu, W.; Misra, P.; Tanaka, E.; Zimmer, J. P.; Itty Ipe, B.; Bawendi, M. G.; Frangioni, J. V. Renal Clearance of Quantum Dots. *Nat. Biotechnol.* **2007**, *25*, 1165–1170.

(43) Boriskina, S. V.; Tong, J. K.; Huang, Y.; Zhou, J.; Chiloyan, V.; Chen, G. Enhancement and Tunability of Near-Field Radiative Heat Transfer Mediated by Surface Plasmon Polaritons in Thin Plasmonic Films. *Photonics* **2015**, *2*, 659–683.

(44) Furube, A.; Yoshinaga, T.; Kanehara, M.; Eguchi, M.; Teranishi, T. Electric-Field Enhancement Inducing Near-Infrared Two-Photon Absorption in an Indium–Tin Oxide Nanoparticle Film. *Angew. Chem. Int. Ed.* **2012**, *51*, 2640–2642.

(45) Lee, H. W.; Papadakis, G.; Burgos, S. P.; Chander, K.; Kriesch, A.; Pala, R.; Peschel, U.; Atwater, H. A. Nanoscale Conducting Oxide PlasMOStor. *Nano Lett.* **2014**, *14*, 6463–6468.

(46) Mendelsberg, R. J.; McBride, P. M.; Duong, J. T.; Bailey, M. J.; Llordes, A.; Milliron, D. J.; Helms, B. A. Dispersible Plasmonic Doped Metal Oxide Nanocrystal Sensors That Optically Track Redox Reactions in Aqueous Media with Single-Electron Sensitivity. *Adv. Opt. Mater.* **2015**, *3*, 1293–1300.

(47) Schimpf, A. M.; Lounis, S. D.; Runnerstrom, E. L.; Milliron, D. J.; Gamelin, D. R. Redox Chemistries and Plasmon Energies of Photodoped In_2O_3 and Sn-Doped In_2O_3 (ITO) Nanocrystals. *J. Am. Chem. Soc.* **2015**, *137*, 518–524.

(48) Kim, J.; Ong, G. K.; Wang, Y.; LeBlanc, G.; Williams, T. E.; Mattox, T. M.; Helms, B. A.; Milliron, D. J. Nanocomposite Architecture for Rapid, Spectrally-

Selective Electrochromic Modulation of Solar Transmittance. *Nano Lett.* **2015**, *15*, 5574–5579.

(49) Llordés, A.; Garcia, G.; Gazquez, J.; Milliron, D. J. Tunable near-Infrared and Visible-Light Transmittance in Nanocrystal-in-Glass Composites. *Nature* **2013**, *500*, 323–326.

(50) Dahlman, C. J.; Tan, Y.; Marcus, M. A.; Milliron, D. J. Spectroelectrochemical Signatures of Capacitive Charging and Ion Insertion in Doped Anatase Titania Nanocrystals. *J. Am. Chem. Soc.* **2015**, *137*, 9160–9166.

(51) Faucheaux, J. A.; Jain, P. K. Plasmons in Photocharged ZnO Nanocrystals Revealing the Nature of Charge Dynamics. *J. Phys. Chem. Lett.* **2013**, *4*, 3024–3030.

(52) Llordes, A.; Hammack, A. T.; Buonsanti, R.; Tangirala, R.; Aloni, S.; Helms, B. A.; Milliron, D. J. Polyoxometalates and Colloidal Nanocrystals as Building Blocks for Metal Oxide Nanocomposite Films. *J. Mater. Chem.* **2011**, *21*, 11631–11638.

(53) Kinsey, N.; DeVault, C.; Kim, J.; Ferrera, M.; Shalaev, V. M.; Boltasseva, A. Epsilon-near-Zero Al-Doped ZnO for Ultrafast Switching at Telecom Wavelengths. *Optica* **2015**, *2*, 616.

(54) Noginov, M. A.; Gu, L.; Livenere, J.; Zhu, G.; Pradhan, A. K.; Mundle, R.; Bahoura, M.; Barnakov, Y. A.; Podolskiy, V. A. Transparent Conductive Oxides: Plasmonic Materials for Telecom Wavelengths. *Appl. Phys. Lett.* **2011**, *99*, 021101.

(55) Schubert, E. F. *Light-Emitting Diodes*; 2 edition.; Cambridge University Press: Cambridge ; New York, 2006.

(56) Manthiram, K.; Alivisatos, A. P. Tunable Localized Surface Plasmon Resonances in Tungsten Oxide Nanocrystals. *J. Am. Chem. Soc.* **2012**, *134*, 3995–3998.

(57) Chopra, K. L.; Major, S.; Pandya, D. K. Transparent conductors—A Status Review. *Thin Solid Films* **1983**, *102*, 1–46.

(58) Haase, M.; Weller, H.; Henglein, A. Photochemistry and Radiation Chemistry of Colloidal Semiconductors. 23. Electron Storage on Zinc Oxide Particles and Size Quantization. *J. Phys. Chem.* **1988**, *92*, 482–487.

(59) Nütz, T.; Felde, U. zum; Haase, M. Wet-Chemical Synthesis of Doped Nanoparticles: Blue-Colored Colloids of N-Doped SnO2:Sb. *J. Chem. Phys.* **1999**, *110*, 12142–12150.

(60) Hammarberg, E.; Prodi-Schwab, A.; Feldmann, C. Microwave-Assisted Polyol Synthesis of Aluminium- and Indium-Doped ZnO Nanocrystals. *J. Colloid Interface Sci.* **2009**, *334*, 29–36.

(61) Gilstrap, R. A.; Capozzi, C. J.; Carson, C. G.; Gerhardt, R. A.; Summers, C. J. Synthesis of a Nonagglomerated Indium Tin Oxide Nanoparticle Dispersion. *Adv. Mater.* **2008**, *20*, 4163–4166.

(62) Choi, S.-I.; Nam, K. M.; Park, B. K.; Seo, W. S.; Park, J. T. Preparation and Optical Properties of Colloidal, Monodisperse, and Highly Crystalline ITO Nanoparticles. *Chem. Mater.* **2008**, *20*, 2609–2611.

(63) Diroll, B. T.; Gordon, T. R.; Gaulding, E. A.; Klein, D. R.; Paik, T.; Yun, H. J.; Goodwin, E. D.; Damodhar, D.; Kagan, C. R.; Murray, C. B. Synthesis of N-Type Plasmonic Oxide Nanocrystals and the Optical and Electrical Characterization of Their Transparent Conducting Films. *Chem. Mater.* **2014**, *26*, 4579–4588.

(64) Ravichandran, A. T.; Xavier, A. R.; Pushpanathan, K.; Nagabhushana, B. M.; Chandramohan, R. Structural and Optical Properties of Zn Doped CdO Nanoparticles Synthesized by Chemical Precipitation Method. *J. Mater. Sci. Mater. Electron.* **2015**, *27*, 2693–2700.

(65) Ghosh, S.; Saha, M.; Dev Ashok, V.; Dalal, B.; De, S. K. Tunable Surface Plasmon Resonance in Sn-Doped Zn–Cd–O Alloyed Nanocrystals. *J. Phys. Chem. C* **2015**, *119*, 1180–1187.

(66) Kim, J.; Naik, G. V.; Gavrilenko, A. V.; Dondapati, K.; Gavrilenko, V. I.; Prokes, S. M.; Glembocki, O. J.; Shalaev, V. M.; Boltasseva, A. Optical Properties of Gallium-Doped Zinc Oxide - A Low-Loss Plasmonic Material: First-Principles Theory and Experiment. *Phys. Rev. X* **2013**, *3*, 041037.

(67) Gaspera, E. D.; Duffy, N. W.; Embden, J. van; Waddington, L.; Bourgeois, L.; Jasieniak, J. J.; Chesman, A. S. R. Plasmonic Ge-Doped ZnO Nanocrystals. *Chem. Commun.* **2015**, *51*, 12369–12372.

(68) Tandon, B.; Yadav, A.; Nag, A. Delocalized Electrons Mediated Magnetic Coupling in Mn–Sn Codoped In_2O_3 Nanocrystals: Plasmonics Shows the Way. *Chem. Mater.* **2016**, *28*, 3620–3624.

(69) De Trizio, L.; Buonsanti, R.; Schimpf, A. M.; Llordes, A.; Gamelin, D. R.; Simonutti, R.; Milliron, D. J. Nb-Doped Colloidal TiO_2 Nanocrystals with Tunable Infrared Absorption. *Chem. Mater.* **2013**, *25*, 3383–3390.

(70) Rini, M.; Cavalleri, A.; Schoenlein, R. W.; López, R.; Feldman, L. C.; Haglund, R. F.; Boatner, L. A.; Haynes, T. E. Photoinduced Phase Transition in VO_2 Nanocrystals: Ultrafast Control of Surface-Plasmon Resonance. *Opt. Lett.* **2005**, *30*, 558.

(71) Zhu, Y.; Mendelsberg, R. J.; Zhu, J.; Han, J.; Anders, A. Structural, Optical, and Electrical Properties of Indium-Doped Cadmium Oxide Films Prepared by Pulsed Filtered Cathodic Arc Deposition. *J. Mater. Sci.* **2013**, *48*, 3789–3797.

(72) Hamberg, I.; Granqvist, C. G. Evaporated Sn-doped In2O3 Films: Basic Optical Properties and Applications to Energy-efficient Windows. *J. Appl. Phys.* **1986**, *60*, R123–R160.

(73) Brown, A. M.; Sundararaman, R.; Narang, P.; Goddard, W. A.; Atwater, H. A. Nonradiative Plasmon Decay and Hot Carrier Dynamics: Effects of Phonons, Surfaces, and Geometry. *ACS Nano* **2016**, *10*, 957–966.

(74) Chattopadhyay, D.; Queisser, H. J. Electron Scattering by Ionized Impurities in Semiconductors. *Rev. Mod. Phys.* **1981**, *53*, 745–768.

(75) Sachet, E.; Losego, M. D.; Guske, J.; Franzen, S.; Maria, J.-P. Mid-Infrared Surface Plasmon Resonance in Zinc Oxide Semiconductor Thin Films. *Appl. Phys. Lett.* **2013**, *102*, 051111.

(76) Naik, G. V.; Kim, J.; Boltasseva, A. Oxides and Nitrides as Alternative Plasmonic Materials in the Optical Range [Invited]. *Opt. Mater. Express* **2011**, *1*, 1090.

(77) Lounis, S. D.; Runnerstrom, E. L.; Bergerud, A.; Nordlund, D.; Milliron, D. J. Influence of Dopant Distribution on the Plasmonic Properties of Indium Tin Oxide Nanocrystals. *J. Am. Chem. Soc.* **2014**, *136*, 7110–7116.

(78) zum Felde, U.; Haase, M.; Weller, H. Electrochromism of Highly Doped Nanocrystalline SnO_2:Sb. *J. Phys. Chem. B* **2000**, *104*, 9388–9395.

(79) McLeod, A. S.; Kelly, P.; Goldflam, M. D.; Gainsforth, Z.; Westphal, A. J.; Dominguez, G.; Thiemens, M. H.; Fogler, M. M.; Basov, D. N. Model for Quantitative Tip-Enhanced Spectroscopy and the Extraction of Nanoscale-Resolved Optical Constants. *Phys. Rev. B* **2014**, *90*, 085136.

(80) Johns, R. W.; Bechtel, H. A.; Runnerstrom, E. L.; Agrawal, A.; Lounis, S. D.; Milliron, D. J. Direct Observation of Narrow Mid-Infrared Plasmon Linewidths of Single Metal Oxide Nanocrystals. *Nat. Commun.* **2016**, *7*, 11583.

(81) Triana, C. A.; Granqvist, C. G.; Niklasson, G. A. Electrochromism and Small-Polaron Hopping in Oxygen Deficient and Lithium Intercalated Amorphous Tungsten Oxide Films. *J. Appl. Phys.* **2015**, *118*, 024901.

(82) Chen, A.; Zhu, K.; Zhong, H.; Shao, Q.; Ge, G. A New Investigation of Oxygen Flow Influence on ITO Thin Films by Magnetron Sputtering. *Sol. Energy Mater. Sol. Cells* **2014**, *120, Part A*, 157–162.

(83) Ágoston, P.; Erhart, P.; Klein, A.; Albe, K. Geometry, Electronic Structure and Thermodynamic Stability of Intrinsic Point Defects in Indium Oxide. *J. Phys. Condens. Matter* **2009**, *21*, 455801.

(84) Hwang, J.-H.; Edwards, D. D.; Kammler, D. R.; Mason, T. O. Point Defects and Electrical Properties of Sn-Doped In-Based Transparent Conducting Oxides. *Solid State Ion.* **2000**, *129*, 135–144.

(85) Sachet, E.; Shelton, C. T.; Harris, J. S.; Gaddy, B. E.; Irving, D. L.; Curtarolo, S.; Donovan, B. F.; Hopkins, P. E.; Sharma, P. A.; Sharma, A. L.; *et al.* Dysprosium-Doped Cadmium Oxide as a Gateway Material for Mid-Infrared Plasmonics. *Nat. Mater.* **2015**, *14*, 414–420.

(86) Bhachu, D. S.; Scanlon, D. O.; Sankar, G.; Veal, T. D.; Egdell, R. G.; Cibin, G.; Dent, A. J.; Knapp, C. E.; Carmalt, C. J.; Parkin, I. P. Origin of High Mobility in Molybdenum-Doped Indium Oxide. *Chem. Mater.* **2015**, *27*, 2788–2796.

(87) Deepa, M.; Srivastava, A. K.; Sood, K. N.; Agnihotry, S. A. Nanostructured Mesoporous Tungsten Oxide Films with Fast Kinetics for Electrochromic Smart Windows. *Nanotechnology* **2006**, *17*, 2625–2630.

(88) Yang, C.; Chen, J.-F.; Zeng, X.; Cheng, D.; Huang, H.; Cao, D. Enhanced near-Infrared Shielding Ability of (Li,K)-Codoped WO 3 for Smart Windows: DFT Prediction Validated by Experiment. *Nanotechnology* **2016**, *27*, 075203.

(89) Shim, M.; Guyot-Sionnest, P. Organic-Capped ZnO Nanocrystals: Synthesis and N-Type Character. *J. Am. Chem. Soc.* **2001**, *123*, 11651–11654.

(90) Schimpf, A. M.; Ochsenbein, S. T.; Buonsanti, R.; Milliron, D. J.; Gamelin, D. R. Comparison of Extra Electrons in Colloidal N-Type Al3+-Doped and Photochemically Reduced ZnO Nanocrystals. *Chem. Commun.* **2012**, *48*, 9352–9354.

(91) Gerlach, E. Carrier Scattering and Transport in Semiconductors Treated by the Energy-Loss Method. *J. Phys. C Solid State Phys.* **1986**, *19*, 4585.

(92) Tandon, B.; Shanker, G. S.; Nag, A. Multifunctional Sn- and Fe-Codoped In2O3 Colloidal Nanocrystals: Plasmonics and Magnetism. *J. Phys. Chem. Lett.* **2014**, *5*, 2306–2311.

(93) Zhou, D.; Kittilstved, K. R. Electron Trapping on Fe3+ Sites in Photodoped ZnO Colloidal Nanocrystals. *Chem. Commun.* **2016**, *52*, 9101–9104.

(94) Hu, M.; Novo, C.; Funston, A.; Wang, H.; Staleva, H.; Zou, S.; Mulvaney, P.; Xia, Y.; Hartland, G. V. Dark-Field Microscopy Studies of Single Metal Nanoparticles: Understanding the Factors That Influence the Linewidth of the Localized Surface Plasmon Resonance. *J. Mater. Chem.* **2008**, *18*, 1949–1960.

(95) Jiang, L.; Yin, T.; Dong, Z.; Liao, M.; Tan, S. J.; Goh, X. M.; Allioux, D.; Hu, H.; Li, X.; Yang, J. K. W.; *et al.* Accurate Modeling of Dark-Field Scattering Spectra of Plasmonic Nanostructures. *ACS Nano* **2015**, *9*, 10039–10046.

(96) Li, W.; Chen, X. Gold Nanoparticles for Photoacoustic Imaging. *Nanomed.* **2015**, *10*, 299–320.

(97) Anker, J. N.; Hall, W. P.; Lyandres, O.; Shah, N. C.; Zhao, J.; Van Duyne, R. P. Biosensing with Plasmonic Nanosensors. *Nat. Mater.* **2008**, *7*, 442–453.

(98) Bechtel, H. A.; Muller, E. A.; Olmon, R. L.; Martin, M. C.; Raschke, M. B. Ultrabroadband Infrared Nanospectroscopic Imaging. *Proc. Natl. Acad. Sci.* **2014**, *111*, 7191–7196.

(99) Jansons, A. W.; Hutchison, J. E. Continuous Growth of Metal Oxide Nanocrystals: Enhanced Control of Nanocrystal Size and Radial Dopant Distribution. *ACS Nano* **2016**, *10*, 6942–6951.

(100) Matsui, H.; Furuta, S.; Tabata, H. Role of Electron Carriers on Local Surface Plasmon Resonances in Doped Oxide Semiconductor Nanocrystals. *Appl. Phys. Lett.* **2014**, *104*, 211903.

(101) Wang, T.; Radovanovic, P. V. Free Electron Concentration in Colloidal Indium Tin Oxide Nanocrystals Determined by Their Size and Structure. *J. Phys. Chem. C* **2011**, *115*, 406–413.

(102) Hutfluss, L. N.; Radovanovic, P. V. Controlling the Mechanism of Phase Transformation of Colloidal In_2O_3 Nanocrystals. *J. Am. Chem. Soc.* **2015**, *137*, 1101–1108.

(103) Yockell-Lelièvre, H.; Lussier, F.; Masson, J.-F. Influence of the Particle Shape and Density of Self-Assembled Gold Nanoparticle Sensors on LSPR and SERS. *J. Phys. Chem. C* **2015**, *119*, 28577–28585.

(104) Chang, J.-Y.; Basu, S.; Wang, L. Indium Tin Oxide Nanowires as Hyperbolic Metamaterials for near-Field Radiative Heat Transfer. *J. Appl. Phys.* **2015**, *117*, 054309.

(105) Babicheva, V. E.; Boltasseva, A.; Lavrinenko, A. V. Transparent Conducting Oxides for Electro-Optical Plasmonic Modulators. *Nanophotonics* **2015**, *4*, 165–185.

(106) Mehra, S.; Bergerud, A.; Milliron, D. J.; Chan, E. M.; Salleo, A. Core/Shell Approach to Dopant Incorporation and Shape Control in Colloidal Zinc Oxide Nanorods. *Chem. Mater.* **2016**, *28*, 3454–3461.

(107) Kuznetsov, A. S. Effect of Proximity in Arrays of Plasmonic Nanoantennas on Hot Spots Density: Degenerate Semiconductors vs. Conventional Metals. *Plasmonics* **2016**, *11*, 1487–1493.

(108) Garcia, G.; Buonsanti, R.; Llordes, A.; Runnerstrom, E. L.; Bergerud, A.; Milliron, D. J. Near-Infrared Spectrally Selective Plasmonic Electrochromic Thin Films. *Adv. Opt. Mater.* **2013**, *1*, 215–220.

(109) Boschloo, G.; Fitzmaurice, D. Spectroelectrochemistry of Highly Doped Nanostructured Tin Dioxide Electrodes. *J. Phys. Chem. B* **1999**, *103*, 3093–3098.

(110) Runnerstrom, E. L.; Llordés, A.; Lounis, S. D.; Milliron, D. J. Nanostructured Electrochromic Smart Windows: Traditional Materials and NIR-Selective Plasmonic Nanocrystals. *Chem. Commun.* **2014**, *50*, 10555–10572.

(111) Wang, J.; Polleux, J.; Lim, J.; Dunn, B. Pseudocapacitive Contributions to Electrochemical Energy Storage in TiO_2 (Anatase) Nanoparticles. *J. Phys. Chem. C* **2007**, *111*, 14925–14931.

(112) Williams, T. E.; Chang, C. M.; Rosen, E. L.; Garcia, G.; Runnerstrom, E. L.; Williams, B. L.; Koo, B.; Buonsanti, R.; Milliron, D. J.; Helms, B. A. NIR-Selective Electrochromic Heteromaterial Frameworks: A Platform to Understand Mesoscale Transport Phenomena in Solid-State Electrochemical Devices. *J. Mater. Chem. C* **2014**, *2*, 3328.

(113) Wang, Y.; Runnerstrom, E. L.; Milliron, D. J. Switchable Materials for Smart Windows. *Annu. Rev. Chem. Biomol. Eng.* **2016**, *7*, 283–304.

(114) Melikyan, A.; Lindenmann, N.; Walheim, S.; Leufke, P. M.; Ulrich, S.; Ye, J.; Vincze, P.; Hahn, H.; Schimmel, T.; Koos, C.; *et al.* Surface Plasmon Polariton Absorption Modulator. *Opt Express* **2011**, *19*, 8855–8869.

(115) Sorger, V. J.; Lanzillotti-Kimura, N. D.; Ma, R.-M.; Zhang, X. Ultra-Compact Silicon Nanophotonic Modulator with Broadband Response. *Nanophotonics* **2012**, *1*, 17–22.

(116) Kinsey, N.; Ferrera, M.; Shalaev, V. M.; Boltasseva, A. Examining Nanophotonics for Integrated Hybrid Systems: A Review of Plasmonic Interconnects and Modulators Using Traditional and Alternative Materials [Invited]. *J. Opt. Soc. Am. B* **2015**, *32*, 121.

(117) Ung, T.; Giersig, M.; Dunstan, D.; Mulvaney, P. Spectroelectrochemistry of Colloidal Silver. *Langmuir* **1997**, *13*, 1773–1782.

(118) Novo, C.; Funston, A. M.; Gooding, A. K.; Mulvaney, P. Electrochemical Charging of Single Gold Nanorods. *J. Am. Chem. Soc.* **2009**, *131*, 14664–14666.

(119) Kim, M.; Kim, B. J.; Son, D.-Y.; Park, N.-G.; Jung, H. S.; Choi, M. Observation of Enhanced Hole Extraction in Br Concentration Gradient Perovskite Materials. *Nano Lett.* **2016**.

(120) Shen, Y.; Zhou, J.; Liu, T.; Tao, Y.; Jiang, R.; Liu, M.; Xiao, G.; Zhu, J.; Zhou, Z.-K.; Wang, X.; *et al.* Plasmonic Gold Mushroom Arrays with Refractive Index Sensing Figures of Merit Approaching the Theoretical Limit. *Nat. Commun.* **2013**, *4*.

(121) Lin, S.-Y.; Wu, S.-H.; Chen, C. A Simple Strategy for Prompt Visual Sensing by Gold Nanoparticles: General Applications of Interparticle Hydrogen Bonds. *Angew. Chem. Int. Ed.* **2006**, *45*, 4948–4951.

(122) Huttanus, H. M.; Graugnard, E.; Yurke, B.; Knowlton, W. B.; Kuang, W.; Hughes, W. L.; Lee, J. Enhanced DNA Sensing via Catalytic Aggregation of Gold Nanoparticles. *Biosens. Bioelectron.* **2013**, *50*, 382–386.

(123) De Jong, W. H.; Hagens, W. I.; Krystek, P.; Burger, M. C.; Sips, A. J. A. M.; Geertsma, R. E. Particle Size-Dependent Organ Distribution of Gold Nanoparticles after Intravenous Administration. *Biomaterials* **2008**, *29*, 1912–1919.

(124) Jiang, W.; Kim, B. Y. S.; Rutka, J. T.; Chan, W. C. W. Nanoparticle-Mediated Cellular Response Is Size-Dependent. *Nat. Nanotechnol.* **2008**, *3*, 145–150.

(125) Zhang, Y.; Wei, T.; Dong, W.; Huang, C.; Zhang, K.; Sun, Y.; Chen, X.; Dai, N. Near-Perfect Infrared Absorption from Dielectric Multilayer of Plasmonic Aluminum-Doped Zinc Oxide. *Appl. Phys. Lett.* **2013**, *102*, 213117.

(126) Bermel, P.; Boriskina, S. V.; Yu, Z.; Joulain, K. Control of Radiative Processes for Energy Conversion and Harvesting. *Opt. Express* **2015**, *23*, A1533.

(127) Boriskina, S. V.; Ghasemi, H.; Chen, G. Plasmonic Materials for Energy: From Physics to Applications. *Mater. Today* **2013**, *16*, 375–386.

(128) Lenert, A.; Bierman, D. M.; Nam, Y.; Chan, W. R.; Celanović, I.; Soljačić, M.; Wang, E. N. A Nanophotonic Solar Thermophotovoltaic Device. *Nat. Nanotechnol.* **2014**, *9*, 126–130.

(129) Adato, R.; Yanik, A. A.; Amsden, J. J.; Kaplan, D. L.; Omenetto, F. G.; Hong, M. K.; Erramilli, S.; Altug, H. Ultra-Sensitive Vibrational Spectroscopy of Protein Monolayers with Plasmonic Nanoantenna Arrays. *Proc. Natl. Acad. Sci.* **2009**, *106*, 19227–19232.

(130) Adato, R.; Altug, H. In-Situ Ultra-Sensitive Infrared Absorption Spectroscopy of Biomolecule Interactions in Real Time with Plasmonic Nanoantennas. *Nat. Commun.* **2013**, *4*.

(131) Kim, J.; Dutta, A.; Memarzadeh, B.; Kildishev, A. V.; Mosallaei, H.; Boltasseva, A. Zinc Oxide Based Plasmonic Multilayer Resonator: Localized and Gap Surface Plasmon in the Infrared. *ACS Photonics* **2015**, *2*, 1224–1230.

(132) Matsui, H.; Badalawa, W.; Hasebe, T.; Furuta, S.; Nomura, W.; Yatsui, T.; Ohtsu, M.; Tabata, H. Coupling of Er Light Emissions to Plasmon Modes on In2O3: Sn Nanoparticle Sheets in the near-Infrared Range. *Appl. Phys. Lett.* **2014**, *105*, 041903.

(133) Nath, N.; Chilkoti, A. A Colorimetric Gold Nanoparticle Sensor To Interrogate Biomolecular Interactions in Real Time on a Surface. *Anal. Chem.* **2002**, *74*, 504–509.

(134) McFadden, P. Broadband Biodetection: Holmes on a Chip. *Science* **2002**, *297*, 2075–2076.

(135) Otsuka, H.; Akiyama, Y.; Nagasaki, Y.; Kataoka, K. Quantitative and Reversible Lectin-Induced Association of Gold Nanoparticles Modified with α-Lactosyl-ω-Mercapto-Poly(ethylene Glycol). *J. Am. Chem. Soc.* **2001**, *123*, 8226–8230.

(136) Lee, K.-S.; El-Sayed, M. A. Gold and Silver Nanoparticles in Sensing and Imaging: Sensitivity of Plasmon Response to Size, Shape, and Metal Composition. *J. Phys. Chem. B* **2006**, *110*, 19220–19225.

(137) Anker, J. N.; Hall, W. P.; Lyandres, O.; Shah, N. C.; Zhao, J.; Van Duyne, R. P. Biosensing with Plasmonic Nanosensors. *Nat. Mater.* **2008**, *7*, 442–453.

(138) Willets, K. A.; Van Duyne, R. P. Localized Surface Plasmon Resonance Spectroscopy and Sensing. *Annu. Rev. Phys. Chem.* **2007**, *58*, 267–297.

(139) Sau, T. K.; Rogach, A. L.; Jäckel, F.; Klar, T. A.; Feldmann, J. Properties and Applications of Colloidal Nonspherical Noble Metal Nanoparticles. *Adv. Mater.* **2010**, *22*, 1805–1825.

(140) Arpin, K. A.; Losego, M. D.; Braun, P. V. Electrodeposited 3D Tungsten Photonic Crystals with Enhanced Thermal Stability. *Chem. Mater.* **2011**, *23*, 4783–4788.

(141) Campion, A.; Kambhampati, P. Surface-Enhanced Raman Scattering. *Chem. Soc. Rev.* **1998**, *27*, 241–250.

(142) Nie, S.; Emory, S. R. Probing Single Molecules and Single Nanoparticles by Surface-Enhanced Raman Scattering. *Science* **1997**, *275*, 1102–1106.

(143) Talley, C. E.; Jackson, J. B.; Oubre, C.; Grady, N. K.; Hollars, C. W.; Lane, S. M.; Huser, T. R.; Nordlander, P.; Halas, N. J. Surface-Enhanced Raman Scattering from Individual Au Nanoparticles and Nanoparticle Dimer Substrates. *Nano Lett.* **2005**, *5*, 1569–1574.

(144) Eustis, S.; El-Sayed, M. A. Why Gold Nanoparticles Are More Precious than Pretty Gold: Noble Metal Surface Plasmon Resonance and Its Enhancement of the Radiative and Nonradiative Properties of Nanocrystals of Different Shapes. *Chem. Soc. Rev.* **2006**, *35*, 209.

(145) Xu, H.; Bjerneld, E. J.; Käll, M.; Börjesson, L. Spectroscopy of Single Hemoglobin Molecules by Surface Enhanced Raman Scattering. *Phys. Rev. Lett.* **1999**, *83*, 4357–4360.

(146) Huang, X.; El-Sayed, M. A. Gold Nanoparticles: Optical Properties and Implementations in Cancer Diagnosis and Photothermal Therapy. *J. Adv. Res.* **2010**, *1*, 13–28.

(147) Huang, X.; Jain, P. K.; El-Sayed, I. H.; El-Sayed, M. A. Gold Nanoparticles: Interesting Optical Properties and Recent Applications in Cancer Diagnostics and Therapy. *Nanomed.* **2007**, *2*, 681–693.

(148) Huang, X.; El-Sayed, I. H.; Qian, W.; El-Sayed, M. A. Cancer Cell Imaging and Photothermal Therapy in the near-Infrared Region by Using Gold Nanorods. *J. Am. Chem. Soc.* **2006**, *128*, 2115–2120.

(149) Oldenburg, S. J.; Averitt, R. D.; Westcott, S. L.; Halas, N. J. Nanoengineering of Optical Resonances. *Chem. Phys. Lett.* **1998**, *288*, 243–247.

(150) Lal, S.; Clare, S. E.; Halas, N. J. Nanoshell-Enabled Photothermal Cancer Therapy: Impending Clinical Impact. *Acc. Chem. Res.* **2008**, *41*, 1842–1851.

(151) Jaque, D.; Maestro, L. M.; Rosal, B. del; Haro-Gonzalez, P.; Benayas, A.; Plaza, J. L.; Rodríguez, E. M.; Solé, J. G. Nanoparticles for Photothermal Therapies. *Nanoscale* **2014**, *6*, 9494–9530.

(152) Kneipp, K.; Kneipp, H.; Itzkan, I.; Dasari, R. R.; Feld, M. S. Ultrasensitive Chemical Analysis by Raman Spectroscopy. *Chem. Rev.* **1999**, *99*, 2957–2976.

(153) Hessel, C. M.; P. Pattani, V.; Rasch, M.; Panthani, M. G.; Koo, B.; Tunnell, J. W.; Korgel, B. A. Copper Selenide Nanocrystals for Photothermal Therapy. *Nano Lett.* **2011**, *11*, 2560–2566.

(154) Routzahn, A. L.; White, S. L.; Fong, L.-K.; Jain, P. K. Plasmonics with Doped Quantum Dots. *Isr. J. Chem.* **2012**, *52*, 983–991.

(155) Buonsanti, R.; Milliron, D. J. Chemistry of Doped Colloidal Nanocrystals. *Chem. Mater.* **2013**, *25*, 1305–1317.

(156) Lounis, S. D.; Runnerstrom, E. L.; Llordes, A.; Milliron, D. J. Defect Chemistry and Plasmon Physics of Colloidal Metal Oxide Nanocrystals. *J. Phys. Chem. Lett.* **2014**, *5*, 1564–1574.

(157) Kriegel, I.; Jiang, C.; Rodríguez-Fernández, J.; Schaller, R. D.; Talapin, D. V.; da Como, E.; Feldmann, J. Tuning the Excitonic and Plasmonic Properties of Copper Chalcogenide Nanocrystals. *J. Am. Chem. Soc.* **2011**, *134*, 1583–1590.

(158) Luther, J. M.; Jain, P. K.; Ewers, T.; Alivisatos, A. P. Localized Surface Plasmon Resonances Arising from Free Carriers in Doped Quantum Dots. *Nat. Mater.* **2011**, *10*, 361–366.

(159) Scotognella, F.; Valle, G. D.; Kandada, A. R. S.; Zavelani-Rossi, M.; Longhi, S.; Lanzani, G.; Tassone, F. Plasmonics in Heavily-Doped Semiconductor Nanocrystals. *Eur. Phys. J. B* **2013**, *86*, 1–13.

(160) Mattox, T. M.; Bergerud, A.; Agrawal, A.; Milliron, D. J. Influence of Shape on the Surface Plasmon Resonance of Tungsten Bronze Nanocrystals. *Chem. Mater.* **2014**, *26*, 1779–1784.

(161) Manthiram, K.; Alivisatos, A. P. Tunable Localized Surface Plasmon Resonances in Tungsten Oxide Nanocrystals. *J. Am. Chem. Soc.* **2012**, *134*, 3995–3998.

(162) Gordon, T. R.; Paik, T.; Klein, D. R.; Naik, G. V.; Caglayan, H.; Boltasseva, A.; Murray, C. B. Shape-Dependent Plasmonic Response and Directed Self-Assembly in a New Semiconductor Building Block, Indium-Doped Cadmium Oxide (ICO). *Nano Lett.* **2013**, *13*, 2857–2863.

(163) Farvid, S. S.; Radovanovic, P. V. Phase Transformation of Colloidal In2O3 Nanocrystals Driven by the Interface Nucleation Mechanism: A Kinetic Study. *J. Am. Chem. Soc.*, **2012**, *134*, 7015–7024.

(164) Lee, J.; Petruska, M. A.; Sun, S. Surface Modification and Assembly of Transparent Indium Tin Oxide Nanocrystals for Enhanced Conductivity. *J. Phys. Chem. C* **2014**, *118*, 12017–12021.

(165) Buonsanti, R.; Llordes, A.; Aloni, S.; Helms, B. A.; Milliron, D. J. Tunable Infrared Absorption and Visible Transparency of Colloidal Aluminum-Doped Zinc Oxide Nanocrystals. *Nano Lett.* **2011**, *11*, 4706–4710.

(166) Choi, S.-I.; Nam, K. M.; Park, B. K.; Seo, W. S.; Park, J. T. Preparation and Optical Properties of Colloidal, Monodisperse, and Highly Crystalline ITO Nanoparticles. *Chem. Mater.* **2008**, *20*, 2609–2611.

(167) Kanehara, M.; Koike, H.; Yoshinaga, T.; Teranishi, T. Indium Tin Oxide Nanoparticles with Compositionally Tunable Surface Plasmon Resonance Frequencies in the Near-IR Region. *J. Am. Chem. Soc.* **2009**, *131*, 17736–17737.

(168) Dorfs, D.; Härtling, T.; Miszta, K.; Bigall, N. C.; Kim, M. R.; Genovese, A.; Falqui, A.; Povia, M.; Manna, L. Reversible Tunability of the Near-Infrared Valence Band Plasmon Resonance in $Cu_{2-x}Se$ Nanocrystals. *J. Am. Chem. Soc.* **2011**, *133*, 11175–11180.

(169) Garcia, G.; Buonsanti, R.; Runnerstrom, E. L.; Mendelsberg, R. J.; Llordes, A.; Anders, A.; Richardson, T. J.; Milliron, D. J. Dynamically Modulating the Surface Plasmon Resonance of Doped Semiconductor Nanocrystals. *Nano Lett.* **2011**, *11*, 4415–4420.

(170) Llordes, A.; Garcia, G.; Gazquez, J.; Milliron, D. J. Tunable near-Infrared and Visible-Light Transmittance in Nanocrystal-in-Glass Composites. *Nature* **2013**, *500*, 323–326.

(171) Runnerstrom, E. L.; Llordes, A.; Lounis, S. D.; Milliron, D. J. Nanostructured Electrochromic Smart Windows: Traditional Materials and NIR-Selective Plasmonic Nanocrystals. *Chem. Commun.* **2014**, *50*, 10555–10572.

(172) Mendelsberg, R. J.; McBride, P. M.; Duong, J. T.; Bailey, M. J.; Llordes, A.; Milliron, D. J.; Helms, B. A. Plasmonic Nanocrystal Sensors That Optically Track (Bio)Chemical Redox Reactions with Single-Electron Sensitivity.

(173) Schimpf, A. M.; Lounis, S. D.; Runnerstrom, E. L.; Milliron, D. J.; Gamelin, D. R. Redox Chemistries and Plasmon Energies of Photodoped In_2O_3 and Sn-Doped In_2O_3 (ITO) Nanocrystals. *J. Am. Chem. Soc.* **2015**, *137*, 518–524.

(174) Mendelsberg, R. J.; Zhu, Y.; Anders, A. Determining the Nonparabolicity Factor of the CdO Conduction Band Using Indium Doping and the Drude Theory. *J. Phys. Appl. Phys.* **2012**, *45*, 425302.

(175) Zhu, Y.; Mendelsberg, R. J.; Zhu, J.; Han, J.; Anders, A. Dopant-Induced Band Filling and Bandgap Renormalization in CdO :In Films. *J. Phys. Appl. Phys.* **2013**, *46*, 195102.

(176) Mendelsberg, R. J.; Garcia, G.; Milliron, D. J. Extracting Reliable Electronic Properties from Transmission Spectra of Indium Tin Oxide Thin Films and Nanocrystal Films by Careful Application of the Drude Theory. *J. Appl. Phys.* **2012**, *111*, 063515.

(177) Kriegel, I.; Rodríguez-Fernández, J.; Wisnet, A.; Zhang, H.; Waurisch, C.; Eychmüller, A.; Dubavik, A.; Govorov, A. O.; Feldmann, J. Shedding Light on Vacancy-Doped Copper Chalcogenides: Shape-Controlled Synthesis, Optical Properties, and Modeling of Copper Telluride Nanocrystals with Near-Infrared Plasmon Resonances. *ACS Nano* **2013**, *7*, 4367–4377.

(178) Draine, B. T.; Flatau, P. J. Discrete-Dipole Approximation For Scattering Calculations. *J. Opt. Soc. Am. A* **1994**, *11*, 1491–1499.

(179) Flatau, P. J.; Draine, B. T. Fast near Field Calculations in the Discrete Dipole Approximation for Regular Rectilinear Grids. *Opt. Express* **2012**, *20*, 1247–1252.

(180) Hooshmand, N.; Bordley, J. A.; El-Sayed, M. A. Are Hot Spots between Two Plasmonic Nanocubes of Silver or Gold Formed between Adjacent Corners or Adjacent Facets? A DDA Examination. *J. Phys. Chem. Lett.* **2014**, *5*, 2229–2234.

(181) González, A. L.; Noguez, C. Optical Properties of Silver Nanoparticles. *Phys. Status Solidi C* **2007**, *4*, 4118–4126.

(182) Jefferson, P. H.; Hatfield, S. A.; Veal, T. D.; King, P. D. C.; McConville, C. F.; Zúñiga–Pérez, J.; Muñoz–Sanjosé, V. Bandgap and Effective Mass of Epitaxial Cadmium Oxide. *Appl. Phys. Lett.* **2008**, *92*, 022101.

(183) Wu, J.; Walukiewicz, W.; Shan, W.; Yu, K. M.; Ager, J. W.; Haller, E. E.; Lu, H.; Schaff, W. J. Effects of the Narrow Band Gap on the Properties of InN. *Phys Rev B* **2002**, *66*, 201403.

(184) Bohren, C. F.; Huffman, D. R. *Absorption and Scattering of Light by Samll Particles*.

(185) Stiegler, J. M.; Abate, Y.; Cvitkovic, A.; Romanyuk, Y. E.; Huber, A. J.; Leone, S. R.; Hillenbrand, R. Nanoscale Infrared Absorption Spectroscopy of Individual Nanoparticles Enabled by Scattering-Type Near-Field Microscopy. *ACS Nano* **2011**, *5*, 6494–6499.

(186) Notarianni, M.; Vernon, K.; Chou, A.; Aljada, M.; Liu, J.; Motta, N. Plasmonic Effect of Gold Nanoparticles in Organic Solar Cells. *Sol. Energy* **2014**, *106*, 23–37.

(187) Manna, L.; Milliron, D. J.; Meisel, A.; Scher, E. C.; Alivisatos, A. P. Controlled Growth of Tetrapod-Branched Inorganic Nanocrystals. *Nat. Mater.* **2003**, *2*, 382–385.

(188) Milliron, D. J.; Hughes, S. M.; Cui, Y.; Manna, L.; Li, J.; Wang, L.-W.; Paul Alivisatos, A. Colloidal Nanocrystal Heterostructures with Linear and Branched Topology. *Nature* **2004**, *430*, 190–195.

(189) Peng, X.; Manna, L.; Yang, W.; Wickham, J.; Scher, E.; Kadavanich, A.; Alivisatos, A. P. Shape Control of CdSe Nanocrystals. *Nature* **2000**, *404*, 59–61.

(190) Li, W.; Zamani, R.; Rivera Gil, P.; Pelaz, B.; Ibáñez, M.; Cadavid, D.; Shavel, A.; Alvarez-Puebla, R. A.; Parak, W. J.; Arbiol, J.; *et al.* CuTe Nanocrystals: Shape and Size Control, Plasmonic Properties, and Use as SERS Probes and Photothermal Agents. *J. Am. Chem. Soc.* **2013**, *135*, 7098–7101.

(191) Cobley, C. M.; Skrabalak, S. E.; Campbell, D. J.; Xia, Y. Shape-Controlled Synthesis of Silver Nanoparticles for Plasmonic and Sensing Applications. *Plasmonics* **2009**, *4*, 171–179.

(192) Chen, H.; Kou, X.; Yang, Z.; Ni, W.; Wang, J. Shape- and Size-Dependent Refractive Index Sensitivity of Gold Nanoparticles. *Langmuir* **2008**, *24*, 5233–5237.

(193) Zhang, S.; Bao, K.; Halas, N. J.; Xu, H.; Nordlander, P. Substrate-Induced Fano Resonances of a Plasmonic Nanocube: A Route to Increased-Sensitivity Localized Surface Plasmon Resonance Sensors Revealed. *Nano Lett.* **2011**, *11*, 1657–1663.

(194) Haes, A. J.; Zou, S.; Zhao, J.; Schatz, G. C.; Van Duyne, R. P. Localized Surface Plasmon Resonance Spectroscopy near Molecular Resonances. *J. Am. Chem. Soc.* **2006**, *128*, 10905–10914.

(195) Aroca, R. F.; Ross, D. J.; Domingo, C. Surface-Enhanced Infrared Spectroscopy. *Appl. Spectrosc.* **2004**, *58*, 324A–338A.

(196) Zuloaga, J.; Prodan, E.; Nordlander, P. Quantum Description of the Plasmon Resonances of a Nanoparticle Dimer. *Nano Lett.* **2009**, *9*, 887–891.

(197) Govorov, A. O.; Zhang, W.; Skeini, T.; Richardson, H.; Lee, J.; Kotov, N. A. Gold Nanoparticle Ensembles as Heaters and Actuators: Melting and Collective Plasmon Resonances. *Nanoscale Res. Lett.* **2006**, *1*, 84–90.

(198) Baffou, G.; Quidant, R.; Girard, C. Heat Generation in Plasmonic Nanostructures: Influence of Morphology. *Appl. Phys. Lett.* **2009**, *94*, 153109.

(199) Arnida; Malugin, A.; Ghandehari, H. Cellular Uptake and Toxicity of Gold Nanoparticles in Prostate Cancer Cells: A Comparative Study of Rods and Spheres. *J. Appl. Toxicol. JAT* **2010**, *30*, 212–217.

(200) Kayal, S.; Ramanujan, R. V. Anti-Cancer Drug Loaded Iron-Gold Core-Shell Nanoparticles (Fe@Au) for Magnetic Drug Targeting. *J. Nanosci. Nanotechnol.* **2010**, *10*, 5527–5539.

(201) Niu, L.; Cheng, K.; Wu, Y.; Wang, T.; Shi, Q.; Liu, D.; Du, Z. Sensitivity Improved Plasmonic Gold Nanoholes Array Biosensor by Coupling Quantum-Dots for the Detection of Specific Biomolecular Interactions. *Biosens. Bioelectron.* **2013**, *50*, 137–142.

(202) Barnes, W. L.; Dereux, A.; Ebbesen, T. W. Surface Plasmon Subwavelength Optics. *Nature* **2003**, *424*, 824–830.

(203) Maier, S. A.; Atwater, H. A. Plasmonics: Localization and Guiding of Electromagnetic Energy in Metal/Dielectric Structures. *J. Appl. Phys.* **2005**, *98*, 011101.

(204) Linic, S.; Christopher, P.; Ingram, D. B. Plasmonic-Metal Nanostructures for Efficient Conversion of Solar to Chemical Energy. *Nat. Mater.* **2011**, *10*, 911–921.

(205) Alvarez, M. M.; Khoury, J. T.; Schaaff, T. G.; Shafigullin, M. N.; Vezmar, I.; Whetten, R. L. Optical Absorption Spectra of Nanocrystal Gold Molecules. *J. Phys. Chem. B* **1997**, *101*, 3706–3712.

(206) Kelly, K. L.; Coronado, E.; Zhao, L. L.; Schatz, G. C. The Optical Properties of Metal Nanoparticles: The Influence of Size, Shape, and Dielectric Environment. *J. Phys. Chem. B* **2003**, *107*, 668–677.

(207) Pérez-Juste, J.; Pastoriza-Santos, I.; Liz-Marzán, L. M.; Mulvaney, P. Gold Nanorods: Synthesis, Characterization and Applications. *Coord. Chem. Rev.* **2005**, *249*, 1870–1901.

(208) Luther, J. M.; Jain, P. K.; Ewers, T.; Alivisatos, A. P. Localized Surface Plasmon Resonances Arising from Free Carriers in Doped Quantum Dots. *Nat. Mater.* **2011**, *10*, 361–366.

(209) Comin, A.; Manna, L. New Materials for Tunable Plasmonic Colloidal Nanocrystals. *Chem. Soc. Rev.* **2014**, *43*, 3957–3975.

(210) Lounis, S. D.; Runnerstrom, E. L.; Llordés, A.; Milliron, D. J. Defect Chemistry and Plasmon Physics of Colloidal Metal Oxide Nanocrystals. *J. Phys. Chem. Lett.* **2014**, *5*, 1564–1574.

(211) Hsu, S.-W.; Bryks, W.; Tao, A. R. Effects of Carrier Density and Shape on the Localized Surface Plasmon Resonances of Cu2–xS Nanodisks. *Chem. Mater.* **2012**, *24*, 3765–3771.

(212) Dorfs, D.; Härtling, T.; Miszta, K.; Bigall, N. C.; Kim, M. R.; Genovese, A.; Falqui, A.; Povia, M.; Manna, L. Reversible Tunability of the Near-Infrared

Valence Band Plasmon Resonance in Cu2–xSe Nanocrystals. *J. Am. Chem. Soc.* **2011**, *133*, 11175–11180.

(213) Kriegel, I.; Jiang, C.; Rodríguez-Fernández, J.; Schaller, R. D.; Talapin, D. V.; da Como, E.; Feldmann, J. Tuning the Excitonic and Plasmonic Properties of Copper Chalcogenide Nanocrystals. *J. Am. Chem. Soc.* **2012**, *134*, 1583–1590.

(214) Palomaki, P. K. B.; Miller, E. M.; Neale, N. R. Control of Plasmonic and Interband Transitions in Colloidal Indium Nitride Nanocrystals. *J. Am. Chem. Soc.* **2013**, *135*, 14142–14150.

(215) Buonsanti, R.; Llordes, A.; Aloni, S.; Helms, B. A.; Milliron, D. J. Tunable Infrared Absorption and Visible Transparency of Colloidal Aluminum-Doped Zinc Oxide Nanocrystals. *Nano Lett.* **2011**, *11*, 4706–4710.

(216) Rowe, D. J.; Jeong, J. S.; Mkhoyan, K. A.; Kortshagen, U. R. Phosphorus-Doped Silicon Nanocrystals Exhibiting Mid-Infrared Localized Surface Plasmon Resonance. *Nano Lett.* **2013**, *13*, 1317–1322.

(217) Schimpf, A. M.; Thakkar, N.; Gunthardt, C. E.; Masiello, D. J.; Gamelin, D. R. Charge-Tunable Quantum Plasmons in Colloidal Semiconductor Nanocrystals. *ACS Nano* **2014**, *8*, 1065–1072.

(218) Liu, M.; Xue, X.; Ghosh, C.; Liu, X.; Liu, Y.; Furlani, E. P.; Swihart, M. T.; Prasad, P. N. Room-Temperature Synthesis of Covellite Nanoplatelets with Broadly Tunable Localized Surface Plasmon Resonance. *Chem. Mater.* **2015**, *27*, 2584–2590.

(219) Agrawal, A.; Kriegel, I.; Milliron, D. J. Shape-Dependent Field Enhancement and Plasmon Resonance of Oxide Nanocrystals. *J. Phys. Chem. C* **2015**, *119*, 6227–6238.

(220) Kriegel, I.; Rodríguez-Fernández, J.; Wisnet, A.; Zhang, H.; Waurisch, C.; Eychmüller, A.; Dubavik, A.; Govorov, A. O.; Feldmann, J. Shedding Light on Vacancy-Doped Copper Chalcogenides: Shape-Controlled Synthesis, Optical Properties, and Modeling of Copper Telluride Nanocrystals with Near-Infrared Plasmon Resonances. *ACS Nano* **2013**, *7*, 4367–4377.

(221) Hsu, S.-W.; On, K.; Tao, A. R. Localized Surface Plasmon Resonances of Anisotropic Semiconductor Nanocrystals. *J. Am. Chem. Soc.* **2011**, *133*, 19072–19075.

(222) Momma, K.; Izumi, F. VESTA 3 for Three-Dimensional Visualization of Crystal, Volumetric and Morphology Data. *J. Appl. Crystallogr.* **2011**, *44*, 1272–1276.

(223) Hussain, A.; Gruehn, R.; Rüscher, C. H. Crystal Growth of Alkali Metal Tungsten Brozes MxWO3 (M □K, Rb, Cs), and Their Optical Properties. *J. Alloys Compd.* **1997**, *246*, 51–61.

(224) Mattox, T. M.; Bergerud, A.; Agrawal, A.; Milliron, D. J. Influence of Shape on the Surface Plasmon Resonance of Tungsten Bronze Nanocrystals. *Chem. Mater.* **2014**, *26*, 1779–1784.

(225) Manna, L.; Scher, E. C.; Alivisatos, A. P. Synthesis of Soluble and Processable Rod-, Arrow-, Teardrop-, and Tetrapod-Shaped CdSe Nanocrystals. *J. Am. Chem. Soc.* **2000**, *122*, 12700–12706.

(226) Noguez, C. Surface Plasmons on Metal Nanoparticles: The Influence of Shape and Physical Environment. *J. Phys. Chem. C* **2007**, *111*, 3806–3819.

(227) Ingham, B.; Hendy, S. C.; Chong, S. V.; Tallon, J. L. Density-Functional Studies of Tungsten Trioxide, Tungsten Bronzes, and Related Systems. *Phys. Rev. B* **2005**, *72*, 075109.

(228) Collins, S. M.; Ringe, E.; Duchamp, M.; Saghi, Z.; Dunin-Borkowski, R. E.; Midgley, P. A. Eigenmode Tomography of Surface Charge Oscillations of Plasmonic Nanoparticles by Electron Energy Loss Spectroscopy. *ACS Photonics* **2015**, *2*, 1628–1635.

(229) Kim, J.; Ong, G. K.; Wang, Y.; LeBlanc, G.; Williams, T. E.; Mattox, T. M.; Helms, B. A.; Milliron, D. J. Nanocomposite Architecture for Rapid, Spectrally-Selective Electrochromic Modulation of Solar Transmittance. *Nano Lett.* **2015**, *15*, 5574–5579.

(230) Agrawal, A.; Johns, R. W.; Milliron, D. Control of Localized Surface Plasmon Resonances in Metal Oxide Nanocrystals. Annu. Rev. Mater. Res. doi.org/10.1146/annurev-matsci-070616-124259.

(231) Akselrod, G. M.; Weidman, M. C.; Li, Y.; Argyropoulos, C.; Tisdale, W. A.; Mikkelsen, M. H. Efficient Nanosecond Photoluminescence from Infrared PbS Quantum Dots Coupled to Plasmonic Nanoantennas. *ACS Photonics* **2016**, *3*, 1741–1746.

(232) Hoang, T. B.; Akselrod, G. M.; Argyropoulos, C.; Huang, J.; Smith, D. R.; Mikkelsen, M. H. Ultrafast Spontaneous Emission Source Using Plasmonic Nanoantennas. *Nat. Commun.* **2015**, *6*, 7788.

(233) Lu, D.; Mao, C.; Cho, S. K.; Ahn, S.; Park, W. Experimental Demonstration of Plasmon Enhanced Energy Transfer Rate in NaYF4:Yb3+,Er3+ Upconversion Nanoparticles. *Sci. Rep.* **2016**, *6*, 18894.

(234) Yin, Z.; Zhou, D.; Xu, W.; Cui, S.; Chen, X.; Wang, H.; Xu, S.; Song, H. Plasmon-Enhanced Upconversion Luminescence on Vertically Aligned Gold Nanorod Monolayer Supercrystals. *ACS Appl. Mater. Interfaces* **2016**, *8*, 11667–11674.

(235) Catchpole, K. R.; Polman, A. Design Principles for Particle Plasmon Enhanced Solar Cells. *Appl. Phys. Lett.* **2008**, *93*, 191113.

(236) Yu, Z.; Raman, A.; Fan, S. Fundamental Limit of Nanophotonic Light Trapping in Solar Cells. *Proc. Natl. Acad. Sci.* **2010**, *107*, 17491–17496.

(237) Gan, Q.; Bartoli, F.; Kafafi, Z. Plasmonic Nanostructures Improve Solar Cell Performance. *SPIE Newsroom* **2013**.

(238) Stiles, P. L.; Dieringer, J. A.; Shah, N. C.; Duyne, R. P. V. Surface-Enhanced Raman Spectroscopy. *Annu. Rev. Anal. Chem.* **2008**, *1*, 601–626.

(239) Schlücker, S. Surface-Enhanced Raman Spectroscopy: Concepts and Chemical Applications. *Angew. Chem. Int. Ed.* **2014**, *53*, 4756–4795.

(240) Huck, C.; Neubrech, F.; Vogt, J.; Toma, A.; Gerbert, D.; Katzmann, J.; Härtling, T.; Pucci, A. Surface-Enhanced Infrared Spectroscopy Using Nanometer-Sized Gaps. *ACS Nano* **2014**, *8*, 4908–4914.

(241) Adato, R.; Artar, A.; Erramilli, S.; Altug, H. Engineered Absorption Enhancement and Induced Transparency in Coupled Molecular and Plasmonic Resonator Systems. *Nano Lett.* **2013**, *13*, 2584–2591.

(242) Wu, C.; Khanikaev, A. B.; Adato, R.; Arju, N.; Yanik, A. A.; Altug, H.; Shvets, G. Fano-Resonant Asymmetric Metamaterials for Ultrasensitive Spectroscopy and Identification of Molecular Monolayers. *Nat. Mater.* **2012**, *11*, 69–75.

(243) Bukasov, R.; Shumaker-Parry, J. S. Silver Nanocrescents with Infrared Plasmonic Properties As Tunable Substrates for Surface Enhanced Infrared Absorption Spectroscopy. *Anal. Chem.* **2009**, *81*, 4531–4535.

(244) Bühler, G.; Thölmann, D.; Feldmann, C. One-Pot Synthesis of Highly Conductive Indium Tin Oxide Nanocrystals. *Adv. Mater.* **2007**, *19*, 2224–2227.

(245) Kanehara, M.; Koike, H.; Yoshinaga, T.; Teranishi, T. Indium Tin Oxide Nanoparticles with Compositionally Tunable Surface Plasmon Resonance Frequencies in the Near-IR Region. *J. Am. Chem. Soc.* **2009**, *131*, 17736–17737.

(246) Buonsanti, R.; Llordes, A.; Aloni, S.; Helms, B. A.; Milliron, D. J. Tunable Infrared Absorption and Visible Transparency of Colloidal Aluminum-Doped Zinc Oxide Nanocrystals. *Nano Lett.* **2011**, *11*, 4706–4710.

(247) Schimpf, A. M.; Knowles, K. E.; Carroll, G. M.; Gamelin, D. R. Electronic Doping and Redox-Potential Tuning in Colloidal Semiconductor Nanocrystals. *Acc. Chem. Res.* **2015**, *48*, 1929–1937.

(248) Alici, K. B.; Gallardo, I. F. Detecting Secondary Structure and Surface Orientation of Helical Peptide Monolayers from Resonant Hybridization Signals. *Sci. Rep.* **2013**, *3*.

(249) Chattopadhyay, D.; Queisser, H. J. Electron Scattering by Ionized Impurities in Semiconductors. *Rev. Mod. Phys.* **1981**, *53*, 745–768.

(250) Auguié, B.; Barnes, W. L. Collective Resonances in Gold Nanoparticle Arrays. *Phys. Rev. Lett.* **2008**, *101*.

(251) Li, S.-Q.; Guo, P.; Buchholz, D. B.; Zhou, W.; Hua, Y.; Odom, T. W.; Ketterson, J. B.; Ocola, L. E.; Sakoda, K.; Chang, R. P. H. Plasmonic–Photonic Mode Coupling in Indium-Tin-Oxide Nanorod Arrays. *ACS Photonics* **2014**, *1*, 163–172.

(252) Urzhumov, Y. A.; Shvets, G.; Fan, J. A.; Capasso, F.; Brandl, D.; Nordlander, P. Plasmonic Nanoclusters: A Path towards Negative-Index Metafluids. *Opt. Express* **2007**, *15*, 14129.

(253) Yazdi, S.; Daniel, J. R.; Large, N.; Schatz, G. C.; Boudreau, D.; Ringe, E. Reversible Shape and Plasmon Tuning in Hollow AgAu Nanorods. *Nano Lett.* **2016**, *16*, 6939–6945.

(254) Nicoletti, O.; de la Peña, F.; Leary, R. K.; Holland, D. J.; Ducati, C.; Midgley, P. A. Three-Dimensional Imaging of Localized Surface Plasmon Resonances of Metal Nanoparticles. *Nature* **2013**, *502*, 80–84.

(255) Nelayah, J.; Kociak, M.; Stéphan, O.; García de Abajo, F. J.; Tencé, M.; Henrard, L.; Taverna, D.; Pastoriza-Santos, I.; Liz-Marzán, L. M.; Colliex, C. Mapping Surface Plasmons on a Single Metallic Nanoparticle. *Nat. Phys.* **2007**, *3*, 348–353.

(256) Kadkhodazadeh, S.; de Lasson, J. R.; Beleggia, M.; Kneipp, H.; Wagner, J. B.; Kneipp, K. Scaling of the Surface Plasmon Resonance in Gold and Silver Dimers Probed by EELS. *J. Phys. Chem. C* **2014**, *118*, 5478–5485.

(257) Barrow, S. J.; Collins, S. M.; Rossouw, D.; Funston, A. M.; Botton, G. A.; Midgley, P. A.; Mulvaney, P. Electron Energy Loss Spectroscopy Investigation into Symmetry in Gold Trimer and Tetramer Plasmonic Nanoparticle Structures. *ACS Nano* **2016**, *10*, 8552–8563.

(258) Leary, R. K.; Kumar, A.; Straney, P. J.; Collins, S. M.; Yazdi, S.; Dunin-Borkowski, R. E.; Midgley, P. A.; Millstone, J. E.; Ringe, E. Structural and Optical Properties of Discrete Dendritic Pt Nanoparticles on Colloidal Au Nanoprisms. *J. Phys. Chem. C* **2016**, *120*, 20843–20851.

(259) Ringe, E.; DeSantis, C. J.; Collins, S. M.; Duchamp, M.; Dunin-Borkowski, R. E.; Skrabalak, S. E.; Midgley, P. A. Resonances of Nanoparticles with Poor Plasmonic Metal Tips. *Sci. Rep.* **2015**, *5*, 17431.

(260) Funston, A. M.; Novo, C.; Davis, T. J.; Mulvaney, P. Plasmon Coupling of Gold Nanorods at Short Distances and in Different Geometries. *Nano Lett.* **2009**, *9*, 1651–1658.

(261) Rechberger, W.; Hohenau, A.; Leitner, A.; Krenn, J. R.; Lamprecht, B.; Aussenegg, F. R. Optical Properties of Two Interacting Gold Nanoparticles. *Opt. Commun.* **2003**, *220*, 137–141.

(262) Kuznetsov, A. S. Effect of Proximity in Arrays of Plasmonic Nanoantennas on Hot Spots Density: Degenerate Semiconductors vs. Conventional Metals. *Plasmonics* **2016**, *11*, 1487–1493.

(263) Diaz-Egea, C.; Sigle, W.; van Aken, P. A.; Molina, S. I. High Spatial Resolution Mapping of Surface Plasmon Resonance Modes in Single and Aggregated Gold Nanoparticles Assembled on DNA Strands. *Nanoscale Res. Lett.* **2013**, *8*, 337.

(264) Hu, H.; Yang, X.; Zhai, F.; Hu, D.; Liu, R.; Liu, K.; Sun, Z.; Dai, Q. Far-Field Nanoscale Infrared Spectroscopy of Vibrational Fingerprints of Molecules with Graphene Plasmons. *Nat. Commun.* **2016**, *7*, 12334.

(265) Huck, C.; Vogt, J.; Sendner, M.; Hengstler, D.; Neubrech, F.; Pucci, A. Plasmonic Enhancement of Infrared Vibrational Signals: Nanoslits versus Nanorods. *ACS Photonics* **2015**, *2*, 1489–1497.

(266) Neubrech, F.; Beck, S.; Glaser, T.; Hentschel, M.; Giessen, H.; Pucci, A. Spatial Extent of Plasmonic Enhancement of Vibrational Signals in the Infrared. *ACS Nano* **2014**, *8*, 6250–6258.

(267) Fan, S.; Suh, W.; Joannopoulos, J. D. Temporal Coupled-Mode Theory for the Fano Resonance in Optical Resonators. *JOSA A* **2003**, *20*, 569–572.

(268) Haus, H. A. *Waves and Fields in Optoelectronics*; Prentice Hall, Incorporated, 1984.

(269) Suh, W.; Wang, Z.; Fan, S. Temporal Coupled-Mode Theory and the Presence of Non-Orthogonal Modes in Lossless Multimode Cavities. *IEEE J. Quantum Electron.* **2004**, *40*, 1511–1518.

(270) Faucheaux, J. A.; Jain, P. K. Plasmons in Photocharged ZnO Nanocrystals Revealing the Nature of Charge Dynamics. *J. Phys. Chem. Lett.* **2013**, *4*, 3024–3030.

(271) Garcia, G.; Buonsanti, R.; Runnerstrom, E. L.; Mendelsberg, R. J.; Llordes, A.; Anders, A.; Richardson, T. J.; Milliron, D. J. Dynamically Modulating the Surface Plasmon Resonance of Doped Semiconductor Nanocrystals. *Nano Lett.* **2011**, *11*, 4415–4420.

(272) Melikyan, A.; Lindenmann, N.; Walheim, S.; Leufke, P. M.; Ulrich, S.; Ye, J.; Vincze, P.; Hahn, H.; Schimmel, T.; Koos, C.; *et al.* Surface Plasmon Polariton Absorption Modulator. *Opt. Express* **2011**, *19*, 8855.

(273) Cheng, H.; Qian, X.; Kuwahara, Y.; Mori, K.; Yamashita, H. A Plasmonic Molybdenum Oxide Hybrid with Reversible Tunability for Visible-Light-Enhanced Catalytic Reactions. *Adv. Mater.* **2015**, *27*, 4616–4621.

(274) Mendelsberg, R. J.; Garcia, G.; Milliron, D. J. Extracting Reliable Electronic Properties from Transmission Spectra of Indium Tin Oxide Thin Films and Nanocrystal Films by Careful Application of the Drude Theory. *J. Appl. Phys.* **2012**, *111*, 063515.

(275) Boles, M. A.; Ling, D.; Hyeon, T.; Talapin, D. V. The Surface Science of Nanocrystals. *Nat. Mater.* **2016**, *15*, 141–153.

(276) Kilina, S. V.; Tamukong, P. K.; Kilin, D. S. Surface Chemistry of Semiconducting Quantum Dots: Theoretical Perspectives. *Acc. Chem. Res.* **2016**, *49*, 2127–2135.

(277) Houtepen, A. J.; Hens, Z.; Owen, J. S.; Infante, I. On the Origin of Surface Traps in Colloidal II–VI Semiconductor Nanocrystals. *Chem. Mater.* **2017**, *29*, 752–761.

(278) Bard, A. J.; Bocarsly, A. B.; Fan, F. R. F.; Walton, E. G.; Wrighton, M. S. The Concept of Fermi Level Pinning at Semiconductor/Liquid Junctions. Consequences for Energy Conversion Efficiency and Selection of Useful Solution Redox Couples in Solar Devices. *J. Am. Chem. Soc.* **1980**, *102*, 3671–3677.

(279) Carroll, G. M.; Schimpf, A. M.; Tsui, E. Y.; Gamelin, D. R. Redox Potentials of Colloidal N-Type ZnO Nanocrystals: Effects of Confinement, Electron Density, and Fermi-Level Pinning by Aldehyde Hydrogenation. *J. Am. Chem. Soc.* **2015**, *137*, 11163–11169.

(280) Gassenbauer, Y.; Schafranek, R.; Klein, A.; Zafeiratos, S.; Hävecker, M.; Knop-Gericke, A.; Schlögl, R. Surface States, Surface Potentials, and Segregation at Surfaces of Tin-Doped In_2O_3 *Phys Rev B* **2006**, *73*, 245312.

(281) Li, W.; Zamani, R.; Rivera Gil, P.; Pelaz, B.; Ibáñez, M.; Cadavid, D.; Shavel, A.; Alvarez-Puebla, R. A.; Parak, W. J.; Arbiol, J.; *et al.* CuTe Nanocrystals: Shape and Size Control, Plasmonic Properties, and Use as SERS Probes and Photothermal Agents. *J. Am. Chem. Soc.* **2013**, *135*, 7098–7101.

(282) Sturaro, M.; Della Gaspera, E.; Michieli, N.; Cantalini, C.; Emamjomeh, S. M.; Guglielmi, M.; Martucci, A. Degenerately Doped Metal Oxide Nanocrystals as Plasmonic and Chemoresistive Gas Sensors. *ACS Appl. Mater. Interfaces* **2016**, *8*, 30440–30448.

(283) Mattox, T. M.; Agrawal, A.; Milliron, D. J. Low Temperature Synthesis and Surface Plasmon Resonance of Colloidal Lanthanum Hexaboride (LaB6) Nanocrystals. *Chem. Mater.* **2015**, *27*, 6620–6624.

(284) Ephraim, J.; Lanigan, D.; Staller, C.; Milliron, D. J.; Thimsen, E. Transparent Conductive Oxide Nanocrystals Coated with Insulators by Atomic Layer Deposition. *Chem. Mater.* **2016**, *28*, 5549–5553.

(285) Space Charge Calculations for Semiconductors. *J. Appl. Phys.* **1958**, *29*, 1034–1040.

(286) Mendelsberg, R. J.; Garcia, G.; Li, H.; Manna, L.; Milliron, D. J. Understanding the Plasmon Resonance in Ensembles of Degenerately Doped Semiconductor Nanocrystals. *J. Phys. Chem. C* **2012**, *116*, 12226–12231.

(287) Berggren, K.-F.; Sernelius, B. E. Band-Gap Narrowing in Heavily Doped Many-Valley Semiconductors. *Phys. Rev. B* **1981**, *24*, 1971–1986.

(288) Hamberg, I.; Granqvist, C. G.; Berggren, K.-F.; Sernelius, B. E.; Engström, L. Band-Gap Widening in Heavily Sn-Doped In_2O_3. *Phys. Rev. B* **1984**, *30*, 3240–3249.

(289) Haase, M.; Weller, H.; Henglein, A. Photochemistry and Radiation Chemistry of Colloidal Semiconductors. 23. Electron Storage on Zinc Oxide Particles and Size Quantization. *J. Phys. Chem.* **1988**, *92*, 482–487.

(290) Templeton, A. C.; Pietron, J. J.; Murray, R. W.; Mulvaney, P. Solvent Refractive Index and Core Charge Influences on the Surface Plasmon Absorbance of Alkanethiolate Monolayer-Protected Gold Clusters. *J. Phys. Chem. B* **2000**, *104*, 564–570.

(291) Saha, K.; Agasti, S. S.; Kim, C.; Li, X.; Rotello, V. M. Gold Nanoparticles in Chemical and Biological Sensing. *Chem. Rev.* **2012**, *112*, 2739–2779.

(292) Fan, X.; Zheng, W.; Singh, D. J. Light Scattering and Surface Plasmons on Small Spherical Particles. *Light Sci. Appl.* **2014**, *3*, e179.